BRNO UNIVERSITY OF TECHNOLOGY

VYSOKÉ UČENÍ TECHNICKÉ V BRNĚ

CENTRAL EUROPEAN INSTITUTE OF TECHNOLOGY BUT

STŘEDOEVROPSKÝ TECHNOLOGICKÝ INSTITUT VUT

PREPARATION OF CHITIN NANOFIBRILS AND THEIR MEDICAL APPLICATIONS

PŘÍPRAVA CHITINOVÝCH NANOFIBRILY A JEJICH MEDICÍNSKÉ APLIKACE

DOCTORAL THESIS

DIZERTAČNÍ PRÁCE

AUTHOR — **Rasha Radwan, M.Sc.**

AUTOR PRÁCE

SUPERVISOR — **prof. RNDr. Josef Jančář, CSc.**

ŠKOLITEL

BRNO 2024

Abstract

This thesis investigates the preparation of chitin nanocrystals with varying degrees of deacetylation and their use as nanofillers to enhance the performance properties of polysaccharide and protein matrices. The study covers fabrication of different material forms, such as films, hydrogel membranes, and 3D scaffolds, using chitin nanocrystals and chitosan-glucan fibril complexes as fillers. The extraction process of chitin nanocrystals from shrimp shells and chitin-based fibril structures from nonanimal sources like Aspergillus niger was optimized by examining the influence of pH, reaction temperature, and time on the degree of deacetylation.

Hyaluronan films incorporating chitin nanocrystals were prepared via an evaporation-induced self-assembly method, resulting in significant enhancements in their chemophysical, mechanical, and biological properties. Additionally, a supramolecular self-assembly nanocomposite hydrogel membrane composed of collagen and chitin nanocrystals was created using the same process, producing layered hydrogel membranes (LHMs). These LHMs demonstrated improved mechanical properties, cytocompatibility, and controlled drug release using Octenidine dihydrochloride (OCT) as a model drug. The combination of collagen and chitin nanocrystals significantly increased modulus, strength, and toughness compared to native collagen, while also improving cytocompatibility and cell adhesion. These insights offer valuable guidance for designing LHMs for medical applications, including controlled drug release and tissue regeneration.

A 3D hybrid scaffold based on collagen grafted with fibrils of the chitosan-glucan complex (CO-g-CSGCF-HBS) was fabricated using a freeze drying technique. Modification of collagen with CSGCF significantly enhanced the scaffold's chemophysical properties, hydrolytic stability, and mechanical strength. In vitro studies showed that the hybrid scaffold improved cell viability using mesenchymal stem cells (MSCs) and exhibited a higher antibacterial reduction rate compared to control samples. The chemical modification of collagen with various ratios of CSGCF significantly improved the scaffold's physicochemical, bactericidal, and cell adhesion properties of the scaffold, indicating its potential for therapeutic and biomedical applications, particularly in bone regeneration.

Keywords:

Chitin nanocrystals, deacetylation, hyaluronan, collagen, chitosan-glucan complex, self-assembly, hydrogel membranes, drug release, 3D scaffolds, mesenchymal stem cells, antibacterial properties, tissue regeneration.

Abstrakt

Tato práce se zabývá přípravou nanokrystalů chitinu s různým stupněm deacetylace a jejich použití jako nanoplnivo pro zvýšení funkčních vlastností hyaluronových a proteinových matric. Studie pokrývá přípravu filmů, hydrogelových membrány a 3D buněčných nosičů, s použitím chitinových nanokrystalů a komplexů chitosan-glukanových fibril jako plniv. Proces extrakce chitinových nanokrystalů z krunýřů krevet a fibrilových struktur na bázi chitinu z neživočišných zdrojů, jako je Aspergillus niger, byl optimalizován nalezením vlipu pH, reakční teploty a časum na stupeň deacetylace. Hyaluronové filmy obsahující chitinové nanokrystaly byly připraveny metodou samouspořádávání vyvolané odpařováním rozpouštědla, což vedlo k významnému zlepšení jejich chemicko-fyzikálních, mechanických a biologických vlastností. Kromě toho byla stejným postupem vytvořena supramolekulární nanokompozitní hydrogelová membrána složená z nanokrystalů kolagenu a chitinu, a byly vytvořeny vrstvené hydrogelové membrány (LHM). Tyto LHM prokázaly zlepšené mechanické vlastnosti, cytokompatibilitu a řízené uvolňování léčiva s použitím Octenidin dihydrochloridu (OCT) jako modelového léčiva. Kombinace nanokrystalů kolagenu a chitinu významně zvýšila modul pružnosti, pevnost a houževnatost ve srovnání s nativním kolagenem a zároveň zlepšila cytokompatibilitu a buněčnou adhezi. Tyto poznatky nabízejí cenné vodítko pro navrhování LHM pro lékařské aplikace, včetně řízeného uvolňování léčiv a regenerace tkání.

3D hybridní buněčné nosiče založené na kolagenu roubovaném fibrilami komplexu chitosan-glukan (CO-g-CSGCF-HBS) byly připraveny za použití techniky lyofilizace. Modifikace kolagenu pomocí CSGCF významně zlepšila chemickofyzikální vlastnosti nosiče, hydrolytickou stabilitu a mechanickou pevnost. Studie in vitro ukázaly, že hybridní nosič zlepšilo životaschopnost mezenchymálních kmenových buněk (MSC) a vykazovalo vyšší míru antibakteriálního působení ve srovnání s kontrolními vzorky. Chemická modifikace kolagenu s různými poměry CSGCF významně zlepšila fyzikálně-chemické, bakteriocidní a adhezní vlastnosti nosiče, což apotvrzuje jeho potenciál pro terapeutické a biomedicínské aplikace, zejména při regeneraci kostí.

Klíčová slova

Chitinové nanokrystaly, deacetylace, hyaluronanu, kolagen, komplex chitosan-glukan, samouspořádávání, hydrogelové membrány, uvolňování léčiv, 3D buněčné nosiče, mezenchymální kmenové buňky, antibakteriální vlastnosti, regenerace tkání.

Declaration

I hereby declare that, except where specific reference is made to the work of others, the contents of this dissertation are original and have not been submitted in whole or in part for consideration for any other degree or qualification in this or any other university. This dissertation is my work and contains nothing which is the outcome of work done in collaboration with others, except as specified in the text and acknowledgments. This dissertation includes fewer than 44,500 words including Appendices, Bibliography, Footnotes, Tables, and equations, and has fewer than 42 figures.

Rasha Radwan
July 2024

Acknowledgment

First and foremost, I thank ALLAH to whom I attribute my success in my work.

I would like to sincerely and gratefully thank my supervisor prof. RNDr. Josef Jančář, CSc for all his valuable support, supervision, patience, useful discussions, understanding, careful reading, and facilities he provided for the completion of this work.

I also acknowledge all my colleagues who cooperated with me in this work.
I deeply thank all my family members and especially my husband for all his encouragement, assistance, and love.

Introduction

Natural biomaterials such as polysaccharides and proteins are gaining significant interest in medical and cosmetic fields due to their inherent biocompatibility and presence in the human body. Hyaluronic acid and collagen, key components of skin and connective tissues, have found extensive applications across these industries. However, drawbacks such as poor mechanical properties and rapid degradation often limit their practical use.

To address these challenges, this thesis explores the integration of chitin nanocrystals to enhance the mechanical and biological properties of both hyaluronan and collagen biomaterials. *In Chapter 1* the foundation theoretical insights with the latest advancements in the fields of polysaccharide nanocrystals, collagen, and the anionic polysaccharide hyaluronan are discussed. This interdisciplinary approach aims to create a robust and comprehensive qualitative framework, enhancing the understanding of polysaccharide nanocrystals and their interactions. *In Chapter 2* chitin nanocrystals (ChNCs) are synthesized from raw chitin. It investigates the nuanced effects of acidic hydrolysis conditions, specifically, the acidity, duration, and pH, on the colloidal stability and crystalline characteristics of the ChNCs. Additionally, the chapter examines how varying degrees of deacetylation influence the stability of ChNCs. A detailed study of the formulation of stable, transparent hyaluronan films incorporating ChNCs, optimizing these composites for enhanced performance. The relationship between the volume fractions of ChNCs and hyaluronan (HA) is analyzed to understand their impact on the thermal, physicochemical, mechanical, and biological properties of the resulting hybrid materials.

Chapter 3 focuses on the innovative application of partially deacetylated ChNCs, produced in *Chapter 2*, to fabricate multifunctional hydrogel membranes. These membranes are composed of collagen (CO) and ChNCs, assembled through a self-assembly process in the presence of the model drug Octenidine dihydrochloride (OCT). This chapter delves into the role of ChNCs as nanofiller biomaterials, systematically investigating how different volume fractions of nanocrystals affect the physical, chemical, mechanical, stability, and biological attributes of the hydrogel membranes. Furthermore, it explores the piezoelectric properties of collagen and the enhancement of these properties by chitin nanocrystals (ChNCs), introducing novel mechanoelectric performance metrics through the development of structurally piezoelectric hydrogel membranes.

Chapter 4 shifts focus to the use of innovative chitin fibril derivatives, specifically the chitosan-glucan fibril complex (CGC), derived from non-animal sources like Aspergillus niger, for the creation of 3D scaffold materials. This chapter investigates the chemical interactions between collagen (CO) and CGC, achieved without the use of cross-linking agents. Provides an in-depth analysis of how different ratios of CGC influence the mechanical, morphological, and biological properties of the collagen scaffold, striving for optimized material formulations.

Chapter 5 concludes the study by summarizing the key findings and providing critical reflections on the research results. It also outlines future directions for nanofiller ChNCs research, highlighting potential advancements and applications in this evolving field.

Table of contents

Chapter 1

STATE OF THE ART

1. Chitin and chitosan

Chitin is a ubiquitous biopolymer found in a diverse array of organisms, including insects, crustaceans, arachnids, mollusks, and fungi[1, 2]. This remarkable substance not only provides structural support but also offers additional functionalities, such as striking structural coloration and crack-resistant shells[3].

A significant amount of chitin is discarded as waste in the fishing and food industries because the tough shells of crustaceans, unlike their tender inner flesh, are not suitable for human consumption[1, 4]. Chitin makes up to 30% of the dry mass of crustacean shells, representing an abundant, inexpensive, and sustainable resource. Consequently, crustacean shells are currently the most accessible raw source of chitin[1]. These mechanically robust shells contain calcium carbonate, proteins, and pigments in addition to chitin. However, purifying chitin is relatively straightforward due to its chemical inertness, a property derived from its molecular structure.

Chitin is a linear polysaccharide composed of repeating β-(1-4)-N-acetyl-D-glucosamine monomers, which offer numerous sites for hydrogen bonding (Fig. 1)[5, 6]. The individual chitin molecular chains organize into elementary fibrils with tight packing[1, 7]. This organization, along with its molecular structure, renders chitin chemically inert compared to proteins, calcium carbonate, and pigments. Therefore, mild acidic and basic conditions are sufficient to dissolve calcium carbonate and proteins, while any remaining red-orange pigments can be removed through gentle bleaching, resulting in pure chitin[1, 8].

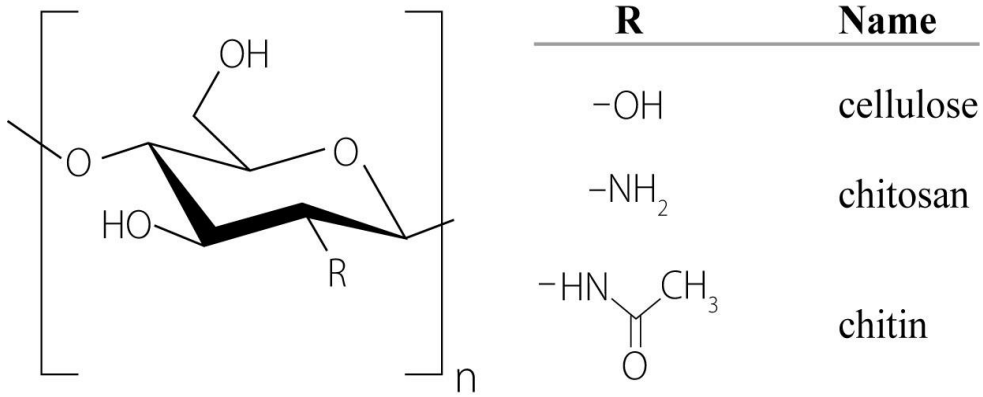

Fig. 1. Molecular structure of cellulose, chitin, and chitosan. While they differ only by a single substituent, the resulting physicochemical properties are significantly different.

1.1. Properties of Chitin and Chitosan

The physical and chemical characteristics of chitin are closely related to its hierarchical molecular organization and its source[1, 5, 9]. In nature, chitin molecules arrange themselves in a circular fashion.

parallel (β) or anti-parallel (α) formations, known as crystalline allomorphs. The α-chitin, where molecular chains are antiparallel, forms tightly packed sheets stabilized by intra-sheet hydrogen bonds from hydroxy and amide groups[10]. This arrangement renders α-chitin fibers resistant to most solvents, exhibiting minimal swelling and reactivity. Consequently, α-chitin is the predominant allomorph found in crustaceans, insects, arachnids, fungi, and various other organisms[10-12].

In contrast, β-chitin occurs in unique organisms like mollusks or Riftia pachyptila worms, where molecular chains align parallel to each other[13, 14]. β-chitin is a metastable allomorph that can convert to more stable α-chitin under certain conditions, such as base treatment, as identified through techniques like X-ray diffraction, FTIR, and solid-state NMR spectroscopy[1, 15]. Natural chitin extracted from sources is typically imperfect, with β-(1-4)-*N*-acetyl-D-glucosamine monomers often partially deacetylated[9]. This partial deacetylation means some amide groups are replaced by amine groups, primarily on the surface molecular chains of chitin fibrils. The extent of deacetylation, quantified as the degree of deacetylation, significantly alters the physical properties of chitin. When this degree surpasses 50 %, chitin becomes soluble in acidic aqueous environments[9, 16]. This soluble form of chitin is termed chitosan, arguably the most significant derivative of chitin[16]. Chitosan is typically produced by deacetylating chitin using concentrated alkali solutions rather than enzymatic methods. In acidic conditions, the protonation of chitosan's amine groups[5, 10]. ($pKa_H \approx 6.3$) induces strong electrostatic repulsion between chains, enhancing the polymer's hydrophilicity and solubility in aqueous solvents (Fig.1)[6, 17]. This deacetylation process is essential, as chitin itself is insoluble in most common solvents unless treated with high concentrations of sodium hydroxide[17].

Chitosan's versatility and affordability have led to its widespread use across diverse industries. It serves as an antimicrobial agent in agriculture, activates plant defense mechanisms, acts as a flocculating agent in wastewater treatment, enhances food products, moisturizes cosmetics, and finds applications in pharmaceuticals for wound healing and biodegradable plastics[17, 18]. Despite these applications, significant quantities of chitin are still discarded, suggesting potential for its valorization as a novel nanomaterial with broader environmental and industrial benefits[1, 12, 19].

1.2. Origin, biological and chemical properties of chitin and chitosan

Chitin is widely distributed across various organisms, comprising anywhere from 3 % to over 40 % of their mass composition[10, 19]. Commercially significant sources of chitin include insects, fungi, and crustaceans, with crustaceans, in particular, being the most utilized. Unlike other polysaccharides in the biosphere, chitin exhibits a unique combination of crystalline morphology and a protein-interfacing interface, which facilitates strong and specific interactions with proteins[10]. This characteristic positions chitin as a structural polymer embedded within a protein matrix, particularly prominent in the exoskeletons of insects, crustaceans, and fungi, as well as in certain microorganisms[10, 15].

The multi-scaled structures and chemical composition of chitin, derived from its biological origins, play a crucial role in defining the properties of nanochitin[1, 16]. This section introduces the diverse sources of chitin and explores its hierarchical structures, highlighting their functional roles, especially in biological structures' optomechanical properties[7, 20]. Furthermore, we delve into the chemistry of different chitin polymorphs found in nature, discussing both laboratory processes and commercial-scale extraction methods. Finally, we examine the biological activities of chitin post-extraction, underscoring its significance in various biomedical and industrial applications[9, 21].

1.2.1. Biological Origins of Chitin and Chitosan

Chitin is found in a wide variety of organisms, each with distinct molecular structures[22] (Fig. 2). This section introduces the sources of chitin and their primary characteristics. Despite the diversity among different groups of organisms, such as terrestrial and marine species, fungi, and insects, research has focused on a limited number of species for chitosan and chitin applications. Often, these species are linked to waste streams, including silkworm larvae, seafood byproducts, and food waste from insect biomass[23, 24]. However, a vast array of organisms produce chitin, including nearly all insects, fungi, crustaceans, seashells, and mollusks. Chitin serves multiple purposes for these organisms, such as providing structural support during growth, enhancing mechanical strength and toughness, regulating opacity and light reflection, facilitating adhesion and communication, and acting as a defense mechanism against microorganisms and environmental stress[24-26].

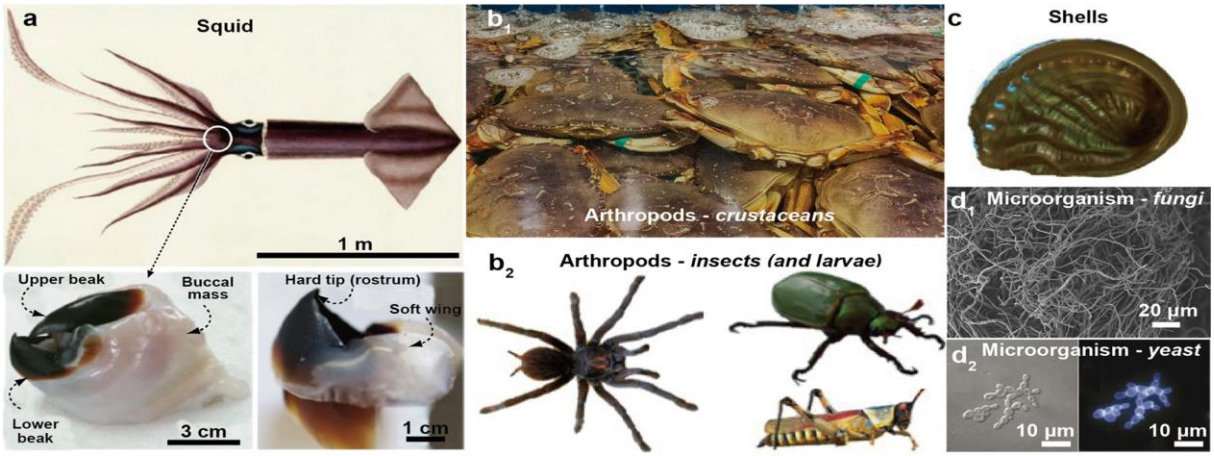

Fig. 2. Chitin is found in a variety of organisms, such as (a) squid, particularly in their beaks and pens (adapted with permission from ref[27]. Copyright 2008 American Association for the Advancement of Science); (b) arthropods, including (b1) crustaceans and (b2) insects and their larvae; (c) shells from terrestrial, river, or sea mollusks; and microorganisms such as (d1) fungi and (d2) yeast. In d1, the dispersed mycelium is harvested from Aspergillus niger, and in d2, the yeast pseudohyphae are stained with Calcofluor white (adapted with permission from refs [28, 29]. Copyright 2021 and 2002, respectively, Springer Nature).

1.2.2. Structure of Chitin in Other Organisms

In addition to arthropods, fungi also contain chitin, which varies between 10-30 % of their dry mass126. In fungi, chitin is primarily found in the mitotic ring of fungal cells[30] and in the growing hyphal tips[31]. The deacetylated form of chitin, known as chitosan, is also present in fungal cell walls. Chitin within fungi is organized into a branched structure composed of β-1,3 and β-1,6 glycans within a hydrated amorphous matrix (Fig. 3)[32]. This structure can be found at the core or edges of the branched polysaccharide superstructure (Fig. 3a)[33, 34]. Chitin synthases in fungi are located primarily within chitosomes (Fig. 3b), spherical lipid-protein assemblies that are 40-70 nm in diameter with a membrane thickness of approximately 7 nm[35]. These structures transport chitin synthase, a membrane-bound protein, to the cell surface where chitin nanofibrils are formed[36].

Other chitin-forming organisms are believed to be used by other chitin-forming organisms for the translocation of chitin synthases. For example, a high density of these synthases has been observed in the apical region of insect microvilli[37]. Like cellulosomes for cellulose, these membrane-bound enzymes produce polymers and fibrils through interfacial biogenesis. In mushrooms, cell walls contain microfibrils superstructured into triple helices, consisting of glucans sparsely branched by chitin fibers. In the mycelium, the vegetative growth

state of fungal filaments, a network rich in chitin and other glucans, forms the three-dimensional architecture of the growing organism[38, 39]. Nematodes and single-celled organisms such as yeast and protozoa also produce chitin[40]. However, in these organisms, chitin may serve more functional than structural functions, as chains are relatively short and contribute to the hydrophilicity of cell walls[41]. In yeast, chitin also plays a role in cell mitosis[42].

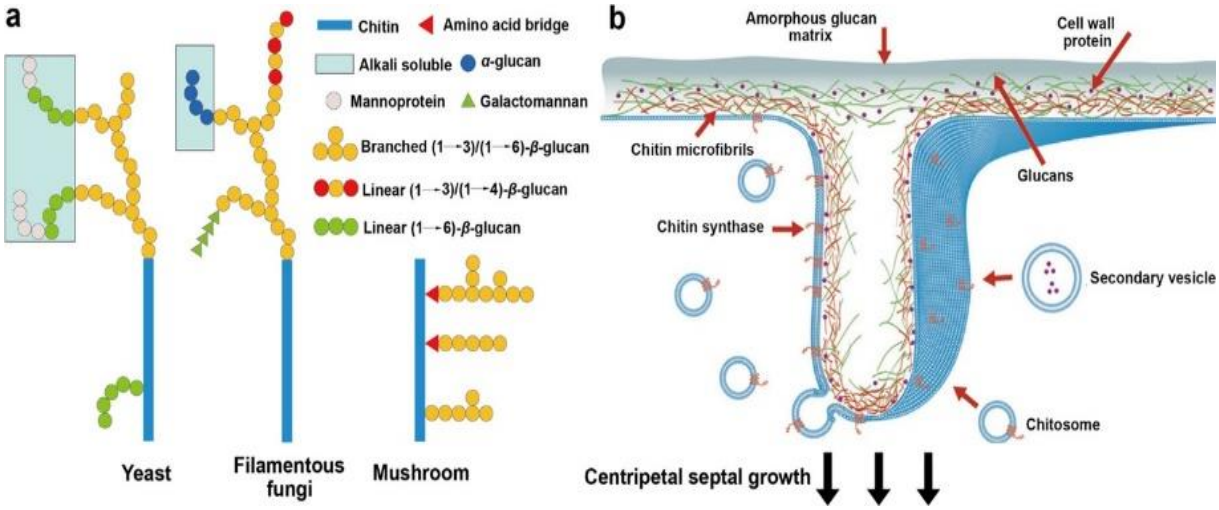

Fig. 3. (a) Schematic illustration showing chitinous structures found in microorganisms. Models of the chitin-glucan complex include Saccharomyces cerevisae and Candida albicans for yeast, Aspergillus fumigatus for filamentous fungi, and *Schizophyllum commune* for the mushroom. Adapted from ref[38, 43]. Copyright 2020 American Chemical Society. (b) Three-dimensional schematic illustration of the use of chitosome, a chitin-generating complex, and its structure in fungi. Adapted from ref[44, 45]. Copyright 2013 Elsevier.

1.3. Nanochitin Structures and Mechanical Resilience

In addition to nanoscale brick-and-mortar architectures, insects and crustaceans possess a variety of structures that improve energy dissipation (Fig. 4)[46, 47]. These structures are optimized at different scales to dissipate compressive, tensile, or flexural stresses from multiple directions. In contrast, materials like collagen, silk, or cellulose nanofibrils (CNF) have simpler, though still multiscale conformations. Collagen and silk are generally aligned, while cellulose twists around cell walls[48]. Chitinous architectures in arthropods often feature Bouligand structures, stacked and rotated fibrous microstructures that form lamellae or layers reminiscent of plywood (Fig. 4). Aligned fibrils create isotropy in the plane, with adjacent layers progressively rotated relative to each other. This helicoidal structure effectively deflects fractures and cracks based on the twist angle, usually less than 10°, allowing three-dimensional

stress dissipation and resistance to delamination. These hierarchical structures are often combined with complex topographical features, resulting in curved, periodic structures or spheroidal contours. For instance, the mantis shrimp's hammer-like appendage, which combines strength and toughness, can easily fracture seashell nacre despite both being mineralized structures made of proteins and chitin[49-51].

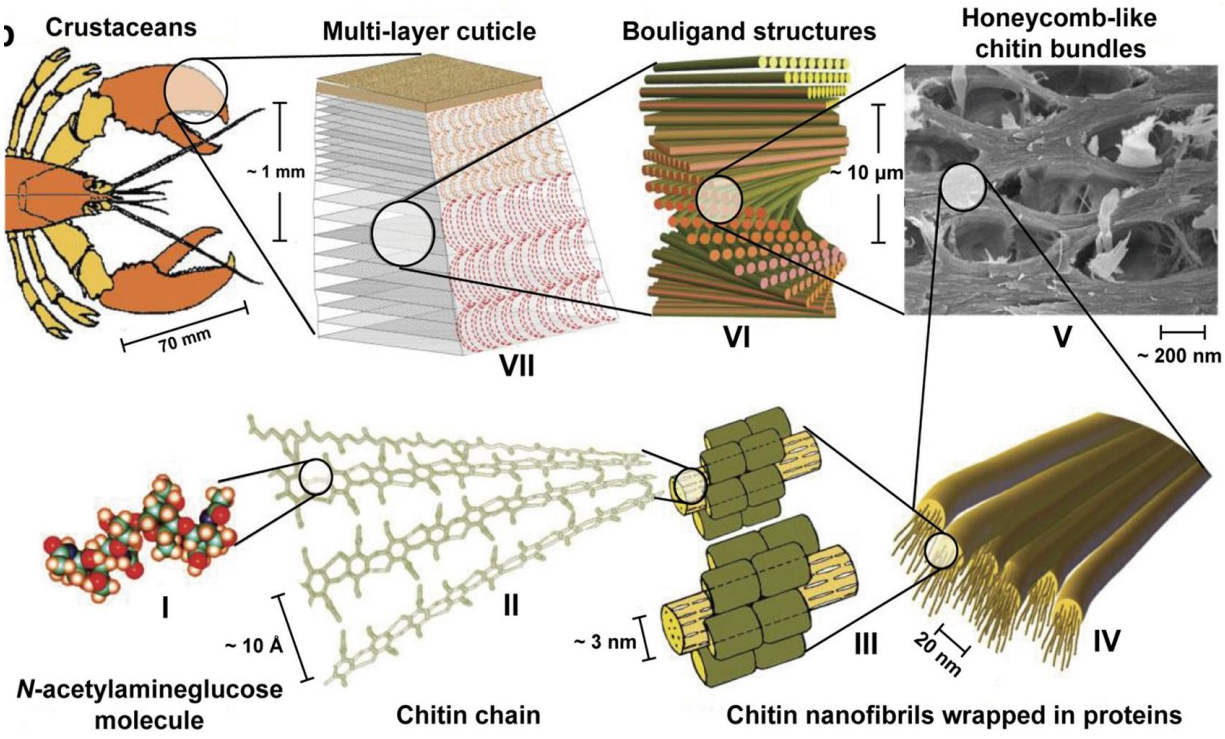

Fig. 4. displays a variety of chitinous structures in biological constructs, highlighting the multiscale arrangements found in crustaceans. The monomeric unit (I) polymerizes into chitin polymers (II), which bundle with proteins that have specific binding sites (III). These bundles form optimized structures for fracture deflection and strain-dependent responses, such as the honeycomb structure (V) and the helicoidal Bouligand structures seen in the cuticle at multiple scales (VI, VII) (adapted with permission from ref[52]. Copyright 2010 John Wiley and Sons). Panel (c1) presents a plane view of the diabolical ironclad beetle, showing distinct internal regions with variable spacing between organs and elytra. Panel (c2) depicts the jigsaw-shaped joints in the beetle that sequentially delaminate (right panel: computed tomography reconstruction of fractured suture), contributing to its exceptional compression resistance in the animal kingdom (adapted with permission from ref[53]. Copyright 2020 Springer Nature).

1.4. Chitin Structural Chemistry

Chitin, a prevalent amino polysaccharide, exhibits a complex molecular organization that involves ring structures within macromolecules and various interactions, both covalent and

supramolecular, that define its functions in organisms where it is synthesized. Nanofibrils and microfibrils interact via hydrogen bonding between amine and carbonyl groups, with small crystalline domains embedded within pseudocrystalline and amorphous regions along the fibrils. The primary crystalline allomorphs—α-, *β*-, and γ-chitin (Fig. 5) display directional properties regarding their reducing ends, which exist in equilibrium between the closed ring and the open aldehyde forms. In α-chitin, chains are arranged antiparallelly, whereas *β*-chitin features a parallel arrangement, and γ-chitin includes two parallel chains neighboring one antiparallel chain (Fig. 5a)[54, 55]. α-Chitin is the most abundant allomorph found in fungal and yeast cell walls, as well as in arthropods such as crustaceans and insects. Compared to cellulose fibrils, chitin nanofibrils are generally less polar, but remain highly hydrated in most animals before tanning. Their hydrophobicity can be enhanced by biosynthesized hydrophobic proteins[55].

β-Chitin exhibits reduced hydrogen bonding interactions compared to α-chitin, forming softer fibrils that are more susceptible to hydrolysis and swelling. α-Chitin is associated with rigid materials, while *β*- and *γ*-chitins contribute to more flexible structures[2].

α-Chitin, an insoluble allomorph in most solvents, forms orthorhombic crystals with both inter- and intrasheet bonding (Fig. 5b). The theoretical axial elastic modulus of α-chitin is 150 GPa, with an experimental value around 59 GPa[56]. The crystalline allomorph influences the surface energy of different facets; for instance, the (010) face of α-chitin matches the spacing of hydrogen bonding groups found in proteinaceous β-sheets like silk[57]. This face is suggested to have strong interactions with proteins in general, and protein residues are expected to be present on this face after fiber isolation[57]. *β*-Chitin, found in structures like the squid pen and beak, forms monoclinic crystals without intersheet bonds (Fig. 5c)[58-60]. It is more susceptible to deacetylation and transformation into α-chitin under specific conditions[60, 61]. Despite its insolubility in many solvents, *β*-chitin exhibits better solubility than α-chitin in formic acid[62]. γ-Chitin, rare in nature, exists in organisms such as certain squid species or beetles[62]. It decomposes at lower temperatures than α-chitin and exhibits microscaled fibers tightly bonded in extracted forms, such as from moth cocoons, showing slower digestion rates compared to α- and *β*-chitin[63].

The solubility of chitin in aqueous media varies with the crystal allomorph and degree of surface acetylation[64]. Chitosan, a highly deacetylated form of chitin, forms viscous acid solutions and is generally insoluble above pH 6 due to its pKa of 6.3[65]. Also, chitin is insoluble in water under any pH conditions, although inorganic salts like $Ca(CNS)_2$, CaI_2, $CaBr_2$, or $CaCl_2$ have been found to aid in its dissolution. The dissolution and regeneration of

chitin produce materials with properties highly dependent on the solvents used[55]. For instance, chitin dissolved in lithium chloride/dimethylacetamide at 2 wt. % forms lyotropic liquid crystals (LCs) whose phase transitions are concentration-dependent, enhancing the long-range order of regenerated fibers[66]. Chitin exhibits thermotropic behavior where phase transitions vary with temperature[67].

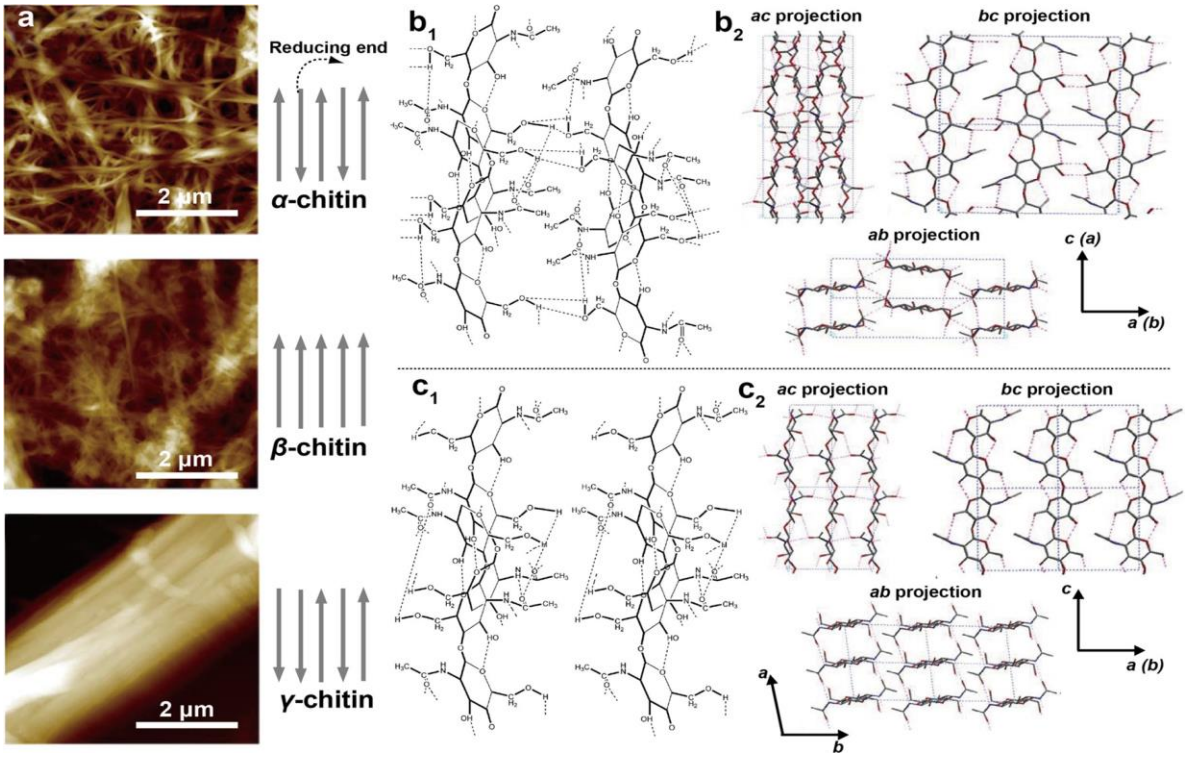

Fig. 5. depicts the three primary polymorphs of chitin. (a) Atomic force microscopy (AFM) images show α-chitin extracted from crab shells (Potamon ibericum), *β*-chitin from squid pens (Sepia sp.), and γ-chitin from moth cocoons (Orgyia dubia), obtained through the same acid/base extraction process (adapted with permission from ref [63]. Copyright 2017 Elsevier). The gray arrows indicate the orientation of chitin macromolecules within the crystalline domains, pointing away from the reducing end. Molecular structures and hydrogen bonding in (b1) α-chitin and (c1) *β*-chitin are illustrated, noting the absence of intersheet bonding in *β*-chitin (Adapted with permission from ref[64]. Copyright 2009 Elsevier). The structure of (b2) α-chitin and (c2) *β*-chitin in different projection planes (ac, bc, and ab) is also presented (adapted with permission from ref[68]. Copyright 2006 Elsevier).

1.5. Chitin Surface Chemistry

Chitin's surface chemistry is characterized by its unique cationic nature resulting from the hydrolysis of surface acetyl groups, which profoundly influences the properties of nanochitin. This discussion focuses on the chemistry of these surface groups, their distribution

along the polymer chain synthesized in biological systems, their interaction with the surrounding matrix, and the resulting superstructures upon extraction[69]. The presence of amine groups, stemming from varying degrees of deacetylation (DDA), is crucial. Below pH 6, ammonium ions carry a positive charge in aqueous environments, facilitating long-range electrostatic interactions that predominate over short-range hydrogen bonding[69]. At pH > 6, interactions among hydroxyls, ethers, acetyls, and amines contribute to a complex network of intracrystalline and interfacial hydrogen bonds. Additionally, the ether and acetyl groups, being less polar, contribute to the amphiphilicity of chitin[69].

The number and distribution of amine groups depend significantly on the chitin source and processing methods. For example, fungi typically yield β-chitin with high deacetylation due to the hydrated nature of their crystals. On the contrary, the chitin of the endocuticles and exocuticles is highly acetylated (> 98%)[16, 70, 71]. Initial deacetylation predominantly affects groups outside crystalline domains and amorphous regions, typically deacetylating one group per every two glucose units initially. This results in a broad distribution of degrees of deacetylation in chitin samples, with some fractions predominantly charged and others minimally charged[72]. Compared to cellulose, the presence of amine groups simplifies modification pathways, enabling diverse functionalization approaches[72]. The amino and hydroxyl groups offer dual functionality for modification, facilitating orthogonal chemistry and enhancing reactivity. This versatility supports applications such as hydrophobic modification to reduce hydrophilicity or improve compatibility with other surfaces. In addition, amine groups facilitate coordination bonds with heavy metals, making chitin suitable for applications in water remediation and heavy metal separation[69, 73].

In chitin extracted from arthropods, surface chemistry is influenced by residual proteinaceous residues post-extraction, which contribute to strong supramolecular and covalent interactions. Protein-chitin interactions are optimized when proteins form β-sheet domains that match the spacing between chitin's saccharide units. Chitinases and other chitin-binding domains further strengthen these interactions[74]. Conversely, chitin extracted from fungi is often contaminated with other glucans, impacting its surface chemistry and accessibility. The source of fungal chitin significantly affects surface charge properties, such as the zeta potential of nanofibrils, which varies between different fungal species and extraction methods[75].

1.6. Extraction and purification of chitin and chitosan

Chitin extraction from crustacean shells typically involves a series of steps aimed at purifying and preparing nanochitin. Initially, the process starts with chitin extraction, followed by demineralization (DM), deproteinization (DP), and discoloration to remove minerals[76],

proteins, and pigments from the shells[69, 71] (Fig. 6). DM involves acid-base reactions to release water-soluble calcium salts and carbon dioxide, requiring multiple cycles depending on the source and intended application of chitin. Various pretreatments such as size reduction, drying, grinding, sieving, and wet processing are employed to facilitate extraction efficiency before DM and DP. For instance, pretreating with hot glycerol has been shown to enhance chitin extraction from prawn shells, while treatments with substances like sodium hypochlorite optimize processing times and energy consumption[9, 10, 77].

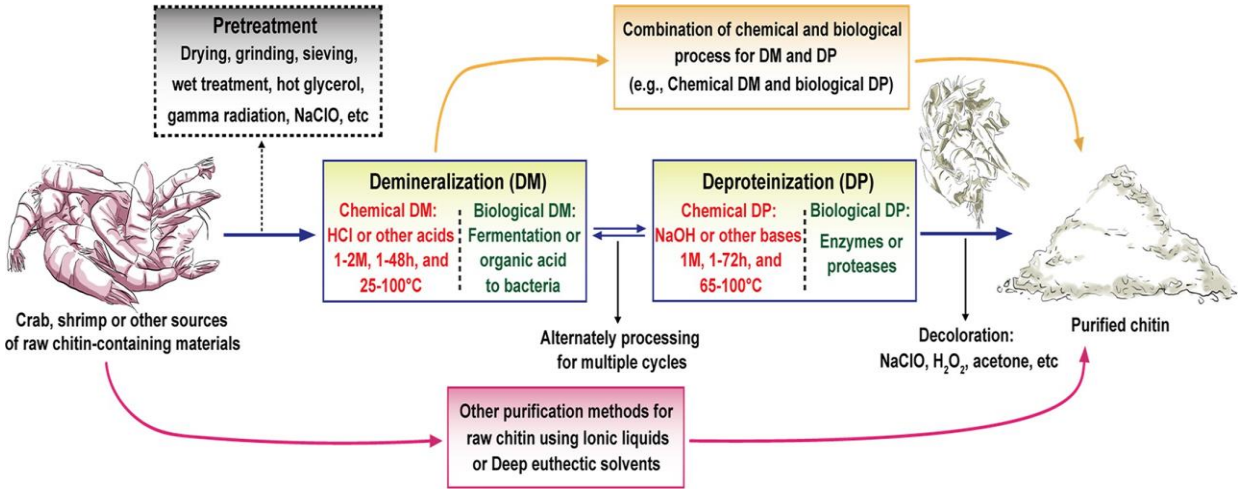

Fig. 6. Overview of the extraction of chitin from crustacean shells that involves demineralization (DM), deproteinization (DP), and discoloration (all shown in solid boxes), as well as alternative pretreatments (dashed box). New extraction methods are emerging given considerations of environmental impact and sustainability. Adapted with permission from ref[69]. Copyright 2020 Springer Nature.

In DM, acids like HCl (typically 0.3−2 M concentration, 1−48 hours, 25−100 °C) are commonly used to dissolve minerals from the shells[71, 78]. Other acids such as HNO_3, H_2SO4, CH_3COOH, HCOOH, and $C_6H_8O_7$, alone or in combination, have also been effective. Conversely, DP involves treating shells with alkaline solutions like NaOH (typically 1 M concentration, 1−72 hours, 25−100 °C) to dissolve proteins adhered to chitin. Alternative alkaline reagents such as Na_2CO_3, $NaHCO_3$, KOH, K_2CO_3, $Ca(OH)_2$, Na_2SO_3, $NaHSO_3$, $CaHSO_3$, Na_3PO_4, and Na_2S have been successfully used in DP processes[79, 80] (Fig. 6).
Despite the effectiveness of chemical extraction methods, there are environmental concerns related to solubilized minerals and proteins that are not recovered or reused. Recent efforts focus on developing environmentally friendly chemical methods and exploring biological routes, such as enzymatic treatments using proteases or microbial fermentation. These biological approaches aim to minimize environmental impact and recover valuable byproducts,

such as proteins and pigments, for reuse. Although biological processes offer environmental advantages, they often require longer processing times and are more costly compared to chemical methods, limiting their scalability beyond laboratory settings[80, 81]. In addition, recent developments in ionic liquids and deep eutectic solvents show promise for chitin extraction because of their efficiency and environmental friendliness. For example, 1-ethyl-3-methylimidazolium acetate has been used to solubilize and precipitate chitin from shrimp shells, demonstrating the potential for practical application despite current limitations in supply, scale and cost considerations[82-84].

1.7. Nanochitin: Chitin Nanofibrils (ChNFs) and Chitin Nanocrystals (ChNCs)

Nanochitin, which encompasses chitin nanofibrils and chitin nanocrystals, represents a burgeoning field of nanotechnology with diverse applications in biomedical, environmental, and industrial domains. Derived from chitin, a ubiquitous biopolymer found in crustacean shells, insects, and fungi, these nanostructures exhibit unique properties that distinguish them as promising materials for advanced applications. This exploration delves into the structural characteristics, synthesis methods, properties, and applications of nanochitin, shedding light on their potential and current state of research.

1.7.1. Isolation of Nanochitin

The isolation of fibrillar chitin is of significant interest due to its potential structural, chemical, and biological advantages derived from its morphological and nanoscale characteristics[85, 86]. A widely adopted approach for this purpose is the top-down method, which allows for the preservation of chitin's semicrystalline structures and 1D nanofibrous morphology, thereby enhancing its intrinsic properties. Typically, two main types of nanochitin can be isolated: chitin nanofibers (ChNFs) and chitin nanocrystals (ChNCs), as depicted in Fig. 7. The properties of nanochitin are influenced by the source of chitin, the conditions used for its isolation and modification, and the specific requirements for its intended applications[86, 87]. The process of isolating ChNFs involves mechanical fibrillation of chitin bundles, resulting in nanoscale lateral dimensions and enhanced interfibrillar repulsion, often facilitated by the ionized surfaces of the nanofibrils that encompass both amorphous and crystalline regions (Fig. 7a). In contrast, the production of ChNCs requires chemical methods that exfoliate the surface of chitin nanofibrils and eliminate disordered chitin structures to obtain ordered, crystalline forms (Fig. 7b). Therefore, the isolation of ChNF typically employs

mechanical nanofibrillation with the aid of chemical or biological processes, while strong acid hydrolysis or oxidation is used for the production of ChNCs[84, 86].

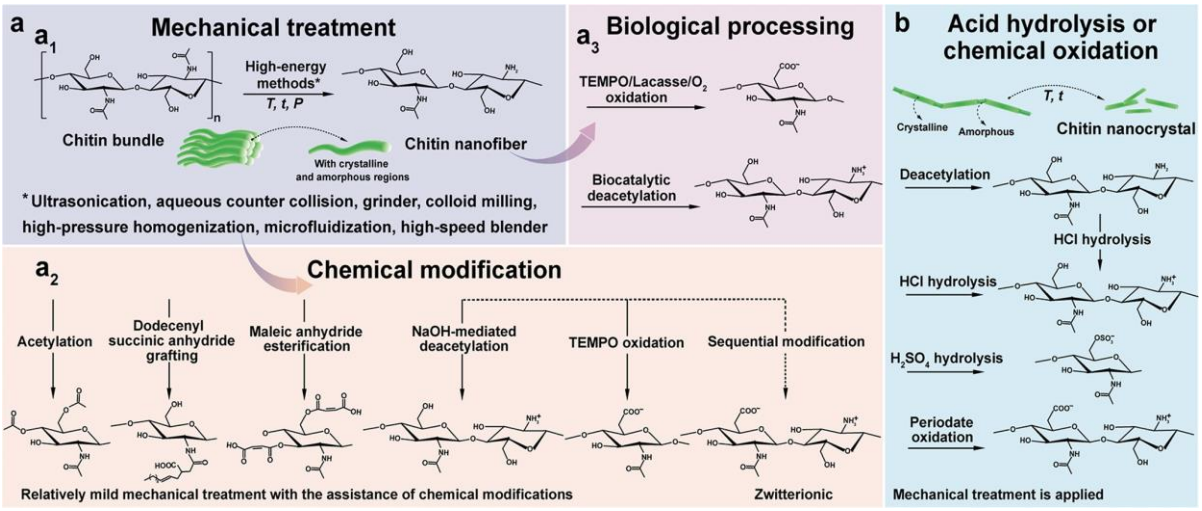

Fig. 7. Overview of the methods used for isolation of (a) ChNFs and (b) ChNCs. ChNFs containing crystalline and disordered structures are produced by (a1) mechanical treatment or mechanical treatment assisted by (a2) chemical modification and (a3) biological processing. The main goal of the chemical and biological modifications is to endow additional chemical features that facilitate mechanical fibrillation. ChNCs are produced by surface exfoliation and by removal of disordered chitin structures using strong chemical processing with acids or oxidizing agents. Adapted from ref[69]. Copyright 2016 American Chemical Society.

1.7.2. Isolation of Chitin Nanofibrils (ChNFs)

1.7.2.1. Mechanical Treatment

Chitin nanofibers (ChNF) isolated through mechanical nanofibrillation exhibit long, fibril-like structures ranging from submicrometer to micrometres in length, with widths spanning from a few nanometers to tens of nanometers[69]. The resulting high aspect ratio depends on the chitin source and the mechanical treatment applied. Several mechanical methods for chitin nanofibrillation are depicted in Fig. 7a[69, 88].

Ultrasonication is a high-energy method that disassembles natural chitin fibers into ChNF. For instance, ultrasonication at 20 kHz, 900–1000W for 30 minutes in neutral pH water produces nanofibers with widths of 25–120 nm (Fig. 8a)[88]. This process relies on acoustic cavitation, where high-frequency sound waves create, grow, and collapse microbubbles in water, generating microjets and shock waves that etch and disintegrate chitin fibers along their length. Ultrasonication can also be conducted in acidic media (pH 3-4), producing a transparent, viscous suspension of individualized ChNF with lengths of several micrometers

and widths of 3-4 nm from squid pen β-chitin under short processing times and low energy input. The protonation of amino groups on the crystalline surface of β-chitin in an acidic medium facilitates efficient nanofibrillation due to electrostatic repulsion, a condition less effective for crab α-chitin due to its high degree of acetylation and strong intermolecular forces[89, 90].

Grinding is another mechanical method that breaks down chitin into ChNFs through continuous shear generated between grinding stones. For example, never-dried crab chitin passed through a grinder at pH 3, 1500 rpm, and a 0.15 mm milling gap results in a gel-like suspension of long nanofibers with widths of 10–20 nm (Fig. 8b). Dried chitin powder from crab shells can also be fibrillated via grinding under acidic conditions, yielding ChNF with high aspect ratios similar to those obtained from never-dried chitin[91]. Electrostatic repulsion generated by amino groups in an acidic medium aids in breaking strong hydrogen bonds between nanofibers. Additionally, ChNFs with 10–20 nm width can be prepared directly from prawn shells using grinding at 1500 rpm in neutral pH water. The finer structure of prawn exoskeletons compared to crab shells facilitates easier disintegration even under weak electrostatic repulsion[90, 91].

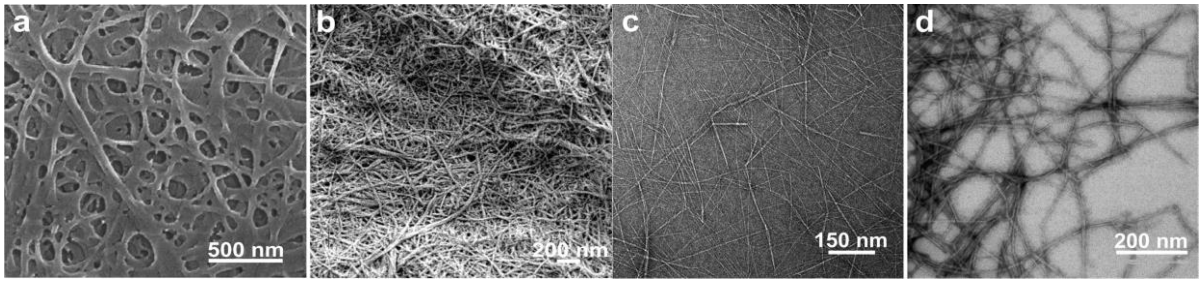

Fig. 8. Microscopic images display ChNFs obtained through standard mechanical nanofibrillation methods. SEM images show (a) ChNFs derived from chitin using ultrasonication in water and (b) ChNFs from crab shell α-chitin after a single-pass grinding in an acetic acid medium. Adapted with permission from ref[92]. Copyright 2007 AIP Publishing LLC. Adapted from ref[91]. Copyright 2009 American Chemical Society. TEM micrographs depict (c) ChNFs from squid pen β-chitin via one-pass microfluidization in an acetic acid medium and (d) low-protein ChNFs from lobster exoskeletons by microfluidization. Adapted with permission from ref[93]. Copyright 2019 The Royal Society of Chemistry. Adapted with permission from ref[94]. Copyright 2014 Elsevier.

High-pressure homogenization is a widely used method to produce ChNF from bulk materials. For instance, dynamic high-pressure homogenization of lobster residues at 1000 bar for 40

passes yields nanofibers with widths of 80–100 nm and high aspect ratios. This method does not require acids or chemical treatments, preserving the chemical and crystalline structure of chitin[95-97]. However, high-pressure homogenization can alter surface properties. For example, ChNFs prepared from crab shell chitin through repeated high-pressure homogenization (200 MPa, 10 passes) in water form a heterogeneous network of nanochitin with widths ranging from a few nanometres to several tens of manometers. Solid-state ^{13}C NMR spectra indicate unchanged chemical shifts, but the weight-average molar mass of ChNFs is about 60 % of the original chitin, and the degree of acetylation (DA) increases from 0.83 to 0.98, showing partial removal of C2-NH_2 groups[97].

Microfluidization is another high-energy method used to produce ChNFs. For example, squid pen *β*-chitin can be fibrillated into ChNFs with lengths of 1–3 μm and widths of 2–7 nm using one-pass microfluidization in acetic acid (Fig. 13c). The presence of amino groups, indicated by a DA of 99%, is crucial for the efficient nanofibrillation of chitin bundles. Microfluidization can also produce protein-containing ChNFs from mineral-free chitin. For instance, lobster exoskeletons processed through microfluidization (5 passes, 900 and 1600 bar) yield individual ChNFs with widths of 3–4 nm and low protein content (Fig. 13d)[98]. A combined mechanical defibrillation approach involving grinding, microfluidization, and homogenization can produce ChNFs without altering their chemical or structural features. This staged process results in nanofibers longer than 1 μm and approximately 50 nm wide[93, 94].

1.7.2.2. Isolation of Chitin Nanocrystals (ChNCs)

The process of isolating chitin nanocrystals (ChNCs) involves the removal of amorphous chitin domains, which loosens the fibrillar structure and facilitates easier nanofibrillation through mechanical treatment (Fig. 7b)[99]. Unlike chitin nanofibers (ChNFs), ChNCs are characterized by their well-ordered structure, resulting in higher crystallinity[99]. These nanocrystals have a rod-like morphology with a shorter length and smaller aspect ratio. To produce ChNCs, strong acid hydrolysis and chemical oxidation are commonly used methods, though other top-down approaches, such as treatment with acidic deep eutectic solvents, are also viable options[100, 101]. The efficiency and properties of ChNCs, including their morphology, crystalline structure, and crystallinity, depend on the chitin source and the method of preparation, influencing their physicochemical performance. However, a significant drawback of these methods is the low yield due to the loss of amorphous material and chitin depolymerization[102].

1.7.2.3. Strong Acid Hydrolysis

The process of using acid hydrolysis to isolate chitin nanocrystals (ChNCs) was first reported in 1959, where purified α-chitin from crab shells was hydrolyzed with 2.5 M HCl for one hour using a reflux system, followed by homogenization through three passes[103]. This method produced a stable suspension of ChNCs exhibiting nematic liquid crystal (LC) ordering, positioning HCl as a viable acid for chitin hydrolysis. Additionally, sulfuric acid and maleic acid have been utilized to hydrolyze chitin from crab and prawn shells, respectively, imparting negative charges to the resulting ChNCs[104].

In recent years, optimized protocols for acid hydrolysis of chitin typically involve several key steps: (1) treating chitin with 3 M HCl at 90−105 °C under vigorous stirring for 0.5−9 hours; (2) diluting the chitin/acid mixture with water to stop the reaction; (3) separating and purifying the suspension through filtration, centrifugation, and dialysis to remove impurities; and (4) using mechanical treatments like ultrasonication to achieve full dispersion of ChNCs in water[9, 16, 105].

Compared to chitin nanofiber (ChNFs) production, creating ChNCs involves more steps, often resulting in less precise control over hydrolysis and subsequent nanofibrillation. Variables such as acid concentration, hydrolysis time, mechanical treatment intensity, and the degree of acetylation (DA) of the native chitin all significantly influence the properties of the resulting ChNCs. For instance, repeated hydrolysis of α-chitin with HCl at 105 °C for three hours led to a decrease in crystallinity of the ChNCs compared to the native α-chitin, due to the harsh hydrolysis conditions converting crystalline structures into amorphous ones[106, 107]. Post-hydrolysis, dialysis of the ChNC suspension is critical as it affects the pH and thus the quality and effectiveness of the ChNC dispersion. Effective dispersion via mechanical treatment requires electrostatic repulsion from the protonated amino groups on the ChNC surfaces, which is highly pH-dependent. For instance, ChNCs were well-dispersed after 10 minutes of ultrasonication when the suspension had a pH of 3 (following 30 minutes of hydrolysis with 3 M HCl). However, at a pH of 6, both dispersed nanocrystals and clusters coexisted due to decreased electrostatic repulsion and stronger interparticle interactions[108, 109].

2. Collagen

Collagen is the main structural protein of the extracellular matrix (ECM) in various connective tissues and the most abundant protein in vertebrates, containing 25-35% of the total body protein content[110-112]. It is present in a diverse array of tissues, including skin, tendons, ligaments, and blood vessels[113], where it plays a crucial role in maintaining their biological and structural integrity. Collagen can also undergo mineralization to enhance rigidity in hard tissues such as bones and teeth, with a mineralization gradient evident in cartilage[114]. Its critical role in both soft and hard tissue structures makes collagen an ideal biomaterial for scaffolding applications[115].

2.1. Collagen Molecule and Types of Collagens

Collagen exists in many forms, each creating a variety of structures and serving distinct functions in body tissues. Despite this diversity, the fundamental molecular building blocks are similar. Collagen is made up of polypeptide chains, each containing the amino acid motif Gly-X-Y, where Gly represents glycine, and X or Y can be any amino acid[115]. These polypeptide chains, known as proto-collagens or α-chains, form a consistent left-handed helix with a pitch of 0.87 nm and 3.3 residues per rotation (Fig. 9). Three α-chains then intertwine in a right-handed triple helix with a pitch of approximately 8.6 nm, forming the structure of tropocollagen molecules. This tertiary peptide structure has an approximate molecular weight of 300 kDa, a length of 300 nm, and a diameter of 1.5 nm[115, 116]. The different forms of α-chains and their specific triple-helical conformations result in various types of collagen molecules. In humans, there are 29 known types of collagen (Fig. 9) [117-119].

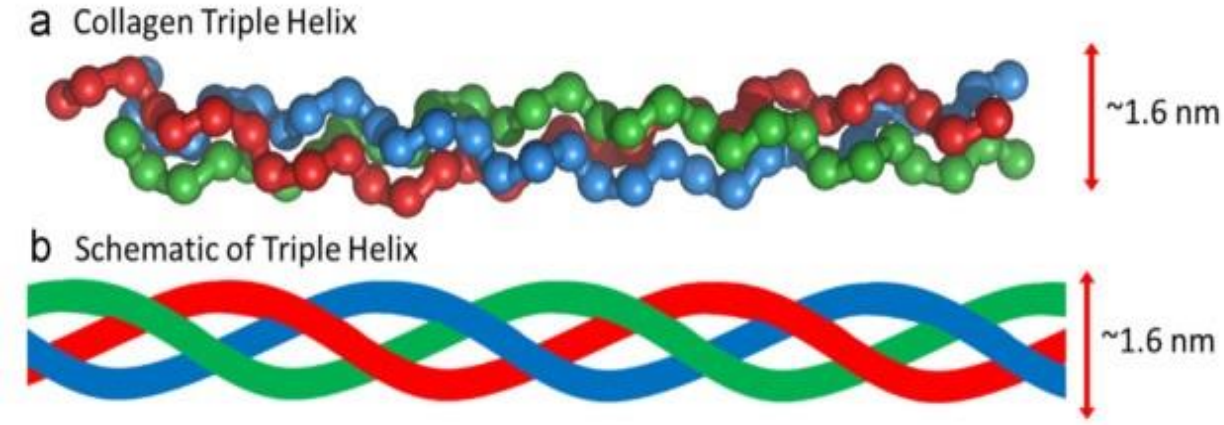

Fig. 9. Structure of three protocollagen chains forming a triple helical tropocollagen structure. Adapted with permission from ref[117]. Copyright 2020 Elsevier.

The various types and compositions of collagen result in a wide range of molecular assemblies[117, 118]. These are classified into several categories: fibrillar collagens, fibril-associated collagens with interrupted triple helices (FACIT collagens)[120], beaded filament collagens, basement membrane collagens (networks)[121], short-chain collagens (hexagonal networks)[122], and transmembrane collagens (anchoring fibrils)[122], The assemblies of these structures are depicted in Fig. 10.

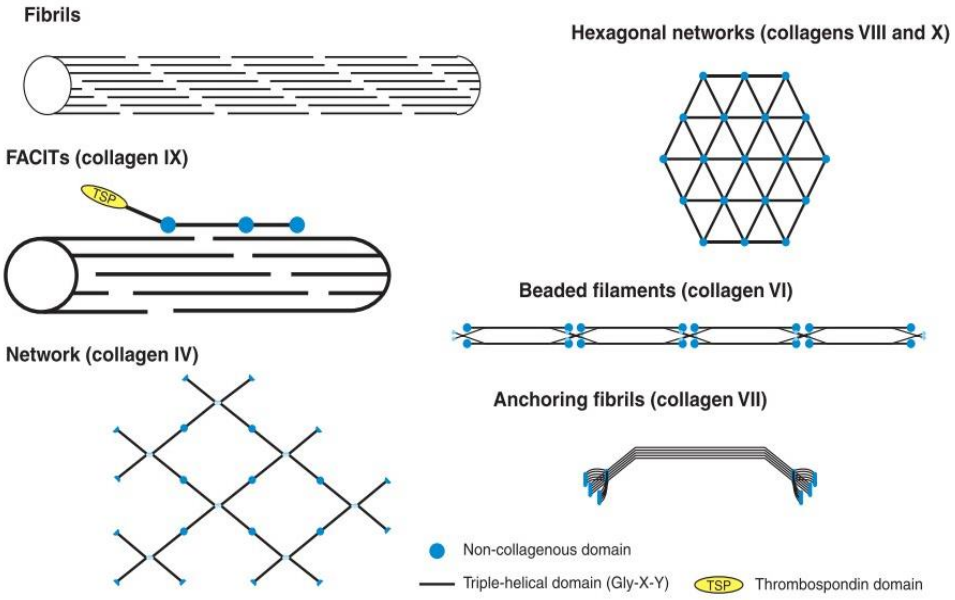

Fig. 10. Different assemblies of each collagen group. Adapted from ref[118]. Copyright 2011 Elsevier.

2.2. Collagen fibrillar

Fibrillar collagens are the most prevalent group of collagens, characterized by their highly aligned and organized fiber structures. These structures typically comprise type I collagen, which is explored in more detail above (Fig. 11). The alignment and organization of fibrillar collagens confers exceptional mechanical strength, which is crucial for providing structural support to various tissues. Fibrillar collagens form the mechanical framework in bone, skin, cartilage, tendons, blood vessels, nerves, intestines, and fibrous encapsulation of organs[115].

Short Chain Collagens: Short-chain collagens form hexagonal networks with shorter triple helical regions, approximately half the length of those in fibrillar collagens. These networks enhance growth factor-induced cell proliferation and are typically found in hypertrophic regions of mineralizing cartilage[121]. **Transmembrane collagens:** Transmembrane collagens, also known as anchoring fibrils, span cell membranes and serve

multiple functions, including intracellular and extracellular binding, and play a pivotal role in cellular adhesion. When they are bound to the membrane, they act as matrix receptors, and when in a soluble state, they can be dissolved to function as signaling factors[123]. **Collagen Type I:** Collagen Type I is the most abundant and consequently the most cost-effective of all types of collagen. As the principal component of fibrillar collagens, it plays a critical role in the formation of the structural framework of the extracellular matrix (ECM). This makes it particularly suitable for tissue engineering scaffolds[124]. Due to these attributes, Collagen Type I is the most extensively utilized collagen in research and will be the primary focus of the following discussions.

2.2.1. Primary Structure of Collagen

The fundamental structure of a collagen molecule is characterized by three polypeptide chains, each consisting of approximately 1000 amino acids, organized into a triple helix[113].Specifically, the triple helical tropocollagen molecule of type I collagen comprises two identical α1(I) chains and one α2(I) chain, each with distinct amino acid compositions[114].

2.3. Collagen as a Biomaterial in Regenerative Medicine

In regenerative medicine and tissue engineering, the main objective is to restore the functionality of tissues or organs affected by malformation, damage, or disease through the repair or replacement of damaged tissue[125]. The selection of scaffold materials is crucial in achieving these objectives. Biomaterial scaffolds are typically engineered to mimic the structure and properties of the native extracellular matrix (ECM). Type I collagen, being the most abundant component of the ECM in humans, is considered an optimal choice for implantable biomaterials. Its abundance and structural properties make it well suited for promoting tissue regeneration and repair. Therefore, type I has garnered significant attention as an ideal biomaterial for tissue engineering applications[125].

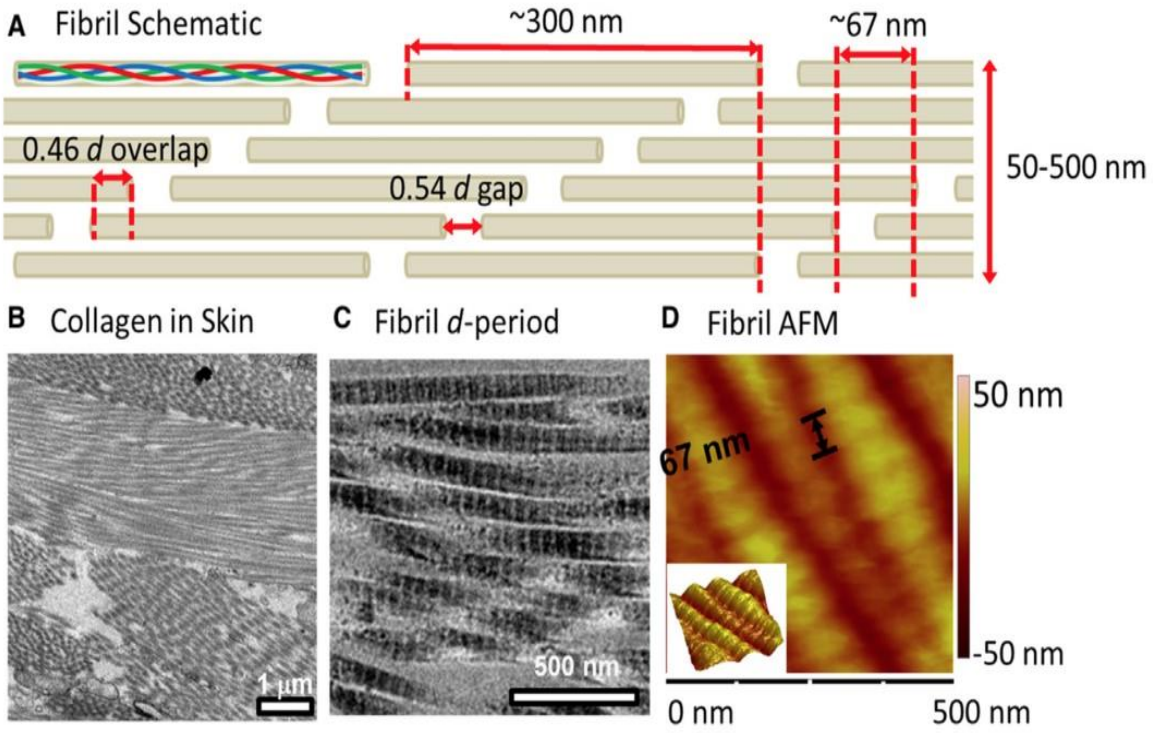

Fig. 11. Structural organization and D-banding in Collagen Fibrils. (A) Collagen fibrils are composed of tropocollagen molecules arranged in a staggered fashion, producing distinctive overlapping regions with a periodicity of 67 nm. (B) A cross-sectional illustration of the skin shows the arrangement of collagen fibrils in layers. (C) An image of collagen fibrils obtained via transmission electron microscopy (TEM). (D) An image of atomic force microscopy (AFM) from Yang et al. 2014, demonstrating the characteristic d banding pattern of collagen fibrils. Reproduced with permission from ref [115, 126].

2.4. Collagen Isolation and Purification Processes

Before collagen can be processed for medical purpose, it first needs to be harvested, isolated, and purified. Collagen type I is often extracted from fibrous, collagen-rich tissues, such as the skin and tendon[115]. It can be sourced from a variety of different species, namely bovine, porcine, and ovine[116]. However, additional sources have included marine species [127], human placenta[128], and human collagen from transgenic animals[129]. In the following section, the different collagen extraction processes are discussed, with the forms of collagen each process can isolate. Neutral salt-soluble collagen: This process is effective for extracting collagens that have only recently been synthesized and are only minimally cross-linked; however, most tissues contain very little or no salt-extractable collagen. These collagens are dissolved in neutral salt solutions and then isolated using dialysis, precipitation, and centrifugation[130].

Acid-soluble collagen: This process is often more efficient than neutral salt extraction, using dilute acids, such as hydrochloric or acetic acid, at a pH of around 2-3. Weak intermolecular crosslinks between collagens are dissociated by acid solvents[131]. However, stronger crosslinks found in structural tissues, such as cartilage, bone, and skin, are not broken, and only about 2% of collagen is extracted with this treatment, the rest is considered insoluble[132]. To extract this 2%, tissue is ground at low temperature and washed in saline to remove any soluble proteins or sugars, before isolating collagen with acidic solvents[133].

2.4.1. Alkali and enzyme-treated collagen: A higher yield of collagen can be solubilized through alkali- and enzyme-treatment methods.

Alkali treatment, collagen is immersed in an aqueous solution of sodium hydroxide (NaOH) and sodium sulfate (Na_2SO_4) for 48 hrs[134]. This process saponifies (breaks down) any associated fats and truncates the nonhelical telopeptide regions at the ends of collagen molecules, causing collagen to fragment[134].

Enzymatic treatment selectively cleaves cross-links in the telopeptide regions without affecting the helical regions, under optimal conditions[135]. Collagen is solubilized in an enzymatic aqueous solution with 0.05 M dilute acetic acid, using a ratio of 1: 1 pepsin to dry-weight tissue [40]. The soluble collagen is then precipitated and isolated by adjusting the pH, salt concentration, or temperature of the solution. It can be preserved by freezing or lyophilization[113].

Insoluble collagen: Approximately 96 to 98% of the extracted collagen remains insoluble[134]. These collagens typically have crosslinks that prevent dissolution in neutral salt or acidic solutions. Instead, they can be broken down into fine fibrils and suspended in media for processing in biomaterial applications, although they do not dissolve. To disperse fine insoluble collagen fibrils, the pH is lowered, often using dilute acetic acid (0.05 M), to disrupt intermolecular interactions, followed by mechanical agitation of the suspension[134]. Due to the lower abundance and higher processing costs of soluble collagen, insoluble collagen finds common use in both research and industry settings.

2.4.2. Collagen Bioapplications

Collagen is widely researched and widely utilized as a biomaterial due to its abundant presence in nature, the ability to self-assemble in vitro under controlled conditions, minimal toxicity, low immunogenicity and antigenicity, presence of cellular attachment sites and biodegradability[136]. Its versatile properties make it highly successful in various biomedical applications. In the following, we dive into specific collagen structures and their applications as biomaterials[137].

Porous Sponges: Porous sponges are made using insoluble type I collagen sourced from animals such as bovine, porcine, and equine[136]. These sponges are created by lyophilizing hydrated aqueous suspensions of collagen, typically containing around 0.1 - 5 w/v% dry protein mass. During the freeze-drying process, ice crystals act as templates, compacting suspended collagen fibers to form a scaffold. Sublimation of the ice crystals leaves behind a network of interconnected pores within the collagen matrix[138]. The development of porous sponges has been refined over the years, focusing on controlling the freezing process to manipulate properties such as porosity, interconnectivity[139], pore diameter[140], and alignment[141], These adjustments tailor the sponges for various tissue replacements including bone[142], soft cartilage[143], skin regeneration[144], peripheral nerves[145], cornea[146], fabrication of blood vessels[147], and cardiac tissue[137].

Collagen hydrogels: Collagen hydrogels are extensively utilized as injectable materials for various applications, including providing structural support and drug delivery. In reconstructive surgeries, collagen hydrogels are injected subcutaneously to address dermatological defects[148]. These hydrogels are also used for localized delivery of growth factors, which improves tissue regeneration directly at the injection site[149]. In addition, collagen gels are utilized for sustained drug release at the injection site. Studies have demonstrated that incorporating local anesthetics into collagen hydrogels significantly prolongs the drug's effectiveness in the targeted area[150].

Wound Dressings: Collagen-based materials are extensively utilized in wound dressing applications due to their biocompatibility and minimal antigenicity[151]. Dressings incorporating collagen have demonstrated effectiveness in promoting tissue regeneration, accelerating epithelialization, supporting the inflammatory phase of healing, and mitigating scar formation[151]. Moreover, collagen wound dressings, often combined with other materials, are employed to reduce infection risks in burn victims while ensuring adequate air and vapor permeability[151].

Collagen fibers: Highly aligned collagen fibers have been engineered to create structures with exceptional tensile strength[152]. These collagen biomaterials are designed to replicate the natural architecture of tendons and ligaments, which predominantly consist of aligned collagen type I fibers crucial for withstanding tensile mechanical loads[153].

Films and Membranes: Collagen membranes are produced by casting collagen suspensions and allowing them to air-dry, resulting in a dry collagen layer ranging from tens to hundreds of microns thick[154]. Collagen films find diverse applications, including wound dressings, closure of dural defects, reinforcement of compromised tissues, and as barrier

membranes[154]. Incorporation of drugs into collagen films enables controlled release at a consistent rate over time as the film biodegrades[155]. Moreover, these films are utilized for directing and supporting cell growth, particularly in dental surgery to guide tissue regeneration[155].

3. Hyaluronan

Hyaluronic acid (HA), also known as hyaluronan in its salt form, is a naturally occurring biodegradable polymer with a high molecular weight ranging from 10^5 to 10^7 Daltons. HA is an unbranched glycosaminoglycan (GAG) that lacks sulfation, composed of repeating disaccharide units: β-1,4-D-glucuronic acid (uronic acid) and β-1,3-N-acetyl-D-glucosamine (Fig. 12)[9, 156-161]. The backbone of HA can consist of several thousand sugar molecules. As a polyanion, HA can self-associate and can bind water molecules, imparting a stiff, viscous texture similar to gelatin when not bound to other molecules [161].

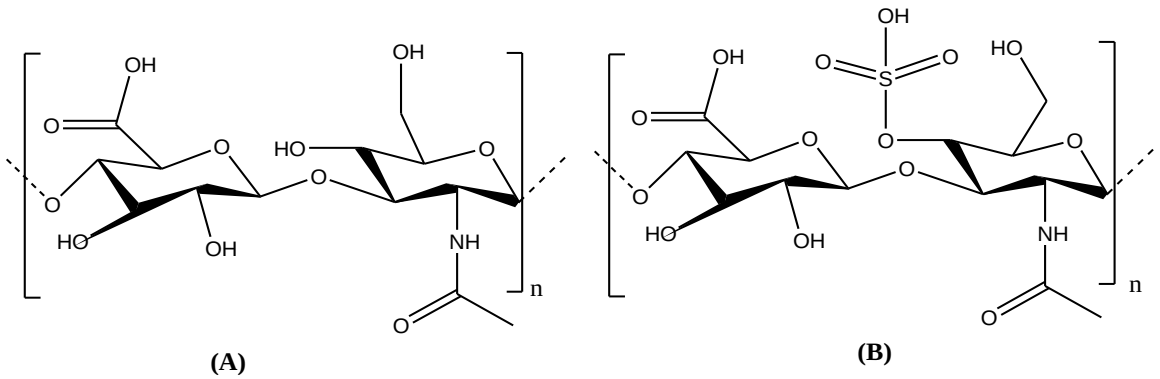

Fig. 12. Chemical structure of two glycosaminoglycans (GAGs) made of disaccharide repeats of *N*-acetyl glucosamine and glucuronic acid. **(A):** Hyaluronic acid (HA); **(B):** Chondroitin sulfate (CS)

Hyaluronic acid is a prominent component of the extracellular matrix (ECM) found in vertebrate tissues, distributed widely in body fluids and tissues such as synovial fluid, vitreous humor of the eye, and hyaline cartilage[158, 161]. This biopolymer acts as a scaffold, binds to other matrix molecules like aggrecan[14], and plays crucial roles in various biological functions. It regulates cell adhesion and motility, influences cell differentiation and proliferation, and contributes to the biomechanical properties of tissues[162]. Several cell surface receptors, including CD44, RHAMM, and ICAM-1, interact with HA, thus influencing cellular processes such as morphogenesis, wound repair, inflammation, and metastasis[163]. HA also supports the viscoelasticity of biological fluids such as synovial fluid and vitreous humor and regulates tissue hydration and water transport[162]. Furthermore, HA has been identified during embryonic development, suggesting that materials containing HA can create favorable conditions for tissue regeneration and growth[164].

The distinctive properties, including its viscosity, biocompatibility, and hydrophilicity, have positioned it as an exceptional moisturizing agent in cosmetic dermatology and skincare products[164]. Beyond skincare, its unique viscoelastic nature and low immunogenicity have also facilitated its application in various biomedical fields. For example, it is used as a viscous supplement in the treatment of osteoarthritis, as well as as a surgical aid in ophthalmology and dermatology to promote wound regeneration[165]. Furthermore, ongoing research is exploring its potential as a versatile drug delivery vehicle through various administration routes, including nasal, pulmonary, ophthalmic, topical and parenteral routes[165-167].

3.1. Chemical properties of hyaluronan

The chemical properties of hyaluronan are elucidated through structural studies revealing a disaccharide unit composed of D-glucuronic acid and *D*-*N*-acetylglucosamine, linked alternately via β-1,4 and β-1,3 glycosidic bonds[166]. In physiological solutions, the HA backbone adopts stiffness facilitated by internal hydrogen bonding, solvent interactions, and the disaccharide's chemical arrangement. Molecular investigations indicate that the axial hydrogen atoms form a relatively hydrophobic face, while the equatorial side chains create a more hydrophilic face, resulting in a coiled ribbon structure known as a "coiled coil" for HA [168]. This coiled structure is pivotal for HA's behavior in solution: at low concentrations, chains entangle, imparting mild viscosity dependent on molecular weight. Conversely, higher HA concentrations exhibit unexpectedly high viscosity due to increased chain entanglement that is sensitive to shear stress. For example, a 1% solution of high molecular weight HA (>~1000 kDa) can resemble a gel, yet easily shear thins under stress, making it suitable for injection through fine needles[168]. Thus, HA is classified as a "pseudoplastic" material, a rheological characteristic dependent on concentration and molecular weight, which renders it effective for lubrication in biomedical applications[156].

In addition to its unique viscosity, hyaluronic acid (HA) exhibits viscoelastic properties arising from the entanglement and self-association of its random coils in solution[159]. Studies suggest that HA molecules self-associate by forming antiparallel double helices, bundles, and ropes, supported by experimental evidence demonstrating chain-chain association in solution [159]. Furthermore, hydrogen bonding between adjacent saccharides and electrostatic repulsion between carboxyl groups have been proposed to contribute to the stiffness of HA[169].

The viscoelastic behavior of HA is intricately linked to these molecular interactions, which are influenced by HA concentration and molecular weight. The impact of electrostatic

and ionic interactions on HA has been studied with the type and valence of counter-ions. Research has shown that these interactions significantly affect HA's rheological and hydrodynamic properties. For instance, a study compared HA solution properties in deionized water (D.I.), 0.5 M NaCl, and 0.5 M NaOH, highlighting how different solution conditions alter hydrogen bonding and electrostatic interactions with HA, thereby influencing HA chain stiffness[158, 168]. Moreover, the hydrodynamic radius of HA was found to vary, being greater in D.I. water compared to solutions with 0.5 M NaCl or 0.5 M NaOH (D.I. water > 0.5 M NaCl > 0.5 M NaOH)[168]. These findings underscore the complex interplay between molecular structure, solvent conditions, and HA's biophysical properties in different environments.

3.2. Biological properties of hyaluronan

Hyaluronic acid serves diverse structural roles within the extracellular matrix (ECM), interacting through specific and nonspecific mechanisms with cells and other biological components. HA facilitates the stabilization of various ECM proteins upon binding, contributing to the structural integrity of tissues. Specific molecules and receptors participate in HA-mediated cellular signal transduction pathways. Examples include aggrecan, versican, neurocan, and receptors such as CD44, RHAMM, TSG6, GHAP, and LYVE-1, each of which plays a crucial role in cellular interactions with HA[162, 168]. Among these receptors, CD44 and RHAMM have attracted considerable attention, particularly due to their implications in cancer metastasis[170, 171]. CD44, a highly versatile and multifunctional cell surface glycoprotein present in most cell types, stands out as the most studied transmembrane receptor for HA to date. Given its widespread distribution and established roles, CD44 is recognized as the primary receptor for HA in various cell types[172].

Hyaluronic acid (HA) influences gene expression in various cell types, including macrophages, endothelial cells, eosinophils, and specific epithelial cells. In particular, only low to intermediate molecular weight HA (2×10^4-4.5×10^5 Da) has been observed to stimulate gene expression, while high molecular weight HA does not appear to be involved in this process[173]. In wound healing and scar formation, HA plays a crucial role. The degradation products of HA, specifically low molecular weight fragments, contribute to the scar formation. In contrast, studies have shown that the high molecular weight HA present in the fetal wound fluid can minimize scar formation. These findings underscore the significant impact of HA's molecular weight on wound healing and scar formation processes. High molecular weight HA promotes cell quiescence and supports tissue integrity, while the generation of HA fragments signals tissue injury and triggers inflammatory responses[174].

3.3. Application of hyaluronan in tissue engineering

Hyaluronic acid (HA), as a major component of body tissues, holds significant promise for tissue engineering applications. Despite its high solubility at room temperature and rapid turnover in the body, which pose challenges for scaffold fabrication and structural integrity, several strategies have been developed to overcome these limitations[175]. To enhance its applicability in tissue engineering, HA can be crosslinked using various methods such as water-soluble carbodiimide crosslinking[175], polyvalent hydrazide crosslinking[176], divinyl sulfone crosslinking[177], disulfide crosslinking[178], and photo-crosslinking through glycidyl methacrylate-HA conjugation[179]. Chemical crosslinking enables the integration of desirable biological and mechanical properties, particularly for applications in bone and cartilage tissue engineering[180]. Additionally, crosslinking prolongs HA degradation in vivo, thereby ensuring long-term stability. Different crosslinking densities of HA have been explored across orthopedics, cardiovascular medicine, and dermatology[180].

Research has demonstrated encouraging outcomes with cell growth on photo-crosslinked HA networks incorporating chondrocytes. Chondrocytes within HA hydrogels maintained viability and successfully generated cartilage within the porous network[181]. This photo-polymerization technique has also been employed in developing heart valves to mimic cardiac valve development[181]. Moreover, HA has been combined with polymers like polypyrrole to create multifunctional copolymers. HA functionalized with polypyrrole exhibits electronic conductivity and supports cell growth, suggesting potential applications in tissue engineering[181, 182]. Benzyl derivatives of hyaluronic acid (HA) represent a class of polymeric scaffolds utilized in cartilage tissue engineering due to their predictable degradation rates. Research indicates that benzyl esters of HA can serve as effective delivery scaffolds for chondrocytes in this context[183]. Given HA's biocompatibility as a natural polymer, scaffolds based on HA are considered suitable for applications involving blood-contacting surfaces. For instance, HA crosslinked with divinyl sulfone (DVS) under ultraviolet light has been proposed to create "non-activating" surfaces conducive to cell adhesion in heart valve tissue engineering [183]. Auto-crosslinked and in situ crosslinked HA hydrogels represent another approach in HA-based scaffolds for tissue engineering. One significant advantage is the ability to crosslink after injection, offering flexibility in shaping and minimizing surgical invasiveness. This method allows for mechanical or chemical interlocking with native tissue, promoting a cohesive scaffold-tissue interface[184]. Studies have demonstrated that in situ crosslinked HA hydrogels using adipic acid dihydrazide and aldehyde chemistry can form flexible hydrogels upon mixing[185].

Chapter 2

Hyaluronan Films Reinforced with Partially Deacetylated Chitin Nanocrystals: Extraction, Fabrication, *In Vitro,* and Antibacterial Properties of Advanced Nanocomposites

Abstract

Fabrication of nanocomposite films with enhanced mechanical and antibacterial properties was successfully achieved from hyaluronan (HA) and partially deacetylated chitin nanowhiskers (ChNWs) by a casting-evaporation method. The hydrolysis process of chitin showed an important role in the dimensions, stability, and crystallinity of extracted ChNWs in a time-dependent manner. The volume fraction of ChNWs nanofillers varying from (0.001 to 0.5) exhibited a great influence on the mechanical properties of the films (young modulus, strength) was enhanced by the high load-bearing capacity of NWs compared with net HA film. The antibacterial activity of the nanocomposite films exhibited significant bactericidal activity against different types of bacteria (-/+ gram). HA/ChNWs Nanocomposite films did not show any toxicity against normal human dermal fibroblasts (NHDF) and human primary osteogenic sarcoma (Saos-2) cell lines. The new films with unique properties like edibleness, environmental friendliness, high mechanical properties, antibacterial performance, and non-cytotoxicity that could be used in skin/bone tissue regenerations, and drug delivery applications.

Keywords: Nanocomposite film, hyaluronan, chitin nanowhiskers, cytotoxicity, bactericidal activity.

Rasha M. Abdel-Rahman, A. M. Abdel-Mohsen, M. Zboncak, J. Frankova, P. Lepcio, L. Kobera, M. Steinhart, D. Pavlinak, Z. Spotaz, R. Sklenářévá, J. Brus, J. Jancar. Hyaluronan films Reinforced with Partially Deacetylated Chitin nanowhiskers: Extraction, Fabrication, *In-vitro* and Antibacterial Properties of Advanced Nanocomposites. Carbohydrate Polymers**,** 2020, 235,115951.

1. Introduction

Polymers filled with nanoscale reinforcement, such as inorganic or organic nano-objects, attracted unprecedented interest in the scientific and engineering community due to the large potential of these nano-sized objects to substantially modify the properties of polymers beyond the capabilities of their micro-sized alternatives [186, 187]. For example, antibacterial, cell growth acceleration or inhibition, thermal resistance, electric or magnetic actuation, or mechanical robustness can be added to the portfolio of polymer properties via the addition of nanoparticles with desired properties and their organization into defined structures. Although modification of the function-oriented properties is a little more straightforward and more successful, the full potential of nanoparticles for modification of the mechanical properties remains rather dormant.

The development of nanocomposites based on natural polymers has attracted great interest from scientists because of several characteristics of polymers, such as resource renewability, easy extraction, lightweight, and multifunction properties. However, natural polymers such as starch, cellulose, chitosan, chitin, and hyaluronic acid have lacked several parameters such as low modulus, poor mechanical performance, and rapid degradation. Therefore, combining a polymeric matrix with polymeric nanoparticles as reinforcement into a nanocomposite could enhance the performance of those materials, such as the mechanical strength and the degradation properties.

Hyaluronan (HA) is a glycosaminoglycan, an anionic polysaccharide made up of glucuronic acid and *N*-acetylglucosamine disaccharide units having one carboxyl group on each disaccharide unit [156]. Today, HA is widely used due to its unique features of biocompatibility, non-toxicity, and healing properties. It can be prepared in various forms, such as a hydrogel [188], fibers [159, 161], or a scaffold [189]. However, hyaluronan showed poor mechanical stability, rapid degradation [190] and does not possess antimicrobial properties; therefore, it often provides a favorable environment for colonization by microorganisms, which can lead to infection and delay healing.

Chitin, a long polymer chain of *N*-acetyl glucosamine and its partly deacetylated form chitosan represents huge natural resources of polysaccharides found in many places throughout the natural world, possessing various parameters such as biocompatibility, biodegradability, nontoxicity and it is potential to be converted into nanofibrils [71]. By acid hydrolysis, a stiff rod-like chitin nanowhisker (ChNWs) can be prepared with many advantages including good mechanical performance [191], low density [8], high surface area [192] and nano-reinforcement ability in polymeric structures [193]. All these properties render ChNWs a

prospective candidate for use as a nanofiller or nano-reinforcement additive for high-performance nanocomposite materials. Hydrolysis of chitin acid using hydrochloric acid is the best choice to extract chitin nanowhiskers without any chemical modification compared to analogical methods using sulfuric acid [194] or phosphoric acid [195] (generate sulfate and phosphate groups, respectively.

The combination of hyaluronan and chitosan shows a synergistic effect on the properties of the final nanocomposite. One additional factor enabling the development of tailored biomaterials based on the combination of HA and chitosan is their capability to form a polyelectrolyte complex (PEC) via ionic interactions. It was concluded that the carboxylate moieties on HA polymer will ionically interact with the free amino groups on chitosan counterparts to generate a 3D matrix, known as a physically cross-linked hydrogel [196]. Because of these opposite charges, a direct mixture of hyaluronan and chitosan solutions would readily coagulate or form gels [197], leading to unfeasible production of the hyaluronan/chitosan membrane/fiber/film from the mixed dope solutions of the biopolymers.

3D scaffolds are made using α-Chitin-whisker-reinforced hyaluronan–-gelatin nanocomposite by freeze-drying technique [198] without information about the DDA of chitin nanowhiskers and bacterial properties of the prepared scaffold and the reinforced properties of ChNWs on the hyaluronan gelation scaffold [198]. Nanocomposite films from α-Chitin nanowhiskers (vinyl alcohol) are fabricated by the solution impregnation method [199]. Partially, chitin nanowhiskers films are prepared first and then immersed in PVA solution and heat treated for a different time and temperature to improve the solubility of PVA/ChNWs in water. Unfortunately, no available data about the DDA of chitin, the stability, or the distribution of nanowhiskers in the film matrix.

In the current study, for the first time, we report a novel method for preparing nanocomposite films from hyaluronan and partially deacetylated chitin nanowhiskers (HA/ChNWs) by a casting-evaporation method of a dope suspension synthesized from a direct mixing of a hyaluronan solution and a nanowhiskers solution. Briefly, ChNWs suspension (without agglomerations) was subsequently added to the HA solution under vigorous stirring to obtain a homogeneous HA/ChNWs dope suspension.

The advantage of the method described here is the homogenization of the target substances before processing, so the homogeneity and composition of the substances could be controlled. Additionally, all the constituents in the dope solution certainly remain in the film, and this method is convenient and easy to scale up for large-scale production. Therefore, the overall goals of this investigation were (i) to develop a new method of nanocomposite

preparation from cationic/anionic biopolymers and maximize the nanofiller content (to provide sufficient beneficial properties of nanowhiskers) by simply avoiding the direct interactions between functional groups while retaining the film-processing ability of hyaluronan; (ii) to investigate altered/outstanding properties of the obtained HA/ChNWs nanocomposite hybridized films thereby obtained; and (iii) improve the mechanical and antibacterial properties, stability, and compatibility of the nanocomposites.

2. Experimental part

2.1. Materials and Methods

Shrimp shells were selected as a source for chitin (Ch) extraction and partially deacetylated chitin nanowhiskers (ChNWs). Sodium hydroxide, hydrochloric acid, ethanol, isopropyl alcohol, and acetone were acquired from Lach-Ner, s.r.o., Czech Republic. Commercial sodium hyaluronate (HA) with molecular weight (Mw = 500 000 g/mol; Mw/Mn = 1.5) was provided by Contipro a.s. (Dolni Dobrouc, Czech Republic) and assigned using the SEC-MALS technique. All chemicals were used as obtained without further purification.

2.2. Extraction and partially deacetylated ChNWs

The extraction of pure chitin from the shrimp shell was performed according to our previous works with minor modifications [71, 157], in summary, the shrimp shells were refluxed with absolute ethanol to remove soluble impurities and then dried at 60 °C overnight in an air-dry oven. The extraction process of chitin (Ch) and chitosan (Cs) consisted of three main steps: demineralization (DM), deproteinization (DP), and deacetylation (DA). The DM step was carried out using aqueous hydrochloric acid (HCl) at ambient temperature (25 ± 2 °C) for 24 h with emission of CO_2 gas observed during the reaction of carbonates with diluted HCl. The solid fraction of crude chitin was washed with Milli-Q water until neutral pH was reached, then dried at 60 °C for 24 h. In the deproteinization (DP) step, aqueous NaOH was used to remove the nonbounded materials like proteins, dyes, lipids, and pigments. Crude chitin was stirred in 5 % NaOH at 90 ° C for 24 h, where the alkaline solution was exchanged every 2 h with a fresh NaOH solution. The product was filtered off and washed with Milli-Q water until neutral pH was achieved, then dried at 60 °C for 12 h.

The suspension of chitin nanowhiskers was fabricated by acid-hydrolysis using different concentrations of hydrochloric acid (1, 3, 5 M) at 90 ° C for a variable time (1 to 6 h) under mechanical stirring. The solid-liquid ratio of the chitin suspension was (1/100). After acid hydrolysis, the suspension was diluted with Milli-Q water and centrifuged at 4000 rpm. The process was repeated five times (each 10 min) until a pH of approximately 4 was achieved. The suspension was transferred to a cellulose dialysis bag (molecular cut 12-14 kDa) and

dialyzed in Milli-Q water until the chitin nanowhiskers suspension was sufficiently neutral (pH = 6- 6.5). Part of the ChNWs suspension was preserved by storing it in sealed vessels placed in a refrigerator at 4 °C. The suspension was cast into a plastic petri dish and kept at -20 ºC. Afterward, it was lyophilized at – 80 °C for 2 days. The partial deacetylation of chitin nanowhiskers (ChNWs) was achieved by refluxing chitin with (5–60 % w/v) of sodium hydroxide solution at 90 ℃ with solid to solvent ratio (1/30 w/w) in the time range of 0.5-5 h. Partially deacetylated ChNWs were collected, washed with Milli-Q water until neutral pH was achieved, rinsed with ethanol, vacuum filtered, and dried at 60 °C for 12 h to remove moisture.

2.3. Preparation of nanocomposite films (HA/ChNWs)

Partially deacetylated chitin nanowhiskers with a DDA of 27 % were selected to prepare nanocomposite films from hyaluronan and different ratios of chitin nanowhiskers (27 % DDA) by casting-evaporation method. A certain amount of HA (3 %) was dissolved into Milli-Q water at room temperature (rm), and then different volume fraction (V_f) ratios from ChNWs (27 % DDA) were added drop by drop into HA solution with a smooth mechanical stirrer at rm for 5 h. the nanocomposite solutions were centrifuged at 5000 rpm for 30 min then, cast into petri dishes, and dried at 50 ℃ for 24 h. The obtained films were hydrothermally crosslinked by placing them into an oven at 125 ℃ for 10 min. All prepared samples with different volume fractions (V_f) between HA and ChNWs (27 % DDA) are listed in Table 1.

Table 1: Different volume fractions ratios of the hyaluronan (HA) and partially deacetylated chitin nanowhiskers (ChNWs) investigated in this study.

Sample Codes	ChNWs/ HA ratio (wt/wt)	V_f of ChNWs to HA
Net HA	0	0
HA/ChNWs (1/0.1)	0.1	0.00125
HA/ChNWs (1/1)	1	0.012
HA/ChNWs (1/10)	10	0.111
HA/ChNWs (1/15)	15	0.159
HA/ChNWs (1/25)	25	0.239
HA/ChNWs (1/35)	35	0.312
HA/ChNWs (1/50)	50	0.386

Notes: HA = hyaluronan; ChNWs = partially deacetylated chitin nanowhiskers (DDA 27 %); **V_f =** Volume fraction, HA concentration was 3 %.

3. Characterization

3.1. Regular light transmittances (T %)

Native hyaluronan and hyaluronan/chitin nanowhiskers films were measured by a UV/Vis spectrophotometer (JASCO-V550) in the wavelength range of 200–800 nm.

3.2. Scanning electron microscope (SEM)

Mira3 XM (Tescan, Czech Republic) was used for imaging of film morphology and further analysis of the diameter of nanowhiskers in transmission mode (STEM). In order to achieve better resolution and prevent overcharging, the samples were coated with a thin conductive metallic layer of Pd/Au alloy (thickness of 20 nm). The morphology imaging was obtained at different magnifications in the resolution regime with the accelerating voltage of 10 kV, using a secondary emission detector.

3.3. Mechanical Measurements

Tensile testing was used to investigate the strength of HA/ChNWs films, which was important when it came to sample handling. It was carried out by Universal testing equipment Z010 from Zwick–Roell (Germany) with a 1 kN measuring cell. Samples were cut into a dog bone shape with a parallel specimen length of 12 mm. Testing rate was 10^{-3} s^{-1} and the tests were performed at laboratory temperature.

3.4. Rheology Measurements

Rheological characterization was executed on nanocomposite solutions prior to the film preparation using ARES G2 rheometer (TA Instruments, USA) with cone-plate 40 mm, 2° geometry at 25 °C. Frequency sweep measurements were performed in the range from 0.05 to 100 Hz at 0.5 and 1 % strain amplitude. The linear viscoelastic region was detected by strain sweeps from 0.05 to 10 % strain amplitude at 1 Hz. Flow tests were performed by ramping the shear rate from 0.1 to 100 s^{-1} at a logarithmic rate. Prior to the flow test, each sample was pre-sheared at 0.1 s^{-1} for 60 s. Evaporation of the solvent was prevented by a solvent trap.

3.5. *In vitro* measurement

Cytotoxicity, proliferation and biocompatibility assay of the films was done by using normal human dermal fibroblasts (NHDF) and cell line human primary osteogenic sarcoma (Saos-2). NHDF were isolated from plastic surgery skin sections with the approval of the Ethical Committee of the University Hospital Olomouc and the patient's consent. The study was performed by the Code of Ethics of the World Medical Association. The morphology and origin of the cells were authenticated in the Histology Department, University Hospital Olomouc. NHDFs were cultured in Dulbecco's Modified Eagle Medium supplemented with 10% fetal bovine serum (FBS) and 1% penicillin-streptomycin under standard culture

conditions (5% CO_2, 37 °C). Cells were used between the 2nd and 3rd passages [200]. The saos-2 cell line was obtained from European Collection and Authenticated Cell Culture (ECACC) and cultivated according to the protocol in McCoys´5A (modified) medium supplemented with 10 % of FBS and % penicillin-streptomycin under (5% CO_2, 37°C) standard culture conditions [201].

Reduction of tetrazolium salt, 3-(4,5-dimethylthiazol-2-yl)-2,5-diphenyltetrazolium bromide (MTT) was used as a parameter for the evaluation of cytotoxicity. MTT was reduced by intracellular dehydrogenases of viable living cells that led to the formation of purple formazan crystals, insoluble in aqueous solutions. After dissolution in an organic solvent, the absorbance is monitored. Cells in 96-well microplates were treated with an extract of tested materials at a final film concentration of film 125, 250, 500 and 1000 µg/ml and quantified after 24 hours. As a control, cells were used only with the cultivation medium. After the incubation period, the medium was removed and serum-free medium supplemented with MTT (5 mg/ml) was applied to cells for 2 h (37 °C, dark). The solution was then removed and the crystals were dissolved in DMSO with NH_3 (1 %, v/v). The absorbance was measured at a wavelength of 540 nm (Tecan, Czech Republic). In addition, live/dead staining was performed. The selected films were fitted and placed on the bottom of 8 well plates (Chamber slide), sterilized under UV for at least 15 min and NHDFs and Saos-2 were added. The samples were incubated for 5 min with the staining solution (2 mg / ml propidium iodide, 5 mg/ml of fluorescein diacetate in PBS). Finally, it was rinsed with PBS before imaging with fluorescent microscopy.

4. Results and discussions

4.1. Extraction of partially de-acetylated (ChNWs)

Chitin is a part of the matrix (chitin-protein mineral deposit) that forms the rigid shell of shrimps [71, 202]. The chitin extraction process could be summarized by two main steps: removal of calcium ions (demineralization step; DM) using diluted HCl, and removal of proteins (deproteinization step; DP) using NaOH (**Fig. 13a).** Residual proteins after 24 h of NaOH treatment with NaOH were less than 0.005 (**Fig.13b**), measured using the standard method [202]. The low residual protein content was very important for the potential medical applications of chitin and chitosan biopolymers.

Effects of acid concentration (1, 3, 5 M) on the degree of deacetylation (DDA) of pure ChNWs were monitored using solid-state NMR spectroscopy (**Fig. 13c**). The DDA of ChNWs slightly increased from 8.3 % for native chitin to 12.2 % when the hydrolysis was done for 6 h at 90 ℃ using different acid concentrations (1, 3, 5 M). From **Fig. 13c,** we can conclude that

the strong acid treatment affected the surface of chitin chains with no significant changes in the skeleton structure of chitin (in DDA percentage). ^{13}C CP/MAS NMR experiments were used to elucidate the chemical structure of ChNWs (i) treated with different acid concentrations (HCl) and (ii) treated with different concentrations of NaOH. The results were compared with the purified raw material (5 % NaOH; **Fig. 13c, d**– black lines). The assignment of signals in ^{13}C CP/MAS NMR spectra was based on data from literature [188, 203], and depicted in **Fig 13c** and **d**.

All ^{13}C CP/MAS NMR spectra of the neat and treated chitosan systems show relatively narrow peaks (half-width ca. 300 Hz), which indicates their well-ordered structure in all cases. Furthermore, no signal was detected at ca. 33 ppm in ^{13}C CP/MAS NMR spectra (**Fig 13c, d**), which indicated the absence of any residual proteins and/or lipids in all systems **[204].** Typically, chitin/chitosan samples are defined by a degree of deacetylation using Eq. 3 from the ^{13}C CP/MAS NMR spectra.

Our system, denoted as neat chitin, contains 9.0 ± 0.5 mol % chitosan units. In the case of acid-treated samples, the chitosan unit content is almost independent of the acid concentration and was defined as 12.8 ± 0.5 mol % for the three samples. However, the concentration of the alkaline solution had a strong influence on the final chitin/chitosan ratio. The number of chitosan units increased at higher concentrations of NaOH. After treatment in 10, 20, 30 and 40% NaOH solutions, the deacetylation process was promoted and the chitosan content was 17.6, 18.8, 23.9 and 27.8 ± 0.5 mol. %, respectively.

Fig. 13d shows ^{13}C CP/MAS NMR spectra of partially deacetylated ChNWs (3 M HCl, 6 h, 90 ℃) which were prepared using different concentrations of NaOH (5, 10, 20, 30, 40, and 50 w/v.%) for 5 h at 70 ℃. The degree of deacetylation (DDA %) slightly increased from 8.3 to 27 % upon increasing NaOH concentration from 5 to 40 %, respectively. Chitin nanowhiskers with 27 % DDA were used for all experiments and preparation of nanocomposite films. **Fig. 13e** explores the residual metal ions after nanowhiskers preparation (DDA 27 %). This residual amount of metal ions completely meets the criteria of European pharmacopeia for medical application materials. The upper right corner of **Fig. 13e** shows the effect of time on the extraction of partially deacetylated ChNWs from chitin using 40 % NaOH, 3M HCl at different treatment times (1-6 h). The neat Ch shows a dense shape after 1 h of sonication at room temperature and after acid treatment (1, 3, 4.5, 6 h) the partially deacetylated ChNWs nanowhiskers solution had a high homogenous distribution.

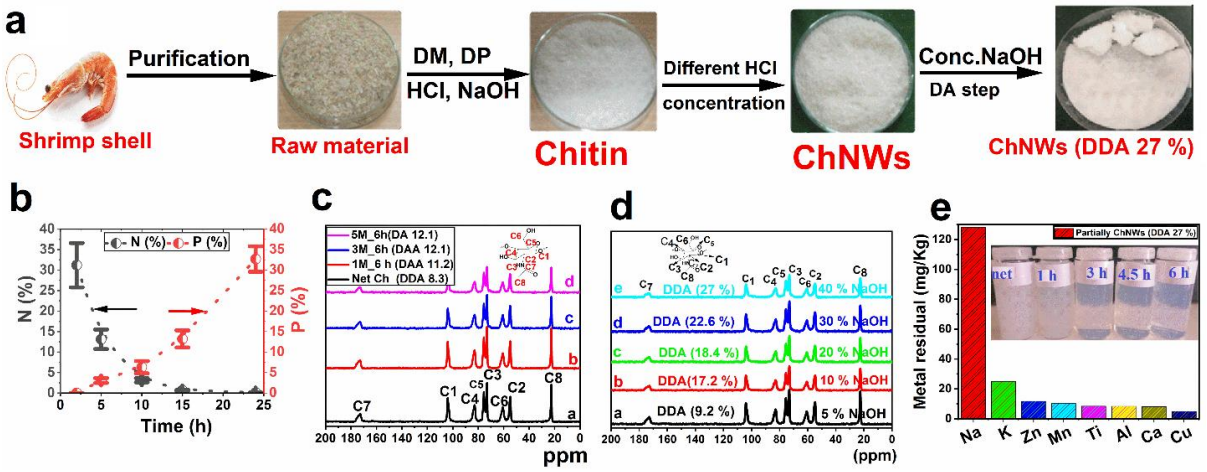

Fig. 13. Representative extraction sequence characterization of partially deacetylated chitin nanowhiskers. **(a)** Extraction sequence of partially ChNWs; **(b)** Relation between treatment time and residual protein content of demineralized shrimp shell measured by elemental analysis and UV/VIS spectroscopy; **(c)** ^{13}C-CP/MAS NMR spectra of net Ch and ChNWs treated with different HCl concentrations (1, 3, 5 M) at 90 °C for 6 h; **(d)** Effect of NaOH concentrations (5, 10, 20, 30, 40, 50 %) on the DDA of ChNWs at 90 °C; (**e)** Residual metal ions content in partially deacetylated ChNWs (27 %), photos in the upper right corner shows the samples of partially deacetylated ChNWs suspension using different treatment time (1-6 h)**.**

Neat shrimp shell has a flat surface morphology with a compact structure and small particles on the shrimp surface (**Fig. S1a, supporting information**). After the demineralization step (DM) for 24 h using 10 % HCl at room temperature (**section 2.2**), shrimp shell had a micro-fibrillose structure with a length of more than 10 µm and a porous surface structure with a pore size of about 500 nm. This shape of shrimp after the acid treatment might be caused by destroying the matrix of the complex chitin/protein/minerals composition and generating by decomposition of the mineral salts (**Fig. S1b, supporting information**). After basic treatment (5 % NaOH) for 24 h, more micro-fibrils of chitin were observed with a much bigger pore size (700 nm) of the porous surface structure pore size (**Fig. S1b, supporting information**). Low concentration of hydrochloric acid acted on the surface of chitin chains and caused intra-chain hydrolysis destroying the chemical bonds between proteins and chitin functional groups which gave rise to more fibrillose chitin structure (**Fig. S1c, supporting information**).

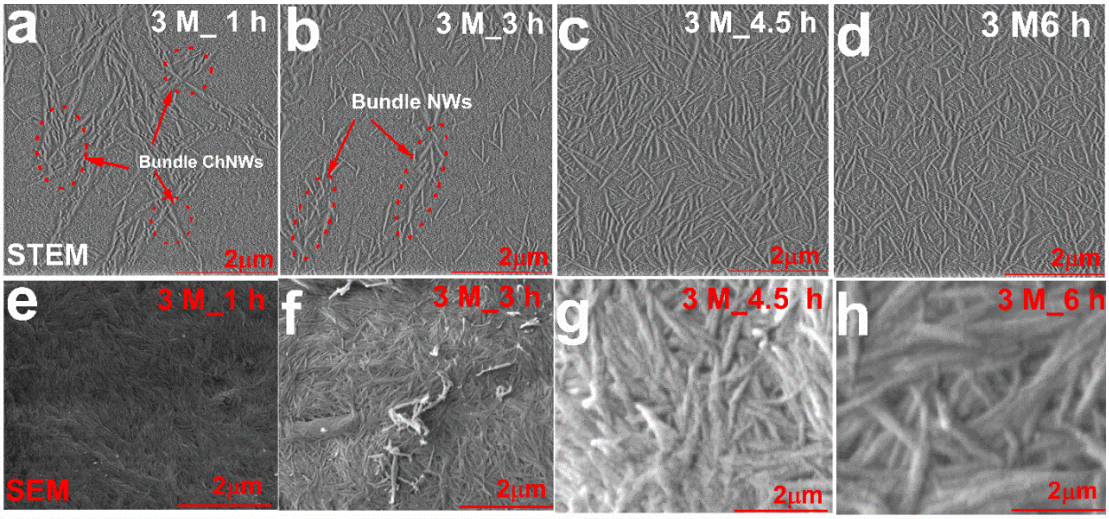

Fig. 14A. Representative STEM and SEM images of partially deacetylated ChNWs (27 % DDA) at different acid treatment times (1- 6h).

Fig. 14Aa shows the effect of acid treatment time using partially deacetylated chitin (DDA 27 %) on the length, width, and morphology of NWs. STEM of ChNWs (27 % DDA) was obtained after 1, 3, 4.5 and 6 h using 3 M HCl at 90 ℃ were shown in **Fig. 14A(a-d)**. STEM showed (**Fig. 14a, b**; red circle) highly agglomerated sections of nanowhiskers after 1 and 3 hours of acid hydrolysis, and SEM (**Fig. 14Ae, f**; 1h, 3h) revealed that nanowhiskers formed strong bundle network between single nanowhiskers. After a longer treatment time using HCl (3M), i.e. 4.5 and 6 h (**Fig. 14Ac, d**), more single fibrils appeared with lesser aggregation without a network structure generated between ChNWs. After 6 h of treatment with HCl, single chitin nanowhiskers were obtained without any aggregation/agglomeration between NWs (**Fig. 14Ad, h**).

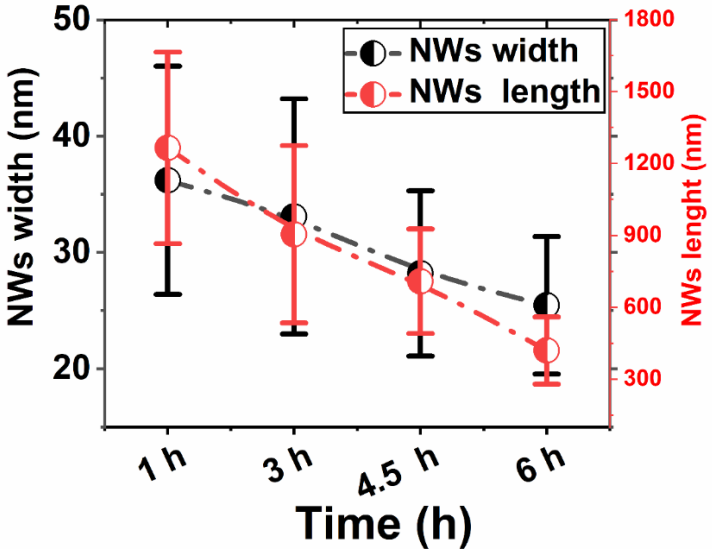

Fig. 14B. Representative effect of time of acid treatments on the length and width of partially deacetylated chitin nanowhiskers (27 % DDA).

Fig. 14B shows the effects of time treatment with hydrochloric acid (3 M) at 90 ℃ on the length and width of partially deacetylated ChNWs with 27 % degree of deacetylation. From Figure 2B and histograms of widths (**Fig. S2a-d, supporting information**) and length (**Fig. S2e-h, supporting information**) of ChNWs (DDA 27 %), the length of the NWs decreased significantly with the increasing time of acid treatment from 1, 3, 4.5, to 6 h and took the value of 1265, 904, 709 and 419 nm, respectively. The width of NWs decreased with the increasing treatment time from 36.4 to 19.7 nm (**Fig. 14B, S2 supporting information)**. The decrease in width and length of the nanowhiskers during the extended time of acid treatment might be caused by the hydrolysis of the amorphous part of the chitin chains while the crystalline part was retained intact.

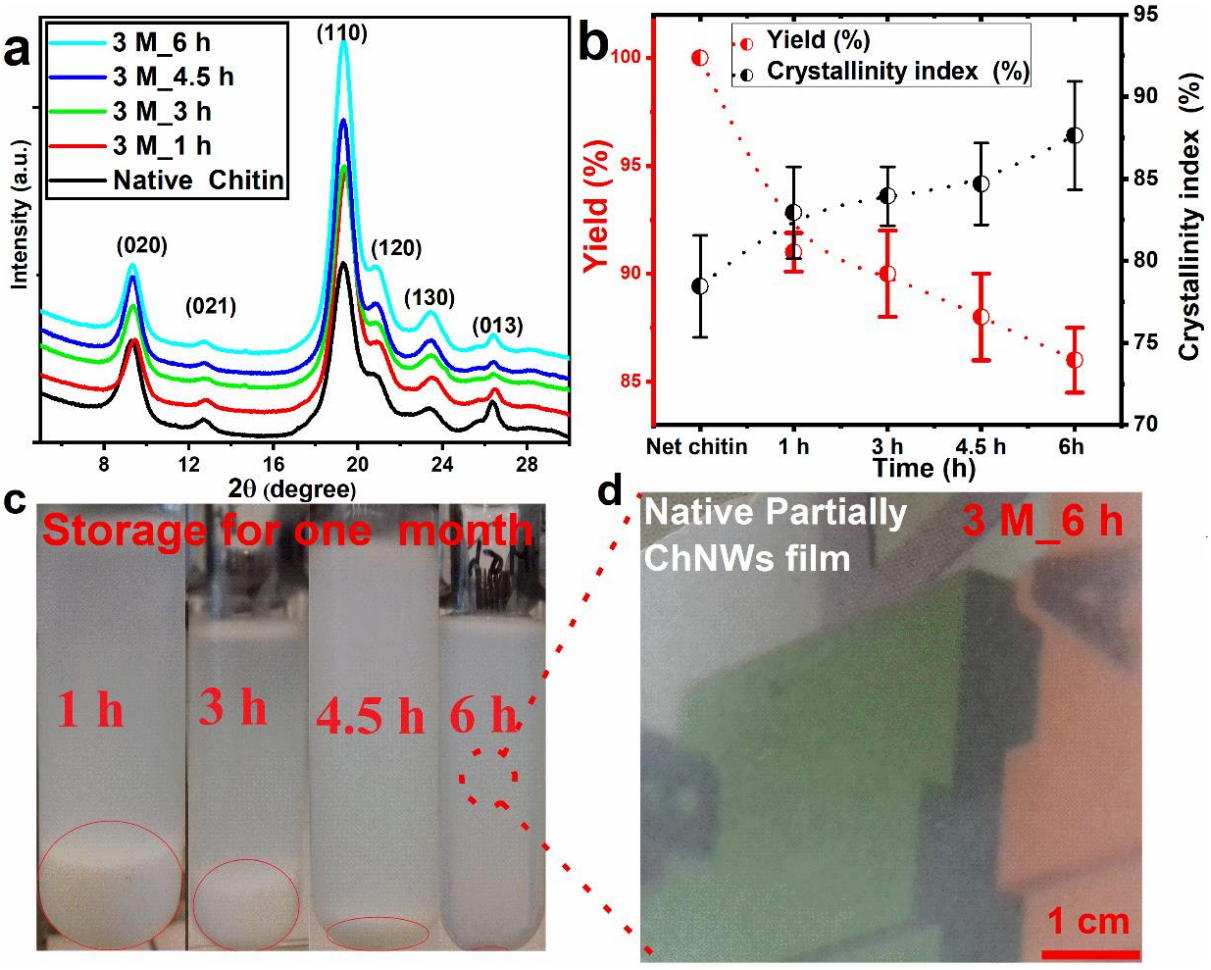

Fig. 15. Representative XRD, percent crystallinity yield, and stability of the extracted partially deacetylated ChNWs.

Fig. 15 shows the XRD, crystallinity index and yield percent of the ChNWs extracted after different hydrolysis times varying from 1 to 6 h using 3M of HCl. XRD measurements were employed to reveal detailed information about the crystallographic structure of the native and partially deacetylated chitin nanowhiskers (ChNWs) using different treatment times (**Fig. 15a, b).** All of the native chitin and partially deacetylated chitin nanowhiskers exhibited six diffraction peaks at 2θ = 9.4°, 12.9°, 19.3°, 20.8°, 23.5°, and 26.5° indexed as (020), (021), (110), (120), (130), and (013), respectively (**Fig. 15a. b**), suggesting a crystalline structure of the α-chitin [191, 205].

The diffraction peaks of the native chitin were much broader and weaker than that of the partially deacetylated chitin nanowhiskers (ChNWs), indicating a decrease in crystallinity (**Fig. 15b**). Meanwhile, the crystallinity content was slightly increased from 78.45 ± 3.1 to 87.63 ± 3.3 % with the increasing time of acid hydrolysis from 1 h to 6 h. Because of these results, the partially deacetylated ChNWs retained the intrinsic structure and the character of the native α-chitin, namely, its native bioactivity. The yield percent of NWs was slightly decreased with the prolonged acid treatment time with a loss percent of about 15 % from the dry weight due to, the smaller size of NWs which was difficult to collect during the purification steps (**Fig. 15b**).

Figure 15c shows the stability of colloid solutions of NWs extracted at different treatment times after one month of storage at room temperature (20 ± 3 °C) with a pH of the solution of about (4.5-5). After one month of storage, at a shorter treatment time, the NWs were highly aggregated into a bulk structure due to the electrostatic interaction between the charges on the surface of the partially deacetylated NWs (free amino groups). This phenomenon was also confirmed in **Figure 13a** using STEM (**Fig. 14Aa**). At longer treatment times above 3 h and 4.5, lower quantities of NWs precipitated (compared with 1h treatment). Partially deacetylated ChNWs were extracted after 6 h of treatment with 3M of HCl and were highly dispersed without precipitations after one month of storage at room temperature (**Fig. 15c**). **Figure 15d** shows the film of net ChNWs after (6 h, 3M HCl, one-month storage at RT), with high transmittance properties and uniform surface morphology with highly oriented nanowhiskers in the film matrix.

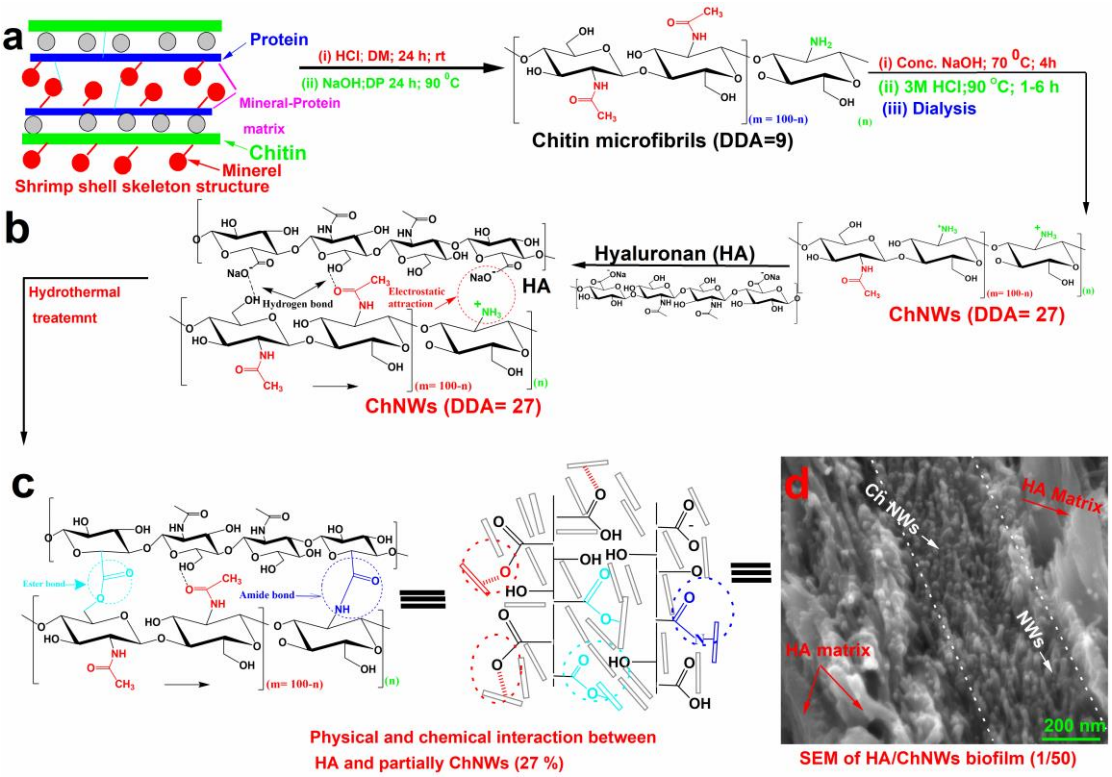

Scheme 1. A representative mechanism of extraction of partially deacetylated chitin nanowhiskers and interactions between hyaluronan (HA) and partially deacetylated chitin nanowhiskers (ChNWs).

4.2. Fabrication of HA/ChNWs films

Scheme 1a shows the skeleton structure of the shrimp shell matrix before and after chemical treatment and generated chitin microfibrils (**Fig. S1b, c, supporting information**). Chitin microfibrils were generated after the DM and DP with highly interconnected and porous structures (**Fig. S1b, c, supporting information)**. Partially deacetylated chitin nanowhiskers (DDA 27 %) with controlled dimensions of short nanofibrils with the width and length of 19 nm, and 410 nm, respectively (**Scheme 1b**), were generated as a result of acid hydrolysis (3M; 6h).

Partially deacetylated ChNWs with DDA 27 % interacted with hyaluronan (negative charge surface) via the physical and chemical interactions (ionic, hydrogen bonds, van der Waals) between the functional groups of NWs and HA (**Scheme 1b, c**). During hydrothermal treatment of nanocomposite film at high temperatures, ester and amide bonds could be partially formed between the functional groups of hyaluronan (-OH, -COONa) and partially chitin nanowhiskers (-OH, -NH2, -$NHCOCH_3$) (**Scheme 1c**). In **Scheme 1**d, it is apparent that the NWs were well dispersed and oriented within the HA matrix with no agglomeration observed between the nano-fibrils with the same size of single nanowhiskers.

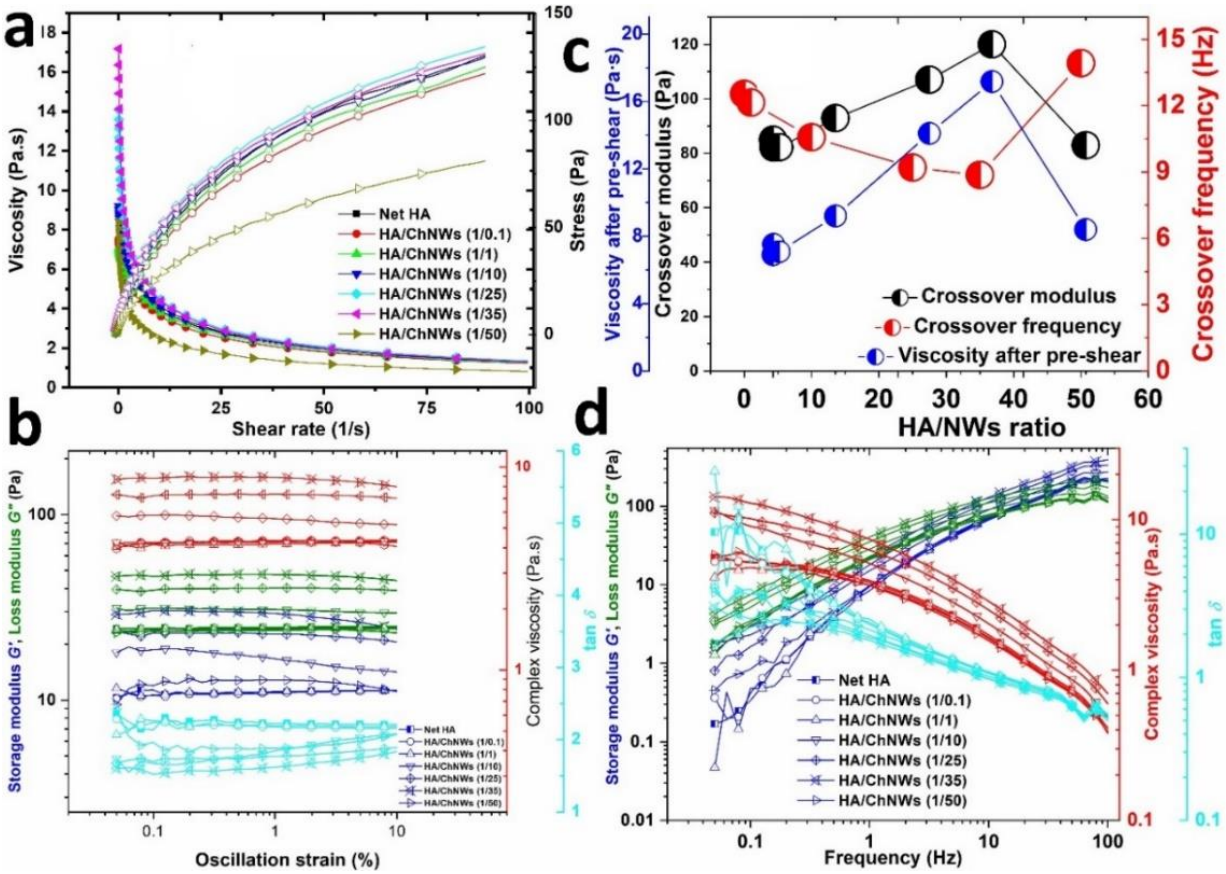

Fig. 16. Rheological properties of net HA and HA/ChNWs nanocomposites.

Rheology is an important parameter of polymer processing, and because of its sensitivity to structural features, it might be used as indirect evidence of structural changes. The rheological properties were altered by the presence of partially deacetylated NWs compared to the net HA solution (**Fig. 16**). All samples show significant shear thinning behavior and conform well to both the Herschel-Bulkley and the power-law viscosity models. The values and meaning of the fitting parameters are discussed in the additional information (**Fig. S3, supporting information**). Moreover, the 1/25, 1/35 and 1/50 HA/ChNWs solutions were slightly thixotropic, the remaining samples showed no thixotropy. The flow viscosity drops from the initial 6.9-17.2 Pa·s (measured after pre-shear) to 0.8-1.3 Pa·s at high shear rates (**Fig. 16a**).

All nanocomposites with different ratios of HA/ChNWs (1-50) showed higher viscosity compared to the net HA, which increased nearly linearly up to 17.2 Pa·s with the increase of the volume fraction of NWs content except 1:50 HA/NW sample (**Fig. 16c**). Provided the viscosity of the net nanowhisker suspension was as low as 9.7 mPa·s, the observed increase in viscosity is far higher than would be expected from a simple flow distortion caused by solid obstacles. However, a similar increase in viscosity was previously reported due to the formation

of the nanoparticle/polymer structure induced by nanoparticle interaction of nanoparticles with polymer chains [206]. As the structure was destroyed upon shearing, the increase in the viscosity of nanocomposite solutions diminished, and most samples dropped below the viscosity of the net HA at higher shear rates. Furthermore, in terms of rheological data, the structuring tendency reached a threshold between 1/35 and 1/50 HA/NW and the sample 1/50 HA / NW was qualitatively dissimilar from the rest of the samples. An analogous situation was observed for the oscillatory tests.

Figure 16d shows the dependence of storage and loss moduli, loss factor tan δ and complex viscosity of HA/NW solutions on the frequency at 1 % strain amplitude. We note that the 1 % (**Fig. 16d**) strain amplitude lies on the very edge of the linear viscoelastic region (LVR) for some samples (**Fig. 16b**), however, comparison with 0.5 % strain amplitude measurements (data not shown) revealed no significant hints of non-linear effects at the higher strain amplitude. Since the 1 % strain amplitude oscillatory tests provided a better signal-to-noise ratio, we chose to present this data. Clearly, the effect of NW on the rheological response of HA solution is more apparent at lower shear rates/frequencies. This finding was consistent with the previous reports on behavior of nanoparticles in polymer fluids [207-211].

The reason for this was that the reputation dynamics of polymer chains was slowed down by nanoparticles, contrary to Rouse dynamics that remain unaffected. The dependence of crossover modulus on HA/NW ratio showed a nearly linear increase from 82 Pa to 120 Pa with the increasing NWs content up to 1/35 HA/NWs, followed by an immense drop to the value of 83 Pa for the 1/50 HA/NWs sample. Crossover frequency, on the other hand, decreased from 12.5 Hz for the net HA to 8.9 Hz for 1/35 HA/NW, followed by an increase to 13.9 Hz for the 1/50 HA/NWs sample. The higher crossover frequency corresponds to a shorter relaxation time and vice versa. Polymer relaxation is slowed down by attractively interacting nanoparticles [187]. Therefore, a lower crossover frequency might indicate an attractive interaction between the HA and ChNWs.

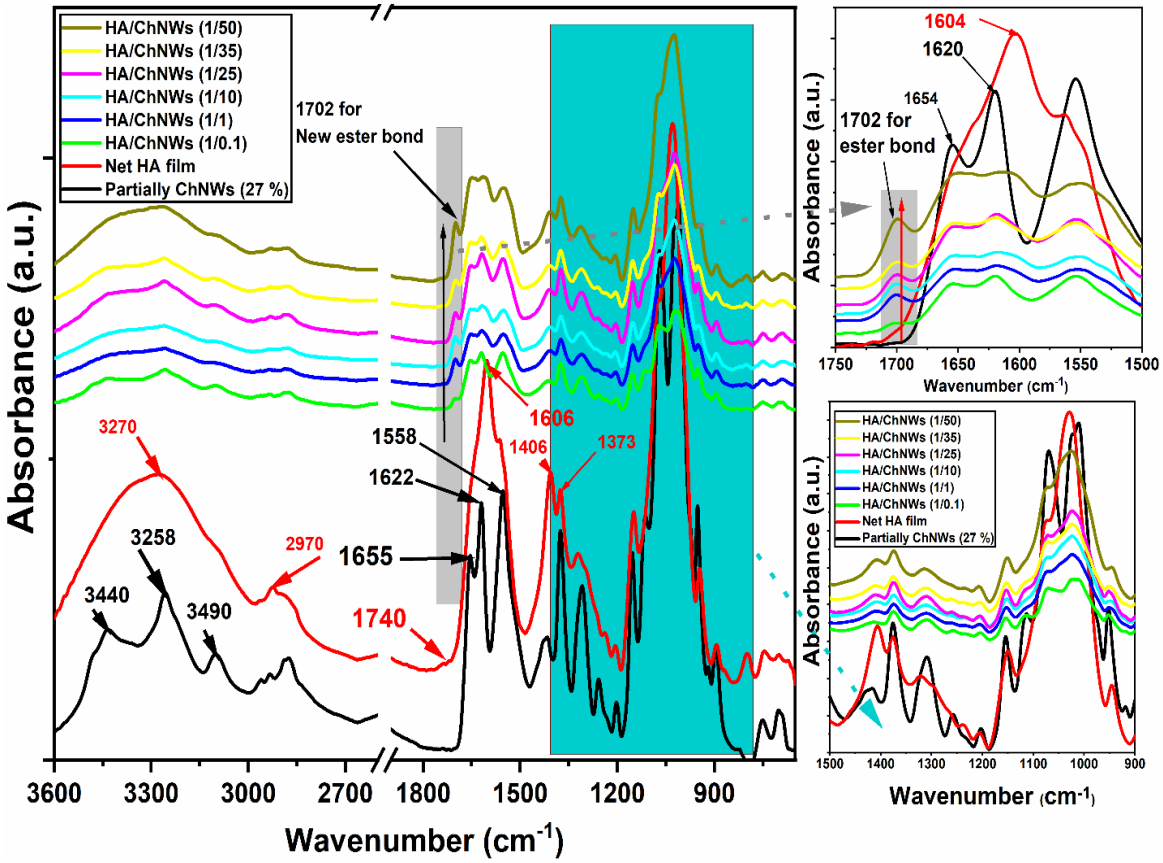

Fig. 17. ATR-FTIR of native hyaluronan and hyaluronan/partially deacetylated chitin nanowhiskers (DDA =27%) nanocomposite films

4.3. Physicochemical Properties of HA/ChNWs nanocomposite films

Fig. 17 shows the ATR-FTIR spectra of net HA, partially deacetylated ChNWs and films of HA/ChNWs with different ratios of ChNWs to HA, confirming the evaluation of the chemical interactions and formations of a polymeric structure (**Fig. 17**). The ATR-FTIR spectra for HA/ChNWs films in the fingerprint region from 900 cm^{-1} to 1800 cm^{-1} evidenced the presence of ionic interactions. In α-chitin, two absorption peaks are observed at 1655 and 1622 cm^{-1} corresponding to the α-chitin phase. *β*-chitin is characterized by only one peak at 1656 cm^{-1}. Consequently, the two peaks around 1655 and 1622 cm^{-1} observed in the FTIR spectrum (**Fig. 17**) confirmed that the chitin from shrimp shells was in α-crystalline form [71]. For high DDA chitosan, the band of amide I at 1655 cm^{-1} had a higher intensity than the band of amide II at 1557 cm^{-1}, which suggests efficient deacetylation. When the deacetylation of chitin occurs, the absorption band assigned to amide II decreases, while the increase in intensity of the amide I band indicates the formation of NH_2 groups. However, in our case, only low DDA showed (27 %) the peak at 1557 cm^{-1} stronger than the peak at 1655 cm^{-1}. The positively charged amino

group of the partially deacetylated ChNWs as observed with the NH_3^+ bending vibrations (1557 cm^{-1}) interacted with the negatively charged COO^- of HA (1622 cm^{-1}).

The formation of polyelectrolyte complex PEC and crosslinking resulted in a reduced absorption for the OH and NH stretching vibration peaks. In addition, the presence of a new peak at 1702 cm^{-1} region indicated the esterification reaction between carboxylic groups of HA and hydroxyl groups of NWs and peak intensity was increased by increasing the ratio of NWs into the matrix. The peak of net HA film at 1744 cm^{-1} corresponded to the physical ester bond between COOH and OH groups of HA and disappeared after the addition of NWs, this could be due to the interaction between COOH of HA and NH_2 and -OH of the partially deacetylated ChNWs (**Fig. 17**) [10, 157]. The peak intensity of free amino groups at 1557 cm^{-1} weakened at higher nanofiller loading in the HA matrix due to the strong ionic interaction between the amino and the carboxylic groups of the partially deacetylated Ch and HA matrix, respectively (**Fig. 17**).

The microstructures of the HA/ChNWs nanocomposite films were investigated by X-ray diffraction. As shown in **Fig. S4 (supporting information)**, neat HA film exhibited a wide diffraction peak around 2θ = 20-22°, indicating the amorphous state of the hyaluronan matrix. Partially deacetylated chitin nanowhiskers (DDA = 27 %) exhibited six diffraction peaks at 2θ = 9.4°, 12.9°, 19.3°, 20.8°, 23.5°, and 26.5 ° indexed as (020 planes), (021 planes), (110 planes), (120 planes), (130 planes), and (013 plane) [91, 191], respectively (**Fig. 16a**). This was consistent with the diffraction peak of native chitin, suggesting that the acidolysis process did not affect the crystalline structure of the purified chitin. When the ratio of HA/ChNWs was less than (1/1) V_f. (0.012), there was no peak assigned to ChNWs. Afterward, a small peak around 9.42° assigned to 020 planes of CNCs gradually appeared in the nanocomposite. Furthermore, the intensity of peaks at 9.42° and 19.34° was increased with the increase of the ratio between the HA and the ChNWs from 1 to 50 and slightly shifted, indicating that no intercalation of NWs into the interlayer of the HA matrix occurred as well as a partial orientation of NWs took place in the HA matrix film via the interfacial interactions with ChNWs. The partially deacetylated chitin nanowhiskers chains with large molecular sizes might be blocked by strong physical and partial chemical bonds among the sheets of the HA matrix. Because the XRD pattern was a statistical result, higher ChNWs loading strengthened the peak intensities and the crystallinity of nanocomposite films was enhanced with the increased volume fraction (V_f) ratios between HA and ChNWs (**Fig. S4, supporting information**). The XRD results suggest that ChNWs were successfully incorporated into the hyaluronan matrix (**Fig. S4, supporting information**). Based on the XRD results, it could be concluded that ChNWs could be

uniformly distributed and partially oriented in the HA film, but their layer space remained unchanged.

Fig. S5 (supporting information) shows the light transmittance spectra of the nanocomposite films from net HA, HA/ChNWs with a different ratio and net ChNWs. The transmittance of net HA film was high (82 %) in the visible light range from (400 to 750 nm). The transmittance properties of films were decreased by increasing the weight ratio between hyaluronan and nanowhiskers from (1/1 to 1/50). At lower ratios (0.1 to 10) the optical transmittance was decreased slightly, up to 1/35 and 1/50 weight ratio. This result suggests that the nanowhisker content had little influence on the transparency of nanocomposite films. Therefore, due to the small diameter of NWs, it was possible to prepare high-strength HA/ChNWs nanocomposite with a high-volume fraction of nanowhiskers combined with a preserved transparency. The partially deacetylated ChNWs showed a large surface area and small dimensions, which provided a higher probability of their mutual interaction with the hyaluronan matrix, leading to the strong adhesion between HA and ChNWs. According to the results of FTIR, XRD, SEM, and optical transmittance, the partially deacetylated ChNWs were dispersed homogeneously and embedded very well in the HA matrix.

The swelling percentage (SP) of the nanocomposite films was evaluated in water and phosphate buffer solution under physiological conditions (PBS, pH 7.5 at 37 ℃). All nanocomposite films showed a high swelling percentage after 1 h (Fig. S6$_{a,b}$, S7, supporting information). After 3 h of immersion in water and PBS, the SP was decreased in both water and PBS medium and showed no significant differences between immersed samples in water and PBS after 24 h (**Fig. S7, supporting information**). The stability of nanocomposite films due to physical and chemical bonds generated between HA and ChNWs functional groups as confirmed by FTIR measurements (**Fig. 17**). Figure 6c shows the weight loss of nanocomposite film after 24 h of immersed in water and PBS solution at 37 ℃. As shown in Figure S6c, an increase in the volume fraction ratio of NWs in the HA matrix improved the hydrolytic stability of films. In the first 1h, the non-bonded HA fast leached than ChNWs (Fig. S6d) and after 24 h of immersion, more NWs were leached from the matrix (Fig. S6d).

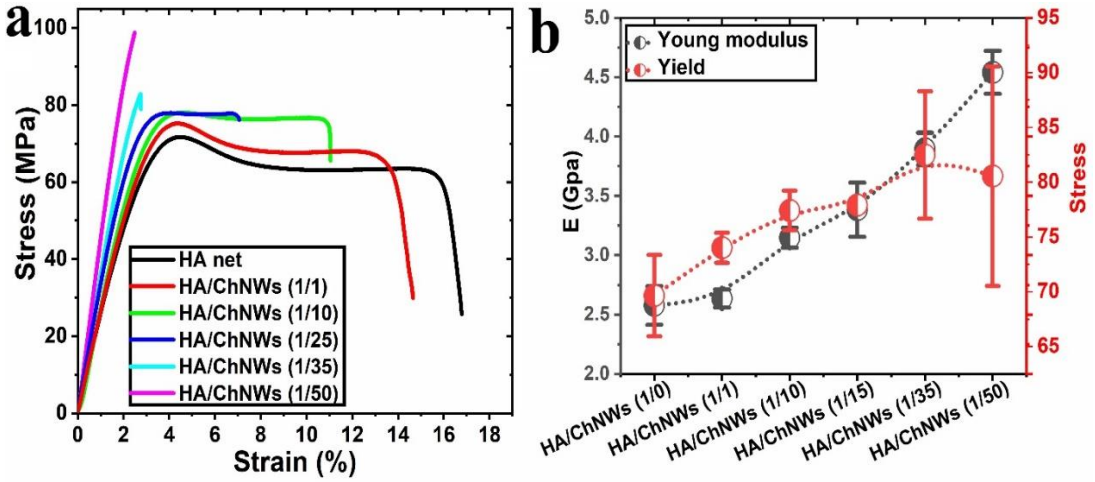

Fig. 18. Representative stress-strain curves for nanocomposites with different content of ChNWs in the HA matrix (**a)**. A plot of change of mechanical properties (tensile modulus and yield/maximum stress) in relative units (divided by properties of the neat matrix) as a function of ChNWs volume fraction **(b)**.

4.4. Mechanical Properties of nanocomposite films

Mechanical robustness, namely tensile modulus and stress was considerably enhanced with an addition of ChNWs to the HA matrix. The modification of property in relative units linearly scales with the volume fraction of ChNWs (Figs. **18a, b**). The yield and further plastic deformation of the nanocomposites were evident at lower volume fractions, however, up to 25 vol. % of ChNWs. Yield and further plastic deformation of the polymer nanocomposites decrease at high volume fractions 35 and 50 vol. % and samples are brittle fracture. The tensile modulus and the yield stress of the HA matrix were measured as 2.58 ± 0.16 GPa and 69.64 ± 3.71 MPa, respectively. With the addition of 50% vol.% ChNWs in the HA matrix, tensile modulus and stress were enhanced considerably to 4.54±0,18 GPa (+76 % increase compared to neat HA) and 80.54±10.02 MPa (+31 % increase compared to neat HA), respectively (**Fig. 18b**).

However, the ductility of the films decreases with the addition of ChNW (**Fig. 18b**). This embrittlement of the system can be caused due to the addition of a stiff reinforcing phase and the increase in the number of NW ends and their aggregation decreasing their reinforcing effectivity at higher loadings. It is mentioned that a similar behavior to what has been observed here was also observed for natural and synthetic films reinforced with α-chitin whiskers, in which the tensile modulus and yield stress of the films initially increased with increasing chitin whisker content and leveled off when the whisker contents were about 20% by weight or greater [198, 199, 212-214]. The mechanical and viscoelastic response of such hybrid nanocomposite systems is not yet well understood, but common theories in the field of polymer

nanocomposites include immobilization of polymer chains adsorbed on the surface of nanosized filler while altering relaxations of the chains and thus their time-temperature-dependent mechanical properties [215, 216]. Strong cationic-anionic interfacial interactions between ChNWs and HA result in the formation of a strong interphase which can be a couple of nanometers thick. HA chains have altered relaxations. This was supported via our rheological and FTIR measurements suggesting attractive interactions and possible esterification between HA and ChNWs that affect the relaxation of HA, which might be responsible for the modification of the properties of the nanocomposites.

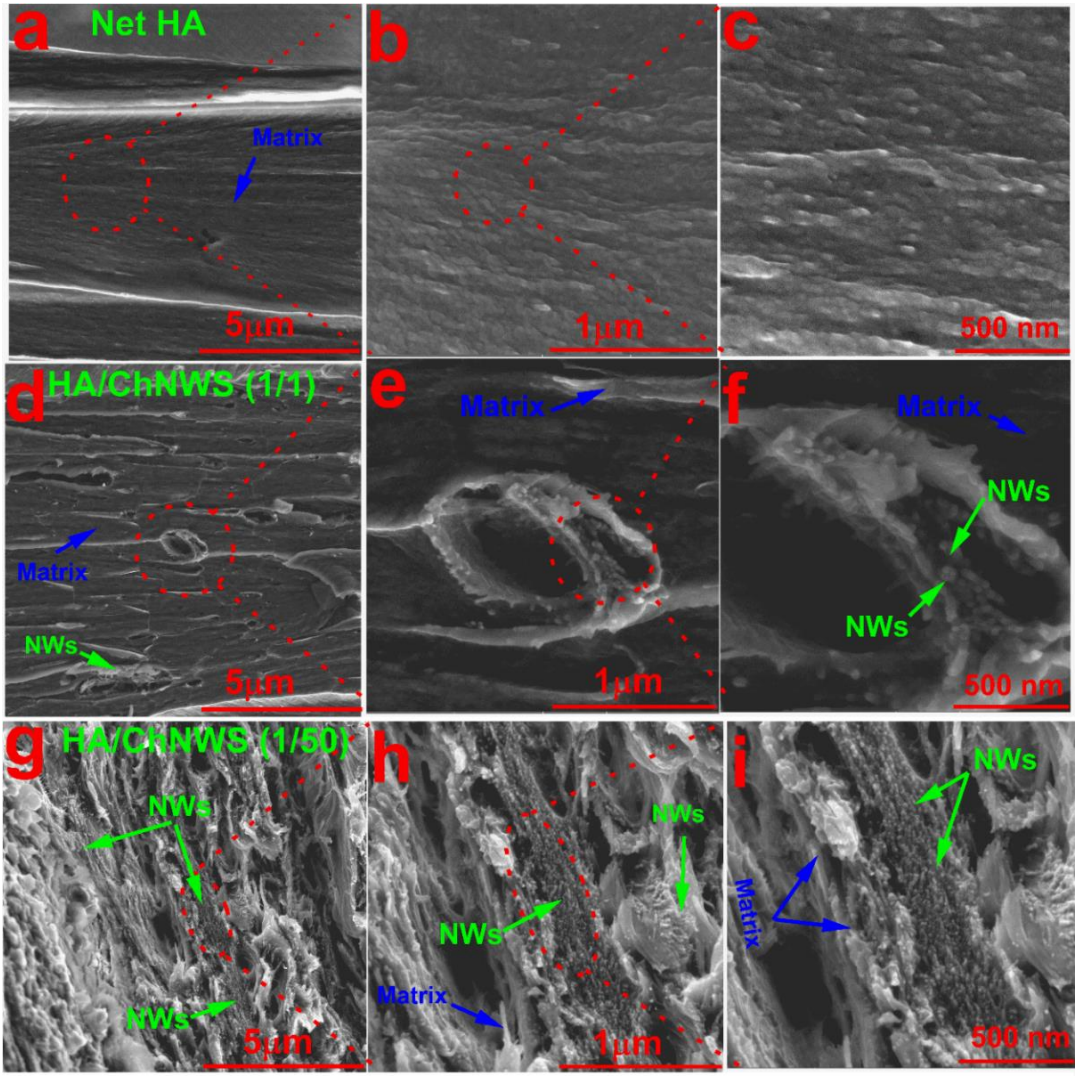

Fig. 19. SEM of fracture surface morphologies of HA/ChNWs nanocomposite films.
The surface fracture after the mechanical experiments was explored in **Fig. 19**. SEM images of fracture surface of native HA film (**Fig. 19a-c**) and nanocomposite films with different NWs ratios HA/ChNWs (1/1, **Fig. 19d-f**), HA/ChNWs (1/10, **Fig. S8a-c; supporting information**), HA/ChNWs (1/25, **Fig. S8d-f, supporting information**), HA/ChNWs (1/35, **Fig. S8g-I, supporting information**), HA/ChNWs (1/50, **Fig. 19g-i**). The modeling results demonstrated that the HA/ChNWs films with different ratios exhibited superior mechanical performance over the net HA film.

It is well-known that the mechanical performance of polymer nanocomposites is directly associated with the dispersion state of the reinforcing agents and interfacial adhesion between the reinforcing agent and polymer matrix. Therefore, to interpret the distinctive reinforcing efficiency of the partially deacetylated chitin nanowhiskers with DDA of 27 % in the HA matrix, their fracture surface morphology was observed using SEM, as shown in **Fig. 19, S8 (supporting information)**. The neat HA film showed a very smooth fracture surface (**Fig. 19a-c**). The incorporation of partially deacetylated ChNWs from 0.1 to 50-volume fraction (V_f) generated a very distinctive fracture morphology. For HA/ChNWs film (**Fig. 19d-f**), a homogeneous fracture surface (1/1), including a smooth phase (corresponding to the unfilled matrix) and a relatively rough phase (corresponding to the ChNWs-filled matrix), was observed.

The formation of ChNWs clusters and a highly entangled network (**Fig.19e.f**) were responsible for the poor dispersion state. However, no microsized fibers could be seen on the fracture surface, suggesting that the ChNWs were still distributed at the nanoscale in the HA matrix at this loading level. At the ratio of (1/10, **Fig. S8a-c, supporting information**) of HA to ChNWs, the fracture surface became rougher with the presence of a considerable number of voids and nanowhiskers (**Fig. S8a-c, supporting information**).

It was postulated that at this loading level, the ChNWs aggregated in the form of microsized fibers, which were further pulled out under an external force, leaving the observed voids. With the further increase in the concentration of the ChNWs to (1/10), more significant ChNWs distrusted and without holes were found on the fracture surface (**Fig. S8a-c, supporting information**). **Fig. S8g-i (supporting information)** visualizes a layered morphology reminiscent of a surface fracture of HA/ChNWs (1/35) with a high distribution of nanowhiskers within the HA matrix without holes in the fracture morphology with highly oriented ChNWs in the matrix. At the high-volume fraction (V_f) of nanowhiskers (1/50), the morphology of nanocomposites showed high orientation with well-distributed nanowhiskers in the HA matrix and without microsized fibers from NWs (**Fig. 19g-i**).

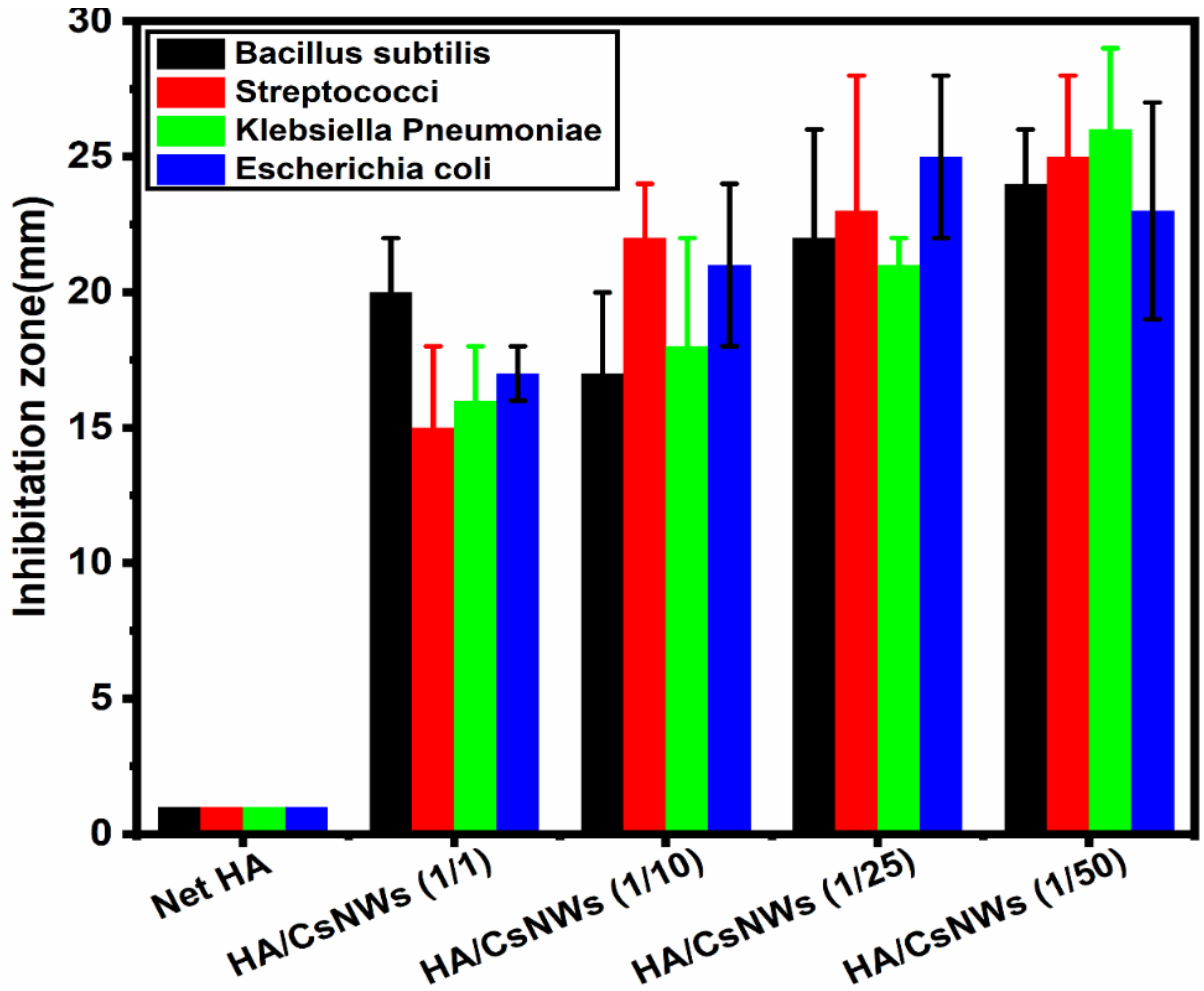

Fig. 20. Bactericidal properties of nanocomposite film against different types of bacteria

4.5. Bactericidal and toxicity properties of films

In addition to mechanical properties, the antibacterial properties were another important issue for active food packaging, as well as for wound dressing and skin regeneration applications. Antibacterial activities of HA/ChNWs nanocomposite films with different ratios against gram negative (*Escherichia coli, Klebsiella pneumoniae)* and gram positive (*Bacillus subtilis, Streptococci*) were examined, as shown in **Figs. (20, S9, supporting information)**. In the net HA film, there was no inhabitation zone around the specimens, indicating that the native HA film had no antibacterial properties against any type of bacteria (**Fig. 20, Fig S9, supporting information**). The inhibition zone gradually increased with increasing the concentration of CHNWs in the film matrix from 1 to 50 % (**Fig. 20, S9**.) Furthermore, the antibacterial properties of the films against Gram-negative bacteria were much better than against Gram-positive bacteria. Chitosan antibacterial activity against the gram-negative bacterium has been reported in recent years [192, 217-219].

The antibacterial mechanisms of partially deacetylated chitin nanowhiskers (ChNWs) were proposed and could be summarized as follows: (i) The presence of partially amino groups on the surface of partially deacetylated chitin nanowhiskers could interact with the anionic groups on the cell membrane of gram-negative bacteria, causing intracellular constitutive leakage [10]; (ii) ChNWs with nano-size (less than 40 nm width) penetrated the cell nucleus, hindering the synthesis of RNA and protein [220]; and (iii) ChNWs could act as an adsorbing agent, which bound metals to inhibit bacterial growth and toxin production [221].

HA/ChNWs films with different ratios (1/1, 1/10, 1/25, and 1/50) effectively inhibited the growth of *Escherichia* coli and *Klebsiella pneumoniae gram negative bacteria* as expected. However, for antibacterial activity against Gram-positive bacteria (*Bacillus subtilis, Streptococci*), it was postulated that the contribution of the first action was very limited because both ChNWs and *Bacillus subtilis, Streptococci,* were positively charged, and therefore the latter two mechanisms dominated. This caused the lesser observed antimicrobial activity against *Bacillus subtilis, Streptococci,* than *Escherichia* coli and *Klebsiella pneumoniae*. Furthermore, the HA/CHNW films had superior antibacterial activities against both *types of* bacteria, as expected. This phenomenon was interpreted by the exposure of more amino groups on the surface through partial deacetylation (DDA = 27 %), which were protonated and bound with the anionic properties on the cell membrane of *Escherichia* coli and *Klebsiella pneumoniae* more intensively, causing significant leakage of intracellular components.

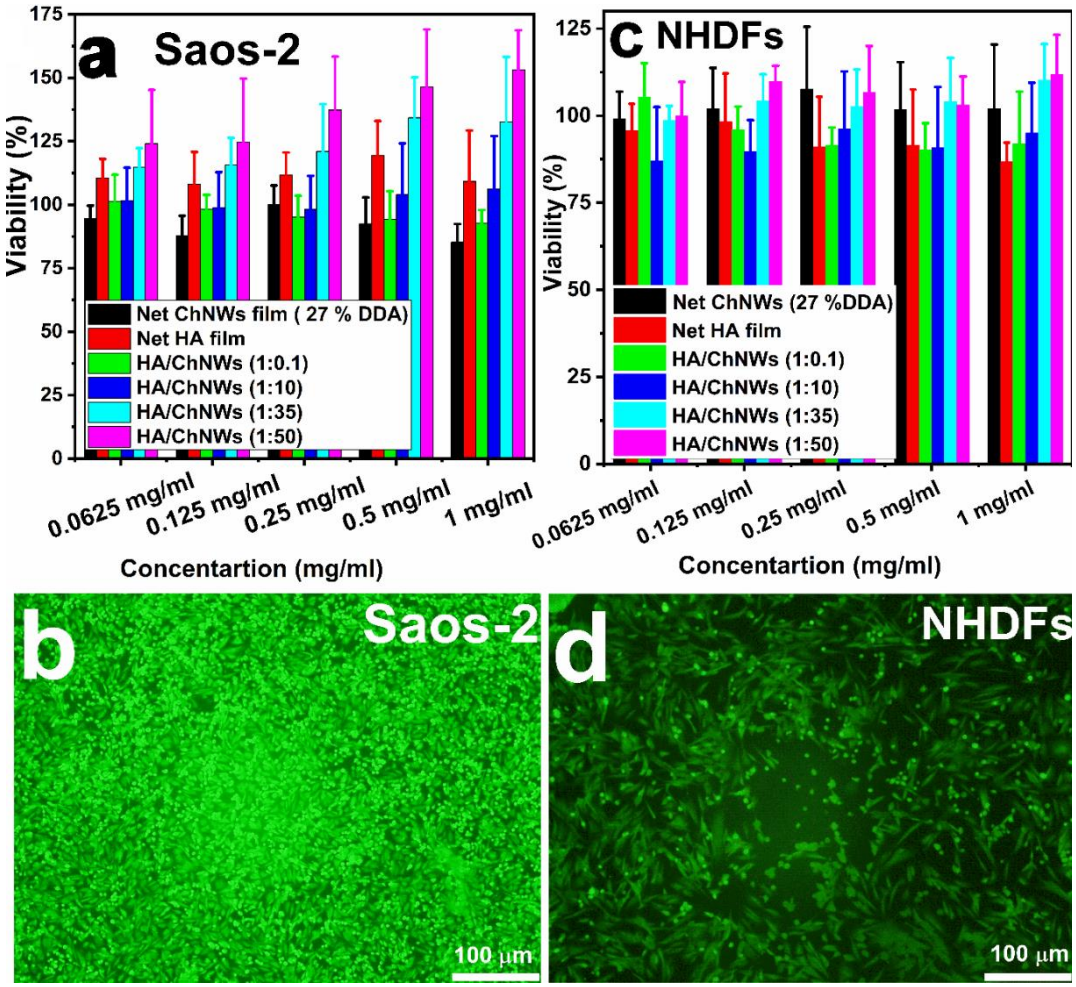

Fig. 21. Representative cytotoxicity of nanocomposite films using primary human fibroblast cells (NHDFs) and human osteogenic sarcoma cells (Saos-2 cells) and visualized cell lines using a fluorescent microscope.

In the presented article, the cytotoxicity and biocompatibility of HA / CHNW nanocomposite films in different rations using Saos-2 cells and NHDF with highly comparable results. These cells were chosen to respect the future applications of nanocomposite films as a wound dressing or drug delivery system. Based on the MTT test, it was determined that none of the prepared nanocomposite films at all the tested concentrations were toxic to the cells (visibility greater than 80 %, **Fig. 21a, b**). Similar results were obtained by Zubareva et al. [222] who postulated that positively charged chitosan did not cause the toxicity of the variety of cells, as well as Haridas et al. [223] who declared that the hydrogel showed almost 100% viability. The rate of increase in cell viability confirmed the suitability of the proper HA and ChNWs combination for further applications. This material was used for further examination and fluorescent visualization of the live cells (**Fig. 21b, d).** In the culture treatment with these items, no cell lysis was observed and demonstrated the number of live cells (green cells) was demonstrated.

Conclusions

Partially deacetylated chitin nanowhiskers (ChNWs) were successfully prepared from shrimp shells with different lengths and diameters by investigating the effect of hydrochloric acid treatment time on dimensions of NWs after extraction of pure chitin by the demineralization, deproteinization, and partially deacetylated steps. The NWs obtained after acid treatment were investigated and characterized by XRD, SEM, TEM, and ^{13}C-ssNMR. The results showed that there were no significant effects of the acid treatment on the DDA of the NWs, but there were significant changes in the dimensions of the NWs.

The width and length of the NWs were decreased from 36 and 1265 nm to 20 and 420 nm, with an increase in the treatment time from 1 to 6 h using 3M HCl, respectively. The HA-ChNWs showed enhanced mechanical properties over the HA films with a high-volume fraction of the NWs. The results of the mechanical and fracture morphology visualized using SEM showed enhanced interfacial bonding through the formation of stronger electrostatic and chemical at the ChNWs-HA interface. Nanocomposite films exhibited good antibacterial properties against different types of bacteria (-/ + G), which was improved with the increasing volume fraction of the NWs loaded into the HA matrix. The novel films significantly enhanced cell viability (NHDF, Saos-2) without any toxicity using different concentrations of nanocomposite film extracts (0.0625 to 1 mg/ml). It was expected that the present work would not only enrich the high value of seafood wastes utilized but also provide an alternative way to prepare edible, sustainable, environmentally friendly, mechanical enhancement, and antibacterial films for active food packaging application, drug-carrier application as well as for tissue regeneration purposes.

Supporting information.

Characterization

XRD was measured at 3 kW diffractometer Lab (Rigaku, Japan) using Cu Kα radiation (λ = 1.54) and detector Dtex Ultra with Bragg-Brentano geometry. The diffraction angle 2θ (XRD) was measured in the range of 5 ° to 50° with a step size of 0.02 ° at speed 4°/min. A generator was operated with a current of 30 mA and the voltage of 40 kV. The crystallinity index (%) of the materials was determined using Eq. (1)

$$Cr.I = \frac{I_{110}}{I_{110}+I_{am}} * 100 \quad (1)$$

where Cr.I is the crystallinity index, I110 is the maximum intensity of the diffraction of the plane at 2θ = 19.6°, and I_{am} was the intensity of the background scatter measured at 2θ = 16 ° using Scherrer's equation [224].

The microanalysis was performed using the FISONS Instruments EA 1108 C, H, N apparatus (Thermo Scientific, USA). First, the elemental analysis was performed, where the total protein content was calculated from the nitrogen content [202] by using the following equation. (2)

$$P\ (\%) = [N\% - 6.9] * 6.25 \quad \textbf{(2)}$$

where P (%) represents the percentage of proteins remaining in the deproteinized shell, N % represents the percentage of nitrogen measured by elemental analysis, 6.9 corresponds to the theoretical percentage of nitrogen in fully acetylated chitin (this value was adjusted as a function of DA, the degree of acetylation), and 6.25 corresponds to the theoretical percentage of nitrogen in proteins. All determinations were done in quadruples. UV/vis spectroscopy was used to determine the P %. The measurements were carried out on UV/VIS 160A, Shimadzu, Japan using a quartz cuvette with an optical path of 1 cm. The concentration of the measured solutions was kept at 0.59 mg/ml**.** The protein content in the supernatant [202]. was calculated from the following Eq. (3)

$$P\ (\%) = 2.37\ (A_{564}/W) \quad \textbf{(3)}$$

where A_{564} was the absorbance value at 564 nm and W was the weight of the sample in mg.

The antibacterial activity of net films of HA and HA-ChNW with different ratios were selected to evaluate the biological activity against *Bacillus subtilis, Streptococci* (gram positive) *and Klebsiella Pneumoniae, Escherichia coli* (gram negative) by the disk plate method. A bacterial suspension of 1×10^8 cells/mL was inoculated in nutrient agar plates using the spread plate method and Muller-Hinton agar was prepared by mixing beef extract powder (3 g), starch (1.5 g) casein hydrolase (17.5 g), and agar (17 g) in 1 liter of Milli-Q water. The

pH was adjusted to 7.5, the mixture was heated to completely dissolved the medium and then the medium was then sterilized in an autoclave at 121 ° C for 25 min. This nutrient agar medium was transferred to sterilized petri dishes in laminar airflow. After solidification of the medium, cultures of *Bacillus subtilis, Streptococci* (gram positive), *Klebsiella Pneumoniae, Escherichia coli* (gram negative) were streaked on the solid surface of the medium. Different films (11 mm) were loaded onto the surface of the solidified agar medium. The discs (control, gauze) were incubated at 5 ° C for 1 h to allow good diffusion. The plates were then incubated for 24 h at 37 ° C. The positive control (streptomycin disc) was tested in the same way to compare antibacterial activities. Plates with discs were monitored and each clearance zone was measured.

Solid-state NMR spectroscopy*:* ^{13}C CP/MAS NMR spectra were recorded on a Bruker AVANCE III HD spectrometer (Larmor frequencies $\nu^{13}C$ = 125.783 MHz) using a 3.2 mm MAS probe. The spinning speed of the rotor sample was 20 kHz. The number of scans for the accumulation of ^{13}C CP/MAS NMR spectra was 2048, a repetition delay of 5 s and a spinlock of 1 ms [225]. During detection, the high-power dipolar decoupling (SPINAL 64) was used to eliminate strong heteronuclear dipolar couplings. The isotropic chemical shift of the ^{13}C-NMR scale was calibrated with glycine as an external standard (176.03 ppm to carbonyl signal). In all cases, the dried samples were placed on the ZrO_2 rotors and all NMR experiments were performed at 303 K. The temperature calibration was performed on $Pb(NO_3)_2$ using a procedure described in the literature [226]. The mol. (%) of chitin units were calculated from the equation referred to in the literature [227] according to Eq. (4).

$$mol\%(N-acetyl\,glucosamine) = \frac{I_{C8}}{(I_{C1}+I_{C2}+I_{C3}+I_{C4}+I_{C5}+I_{C6})/6} \times 100 \quad \textbf{(4)}$$

The percentage of films was carried out in water and phosphate buffer solution (PBS). Films were cut into small pieces (1× 1 cm), weight, placed in glass vials, immersed in water or PBS and incubated at 37 ° C. At regular interval time (1, 3, 6, 12, 24 h). The HA/CHNW films were removed, dried with filter paper to eliminate excess of water or PBS from the film surface. The percentage of swelling was calculated according to Equation (5).

$$\text{Swelling ratio} = Ws - \frac{Wd}{Wd} \times 100 \quad (5)$$

Where Ws was the weight of the swollen film and Wd was the weight of the dry film, each value was averaged from three parallel measurements.

The weight loss of the nanocomposite films was determined gravimetrically under physiological conditions (PBS, pH= 7.5, 37 ° C). After 1 day of immersion, the films were removed and washed well with Milli-Q water to remove any attached salts from the film surface

and then freeze-dried for two days at – 50 ° C. The weight loss was calculated according to equation 6.

$$\text{Weight loss} = Wi - \frac{Wf}{Wi} \times 100 \qquad (6)$$

Where Wi was the weight of the film after 24 h and Wf was the weight of starting a dry film, each value was averaged from three parallel measurements.

Rheological evaluation: The fitting parameters of the Herschel-Bulkley and power-law viscosity models are presented in Fig. S3, the rate index n was obtained independently for both models. For n < 1, the fluid is shear thinned, whereas for n > 1, the fluid is shear-thickening. Both models showed that the shear thinning tendency strengthened with the presence of ChNWs up to the HA/ChNWs ratio of 1/35 while it was weakened for the highest ChNW content. The Herschel-Bulkley model features an additional yield stress which was estimated negative for all measurements. Negative yield stress has no physical meaning and was likely caused as an artifact caused by residual stress after preshear. However, it correlated well with the relaxation times, with the fastest relaxing samples showing the least negative value of yield stress and the slowest relaxing samples providing the largest negative values.

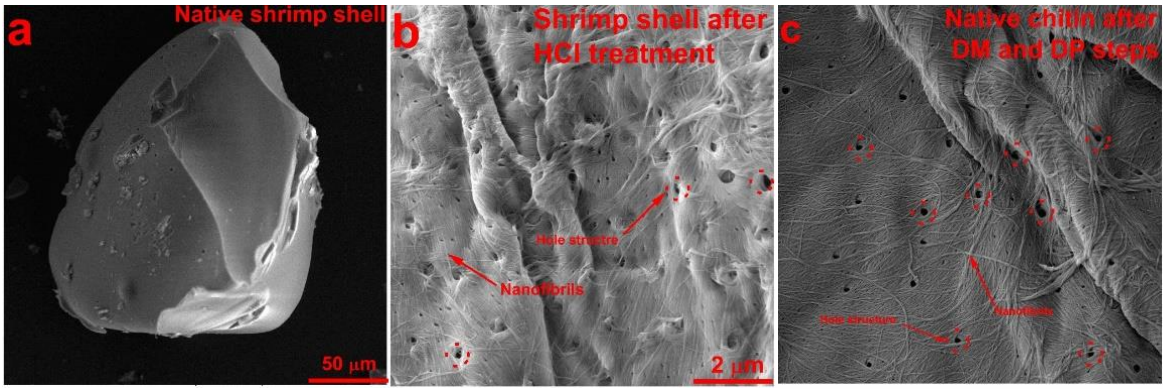

Fig. S1: SEM of native shrimp shells (a) and shrimp shells after the demineralization (b) and deproteinization (c) steps.

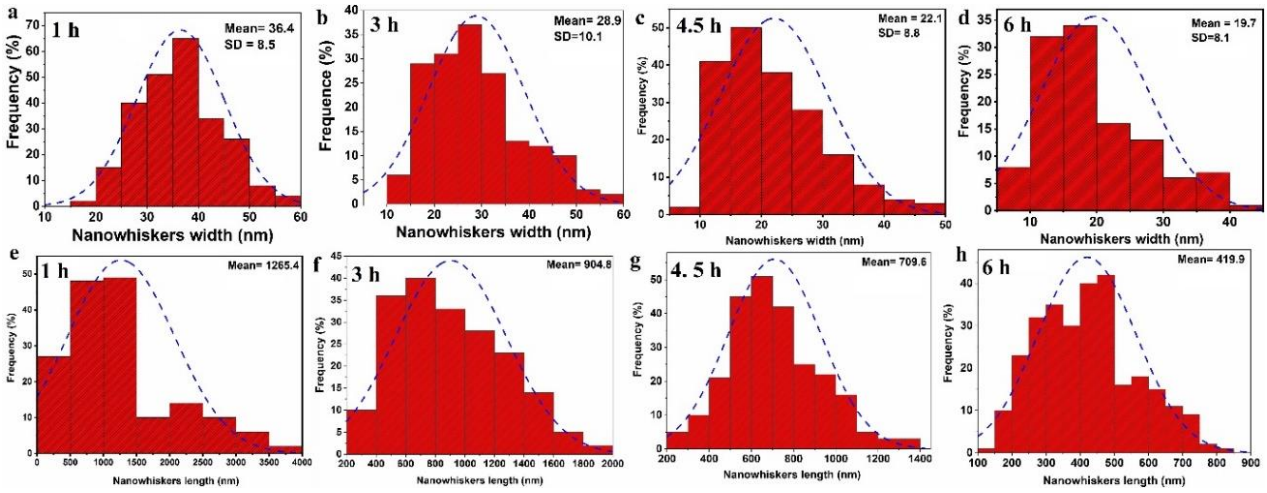

Fig. S2: Histograms of the widths and lengths of partially chitin nanowhiskers after acid treatment (3 M) at different treatment times (1-6 h). The length and width histograms were plotted from 300 points.

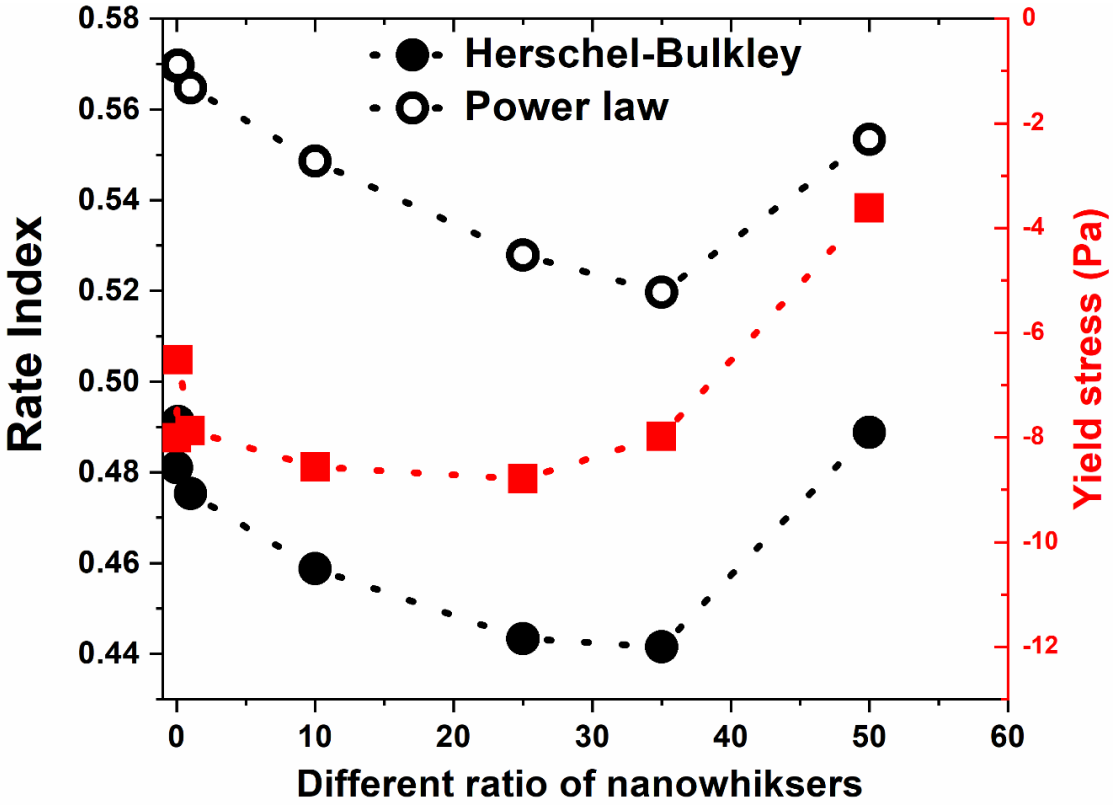

Fig. S3. Dependence of the Herschel-Bulkley and Power-law viscosity models that fit parameters on the HA/ChNWs ratio of the nanocomposite solutions.

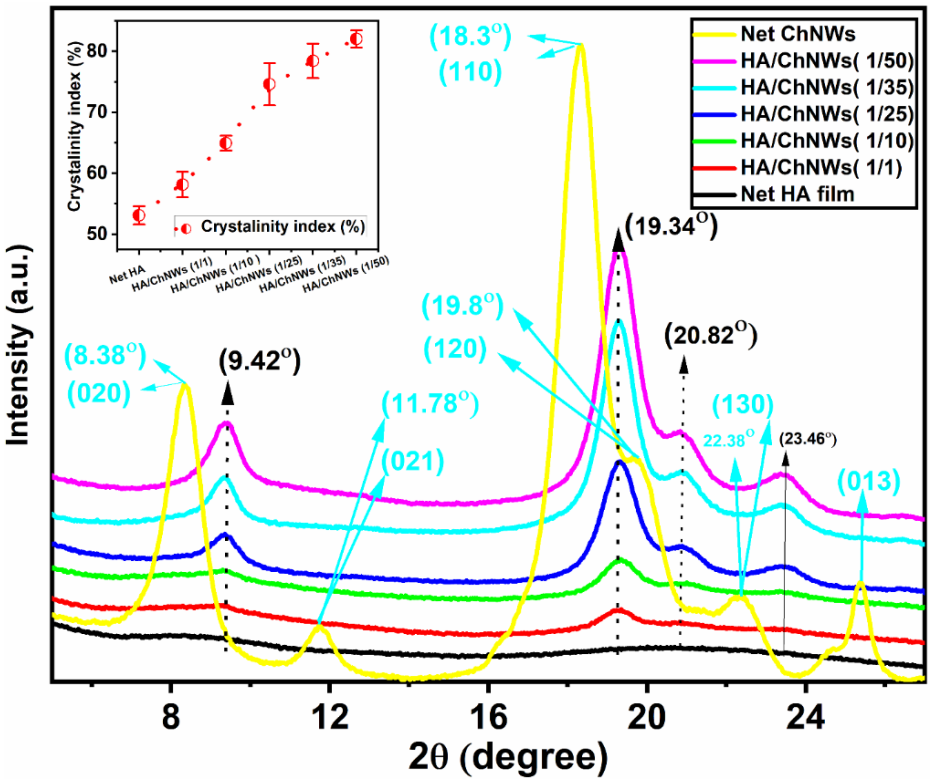

Fig.S4: XRD and Crystallinity Index of nanocomposite films

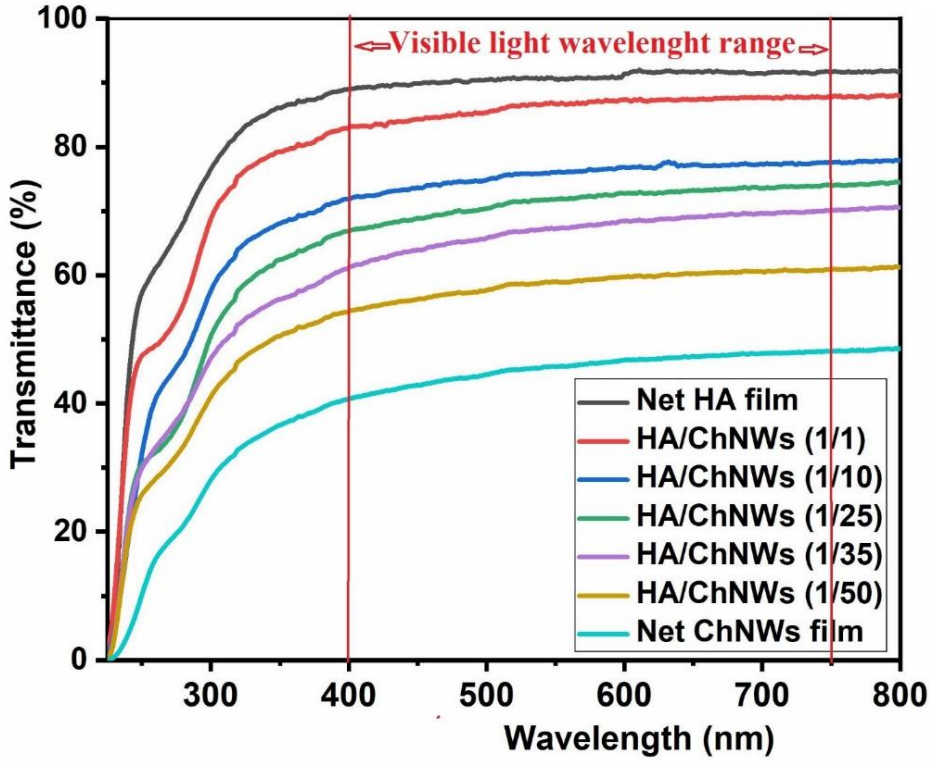

Fig. S5: Optical transmittance of native HA and HA/ChNWs nanocomposite films

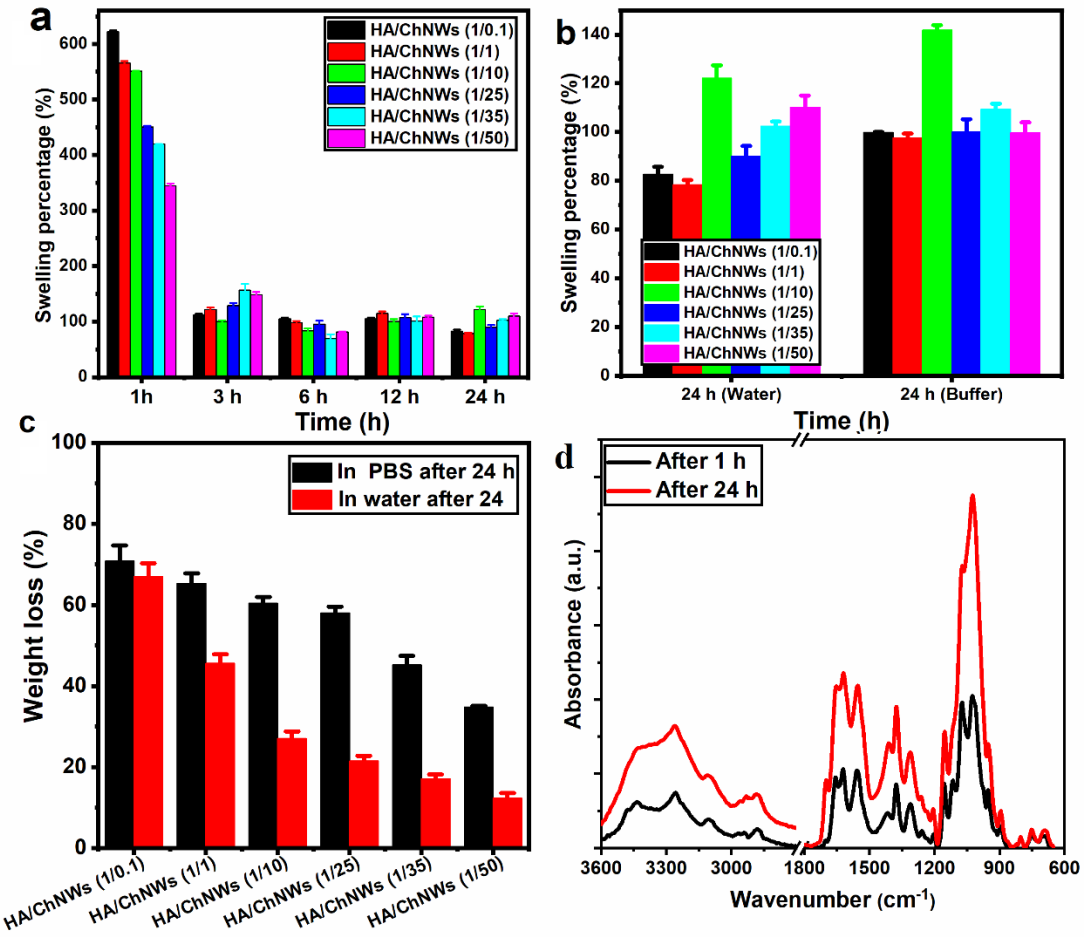

Fig. S6. Swelling and hydrolytic degradation of HA/ChNWs nanocomposite films

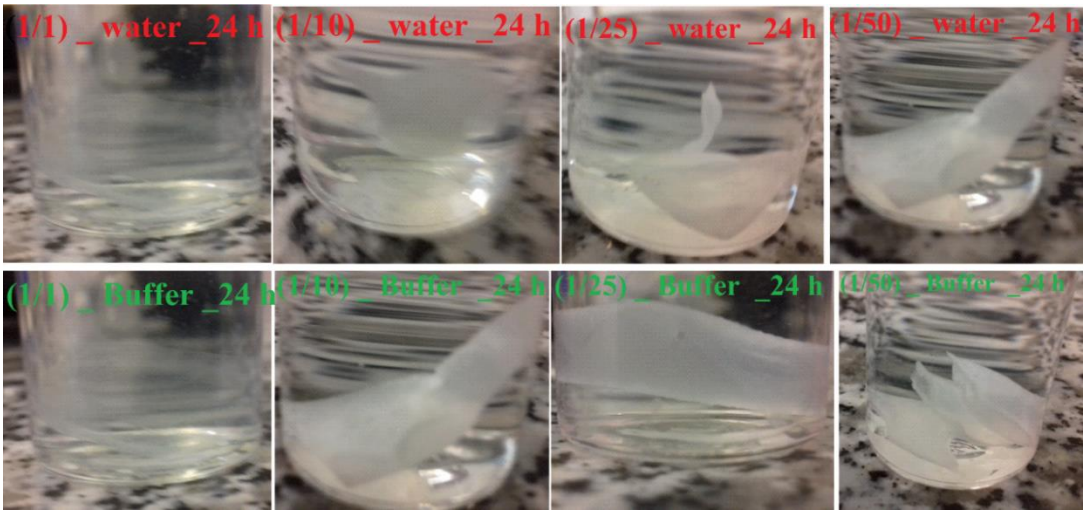

Fig. S7. Representative of the swelling behavior of nanocomposite films with different ratios in water and PBS solutions after incubation for one day at 37 ° C.

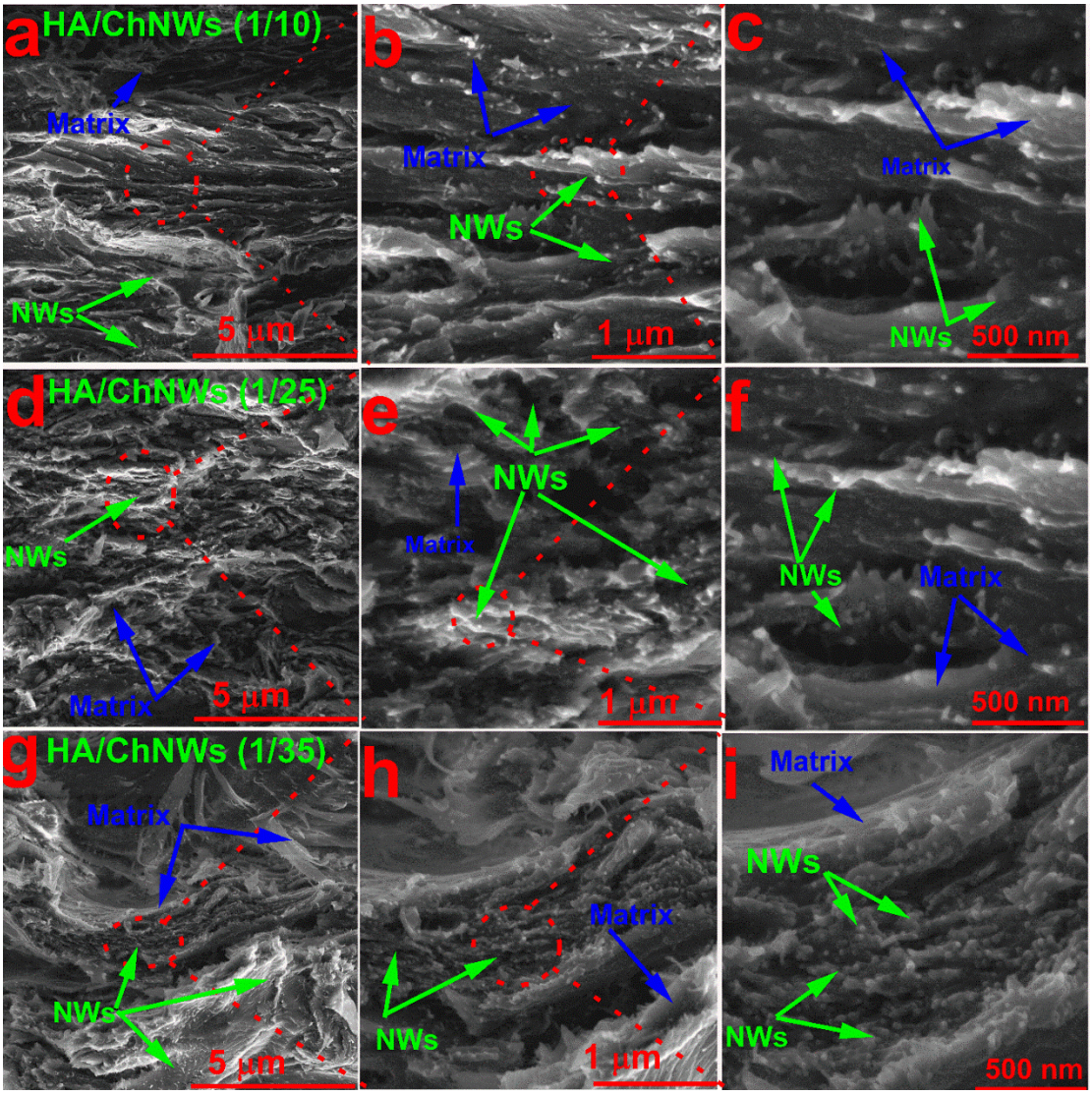

Fig. S8. SEM of fracture surface morphologies of HA/ChNWs nanocomposite films.

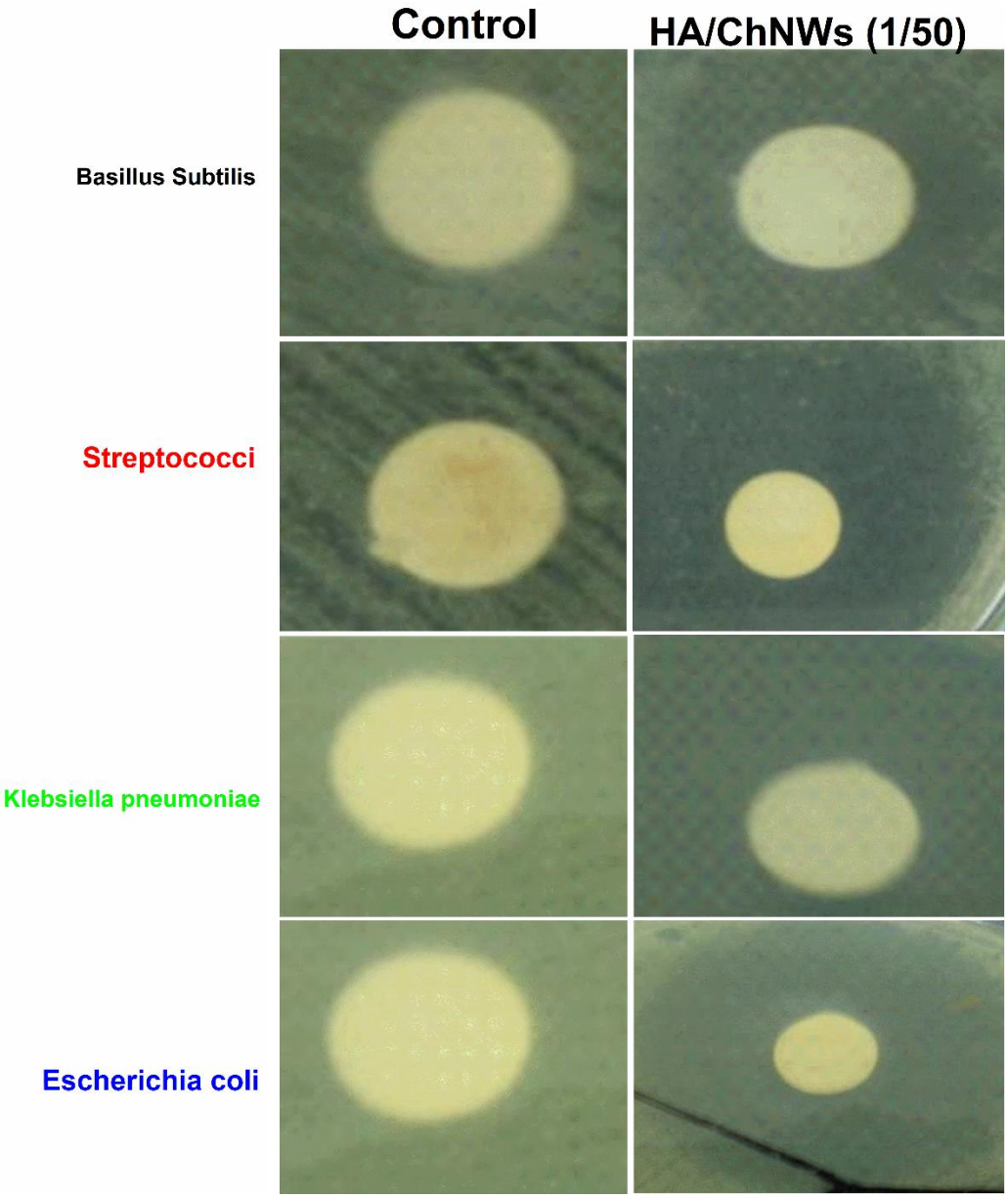

Fig. S9. Inhabitation zones of different films measured using different types

Chapter 3

Self-assembled hydrogel membranes with structurally tunable mechanical and biological properties

Abstract

Using supramolecular self-assembled nanocomposite materials made from protein and polysaccharide components is becoming more popular because of their unique properties, such as biodegradability, hierarchical structures, and tunable multifunctionality. However, the fabrication of these materials in a reproducible way remains a challenge. This study presents a new evaporation-induced self-assembly method producing layered hydrogel membranes (LHMs) using tropocollagen grafted by partially deacetylated chitin nanocrystals (CO-g-ChNCs). ChNCs help stabilize tropocollagen's helical conformation and fibrillar structure by forming a hierarchical microstructure through chemical and physical interactions.

The LHMs show improved mechanical properties, cytocompatibility, and the ability to control drug release using octenidine dihydrochloride (OCT) as a drug model. Because of the high synergetic performance between CO and ChNCs, the modulus, strength, and toughness increased significantly compared to native CO. The biocompatibility of LHM was tested using the normal human dermal fibroblast (NHDF) and the human osteosarcoma cell line (Saos-2). Cytocompatibility and cell adhesion improved with the introduction of ChNCs. The extracted ChNCs are used as a reinforcing nanofiller to enhance the performance properties of tropocollagen hydrogel membranes and provide new insights into the design of novel LHMs that could be used for various medical applications, such as control drug release in the skin and bone tissue regeneration.

Keywords:

Tropocollagen self-assembly, chitin nanocrystals, nacre-like, mechanical performance, piezoelectric properties, *in vitro* evaluation

Rasha M. Abdel-Rahman, A. M. Abdel-Mohsen, Jana Frankova, Francesco Piana, Lukas Kalina, Veronika Gajdosova, Ludmila Kapralkova, Muhammed Arshad Thottappali, Josef Jancar. Self-assembled hydrogel membranes with structurally tunable mechanical and biological properties. ACS Biomacromolecues, 2024, 25, 6, 3449–3463.

1. Introduction

Nacre-like materials from natural biomaterials have potential applications in different fields, including tissue engineering, regenerative medicine, biomineralization studies, and biomaterial coatings[111, 228-231]. These materials can serve as scaffolds to promote cell adhesion, proliferation, and tissue regeneration in tissue engineering. They can also be used as substrates to study biomineralization processes and to form calcium carbonate-based structures. In addition, they can be applied as coatings on medical devices or implants to improve biocompatibility, reduce inflammation, and improve integration with surrounding tissues. Using the properties of natural biomaterials and mimicking the layered structure of nacre, these materials offer opportunities to develop advanced biomaterials with improved functionalities and performance for various biomedical applications[231, 232].

Collagen is the most abundant natural protein found in the extracellular matrix of different tissues and organs in mammals. It is commonly used in tissue engineering and regenerative medicine applications due to its biocompatibility and the ability to promote cell adhesion and proliferation[111]. However, collagen-based hydrogels generally have limited mechanical strength and structural stability[111]. The introduction of nanoparticles into the collagen matrix allows the resulting nanocomposite hydrogel to exhibit improved mechanical properties, such as increased strength, modulus, and toughness. Nanoparticles can strengthen the collagen network, provide structural support, and prevent collapse or disintegration of the hydrogel structure[233]. The choice of nanoparticles for the nanocomposite hydrogel depends on the desired properties and applications. Commonly used nanoparticles include inorganic materials such as silica[234], gold[235, 236], silver[237] and organic nanoparticles such as nanocellulose[238]. These nanoparticles can be incorporated into the collagen matrix through various methods, including physical mixing[112], co-assembly[239], or cross-linking[236, 240].

Chitin nanocrystals are promising nanofiller materials with high biocompatibility, biodegradability, excellent mechanical properties, and antibacterial activity**[9]**. Chitin nanowhiskers have been used as nanofiller material to improve the mechanical properties of natural polymers such as hyaluronan[158, 160], chitosan**[5],** and synthetic polymers such as PMMA[241]. The chitinous matrix promotes different bone cells (mesenchymal and osteoblast stem) and the surrounding tissues[242, 243]. Chitin microfibers were used to prepare collagen/chitin composite scaffolds to improve the biological properties of collagen. However, this study does not show the effect of chitin on the mechanical and piezoelectric properties of collagen and the chemical interaction between collagen and chitin**[244]**. Another study focused

on the preparation of sponge-like collagen with polyvinylpyrrolidone (PVP) in the presence of chitin microparticles to improve the hemostasis properties of the wound dressing sheet**[245]**. A hybrid scaffold from β-chitin and collagen was prepared using freeze-drying techniques from a chitin macromolecule solution dissolved in a lithium chloride / dimethylacetamide for bone tissue regeneration of bone tissue**[246]**. The results show that the scaffold lacks mechanical properties after the chitin scaffold is treated with a different ratio of collagen solution**[246]**. In addition, few studies focused on the preparation of collagen composite materials to improve their properties using chitin nanocrystals. Unfortunately, no data on mechanical properties, collagen denaturation during the preparation process, toxic solvents used, low biocompatibility and no synergetic properties between collagen and chitin were provided**[240, 244, 247, 248]**.

Another common feature of these two biomaterials is that tropocollagen and chitin nanocrystals are self-assembled under controlled conditions (pH, temperature, and concentration), leading to precisely assembled micro- and nanostructures. Synergistic effects of the combination of protein and polysaccharide during self-assembly in an aqueous solution have never been investigated.

This paper focuses on three main goals: i) Development of layered flexible hydrogel membranes resembling the structure of nacre. Fabricating these materials will involve the combination of tropocollagen and partially deacetylated chitin nanocrystals employing evaporation-induced self-assembly avoiding the use of hazardous solvents. ii) Investigation of the effects of ChNCs on mechanical, physiological and piezoelectric properties of CO hydrogel membranes. iii) Investigation of the relationships between chemical composition and biocompatibility of membranes using skin and bone cells.

2. Experiment Part

2.1. Materials and Methods

Acid insoluble collagen type I (CO) is purchased from VUP, Brno, Czech Republic, in the wet state with a dry mass of approximately 8 wt. %. Native chitin from crab shells (Ch), 3-(4,5-dimethylthiazol-2-yl)-2,5-diphenyltetrazolium bromide, fetal bovine serum, Dulbecco's modified Eagle medium, authenticated cell culture (ECACC), DMSO, ammonia solution, potassium chloride, sodium chloride and potassium dihydrogen phosphate were purchased from Sigma-Aldrich (Darmstadt, Germany). Hydrochloric acid, ethanol, and isopropyl alcohol were purchased from the Penta Chemical Company (Prague, Czech Republic). Octenidine dihydrochloride (OCT) was obtained from TCI Company (Sofia, Bulgaria). All reagents and chemicals were used in this study without further purification.

2.1.1. Synthesis of partially deacetylated chitin nanocrystals (ChNCs)

Pure chitin and partially deacetylated chitin nanocrystals were extracted and purified as previously described with slight modification[9, 157]. Chitin nanocrystals (ChNCs) were synthesized by an acid hydrolysis process using HCl (5 M) for 6 h at 90 ˚C and the ratio of solid to medium solution ratio was approximately (1/100). The nanocrystals were obtained after centrifugation at 7500 rpm for 30 min at room temperature. ChNCs were dialyzed using a cellulose membrane cut (12-14 KDa) for one week at room temperature using deionized water changed every 12 h until pH reached 4.5. The ChNCs were stored at 4 ˚C in a refrigerator until further use.

2.1.2. Fabrication of the Hybrid LHM

Native insoluble wet acid tropocollagen (CO) was freeze-dried for 72 h to obtain 100 wt.% dry material using the freeze-drying technique. One gram of dry CO was dispersed in 0.05 M hydrochloric acid at 0 ˚C for 48 h to obtain a homogeneous tropocollagen solution with high dispersibility. The swelled tropocollagen solution is homogenized at high speed (6 000 rpm) for 30 min at 0 ˚C. The highly dispersed solution obtained was placed in a Petri polypropylene plate to air dry for 72 h at room temperature (15-17 ˚C) to obtain a native tropocollagen hydrogel membrane (CO). From our previous work, 1 wt. % tropocollagen was selected for our study[111].

CO-g-ChNCs-LHM was synthesized using a certain weight ratio of CO to ChNCs (1, 5, 10 wt. %). The ChNCs were added dropwise to a slightly acidic CO medium (pH 4.5-5) at 0 ˚C to obtain a homogeneous mixture with high dispersibility of ChNCs without agglomeration. The resulting mixture of CO and ChNCs was agitated overnight at 4 ˚C to improve the assembly of the agitation and the high dispersibility of ChNCs in CO macromolecules. The dispersed solution is then cast into a polypropylene Petri dish and air-dried for 72 h at rt to obtain a layered material from the LHM assembly. The prepared samples were coded as mentioned in **Table 2.** In a water-aqueous solution, CO and ChNCs were cross-linked using a carbodiimide cross-linking system (EDC/NHS with a molar ratio of 2: 1). After 3 hours of cross-linking, CO-g-ChNCs-LHM was washed twice with 0.1 M Na_2HPO_4 and the fourth time with deionized water to remove by-products.

A certain amount of Octenidine dihydrochloride (OCT) was added to the CO, ChNCs mixture of 1 to 10 % by weight. The OCT was dissolved in 1 ml (ethanol: water 1/1 v/v) and then added to the homogeneous mixture of CO / ChNCs before the cross-linking step. The mixture was stirred for 5 h after adding OCT at 0 ˚C to obtain a homogeneous mixture with high dispersibility of OCT nanosphere drug without agglomeration. The resulting CO / ChNCs

/ OCT mixture was agitated overnight at 4 ˚C to improve the agitation and dispersibility of OCT in the CO / ChNCs matrix. The dispersed solution is then cast into a polypropylene Petri dish and air-dried for 72 h at room temperature to obtain an LHM assembly. The CO/ChNCs/OCT membrane was cross-linked, as described above.

Table 2: Composition of the prepared LHM materials.

Code	Abbreviations	CO	ChNCs	OCT	V_f (%)	CO/ChNCs/OCT ratio
I	Native CO	1	0	0	0	100
II	CO-g-$ChNCs_1$	99	1	0	1.1	99/1
III	CO-g-$ChNCs_5$	95	5	0	5.7	95/5
IV	CO-g-$ChNCs_{10}$	90	10	0	11.4	90/10
V	CO-g-$ChNCs_{10}$/$OCT_{0.1}$	90	10	0.1	0.15	90/10/0.1
VI	CO-g-$ChNCs_{10}$/OCT_1	90	10	1	1.5	90/10/1
VII.	CO-g-$ChNCs_{10}$/$OCT_{2.5}$	90	10	2.5	3.9	90/10/2.5

CO = Collagen; ChNCs = Chitin nanocrystals; OCT = Octenidine dihydrochloride; V_f = volume fraction.

2.2. Characterization of LHM

Attenuated total reflectance Fourier transform infrared spectroscopy (ATR-FTIR) was carried out using a Bruker Vertex V70 FTIR spectrometer and a Bruker Platinum ATR accessory with single reflection diamond crystal mount (Bruker Optik GmbH, Ettlingen, Germany). Samples were clamped directly against the diamond crystal using the platinum ATR sample clamp mechanism, ensuring consistent pressure per sample. Spectra were collected in the wavenumber region 3900–400 cm^{-1}. Four data sets per sample were recorded, adding 128 interferograms per set. Spectra were measured at a scanner velocity of 40 kHz and a resolution of 4.0 cm^{-1}. Using air as a reference, 128 background scans per sample were collected. Averaged spectra per sample were generated using Bruker OPUS version 7.2 software, where all spectra were corrected for ATR and vector normalized throughout the range. The second derivative spectra were calculated using a 13-point smoothing point Savitzky–Golay algorithm to better separate overlapping absorption bands within the Amide I band.

Swelling ratio*:* To determine the swelling ratio of the LHM, the membranes were cut into small pieces measuring 0.5 × 0.5 cm and weighed. Then, they were placed in glass vials containing solutions of water or phosphate-buffered saline (PBS) solutions and incubated at 37 ˚C. At regular intervals (1, 2, 4, 8, 12, 24, 48, 72 h). Native CO and LHM were removed and dried using filter paper to remove excess water or PBS from the hydrogel membrane surface. The percentage of swelling (%) of the LHM was then calculated using Eq. 1[158, 159].

$$\text{Swelling ratio (\%)} = \frac{Ws-Wd}{Ws} \times 100 \quad (1)$$

where W_s is the weight of the swollen LHM, and W_d is the weight of the dry membrane; each value is averaged from three parallel measurements.

Tensile testing was used to investigate the strength of native CO, CO-g-ChNCs, and CO-g-ChNCs/OCT, which was necessary for sampling handling. It was carried out with Universal testing equipment Z010 from Zwick–Roell (Germany) and ASTM D5083 with a gauge length of 5 mm and a loading rate of 1 mm/min measuring cell. The samples are cut in a dog bone shape with a parallel specimen length of 12 mm. The testing rate was 10^{-3} s^{-1}, and the tests were performed at laboratory temperature. The thickness of the samples was measured using SEM. Young modulus and tensile strength were calculated from the linear region of the stress-strain curves. The area calculated the toughness under the stress-strain curves.

The mechanical properties (tensile strength, young modulus, toughness, elongation at break) were based on average values of 5-10 samples. The synergistic properties of the hybrid hydrogel membrane were calculated from the following Eq. 2[228, 229, 239, 249, 250].

$$S\ (\%) = \frac{2M_{hyb} - (M_{CO} + M_{ChNCs})}{(M_{CO} + M_{ChNCs})} \times 100 \quad (2)$$

where M_{hyb}, M_{CO} and M_{ChNCs} represent the tensile strength, modulus, and toughness of the CO-g-ChNC hydrogel membrane, CO membrane, and the ChNCs membrane, respectively.

The morphology of native CO and CO-g-ChNCs and CO-g-ChNCs/OCT of the drug was visualized by transmission electron microscopy (TEM). The experiment was carried out with a Tecnai G2 spirit 12 electron microscope (FEI, Brno, Czech Republic). Native CO, CO-g-ChNCs, and CO-g-ChNCs/OCT were stained with uranyl acetate (UA) to increase the photos from the TEM contract. The staining agent was located on the surface of ChNCs, not on the surface of CO fibrils. The surface and cross-sectional morphology of LHM were observed using a scanning electron microscope (SEM, KEYENCE, VE7800) at 3 kV. LHM was fractured in liquid N_2 and coated with an ultrathin layer of gold (10 nm) before being placed under the microscope. The samples were stained with uranyl acetate in CO-g-$ChNCs_{10}$ and CO-g-ChNCs10/$OCT_{2.5}$. The staining agent was located on the surface of ChNCs, not on the surface of the CO fibril. This explained why the dark and light bands of the tropocollagen fibrils were not visualized compared to the native CO fibrils, and the tropocollagen crossbanding was masked by the presence of these aggregates of ChNCs and OCTs@CO (Fig. 3a, b).

Rheological properties of native collagen and collagen grafted with chitin nanocrystals in the presence and absence of Octenidine dihydrochloride were investigated at rt and 37 ◦C

using a rheometer. According to the preliminary results of the strain sweep test, native CO and the grafted hydrogel membrane were loaded into a parallel plate and subjected to a shear strain of 1 % at a 0.5 mm gap under continuous oscillation. In the frequency mode, the storage moduli (G') and loss moduli (G") of native and grafted hydrogel membranes were measured in the range of 0.1-100 rad/s at two different temperatures (rt and 37 ˚C).

X-ray photoelectron spectroscopy (XPS) was carried out with the Kratos Analytical Axis Ultra DLD system using a monochromatic Al Kα (hν = 1486.7 eV) operating at 75 W (5 mA, 15 kV). Spectra were obtained using an analysis area of ~300 × 700 μm. The Kratos charge neutralizer system was used for all analyses. The high-resolution spectra were measured with a step size of 0.1 eV and a pass energy of 20 eV. The instrument base pressure was $2 \cdot 10^{-8}$ Pa. Spectra were analyzed using the CasaXPS software (version 2.3.15) by applying a Gaussian – Lawrence line shape for fitting and the ORIGIN 2016 software.

In vitro drug release kinetics. The experiment involved cutting the LHM into 1 mg pieces and placing them in centrifuge tubes with 10 ml of PBS. Tubes were incubated at room temperature and 37 ˚C while shaken at 100 rpm. At various time intervals (1, 2, 4, 8, 12, 24, 48, and 72 h), 50 μL of the release medium was removed and replaced with fresh PBS. The amount of OCT released was quantified using a UV-visible spectrophotometer at a wavelength of 281 nm ($R^2 = 0.99$). A standard calibration curve determined the corresponding cumulative percentage of OCT released. The control of drug release measurement was carried out at 37 ˚C in an incubator with a shaking rate of 100 rpm for a specific time interval, and 50 μL of release medium (in PBS) was pipetted and replaced with fresh PBS. Subsequently, the vials were transferred to an incubator at room temperature. The amount of drug in the pulse release assay was determined using the same method to quantify cumulative OCT release. The cumulative percentage release of Octenidine dihydrochloride was calculated using Eq.3 [242, 251].

$$\text{Cumulative release (\%)} = \frac{\text{OCT released at differnt time points}}{\text{Total OCT entraped hydrogel membrane}} \times 100 \qquad (3)$$

Piezoelectric measurements. Impedance spectroscopy was performed with Quatro Power Source (Novocontrol Technologies, Montabaur, Germany) and an E4991A RF analyzer (Agilent, Santa Clara, California, USA). Circular gold electrodes were deposited on both film sides with a Minilab 060 (Moorfield Technology, Knutsford, UK). The average thickness of the deposited gold electrode was measured to be 48 ± 2 nm using the in-built crystal balance. Their average diameter was 10.0 ± 0.1 mm, verified with the P-17 stylus profilometer (KLA, Milpitas, California). Two golden brass plates, each measuring 10 mm in diameter, served as contacts on the electrodes. Line and cell calibrations were performed before performing

measurements. Each sample was measured five times in the frequency range $10^6 – 3 \times 10^9$ Hz, with an applied voltage of 0.1 V, in air and under controlled conditions of ~22.0 ± 0.1 °C temperature and ~55 ± 1 % humidity level.

From impedance spectroscopy, it was possible to extrapolate and calibrate the data necessary for the estimation of the piezoelectric constant[252]. Usually expressed as a matrix, in biopolymers the symmetry D∞(∞2), corresponds to an infinite cylindrical axis 38. It implies that the piezoelectric coefficient matrix is highly anisotropic and can be described by just two independent components d_{14} and d_{25}. These components represent the degree of coupling between the mechanical stress and the electric field along the cylindrical and perpendicular directions, respectively. Moreover, $d_{25} = -d_{14}$ thus the matrix representation was simplified to one single term using Eq. 4.

$$d_{14} = k_{14}\sqrt{\varepsilon_{11}^{T}\, S_{55}^{E}} \quad , \quad \left[\frac{Q}{N}\right] \tag{4}$$

Whereas, ε_{11}^{T} is the product $\varepsilon_0\varepsilon_r$ of the vacuum permittivity (ε_0) with the dielectric constant (ε_r) at the resonance frequency (f_R), k_{14} is the component of the piezoelectric coupling coefficient tensor, which represents the ratio of the induced electric charge in the *4* direction to the applied mechanical stress or strain in the *1* direction, and S_{55}^{E} is a component of the elastic compliance tensor that describes the deformation response of a material to an applied stress[253]. The element ε_{11}^{T} can be extrapolated from the graph of the real part of the dielectric constant after finding f_R in the graph of the real part of the parallel impedance (Z_p'), where it usually corresponds to a vertical asymptote.

In vitro cell culture*:* NHDFs were isolated from skin sections from plastic surgery with the Ethics Committee the approval of the Olomouc University Hospital and the patient's consent. The study was carried out according to the Ethics Code of the World Medical Association. The morphology and origin of the cells were authenticated in the Department of Histology, Palacky University Olomouc. NHDFs were cultured in Dulbecco's modified eagle medium supplemented with 10 % FBS (fetal bovine serum) and 1 % penicillin-streptomycin under standard culture conditions (5 % CO_2, 37 ˚C). Cells were used between the second and third passages[254, 255]. The Saos-2 cell line was obtained from European Collection and Authenticated Cell Culture (ECACC) and cultivated according to the protocol in McCoys 5A (modified) medium supplemented with 10 % FBS and 10 % penicillin-streptomycin under standard culture conditions (5 % CO_2, 37 ˚C) standard culture conditions[255].

The hydrogel membranes were cut into circles that fit in the 24-well plates. After 20 min of UV irradiation on both sides, the samples were hydrated with 500 µL serum-free culture

medium for 24 h at 37 °C. Cells were seeded at a final concentration of 0.5 x 10^5 cells per well, and cell viability was quantified after 1 day, 1 week and 3 weeks. After the incubation period, the medium was removed, and a serum-free medium supplemented with MTT (5 mg/ml) was applied to the cells for 2 h (37 °C, dark). The solution was removed, and the crystals were dissolved again in DMSO with NH_3 (1 %, v/v). The absorbance was measured at a wavelength of 540 nm (Tecan, Czech Republic)[256].

SEM microscopy was provided to evaluate biocompatibility using a modified method by Shu et al. Cells were seeded in prewetted and UV irradiated samples at a final concentration of 0.16 x 10^5 cells per well and allowed to adhere for 24 hours. Cells were fixed by rinsing three times in PBS buffer before adding 2.5 % glutaraldehyde for 30 minutes. After cell dehydration, the samples were dried with ethanol at different concentrations: 25, 40, 60, 80, 90 and 100 %. Each concentration was incubated for 15 minutes. Immediately after 15 minutes of 100 % ethanol, cells were incubated for 10 min with HMSD (hexamethyldisilazane)[257].

Statistical analysis. All data represented the mean ± standard deviation (SD). Statistical significance was determined using a one-way analysis of variance with Turkey's test for multiple comparisons using OriginPro2020b (Originlab, Northampton, MA, USA).

3. Results and discussions

3.1. Fabrication of LHM

Triple-helical tropocollagen (CO) was dispersed in a slightly acidic HCl medium to obtain a well-dispersed solution of CO without denaturation (Fig. 22a). Chitin nanocrystals (ChNCs) were prepared by acid hydrolysis of ChNCs with 27 % DDA (%) and the DDA was confirmed by FTIR and ss-NMR[9]. The resulting ChNCs exhibit a crystal diameter of approximately 45 ± 10 nm and a crystal length of approximately 400 ± 160 nm (Fig. 22b). Never dried ChNCs were added dropwise to CO solution under slightly acidic conditions to prevent CO denaturation, ChNCs aggregation and improve the physical interaction of functional groups of both components at low stirring speed (100 rpm). Furthermore, the OCT suspension was slowly added to the mixture of CO / ChNCs and then evaporated (Fig. 22a).

The layered structure of hybrid nanocomposite membranes was proposed as shown in Fig. 22a. The OCT nanosphere particles and ChNCs adhered to CO through covalent solid and hydrogen bonds between different functional groups of the three components (Fig. 22a). Different weight ratios of CO and ChNCs (1/1, 1/5, 1/10) and coded as CO-g-$ChNCs_1$, CO-g-$ChNCs_5$, and CO-g-$ChNCs_{10}$, respectively. The CO-g-$ChNCs_{10}$ have been selected to study the effects of OCT on LHM performance properties. The different weight ratio of OCT was added to CO-g-$ChNCs_{10}$ and coded as (CO-g-$ChNCs_{10}$/$OCT_{0.1}$, CO-g-$ChNCs_{10}$/OCT_1 and CO-g-

ChNCs$_{10}$/OCT$_{2.5}$). During the evaporation process, the ChNCs were aligned into the CO helical structure macromolecule. The SEM of native CO (surface and cross section) shows the triple helical stricture of CO and the compact structure of native CO (Fig. 22b). Furthermore, the flexibility and mechanical properties of the LHM were tested. Fig. 1c depicts the photographs of the LHM at various positions in the wet state with a high optical transmittance above 90 %. The LHM could be twisted, rolled, bent, and folded without any damage under various arbitrary deformations. These results show the high flexibility of the LHM membrane. It has also been noted that the gel membrane regained its original shape after releasing these external stresses.

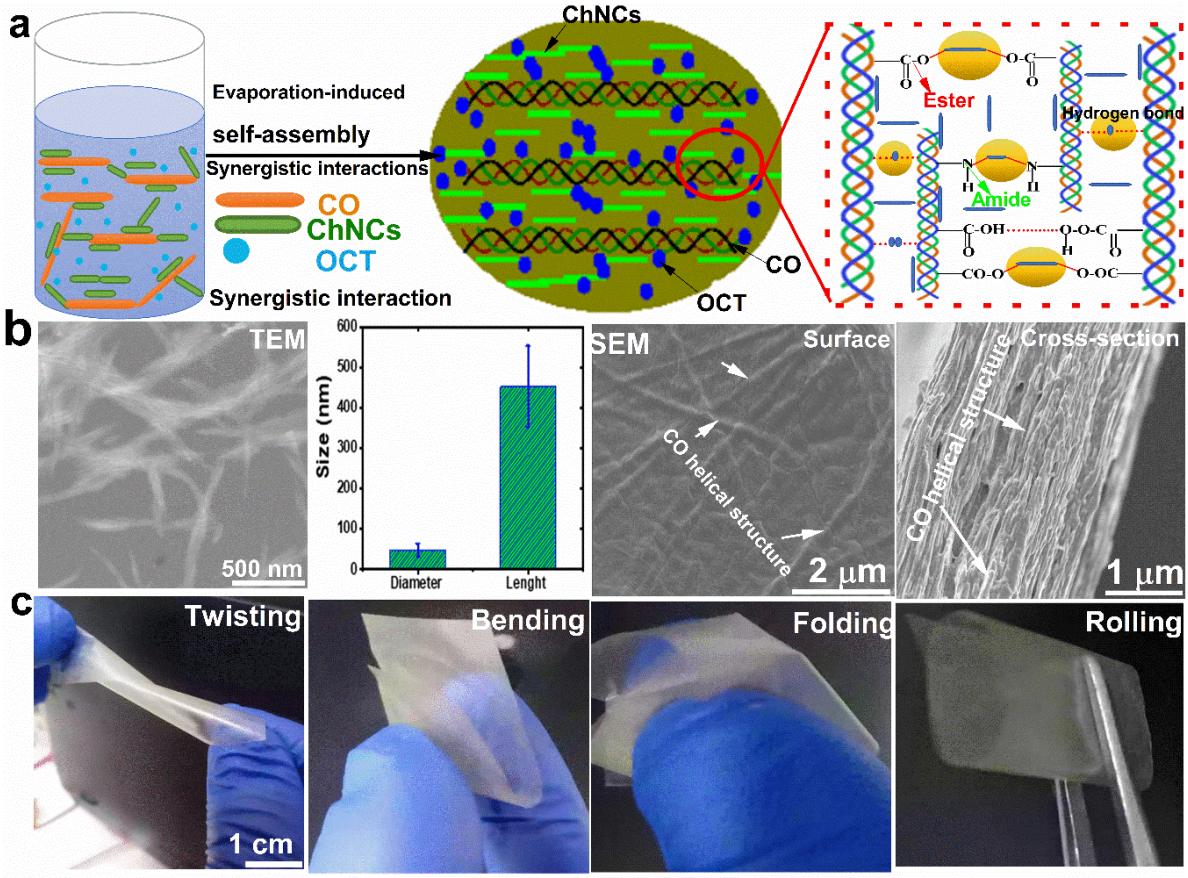

Fig. 22. Aqueous dispersion of triple-helical tropocollagen (CO), partially deacetylated chitin nanocrystals (ChNCs) and Octenidine dihydrochloride (OCT), which were assembled into artificial nacre by evaporation; proposed structural model for artificial LHM nacre, in which the CO, ChNCs and OCT network layer are alternatively stacked into a layered structure, anionic CO and cationic ChNCs were chemically (via ester/ amide) and physically (hydrogen bonds, van der Waals force) in the presence of OCT (a); STEM of ChNCs, diameter/ length of ChNCs, SEM of the surface and cross-section of native (arrows indicate helical CO fibrils). CO (b); digital photographs of the CO-g-ChNCs$_{10}$/OCT$_{2.5}$-LHM hydrogel membrane under arbitrary deformation showing a high level of transparency (c).

3.2. Morphological Properties

Fractographic analysis was performed to investigate structural variables that influence the mechanical response of the material. Native CO exhibits brittle behavior (Fig. 23a-c), while the CO-g-ChNCs$_{10}$ membrane shows a different behavior, with many layers of materials pulled during fracture (Fig. 23d-f). The edges of the CO-g-ChNCs$_{10}$ layers are curved rather than flat, indicating their deformation during crack propagation. This requires more deformation energy. The SEM micrograph in Fig. 2f shows the detailed shape of the bent sheets on the nanometer scale.

After adding OCT nanosphere particles with a size of about 30-40 nm into the CO-g-ChNCs matrix, the scanning electron microscope (SEM) analysis reveals that all three components (CO, ChNCs, OCT) form a completely homogeneous layered sheet (Fig. 23g-i). Furthermore, the edges of the CO-g-ChNCs$_{10}$ sheet appear thinner and more strongly curved. This suggests that the addition of OCT influences the morphology of the CO-g-ChNCs$_{10}$ sheets, potentially improving their mechanical properties (Fig. 29, 30). The fracture morphologies of CO-g-ChNCs$_{10}$ and natural nacre-like layers are compared. In both cases, irregularly shaped platelets were pulled out (Fig. 23g-i). However, sheets layered with tropocollagen/chitin nanocrystals exhibit a curved morphology because of their flexibility. This distinction in fracture morphology highlights the unique properties of CO-g-ChNCs layered sheets. The SEM photos indicated that the ChNCs increase the surface roughness of the hydrogel membrane compared with CO hydrogel membrane surface (Fig. 23). The synergistic performance of interaction between CO and ChNCs and the potential for enhancing CO mechanical properties sheets through improved interfacial bonding and load transfer are highlighted.

Fig. 24 shows the high-resolution transmission electron microscope (HR-TEM) of native CO and CO-g-ChNCs$_{10}$ and CO-g-ChNCs$_{10}$/OCT$_{2.5}$. Dispersion of CO in a slightly acidic medium did not affect the tropocollagen helical structure (Fig. 24a, b). The dark band represents the "gap region" caused by a void between consecutive triple-helices; the light bar represents the overlap region between neighboring triple helices (Fig. 24a). The TEM of CO-g-ChNCs$_{10}$ shows the interactions between CO and ChNCs (Fig. 24c, d) showing the chitin nanocrystal adhered to the CO fibrils. The TEM of CO-g-ChNCs$_{10}$/OCT$_{2.5}$ shows the OCT nanospheres attached to the CO fibrils in small clusters (Fig. 24e, f). The OCT nanosphere protects the ChNCs from directly adhering to the CO surface (Fig. 24e, f).

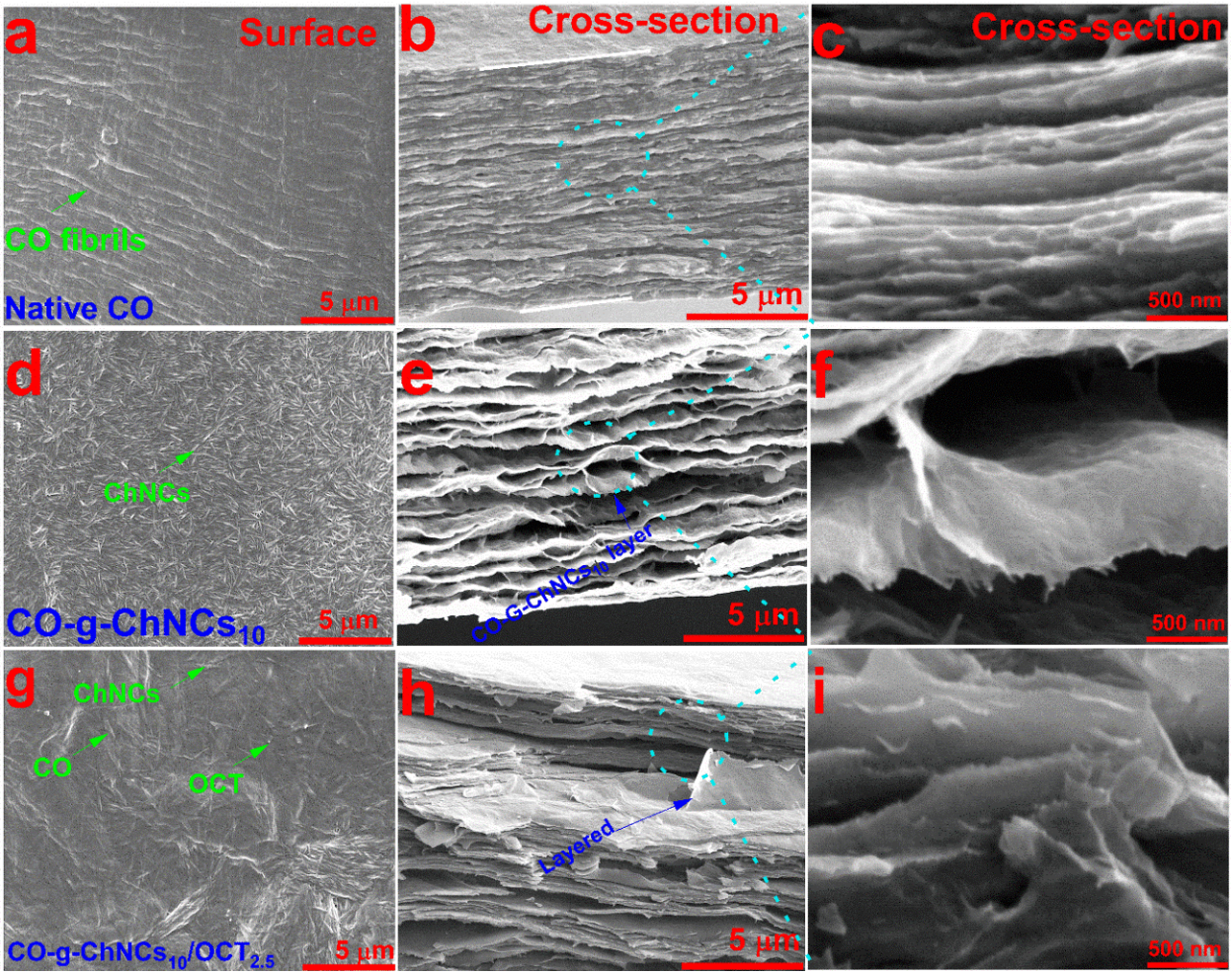

Fig. 23. Surface and cross-sectional SEM images of CO (a-c), CO-g-ChNCs$_{10}$(d-f), and CO-g-ChNCs$_{10}$/OCT$_{2.5}$(g-i).

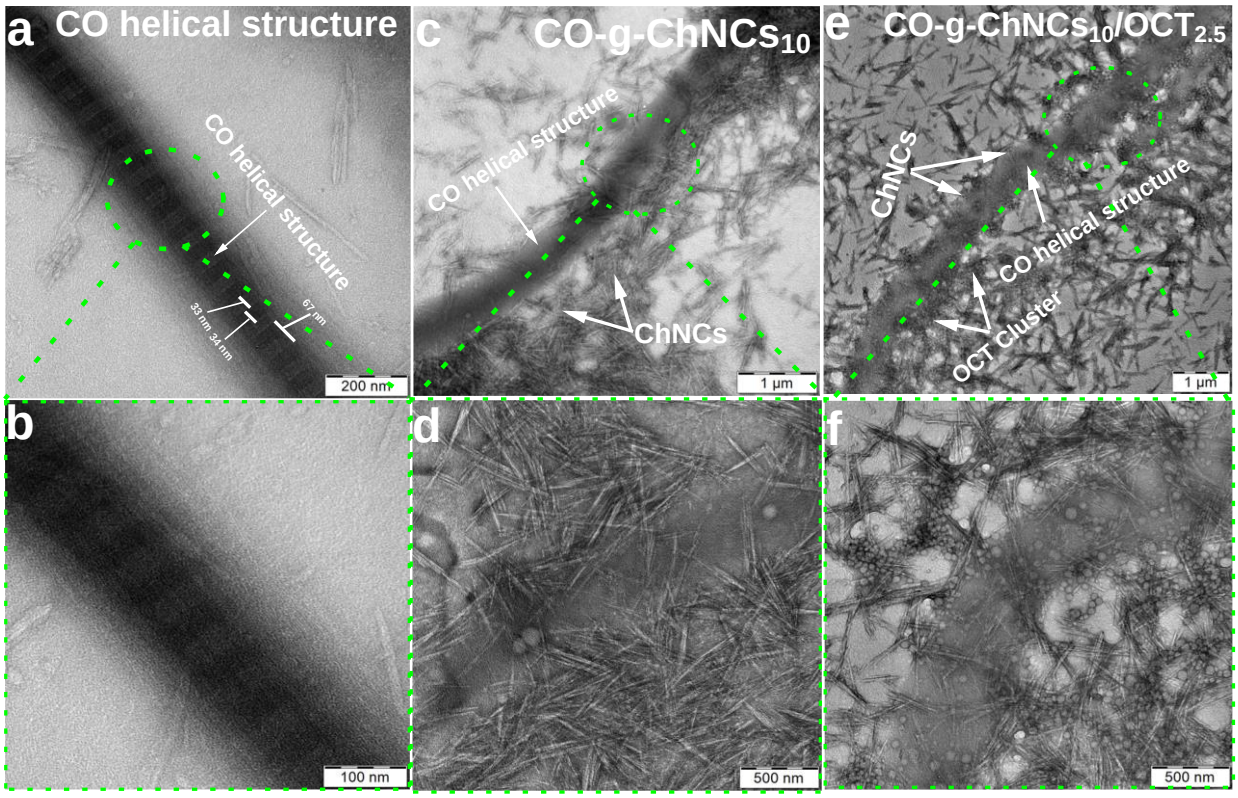

Fig. 24. TEM images of native CO (a, b), CO-g-ChNCs$_{10}$ (c, d), and CO-g-ChNCs$_{10}$/OCT$_{2.5}$ (e, f).

3.3. LHM Characterization

To determine whether triple-helical tropocollagen material was present in the hydrogel membrane matrix, we analyzed the samples using ATR-FTIR (Fig. 25). This method detects the absorbance from bond vibrations. It can describe the tertiary structure of tropocollagen macromolecules. Fig. 25 compares the ATR-FTIR spectra for native CO, CO-g-ChNCs, and CO-g-ChNCs/OCT, showing apparent differences in the spectra. The native triple helical peaks at 3400-2900 cm^{-1}, 1650 cm^{-1}, 1550 cm^{-1}, and 1400–1200 cm^{-1} for amide A, amide I, II, and III, respectively[258, 259]. The amide I peak was mainly associated with the C=O stretching vibration and was directly related to the backbone conformation. The Amide II is due to N-H/C-N bending/stretching vibrations in a triple-helical tropocollagen macromolecule. The Amide III was a very complex and sharp band, depending on the nature of the side chains and hydrogen bonding, and therefore was only of limited use to extract structural information[258, 260].

In this study, the integrity of the tropocollagen triple helix was evaluated considering the maximum absorbance ratio of the Amide III (1235 cm^{-1}) and the 1450 cm^{-1} band corresponding to the stereochemistry of the pyrrolidine rings of the proline and hydroxyproline residues[112], essential for the triple helix conformation. The triple-helix tropocollagen

conformation was intact if this ratio is close to 1.0, while the ratio values for denatured tropocollagen are around 0.5[260, 261]. The triple helical of CO was constant after adding different percentages of ChNCs (up to 95 %; Fig. 25). Due to the overlap between functional groups of tropocollagen (amino, amide, carboxylic, hydroxyl) and chitin nanocrystal groups (-NH_2,-$NHCOCH_3$, -OH), it was not easy to quantify the new amidation and esterification bond between both components. Small peaks were observed at 1743, 1468 and 791 cm^{-1}, which were attributed to NH bending and rocking of the ester and amide, respectively, indicating the successful coupling of the amide by the EDC / NHS coupling agent.

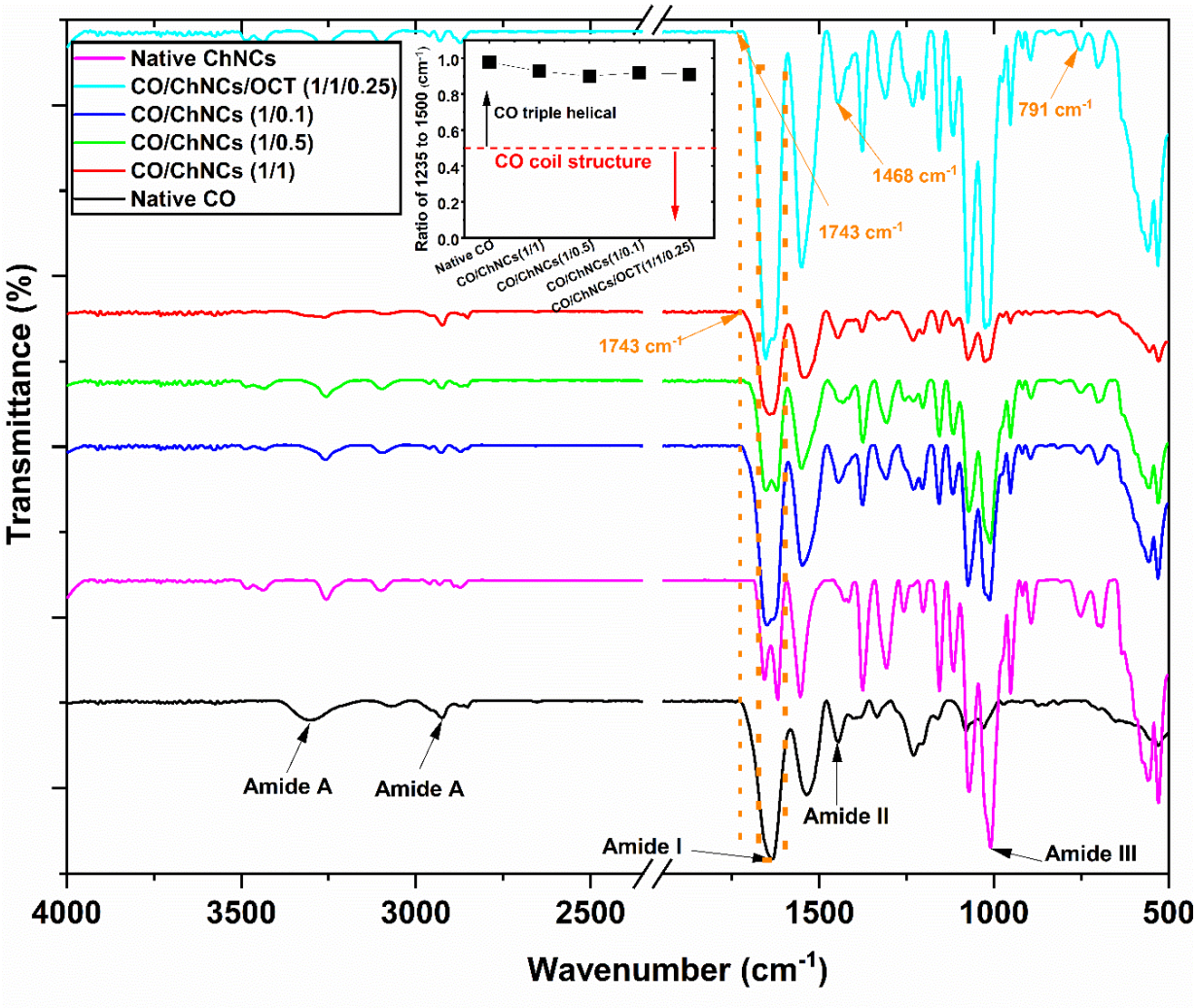

Fig. 25. FTIR spectra of LHM.

XPS analysis was used to examine the changes in the chemical environment of the elements to investigate the interactions between the CO-g-ChNCs and CO-g-ChNCs/OCT at the molecular level. Fig. 26 shows the XPS of CO-g-ChNCs$_{10}$ and CO-g-ChNCs$_{10}$/OCT$_{2.5}$. The broad spectrum of all samples shows signals of only peaks of elements O 1s, C 1s, and N 1s, except CO-g-ChNCs$_{10}$/OCT$_{2.5,}$ which shows one more Cl 2p peak related to chloride atoms of the OCT drug. In a comparison of native CO before and after crosslinking (Fig. 26a, S1), there were no significant differences in the XPS shift obtained before and after crosslinking the tropocollagen hydrogel, confirming that the EDC-NHS crosslinking agent cannot enter the gap between tropocollagen molecules in microfibrils. Furthermore, we confirm that the D-periodic banding pattern of tropocollagen fibrils is not altered by using the EDC / NHS crosslinker agent and that there is no denaturation during tropocollagen crosslinking with EDC / NHS. In particular, the intensities of the native cross-linked CO hydrogel O 1s O-C=O- and N 1s -NH_2 were decreased after cross-linking the CO hydrogel membrane with EDC/NHS. The O-C=O- area (%) decreased from 23.5 to 18.9 %, indicating more selective esterification than the amidation reaction[262].

In CO g-ChNCs (Fig. 26b), the C 1s spectra of CO and ChNCs could be deconvoluted into four peaks of 285.0, 286.4, 288.1, and 289.1 eV that belong to C-C / CH, C-O / C-OH / C-N, N-C = O and O-C=O- ester bonds. Compared to C1s- COO^- of the native CO hydrogel (289. 2 eV), the intensity of CO-COO^- of CO-g-ChNCs was shifted to 288.1 eV. In the O 1s spectrum, the new peak appeared at 533.8 eV after the chemical modification of CO with ChNCs, indicating not only the chemical interaction between CO and ChNCs but also the physical bonding. The new peak indicated that the chemical interaction between CO and ChNCs was not only physical bonding. This new peak is due to the chemically boned bonds between CO and ChNCs through amidation/esterification reactions. Furthermore, the binding energy of the component at 288.1 eV of N-C = O does not change after modification with ChNCs loaded with the OCT drug, indicating the unbroken triple helical conformation of the tropocollagen macromolecule with the introduction of ChNCs. No significant differences were visualized in the CO-g-ChNCs$_{10}$/OCT$_{2.5}$ spectrum compared to those observed for the CO-g-ChNCs$_{10}$ hydrogel membrane (Fig. 26c), indicating that the binding between the CO-g-ChNCs$_{10}$ hydrogel membrane matrix and the OCT drug was physically bonded only.

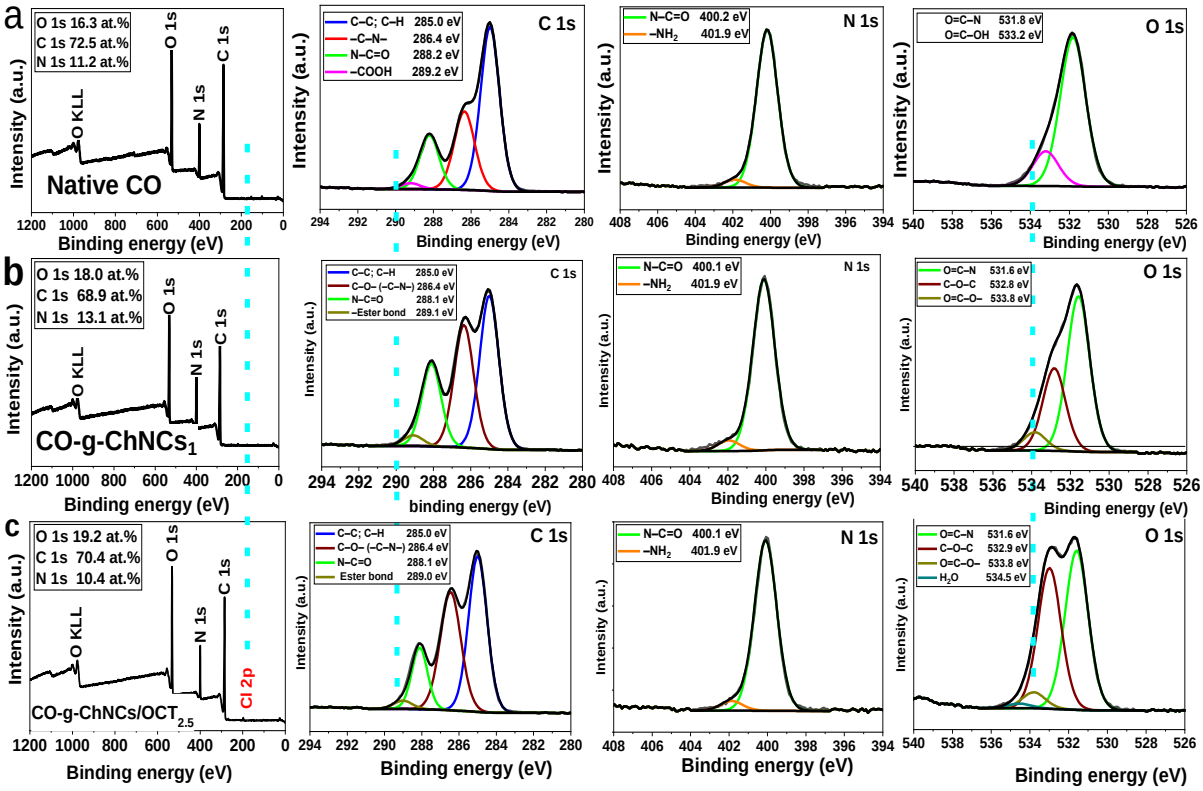

Fig. 26. XPS spectra of native CO (a); CO-g-ChNCs$_{10}$ (b); CO-g-ChNCs$_{10}$/OCT$_{2.5}$ (c).

3.4. Rheological Behavior

The rheological results of the CO-g-ChNCs solution with various loads of ChNCs are shown in Fig. 27 at both temperatures (rt, 37 ˚C). The first observation is that G" was more significant than G' for pure CO and CO-g-ChNCs, indicating that these solutions behaved as elastic liquids. As shown in Figs. 27a, b, the G' modulus of CO-g-ChNCs increased with increasing doses of ChNCs (1 to 10 wt. %). Under the frequency of 100 rad s^{-1}, the G' of native CO was 3.1 Pa, and the G' of the CO-g-ChNCs with ChNCs of 10 wt. % was 7.3 Pa, almost twice higher. The interactions between ChNCs and CO via hydrogen bonds that act as physical crosslinks formed a cross-linked network in the CO and ChNCs matrix, leading to the increasing mechanical properties of the CO-g-ChNCs hydrogel membrane. The increase in G' also reflects the increase in the CO cross-linking density. The loss modulus G" also increased with increasing loading of ChNCs, and it was insensitive to frequency. No cross-over of G" at low frequencies was observed, a characteristic of a cross-linked network (Fig. 26a, b) at rt and 37 ˚C. Figs. 27c, d show the rheological properties of CO-g-ChNCs$_{10}$/OCT (0.1, 1, 2.5 wt. %) at different temperatures (rt, 37 ˚C). The G' modulus of CO-g-ChNCs increased with the increasing ratio of OCT (0.1, 1, 2.5 wt. %). CO-g-ChNCs10 / OCT0.1 shows a high G' compared to CO-g-ChNCs10 / OCT2.5 at rt and 37 ˚C (Fig. 27 c, d). Due to the high OCT ratio generated by the cluster system interacting with the CO-g-ChNCs matrix (Fig. 24e, f).

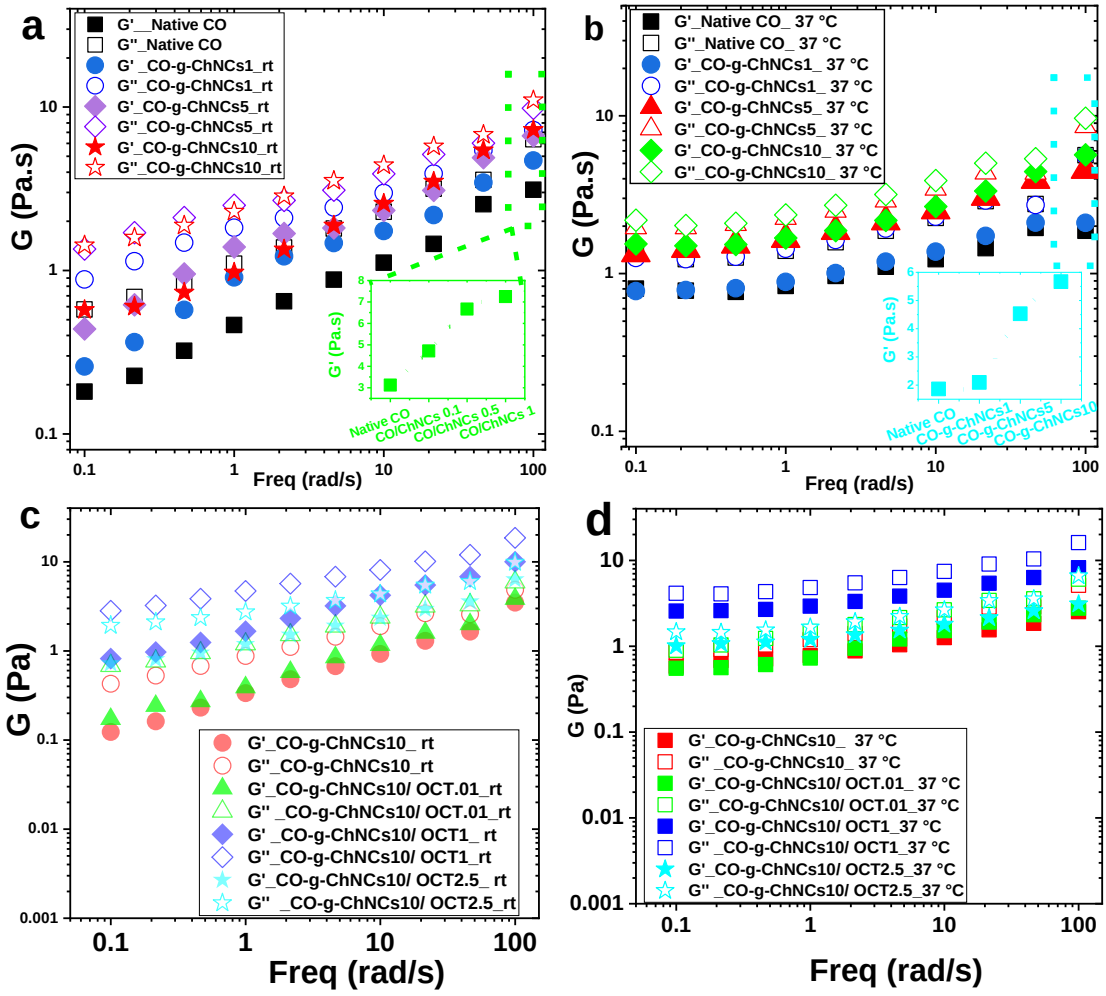

Fig. 27. Rheological properties of native CO, CO-g-ChNCs (different ChNCs content) at rt (a) and 37 ˚C (b). CO-g-ChNCs/OCT (different OCT content) at rt (c) and 37 ˚C (d).

3.5. Swelling Behavior

Fig. 28 represents the swelling properties of native CO and CO-g-ChNCs with different ratios of ChNCs and OCT. In the first hour, CO shows a high percentage of absorbing (%) in both water and PBS compared to the dry weight of the tropocollagen membrane due to the increased hydrophilicity of the tropocollagen macromolecule in both water and PBS medium (Fig. 28a, b). The percentage of swelling of native CO decreased significantly after 1 h of immersion in both PBS and water (Fig. 28a, b). The addition of different ChNCs ratios increased the swelling percentage compared to CO after 3 h of immersion in PBS and water solution medium. The maximum swelling percentage was visualized on the CO-g-ChNCs$_5$ hydrogel membrane in a buffer and water medium (Fig. 28a, b). With the addition of OCT, the swelling rate of the LHM decreased with increasing OCT ratio of OCT in the matrix. It was lower than the native CO hydrogel membrane, but still showed an acceptable value above 500 % compared to the dry hydrogel membrane (Fig. 28a, b).

The OCT-loaded hydrogel membrane depot was covered by adding PBS buffer, and a slight shake initiated the release of OCT. As shown in Fig. 28c, the release of OCT from both formulations was controlled and presented a controlled release. In particular, the initial burst from the hydrogel membrane was controlled, indicating that the OCT nanosphere was effectively loaded into the CO-g-ChNCs hydrogel matrix. The extent of OCT release control was low in the CO-g-ChNCs hydrogel membrane, implying that the OCT released from CO hydrogel membrane further interacted with ChNCs and delayed the release of OCT. The 55 % release of OCT from the CO-g-ChNCs hydrogels was observed 3 days after incubation in PBS. On the contrary, 70 % of OCT was released from the native CO hydrogel membrane, indicating that the ChNCs reinforcement in the LHM networks controlled the release pattern.

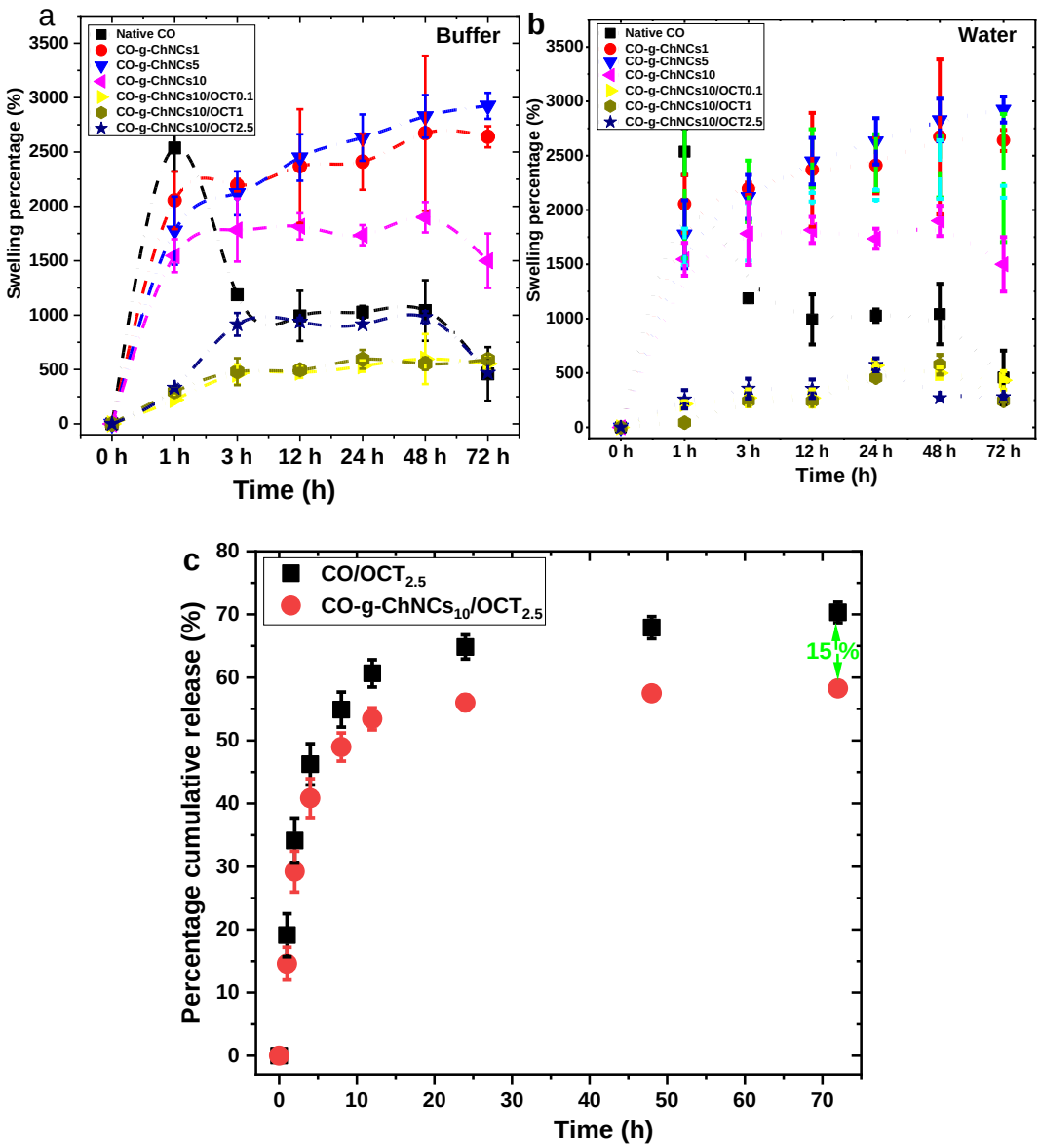

Fig. 28. Swelling ratio in buffer (a); in water at 37 ˚C (b); *In-vitro* cumulative percentage of OCT release from LHM (c).

3.6. Mechanical Properties of LHM

The mechanical properties of the CO hydrogel membrane are crucial for applications related to tissue regeneration purposes. Fig. 29 shows the effects of different ratios of ChNCs on the mechanical properties, specifically modulus, toughness, elongation at break, and strength of the LHM. The native CO membrane exhibited a modulus of 2500 MPa. However, after adding nanofiller chitin nanocrystals, the modulus was significantly increased as the amount of ChNCs (1 to 10 wt. %) increased, reaching 5300 MPa (110 % increase) (Fig. 29a). The tensile strength of the hydrogel membrane showed notable improvements with an increasing ratio of nanocrystals added to a solution of CO triple-helical structure.

The highest modulus and strength values were obtained in a CO-g-ChNCs$_{10}$ ratio (as depicted in Fig. 29a). Although the modulus and strength of the hydrogel membrane slightly decreased with an increase in the percentage of OCT nanospheres in the CO/ChNCs matrix, they remained higher than that of CO hydrogel membrane. Fig. 29b focuses on the toughness and elongation at break (%) of LHM. The native hydrogel membrane exhibited a high elongation at break (EP) value. However, upon the addition of ChNCs and nanosphere drug, the EP decreased slightly compared with that of native CO hydrogel membrane, although the decrease was insignificant. The toughness properties of the LHM increased significantly after adding different ratios of ChNCs (1 to 10 wt. %). They decreased slightly with the introduction of the OCT nanospheres into the LHM (Fig. 29b).

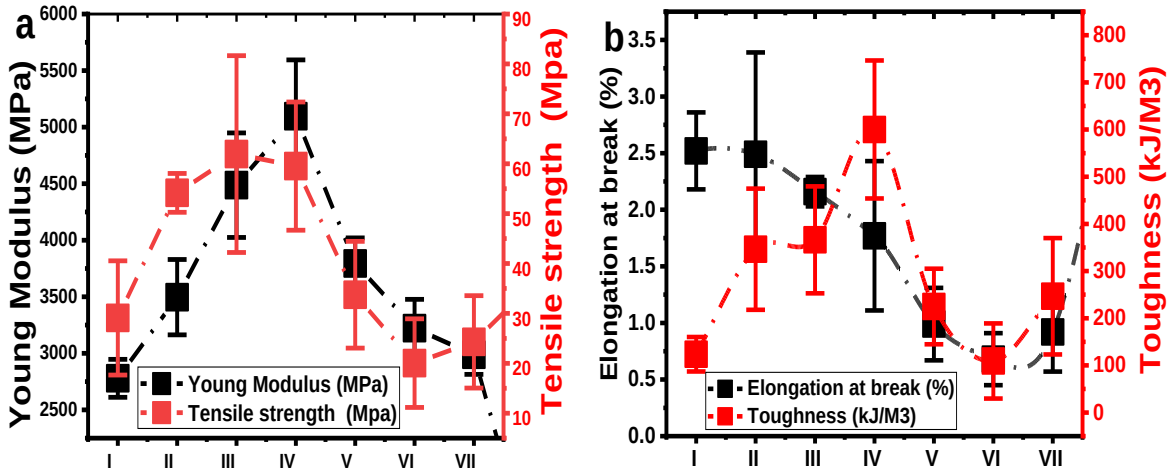

Fig. 29. Mechanical properties of CO and CO-g-ChNCs/OCT–LHM Modulus and strength (a); Toughness and elongation at break (b).

The synergistic effects of the building blocks of triple helical tropocollagen and partially deacetylated chitin nanocrystals on improving mechanical properties can be quantified by the percentage of synergy, as shown in Figs. 30a-c. The rate of strength synergy of CO-g-ChNCs increases with increasing ChNCs content (1 to 10 wt. %) and reaches a maximum value of 152.7 % for CO-g-ChNCs$_5$ (Fig. 30a). Meanwhile, the percentage of modulus synergy also gets the maximum value of 163.08 % for CO-g-ChNCs$_{10}$ in the hydrogel membrane matrix, indicating that the synergistic effect can be optimized and adjusted with the change in the ChNCs ratio in the matrix (Fig. 30b). The percentage of toughness synergy also increases with increasing ChNCs and reaches a maximum of 840.75 % for CO-g-ChNCs$_{10}$ (Fig. 30c). The addition of nanosphere OCT drug decreased the synergistic performance between CO and the ChNCs; the OCT nanospheres generated some cluster structure that inhabits the direct inceration between CO and the ChNCs. The same behavior was investigated by adding nanosiliate (SiO_2) to the acrylamide-based hydrogel[263].

Furthermore, the percentage of synergy can be further enhanced through strong covalently crosslinking interface interactions and the construction of different types of hydrogen bonds between CO and ChNCs, as shown in Figs. 25 and Fig.27a, which also provides a new strategy for improving the mechanical properties of nanocomposites-layered hydrogel membranes[230].

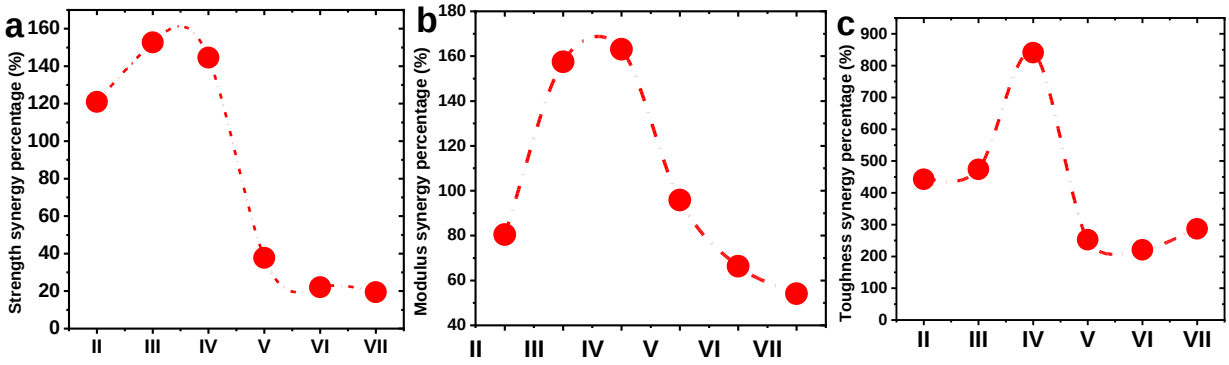

Fig. 30. Synergy percentage of LHM increases with ChNCs content in grafted CO-g-ChNCs–LHM. Modulus synergy percentage (a); Strength synergy percentage (b); Strength synergy percentage (c). I = native CO; II= CO-g-ChNCs$_1$; III= CO-g-ChNCs$_5$; IV= CO-g-ChNCs$_{10;}$ V= CO-g-ChNCs$_{10}$/OCT$_{0.1}$; VI= CO-g-ChNCs$_{10}$/OCT$_1$; VII= CO-g-ChNCs$_{10}$/OCT$_{2.5}$.

The mechanical performance of our nacre-like layers with those of natural nacre and the reported layered composite material with a higher nanofiller chitin content is shown in Fig. 10. Our LHM was stronger than cancellous bone[228, 264], cartilage[265], human skin[266], a few artificial nacre materials[249, 266, 267] and synthetic composites such as CS/HAP[268] , Ch/$CaCO_3$[269] and CNF/MTT[239]. As discussed above, the LHM compounds synthesized in this study displayed multilevel controllable hierarchical structures.

In conclusion, the addition of ChNCs and OCT nanospheres influenced the mechanical properties of CO hydrogel membrane by enhancing its modulus, toughness, and strength, but potentially reducing its elongation at break. These findings are essential to tailor the mechanical characteristics of tropocollagen hydrogel membranes for specific tissue regeneration applications.

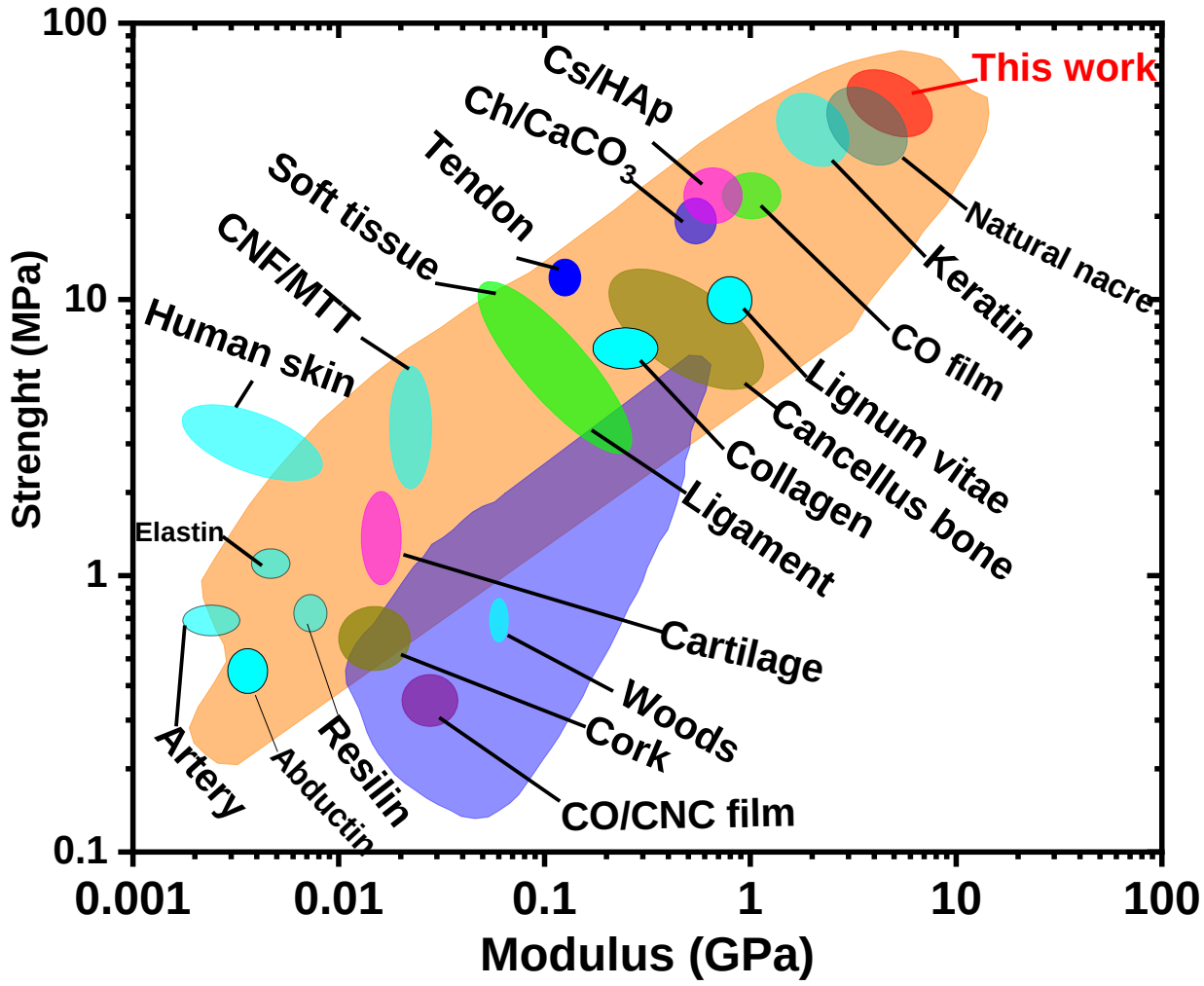

Fig.31. Ashby plot graph of the comparison of mechanical properties of our nacre-like NPs-type of CO-g-$ChNCs_{10}$/$OCT_{2.5}$-LHM with natural nacre and prepared layered CO/polymer composite.

3.7. Piezoelectric Properties of LHM

The dielectric analyses performed with the impedance spectroscopy provided us with the value of piezoelectric constant and loss useful to predict the performance as cell growth scaffold (Fig. 32). They revealed a quite high value of d_{14} for the native CO hydrogel membrane of 0.14 pC/N. This value was much higher than the literature value, where the highest value found was 0.102 pC/N[253], while other studies claimed much lower values: 0.057 pC/N[270] and 0.036 pC/N[252]. The high value of d_{14} could be attributed to the higher stiffness and compactness of the piezoelectric sites because of the well-preserved helical structure of the prepared hydrogel membrane.

The introduction of ChNCs decreased as 14 logarithmically An analogous decrease in the piezoelectricity of the native CO nanocomposite was observed in the literature by adding hydroxyapatite[271] and natural rubber[239] to native CO. This behavior was attributed to the warping deformation caused by the extraneous element within the triple-helical tropocollagen macromolecules, dependent on the geometry of the filler rather than on its nature. Fitting the function of the collagen concentration and fitting it with an exponential growth equation, it was possible to extrapolate the theoretical value of 14 for the pure ChNCs, which would be approximately 0.036 pC/N (Fig. S4). In parallel, the addition of ChNCs to collagen composites resulted in a significant increase in L, which was directly proportional to the concentration of collagen. This increase in L suggests that any energy missing due to a lower piezoelectric effect in the composites is dissipated by the system either through heat or by moving the nanocrystals, leading to faster degradation of the material.

The addition of OCT conveyed a noticeable increase in d_{14}, almost nullifying the negative impact of the nanofiller, even though CO concentration was even lower. This effect was attributed to the more homogeneous dispersion of the chitin nanocrystals evidenced by the morphological analyses (Fig. 23, 25). The ChNCs clusters were much smaller and better oriented under sheer stress during membrane preparation, resulting in a smaller warping impact on the collagen structure (Fig. 3e, f). This behavior was visible in the piezoelectric loss results as well. The OTC surfactant decreased L even under the value of the pristine collagen. The finer dispersion of the ChNCs in the collagen matrix sank the resistance that the larger clusters were not homogenously dispersed as opposed to the mechanical deformation of the matrix during the performance of the piezoelectric phenomenon. Moreover, in the presence of OTC, a synergistic effect between the filler and the matrix justifies a lower dissipation than in the

pristine matrix. Such a synergy with effects on the mechanical behavior was also suggested by the elongation tests (Figs. 29, 30).

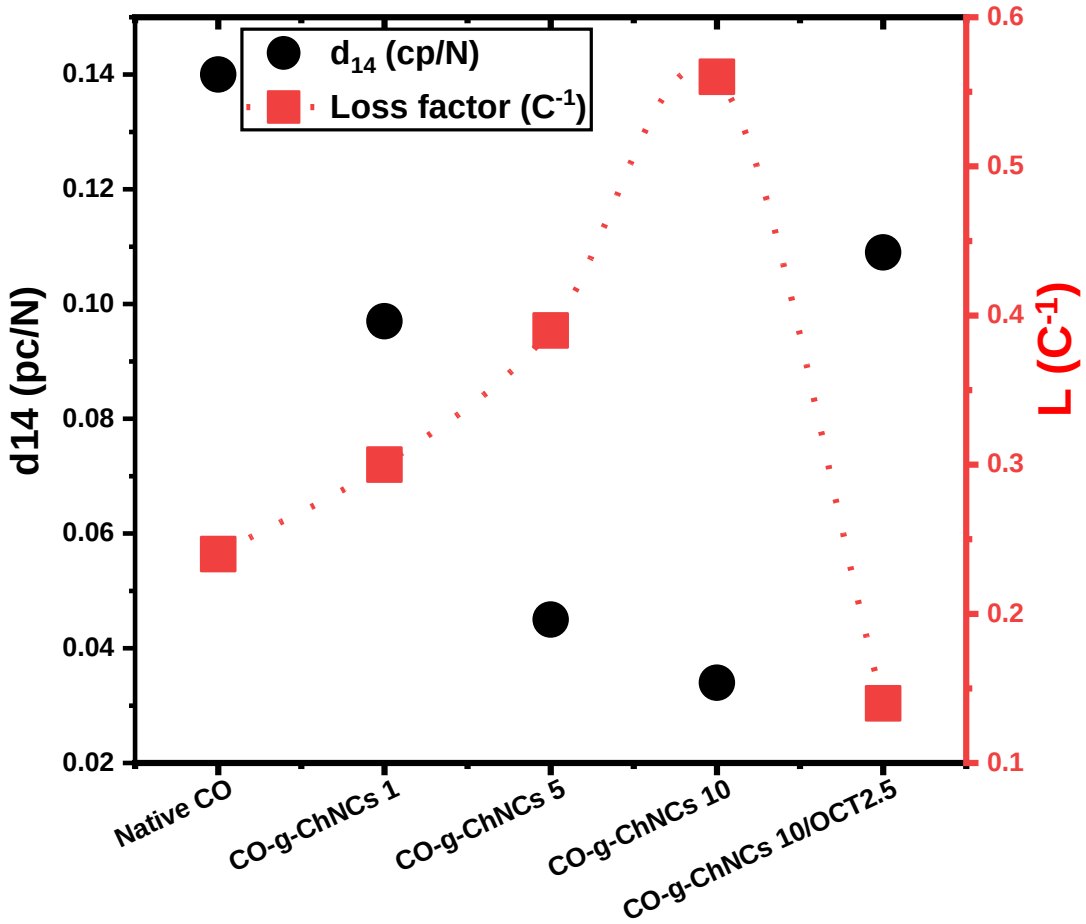

Fig.32. Plot of the piezoelectric tensor element d_{14} and piezoelectric loss L.

The curing of the polymer did not significantly affect the piezoelectric loss of tropocollagen (cap L). This suggests that the increase in stiffness and compactness resulting from the curing process led to rasterized d_{14} without any negative effects of ChNCs on CO compounds, resulting in a significant increase in L, which was directly proportional to the tropocollagen concentration. This increase in L suggests that any energy missing from a lower piezoelectric effect in the composites is dissipated by the system through either heat or by moving the nanocrystals. The OTC decreases L even under the value of pure native CO (Fig. 11). The finer dispersion of the ChNCs in the CO matrix sinks the resistance that more giant clusters are nonhomogeneous dispersed as opposed to mechanical deformation of the matrix during the piezoelectric phenomenon. Moreover, in the presence of OTC, a synergistic effect appears between the filler and the matrix to justify a lower dissipation than in the native matrix (CO/ChNCs). Another hypothesis is that OTC acts not only on the ChNCs dispersion but also on the CO morphology.

3.8. Cytotoxicity and cell adhesion properties

This study investigated how the composition and assembly of triple-helical tropocollagen/nanocrystal chitin and drug compounds influence the growth of *NHDF* and Saos-2 cells (Fig. 33, S2). Cells proliferated on the native CO, CO-g-ChNCs, and CO-g-ChNCs / OCT nanocomposite hydrogel membrane and were determined after 1, 7 and 21 days by the MTT assay. Cell viability increased with different ratios of chitin nanocrystals (1 to 10 wt. %) after all incubation periods (Fig. 33a). The cell viability of the CO-g-ChNCs/OCT hydrogel membrane was slightly decreased compared to different ratios of native CO and CO-g-ChNCs (Fig. 33b). The behavior was also observed with Saos-2 cells by introducing the nanosphere OCT drug. The decrease in cell viability in the presence of OCT is due to the fast release of OCT (nonbonded OCT) from the CO / ChNCs matrix in the first 72 h. From the literature, OCT shows cytotoxic properties against different cell types (*NHDF, Saso2*) at certain concentrations. Cell viability decreased slightly compared to CO and CO-g-ChNCs with different ChNCs ratios (Fig. S2a, b). The cell structure was preserved without visible breakage and basic details of the adhered cells were observed.

SEM examined the morphology of the *NHDF* cells on the hydrogel membranes. Figs. 33c-f shows the SEM micrographs of *NHDF* on the nanocomposite hydrogel membrane after 24 h of culture. Cells grown on native CO and CO-g-ChNCs$_{10}$ have typical fibroblast morphology with filopodia (Fig. 33c-f). Cells grown in CO-g-ChNCs/OCT$_{2.5}$ were more rounded and lacked the classical stretched structure (Fig. 33g, h, Fig. S3). Osteoblast cells (Saos-2) (Fig. S2c-f) cultured on the nanocomposite hydrogel membranes connected by discrete filopodia formed an entangled network. From the enlarged magnification (Fig. S2d, f), the Saos-2 cells spread on the surface of the hydrogel membrane, and the number of cells increased as the ChNCs ratio in the matrix increased (Fig. S3). From Fig. S2c-f and Fig. S3, NHDF and Saos-2 exhibited an elongated shape. They were anchored onto the surface of the nanocomposite hydrogel membrane by discrete filopodia, indicating the excellent adhesive performance of the hydrogel membrane.

No obvious cell spreading of both *NHDF* and Saos-2 was observed in CO-g-ChNCs/OCT$_{2.5}$, probably due to two reasons, first: drastic swelling of CO-g-ChNCs/OCT$_{2.5}$ (more hydrophobic like in Fig. 28) in salty culture medium and the resultant shrinkage during drying, along with deformation or detachment of adherent cells, second: The presence of OCT could prevent the well adhesion of cells to the LHM surface. Chitin has been confirmed to support the initial attachment and spread of *NHDF* and *Saos2* [243, 272]. On the other hand, chitin nanocrystals could increase the surface roughness of the layered nanocomposite hydrogel

membrane, as visualized in Fig. 23. Chitin nanocrystals (ChNCs) were able to promote cell adhesion[243, 244]. Furthermore, the hydrophilicity of partially deacetylated chitin and functional groups such as NH2 was supposed to facilitate effective calcium phosphate deposition[273], and the formation of an apatite layer, which can further promote osteoconductive[274]. and anti-inflammatory properties can prompt skin healing. Therefore, the introduction of chitin nanocrystals significantly improved the LHM affinity and cytocompatibility of NHDF and Saos-2 cells, resulting in a significant potential in scaffold materials for the regeneration of skin and bone tissue and control drug release applications.

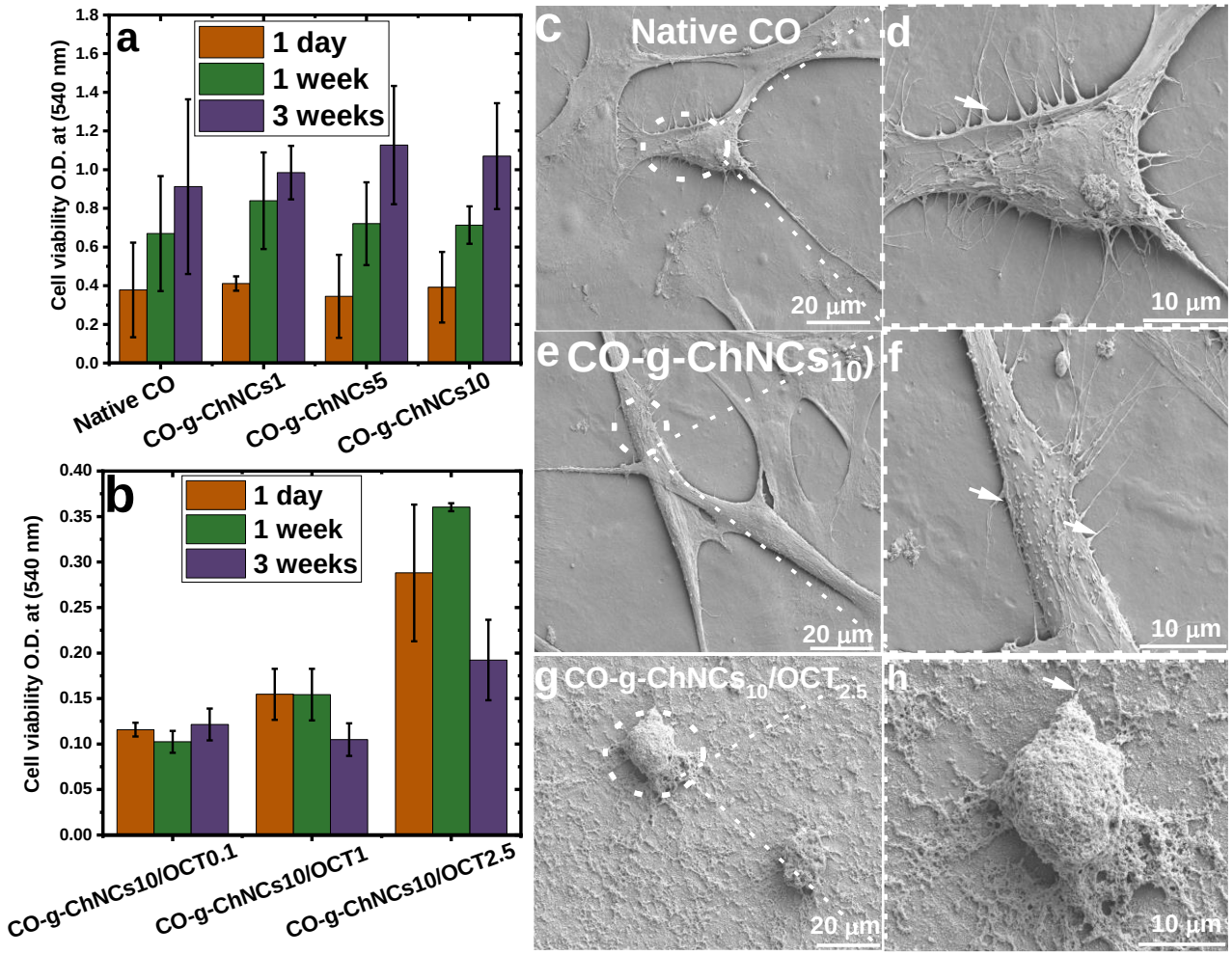

Fig. 33. Cytocompatibility of native CO, CO-g-ChNCs, and CO-g-ChNCs/OCT after seeding with *NHDF* cells for one day, week, and three weeks (a, b). SEM of native CO (c, d); CO-g-ChNCs$_{10}$ (e, f) and CO-g-ChNCs$_{10}$/OCT$_{2.5}$ (g, h). The white arrow indicates the filopodia. Scale bars for (c, e, g) were 20 µm, and for (d, f, h) were 10 µm. All samples were measured three times to calculate the standard division (n ± 3).

4. Conclusions

In this study, a novel method for creating a layered nacre-like material has been introduced, utilizing triple-helical tropocollagen (CO) and partially deacetylated chitin nanocrystals (ChNCs), along with Octenidine dihydrochloride nanosphere particles (OCT). ChNCs play a crucial role in enhancing the stability of the triple-helical structure of tropocollagen and promoting fibrillar arrangement through hydrogen bonding and other weaker electrostatic interactions. This hierarchical microstructure formation resulted in the development of a layer material, referred to as LHM. The addition of ChNCs and OCT nanospheres influenced the mechanical properties of the CO hydrogel membrane by enhancing its modulus, toughness, and strength, but potentially reducing its elongation at break.

The LHM exhibited remarkable improvements in mechanical properties, including increased modulus, strength, and toughness, compared to the LHMs prepared without ChNCs. These enhancements were attributed to the incorporation of ChNCs and OCT, a drug model. The synergy between ChNCs and OCT further contributed to the enhanced mechanical performance of the material, surpassing that of natural nacre and other synthetic layered composite materials.

A notable aspect of the synthesized nacre-like material was its excellent biocompatibility, demonstrated by its ability to support the adhesion, spread, and proliferation of *NHDF* and *Saos-2* cells. By varying the ratios of ChNCs, the material properties may be tailored to meet specific requirements. Overall, this study presented a promising high-performance layered nanocomposite material that combines the strengths of protein and polymer nanocrystalline chitin. The LHM material exhibited outstanding mechanical properties and biocompatibility and holds great potential for a wide range of applications, including skin/bone tissue engineering, drug delivery systems, and potentially more.

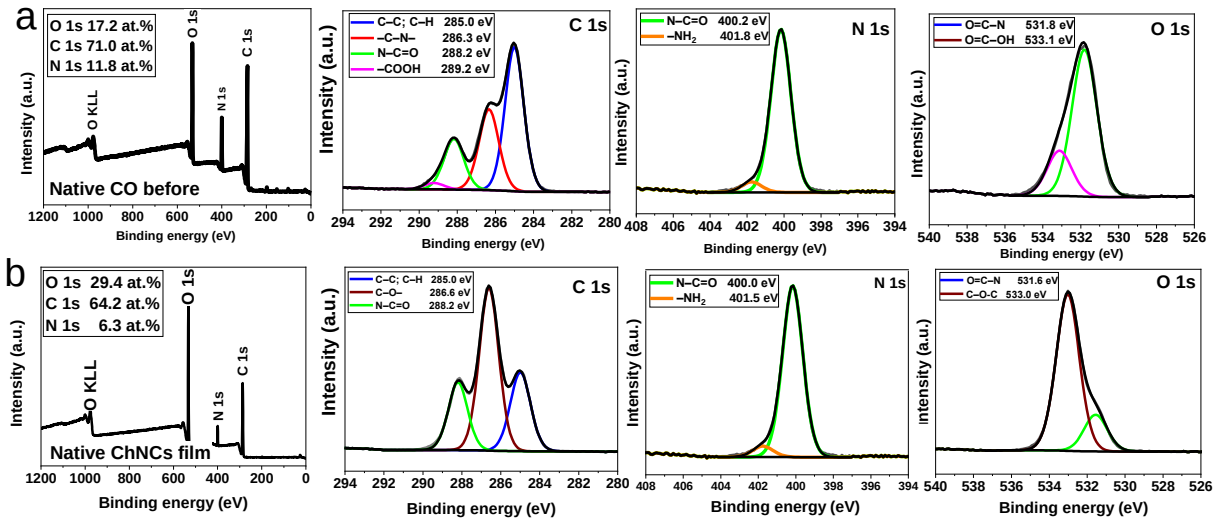

Fig. S1. XPS of native CO before crosslink (a) and native nanocrystals chitin membrane (b). The broad spectrum of native chitin film shows only three element signals: O 1s, C 1s, and N 1s peaks. C 1s was deconvoluted to three peaks at 285.0, 286.6 and 288.2 eV related to C-C/C-H, C-O/C-OH, and N-C=O, respectively. In the N 1s spectrum, two peaks appeared at 400.0 and 401.5 eV related to N-C=O and NH_2 groups. For the O 1s spectrum, two peaks were deconvoluted at 531.6, and 533.0 eV corresponding to O=C-N and C-O-C-, respectively.

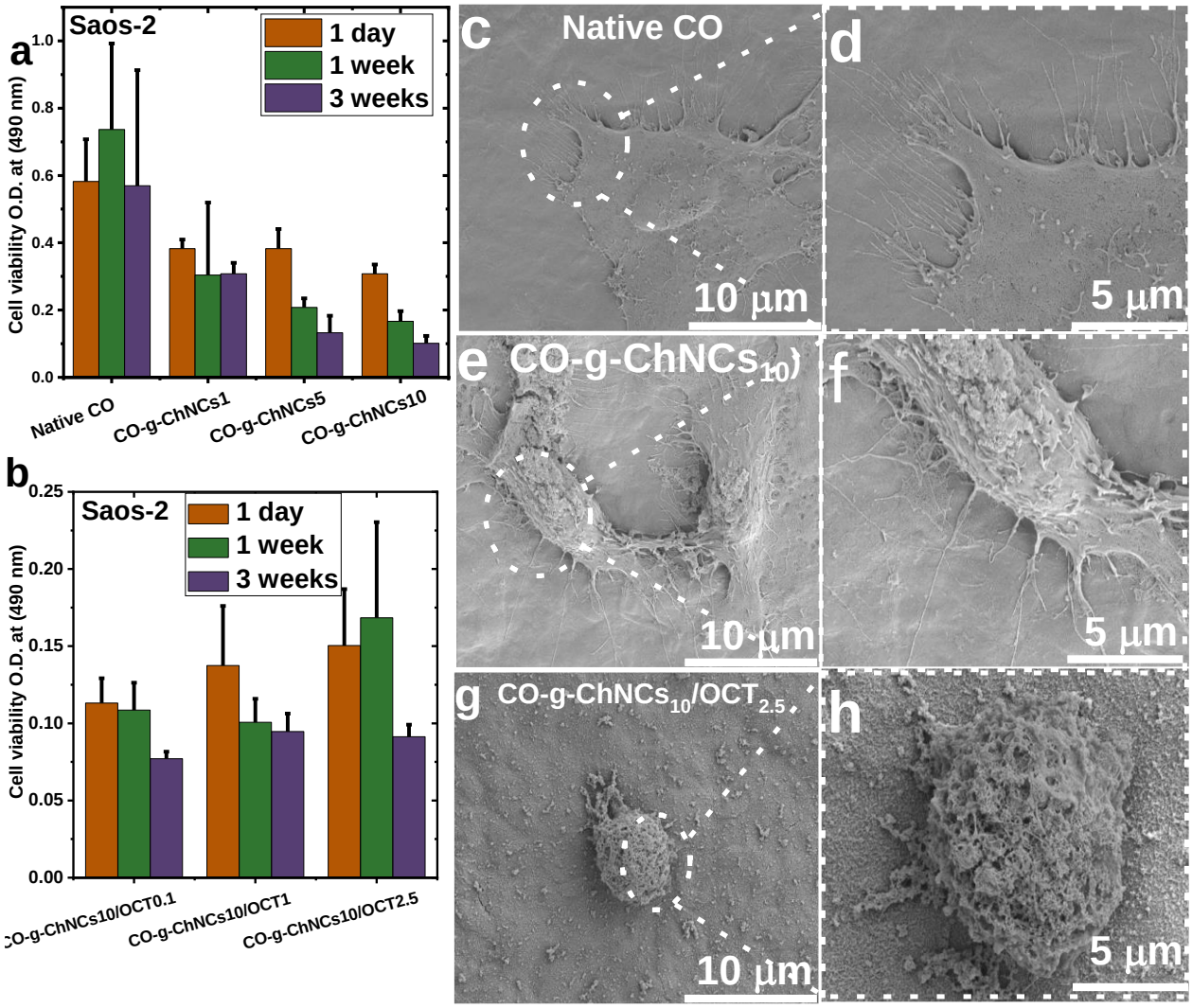

Fig. S2. Cytocompatibility of native CO, CO-g-ChNCs$_{10}$ and CO-g-ChNCs$_{10}$/OCT$_{2.5}$ after seeding with Saos-2 stem cells for one day, one week and three weeks (a, b). SEM of native CO hydrogel (c, d); CO-g-ChNCs$_{10}$ (e, f) and CO-g-ChNCs$_{10}$/OCT$_{2.5}$ (g, h). Scale bars for (c, e, g) are 20 µm and for (d, f, h) are 10 µm. All samples were measured three times to calculate the standard division (n ± 3).

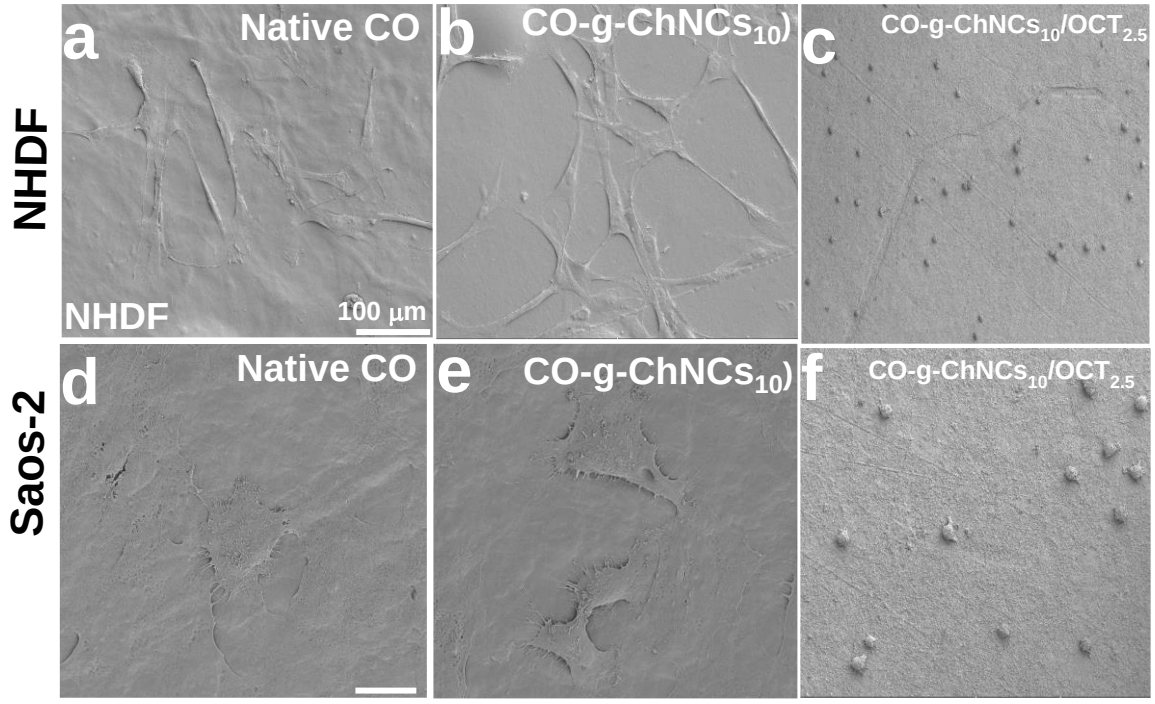

Fig. S3. SEM photos of the NHDF and Saos-2 spreading on the native CO, CO-g-ChNCs$_{10}$ and CO-g-ChNCs$_{10}$/OCT$_{2.5}$ hydrogel after 24 h of culture. Scale bars was 100 µm.

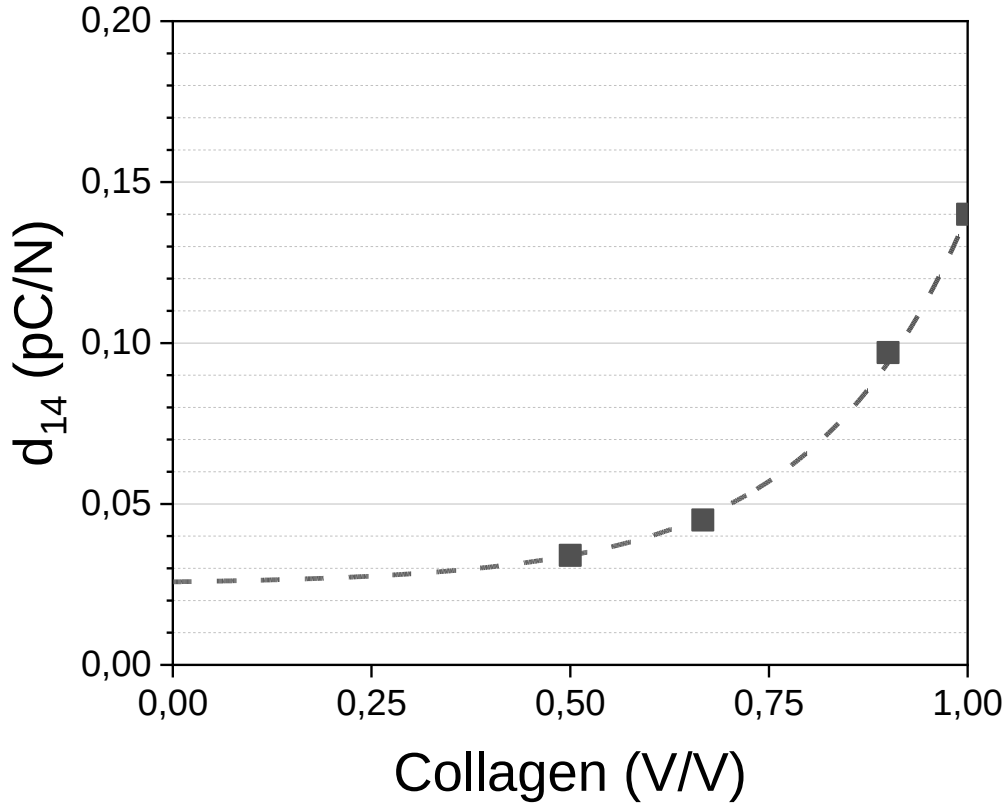

Fig. S4. Piezoelectric constant as a function of the CO-V$_f$ in CO-g-ChNCs hydrogel membrane (black squares) with exponential growth trend line (black dashed line). The extrapolated d_{14} value for collagen 0 V/V (pristine ChNCs) was $0.036\,C/N$.

Chapter 4

Synergistic Performance of Collagen-g-Chitosan-Glucan Fibril Biohybrid Scaffold with Tunable Properties

Abstract

Hybrid biocomposite scaffolds (HBSs) that serve as carriers for cell proliferation and differentiation are increasingly being used for tissue regeneration purposes. A 3D hybrid scaffold based on collagen-grafted-chitosan-glucan complex fiber (CO-g-CSGCF-HBS) was fabricated by the freeze-drying technique. The swelling percentage, hydrolytic stability, and modulus of elasticity of HBS were enhanced after CO was modified by CSGCF. The size and porosity of HBS pores decreased slightly with an increase in the CSGCF ratio. From *in vitro* measurements, the cell viability of HBS was enhanced compared to native CO using mesenchymal stem cells (*MSCs*). HBS exhibited a higher reduction rate against different types of bacteria compared to a control sample. Thus, chemical modification of CO with different ratios of CSGCF significantly improved the physicochemical, bactericidal, and cell adhesion properties of HBS. The viability of *MSCs* suggests potential for a range of therapeutic and biomedical applications, especially for bone regeneration purposes.

Keywords: Hybrid scaffolds, collagen, chitosan-glucan fiber, antibacterial and mechanical properties

Rasha M. Abdel-Rahman, V. Vishakha, I. Kelnar, J. Jancar, A. M. Abdel-Mohsen. Synergistic Performance of Collagen-g-Chitosan-Glucan Fiber Biohybrid Scaffold with Tunable Properties. International journal of biological macromolecules **2022,** 202, 671-680.

1. Introduction

Proteins are the main component of the extracellular matrix (ECM) in many mammalian tissues. Collagen type I (CO) has been extensively investigated for different biomedical applications [275, 276], and the nano-fibrillar collagen structure existing in many organs (bone, cornea, skin, tendon) was considered its characteristic feature, based on which the excellent mechanical and other functional performances of tissues are guaranteed[277, 278]. Collagen was considered one of the most interesting proteins that have been used for various purposes in tissue engineering due to its brilliant and unique properties, like biocompatibility[279], biodegradability[280] and low cytotoxicity[281]. However, the biodegradation rate and poor mechanical properties of native collagen are critical issues that limit further application of CO. The chemical cross-linking step of collagen-based scaffolds was an effective method to control the degradation rate and optimize the physicochemical and mechanical properties of collagen[282-284]. For the above reasons, the collagen cross-linking step has become one of the most significant steps in the preparation of collagen-based scaffolds. Currently, two different crosslinking processes are used to improve the chemical, physical, and mechanical properties of collagen-based scaffolds: chemical[285] and physical methods[286].

Chitin and chitosan biopolymers offer excellent biological characteristics, which have paved the way for their uses in medicine and drug-delivery applications[276] or as a scaffold for tissue regeneration[287]. In fact, chitosan has good mucoadhesive characteristics due to its polycationic nature[288], which increases the adhesion to the mucosa and thus the contact time for drug penetration. Chitosan is considered one of the cell walls of the main components of different fungi, such as *Gongronella spp*., *Penicillium*, *Aspergillus niger (A. niger)* and *Schizophyllum commune (S. commune)[289, 290]*.

Chitin-glucan complex from mycelia Tremella fuciformis with a controlled ratio of the chemical composition of the complex between glucose amine and *N*-acetyl glucose amine glucosamine and glucose (GlcN: Glc =26:74 mol%) has been extracted in powder form[291]. White button mushrooms and pleurotus ostreatus were used as a new source to extract chitin-glucan complex, controlling the degree of deacetylation. Unfortunately, the isolated complex exhibited a small particle shape[292-294]. The chitin-glucan and chitosan-glucan complex were isolated from *Aspergillus niger* in powder form and used for wastewater treatment [204, 295-297]. The fungal cell wall was used to extract the chitin-glucan complex in powder morphology, and nanoapaper fabrication was obtained from dispersed solution and used for heavy metal adsorption[298-300]. Hollow fibers from the chitin and chitosan-glucan complex

with a controlled degree of deacetylation have been extracted from the mycelium of Schizophyllum commune fungi and used as new wound dressing material[9, 10, 112]**.** A new soft hydrogel with low porosity was fabricated using a chitin-glucan complex dissolved under harsh alkaline conditions using concentrated sodium hydroxide. The extracted complex was in powder form with a low degree of deacetylation[10, 112, 301-303]. From all sources we mentioned above, all of the chitin-glucan and chitosan-glucan complexes were extracted only in powder form; neither short nor longer micro/nanofibers were obtained. So far, there has been no literature information on the extraction of fiber-based chitin-glucan or chitosan-glucan complexes from the mycelium of Aspergillus niger.

The extraction of chitin-glucan (ChGF) or chitosan-glucan CGF (CGF) in fiber forms from non-animal sources (mushrooms, bacteria, fungi) has several benefits over animal sources such as shrimps, crabs, crawfish shells, lobsters**[71, 304]**. These include the following. In our study, (I) ChGF or CGF is extracted for the first time in the form of microfiber from *Aspergillus niger (A. niger)* with controlled fiber dimensions between 2.5-3 ± 0.5 µm; (II) A raw biopolymer that was constant in composition and available throughout the year[305]; (III) Free-heavy metal attached to the starting material[306]; (IV) Removal of minerals was not necessary for the extraction of chitosan from fungal mycelia[307].

Individual CGF chains of CGF were agglomerated in microfibrils with hydrogen bonds and, together with the chemically cross-linked network of glucan, they resulted in a mechanically robust and rigid structure[111, 112, 308, 309]. The goal of this work is to synthesize a new hybrid biocomposite scaffold (HBS, CO-g-CGF) via chemical modification of collagen (CO) with chitosan-glucan complex fibers (CGF) and to study the effects of the CGF on the physicochemical, mechanical and antibacterial properties of HBS.

2. Experimental

2.1. Materials

Type I water-insoluble dermal collagen with partial hydrochloride of purified bovine was supplied as a 10 wt. % suspension from VUP (Brno, Czech Republic). The suspension of CO I was lyophilized using (ALPHA 1-4 LSC, CHRIST, Germany) at -90 $^{\circ}$C for 48 h to obtain dry CO sheets. *Mycelium* was produced from strain *Aspergillus niger (A. niger)* as a source of ChGF and CGF (Brno, Czech Republic). *N*-(3-dimethylamino propyl)-*N*-ethyl-carbodiimide hydrochloride (EDC), NHS (N-hydroxy succinimide) are purchased from Sigma-Aldrich (Brno, Czech Republic), sodium hydroxide, acetic acid ethanol, hydrochloric acid, and isopropyl alcohol was purchased from Lach-Ner, sro. (Czech Republic). All chemicals are used without further purification.

2.2. Preparation of CGF and CO-g-CGF

Chitin-glucan (ChGF) and chitosan-glucan complex fibers (CGF) were extracted from the industrial strain of the Aspergillus niger (*A. niger*) cell wall by a chemical treatment process. Briefly, 10 g of native *mycelium* (fermented from *A. niger)* was treated with 1 % NaOH at room temperature (RT) for 5 h, filtered, and washed with Milli-Q water to neutral pH. The mycelium obtained in a wet state was treated with 5 % sodium hydroxide at 90 ° C for 10 h, filtered off, and collected the insoluble part collected. The insoluble alkaline *mycelium* (IAM) was washed three times with Milli-Q water until pH was neutral, then treated with 75 % isopropyl alcohol and absolute isopropyl alcohol (IPA). The product was dried at 70 °C; chitin-glucan CGF fiber chitin-glucan (ChGF) was 85 %. 5 g of dry ChGF was dispersed in 25 % NaOH at 50 ° C using a water bath for 5 h combined with a mechanical stirrer with a large blade impeller at high speed (2000 rpm). The product was filtered off, washed to pH neutral, and dried at 50 ° C. In the final step, the alkali-insoluble material of the CGF fibers was treated with 1 M acetic acid at 50 ° C for 2 h to remove the acid-soluble chitosan (C) and branched glucan (G), then filtered, washed with distilled water until pH neutral and dried at 50 °C for 24 h. From SEM, the chitosan-glucan complex fibers showed a diameter of about 2.5± 0.5 µm with a microfiber length of approximately 300-500 µm (Fig. S1).

Hybrid biocomposite scaffolds (HBS) collagen-grafted-chitosan-glucan CGF fibers (CO-g-CGF) were synthesized via chemical modification of CO with CGF in the presence of EDC/NHS as a crosslinking agent. Different weight ratios of CGF were added to the CO solution as described in **Table 2**. CO (0.5 wt%) and CGF (0.5 wt.%) were mixed in Milli-Q water, swelled for 48 h at 4 ± 2 ° C with pH about 4.5, then homogenized for 20 min using an IKA disintegrator. The dispersed solutions are subsequently centrifuged at 4000 rpm (4 ° C) for 10 min to remove air bubbles, frozen in 48-well culture plates at -25 $^{\circ}$C overnight, and then lyophilized at -90 ^{o}C for 48 h.

CO-g-CGF-HBS was crosslinked with 50 mM EDC/25 mM NHS using 90 % ethanol solution at pH 6.5. Carbodiimide crosslinker was achieved by immersing the native CO, CSGC, and CO-g-CGF-HBS in EDC into ethanol at rt. After the dispersion of CO, CGF and CO/CGF at 22 ± 2 °C for 5 h. A hybrid biocomposite scaffold (HBS) was washed in 0.1 M $Na_2HPO_4.12H_2O$ twice for 1 h, followed by washing with Milli-Q water for 2 h (changing the medium every 30 min). All samples (**Table 3**) were frozen and lyophilized again, as previously described. Native CO, CGF and HBS were coded as (100/0; 70/30; 50/50; 30/70; 0/100) corresponding to CO/CGF ratios, respectively. The cross-linked density between collagen and the fiber of the chitosan-glucan complex in the presence of EDC/NHS was measured using

2,4,6-trinitrobenzene sulfonic acid (TNBS) to determine the free amino groups collagen by UV-VIS spectroscopy and lysine as a standard amino acid for the calibration curve[310-313].

Table 3: Different compositions of hybrid biocomposite scaffold (HBS) grafted using different ratios between CO and CGF.

Sample codes	Weight ratio between CO to CGF	Wt. of CO (g)	Wt. of CGF (g)
Native CO scaffold	0	0.5	0
CO-g-CGF (70/30)	70/30	0.375	0.125
CO-g-CGF (50/50)	50/50	0.25	0.25
CO-g-CGF (30/70)	30/70	0.125	0.375
Native CGF scaffold	0	0	0.5

2.3. Characterization

Hydrolytic degradation of CO-g-CSGCF-HBS was measured using phosphate buffer solution (pH 7.4) in an incubator at 37 ˚C. Cylindrical samples were weighed W_1, submerged in PBS (pH 7.4), and kept in an incubator at 37 °C. A piece of each dried HBS was weighed and immersed in 10 ml of phosphate buffer saline solution (PBS, pH 7.4) at 37 ℃ for a certain time, and the swollen samples were gently pressed between filter papers to remove the excess water remaining from the surface of HBS and weighed (W_w). Each value was averaged from five parallel measurements. The swelling ratio of the scaffold was defined as the ratio of weight of the swollen samples (W_s) to the initial weight (W_i) at different swelling times (0 to two months) according to the following **Eq. 1**.

After different time inverters (7, 14, 28, 56 days), samples were washed with water to remove the rest of the buffer saline salts and gently pressed between two filter papers to remove the excess water. The final mass was recorded (W_2) and used to calculate the weight loss percentage from the following **Eq. 2.** The porosity of the native and HBS was measured using the Archimedes principle[314, 315], and ethanol was used as a liquid medium for 2 h at room temperature. The porosity percentage was calculated from the following **Eq. 3**.

$$\textbf{Swelling percentage} = \frac{Ws-Wi}{Wi} \times 100 \qquad (1)$$

$$\textbf{Weight loss} = \left(100 - \frac{W1-W2}{W1}\right) \qquad (2)$$

$$\textbf{Porosity (\%)} = \frac{M2-M1}{M2-M3} \times 100 \qquad (3)$$

Where M_1 was the dry weight of the scaffolds, M_2 was the weight of scaffolds saturated with ethanol, and M_3 was the weight of scaffolds suspended in ethanol. Five samples were used to calculate the standard division (± SD).

Young's modulus of elasticity of collagen, chitosan-glucan complex fiber, and hybrid bioscaffold was measured at room temperature using a Zwick/Roel traction machine. The loading velocity was 1 mm/min. The samples had a cylindrical shape (about 12mm in height and 6 mm in diameter), and native and HBS with different ratios (100/0; 70/30; 50/50; 30/70 and 0/100) were tested and evaluated. Each group had five specimens. Mechanical loading was applied until the scaffold was compressed to 50 % of its original height. Compressive moduli were determined to apply linear regression to a part of the stress-strain curves at 2-10 % strain (initial modulus E_{init}). The stress was defined as the force divided by the initial area and the strain was defined as the deformation of the specimen (height) divided by the initial height of the specimen. Due to the cylindrical shape of specimens, the initial area of each specimen was determined using Ellipse 3D (ViDiTo, Košice, Slovak Republic). Each specimen was captured with a camera, and the perimeter of the initial area was manually marked using Freehand plugin.

Antibacterial evaluation of native and hybrid bioscaffolds was performed using the Shake-Flask assay[316-320]. *Escherichia coli (E. coli) was used as a Gram-negative bacterium model, while Staphylococcus aureus (S. aureus) was used as a Gram-positive bacterium model.* A certain concentration of living organisms (*E. coli* and *S. aureus*) was suspended in an Erlenmeyer flask (1–2 10^5 / ml of microorganism). The test solution was shaken for 24 h (320 rpm) at 25 ° C (control sample). After adding native CO, CSGCF and CO-g-CSGCF (70/30, 50/50, 30/70), the reduction rate of living microorganisms was estimated by comparing the number of microorganisms before adding the scaffolds to the following equation. **5**.

$$\text{Reduction rate (\%)} = \frac{[A1-A2]}{A1} \times 100 \qquad (5)$$

Where *A*1= the number of microorganisms without a scaffold, *A*2= number of microorganisms with a scaffold after incubation. Data were shown as mean (± SD; n= 4).

XRD patterns were collected on a device: D-8 Advance diffractometer (Bruker AXS, Germany) with Bragg-Brentano (θ-θ) goniometer (-) (radius 217.5 mm) equipped with a secondary beam curved graphite monochromator and Na (Tl) I scintillation detector. The generator was operated at 40 kV and 30 mA. The scan was completed at room temperature from 5 to 30° (2θ) in a 0.02 ° step with a counting time of 8 s per step. The thermal decomposition of HBS was evaluated using a thermogravimetric instrument (TG, Entsch 209F3), Al_2O_3 crucible with a heating rate of 10 °C/ min (with a data collection rate of 40 points per Kelvin).

Attenuated total reflectance Fourier transform infrared spectroscopy (ATR-FTIR) performed using a Nicolet Impact 400 D ATR-FTIR spectrophotometer (Nicolet, Prague, CZ) equipped with a ZnSe crystal for ATR-FTIR spectroscopy. Absorbance is measured as a function of wavenumber (cm^{-1}) between 4000 cm -1cm -1 and 600 cm^{-1} with a resolution of 8 cm -1. The structure and surface morphology of the HBS were visualized using scanning electron microscopy (MIRA 3, Brno, Czech Republic). The HBS was cut with a razor scalpel after being frozen, coated with a layer of gold / platinum (20 nm), and then observed in secondary electron emission mode with a high voltage of 10 kV. The histograms were plotted from the average pore size by measuring (250-300) of pores chosen randomly throughout the surface and central cross section of native CO, CGF and HBS samples. The image analysis program (Image J) was used to determine the average diameter of the pores, and at least 100-150 pore points were evaluated from 10 SEM photos.

Statistical analysis: Data analysis was carried out using Anova: Single-factor test and T-Test: Two-Sample Assuming Equal Variances. The error bars represent the mean ± standard deviation (SD) of the measurements p values <0.05 were considered statistically significant. (*p<0.01, **p<0.0001, and***p<0.00001). All experiments were carried out in triplicate and data were given as mean ± standard deviation and the graphs were drawn in OriginPro 2019b.

3. Results and discussion

3.1. Extraction and Chemical Modification of CGF

ChGF and CGF were extracted from the *mycelium* of *A. niger* using different sequence steps, as shown in **Fig. 34. Fig. 34a** explores the acid-base treatment sequencing process to remove the non-bonded impurities linked to the cell wall matrix-like proteins, lipids, and dyes; this step was called the digestion process [10, 111, 112]. Insoluble alkaline *mycelium* (IAM) was treated with NaOH to hydrolyze the chemical bonds between the lipid-protein-dyes matrix to obtain pure ChGF (Deproteinization step (DP). In the final step (deacetylation process), ChGF was treated with highly concentrated NaOH to remove acetyl groups from the ChGF chain (deacetylation step (DDA). A large blade impeller was used to avoid destroying the CGF fibers. Insoluble CGF was filtered, washed several times with a mixture of alcohol and water (80/20 v/v), then dried at 70 ° C for 24 h. The degree of deacetylation (DDA) of CGF was 71 % (measured by ss-NMR spectroscopy, Fig. **S2**). The fiber diameter was about 2.5± 0.5 µm with a length of approximately 300-500 µm (Fig. S1).

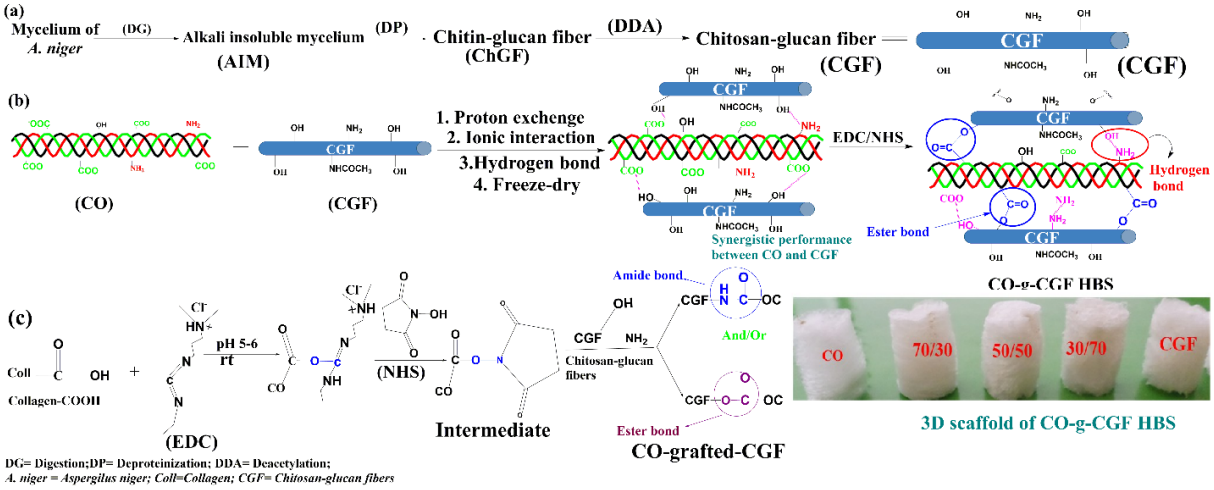

Fig. 34. Representative extraction sequences of CGF and chemical modification of (CO)

Hybrid biocomposite scaffolds (HBSs) were synthesized by chemical modification of CO with CGF. Collagen and CGF fiber (DDA= 71 %) were mixed for 10 min to obtain homogenized, well-dispersed and one-phase material from both suspensions. The mixing was done using an IKA homogenizer at 8000/min in a slightly acid medium (pH 4.5) and a lower temperature of 0 ° C for 30 minutes. Physical synergistic interactions (proton exchange, ionic interaction, hydrogen bonds) between the functional groups of CO and CGF (**Fig. 34b**) were generated. The CO and CGF were centrifuged at 4000 rpm for 5 min to remove air bubbles and obtain homogeneous pores from the CO-CGF composite. The mixed mixture was transferred into 48 well plates and agitated at -30 $^{\circ}$C for about 24 h. After agitation, the samples were dried in a -90 ^{o}C for 48 h. During the freeze-drying step, the interactions between CO and CGF were improved and enhanced as described below (**Fig. 34b**).

EDC/NHS was used as a crosslinking agent of collagen scaffold materials[321] due to the low toxicity and higher stability of the CO scaffold after the cross-linking step. There were many physical and non-ionic interactions between the functional groups of CO and CGF (**Fig. 34b**) created after the modification of CO with CGF. Synergistic performance during the chemical interactions between CO and CGF improved significantly after the use of EDC and NHS as crosslinking and catalyzing agents. The cross-linked density between the collagen and chitosan-glucan complex fiber was 0.2, 0.4, 0.5 for HBS with 70/30, 50/50 and 30/70, respectively.

Fig. 34c shows the proposed chemical interaction mechanism between -COO^- in the CO helical structure and the -OH groups in the CGF. Due to the lower ratio of chitosan (C) to glucan (G) in the composition of CGF (**Fig. 1S**; 9: 1)[111], the possibility of interaction of -COO^- (in CO) with OH (in chitosan and glucan chains) was higher than that of the -NH_2 groups

in chitosan. New chemical bonds were generated and improved mechanical stability, swelling, and degradation of the hybrid scaffold, which was an essential point of applications of 3D scaffold tissue engineering as described in the following sections.

3.2. Physicochemical Properties of HBS

One of the significant purposes of adding CGF to CO was to improve the interaction between complex functional groups (amino and hydroxyl) with collagen groups (carboxylic and amino) that function as binding sites to increase the EDC / NSH cross-linking efficiency. **Fig. 35** shows the FTIR spectra of the native CO, CGF and HBS with different ratios between CO and CGF. The absorption peaks of the cross-linked native CO scaffold appear at 3500 cm^{-1} for -OH groups, 3278 cm^{-1} for amide A, 3072 cm^{-1} for amide B, 2930 cm^{-1} for asymmetrical stretch CH_2, 1646 cm^{-1} for amide I, 1548 cm^{-1} for amide II, 1250 cm^{-1} for amide III, and at 750 500 cm^{-1} for amide (IV-VII)[111, 112, 322, 323]. From the FTIR spectrum of native CO, we confirmed no denaturation of native CO scaffold during preparation steps and crosslinking via EDC/NHS mixture. The CGF shows specific peaks at 3320 cm^{-1} corresponding to -OH of the compositions (Ch, C, G) and 2930 cm^{-1} related to an asymmetric stretch of methylene groups of the CGF (**Fig.35**). The characteristic vibration peak for the carbonyl groups in chitin at 1650 cm^{-1} and 1550 cm^{-1} was related to the free amino groups of chitosan (part of CGF). The peaks at 1070 and 1040 cm^{-1} were characteristic of ether linkage (-C-O-C-) between chitin, chitosan, and glucan polymers. The β-anomeric configuration was signalized by absorption at 890 and 1371 cm^{-1}.

A hybrid biocomposite scaffold (HBS) shows another new peak at 1732 cm^{-1} suggesting the formation of chemical ester bonds ($-O-C=O^-$) between CO and CGF[111, 284, 324, 325] that improve synergistic performance between CO and CGF. The intensity of the new peak increased slightly with increasing the CGF grafting ratios (**Fig. 35**). The absorption bands were shifted because of interaction between CO and CGF, which indicates the occurrence of molecular interactions in the hybrid synthesis process. Such a band involves the -OH group of CGF (in C and G parts) and carboxylic groups of CO. The sharp and strong peak at 1130 cm^{-1} in the hybrid scaffold spectrum relates to the -C-O-C- ether linkage in CO and CGF. After the chemical modification of CO by CGF, the peak corresponding to amide I shifted from 1629 to 1641 cm^{-1} due to interactions with functional groups of CGF.

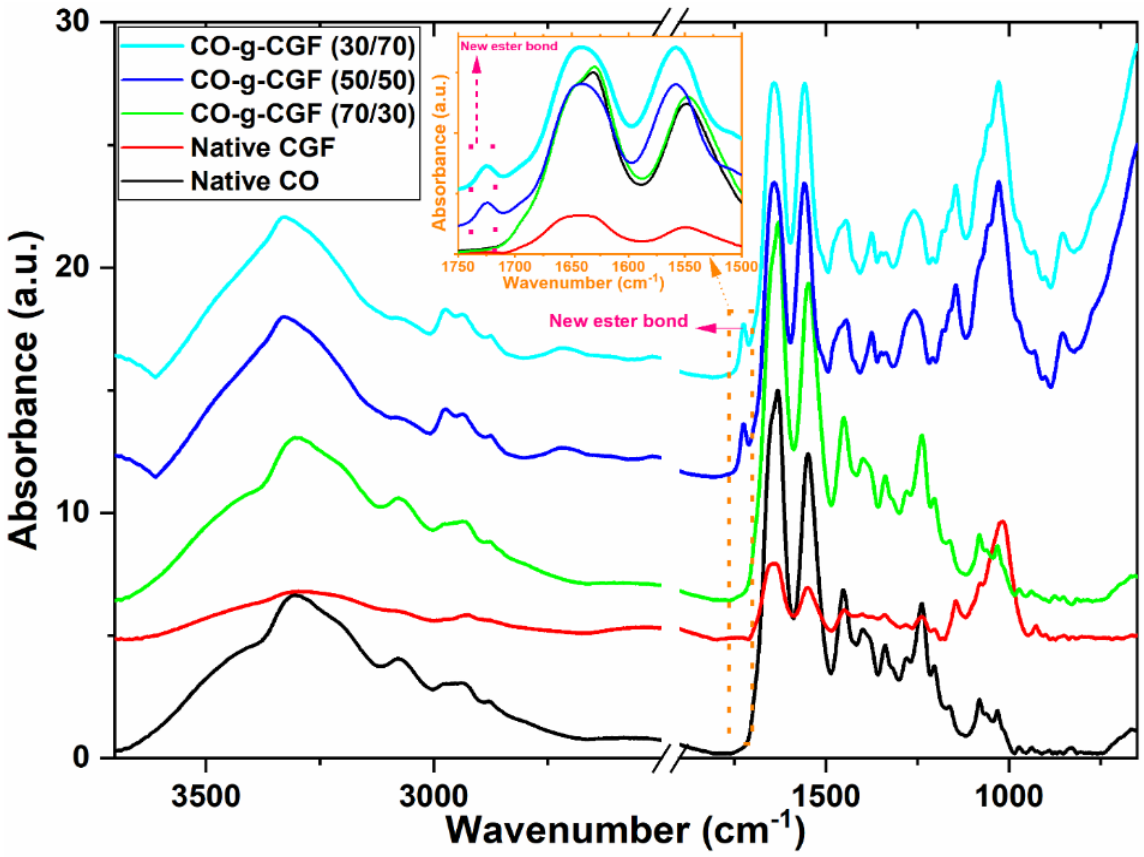

Fig. 35. ATR-FTIR of native CO, CGF and HBS.

The thermal stability of native CO, CGF, and HBS was measured and evaluated as shown in **Fig. 36**. The native CO scaffold shows two different peaks characteristic of the two-stage sample devastation due to higher temperature. In the first stage (between 25-75 °C), the peak with a maximum of 70 ° C (mass loss approx. 15 %) was due to the evaporation of absorbed water (non-bonded) to the native CO scaffold. In the second stage (between 225 and 375 °C), the maximum peak was 330 °C (mass loss approx. 55 %). The DTG curve, the significant degradation that occurs in three steps at 240, 330, and 340 $^{\circ}$C, was caused by concurrent collagen degradation processes such as depolymerization, dehydration, and decomposition of the monoCO chain unit followed by the formation of the charred residue. The DTG peak above 340 $^{\circ}$C was attributed to the oxidation and breakdown of the charred residue to low molecular weight gaseous products.

The native CGF scaffold shows three different peaks, as shown in **Fig. 37(a, b)**; these peaks were representatives of the three-stage sample destruction. The first stage (between 25 and 75 °C) with a maximum peak at 56 ° C (mass loss approximately 5%) relates to the evaporation of water absorbed into Ch, C, and G compositions in the CGF chains. In the second and third stages (between 210 and 340 °C), the maximum of the second peak was at 260 ° C

(mass loss approximately 28%), the maximum of the third peak was at 270 ° C (mass loss approximately 38%) that were attributed to release of water bonded to different functional groups in CGF (-OH,-$NHCOCH_3$ and -NH_2) and small molecular products released by thermal degradation of CGF [10, 111, 112].

Hybrid scaffolds with different grafting ratios (Figs. **37a, b)** exhibit peaks representing the two-stage destruction of the sample due to temperature. The first stage (between 25 and 75 °C) with a maximum peak at 55 ° C (mass loss approximately 6%) is related to the evaporation of water absorbed by the CO-g-CGF scaffold. In the second stage (240 and 390 °C), the maximum peak at 290 °C (mass loss approx. 30.5 %) corresponds to the release of water molecules attached to CO-CGF and small molecular products released on thermal degradation. The maximum of the third peak-at 300 ° C (mass loss of approximately 37%) was attributed to the release of water bound to different functional groups in the CGF (-OH, -$NHCOCH_3$ and -NH_2) CO chains and small molecular products liberated on thermal degradation of the hybrid scaffold. From **Figs. 37 (a, b)**, we can conclude that HBS (CO-g- CGF) was thermally more stable than native CO and CGF, and the thermal stability decreased slightly with the increasing grafted ratio of CGF in the HBS.

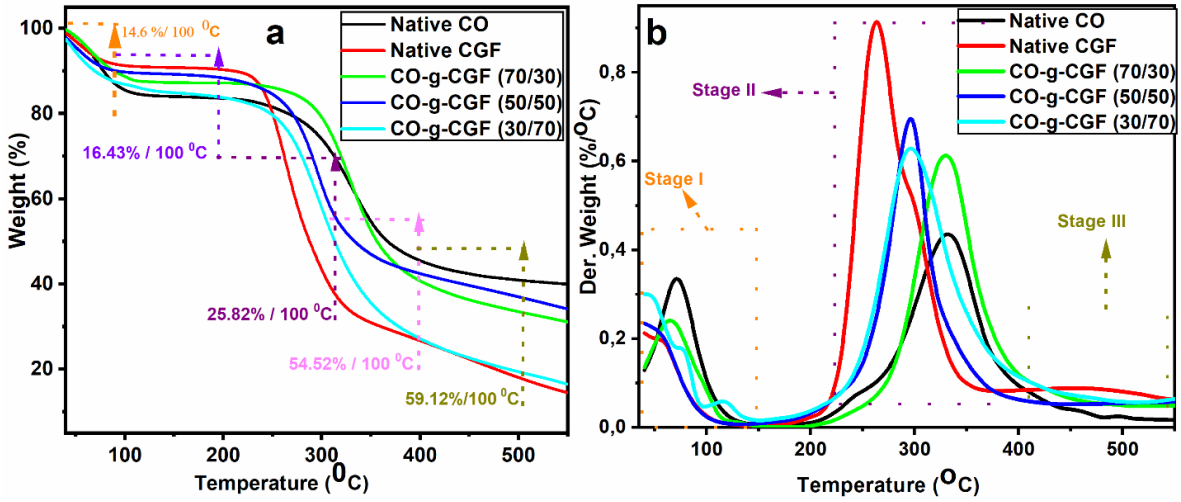

Fig. 36. TG (a); DTG (b) curves of native CO, CGF and HBS scaffolds

Fig. S3 shows the X-ray diffraction of native CO, CGF, and HBS. In a neat CO scaffold, broadband appears at 2θ = 15-25°, corresponding to the triple helical structure of CO[326]. In CO-g-CGF (**Fig. S3),** different peaks appear at 2θ = 9, 19.2, 22.5, and 26 ° corresponding to chitin[327], chitosan[328], and glucan[329] chemical composition of the complex. The different HBS grafting ratio (CO-g-CGF) shows the same peaks at 2θ = 9, 19.2, 22.5, and 26 ° with higher intensity due to the strong interactions between different functional groups of CO (semicrystalline) and CGF (amorphous structure).

Fig. 36 shows the effect of the chemical compositions of the CO, CGF and (CO-g-CGF) scaffolds on their hydrolytic stability under physiological conditions (37 ℃; pH 7.5). After three days of incubation, the native CO scaffold showed a high degradation rate (69.5 %) compared to native CGF (27.9 %) and CO-g-CGF (70/30; 50/50; 30/70) were 37.71; 27.65; 26.6%), respectively. Native CO scaffolds show significantly lower hydrolytic stability (degradation rate above 85 %) after 7 days of incubation compared to native CGF and CO-g-CGF **(Fig. 37)**.

The CGF scaffold shows high weight loss compared to native CO (27.9, 41.9 %) after 3 and 7 days of incubation, respectively. Interestingly, the hydrolytic degradation percentage was significantly enhanced compared to native CO and CGF after 56 days of incubation and physiological conditions. This significant improvement in the stability of CO-g-CGF is due to the strong synergistic performance **(**chemical/physical interactions) between CO and CGF.

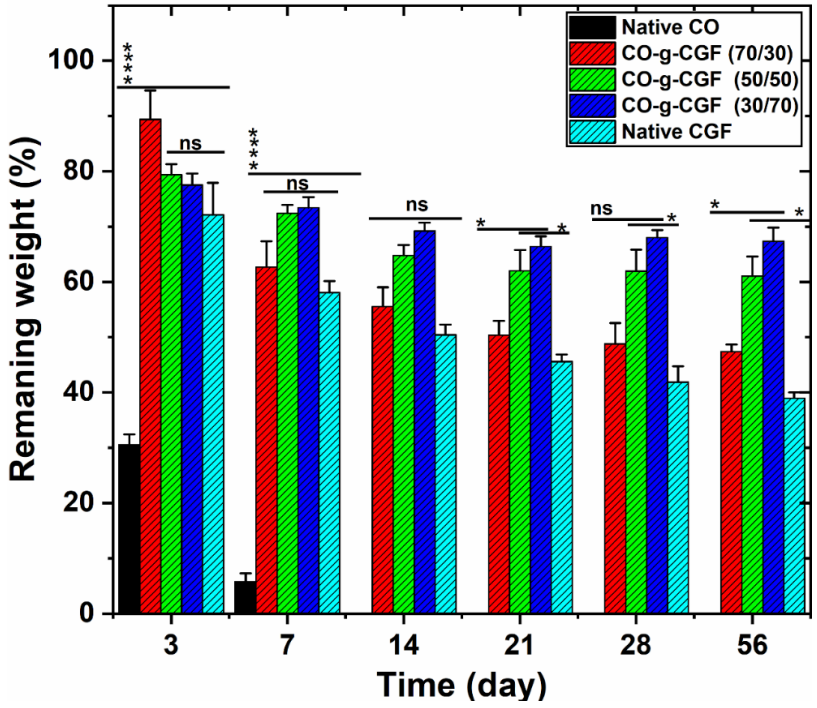

Fig. 37. Representative hydrolytic stability of the CO, CGF, and HBS scaffolds.
Notes: Data were represented as the mean ± SD, n=3; (*p<0.01, **p<0.0001, ***p<0.00001, and * *** p0.000001) and ns: no significant differences. After 3 days: CO-g-CGF (70/30, 50/50, 30/70) >native CO; ns between grafted scaffold; After one week: CO-g-CGF (70/30, 50/50, 30/70) >native CO; ns between the grafted scaffold; After 14 days: ns between the grafted scaffold (70/30, 50/50, 30/70); After 21 days: CO-g-CGF (30/70) > (70/30, 50/50, native CGF); one 30 day: ns significant differences between different HBS (CO-g-CGF) group; CO-g-CGF(50/50, 30/70) > native CGF; 56 day: CO-g-CGF (30/70) > (50/50, 30/70, native CGF).

The percentage of swelling percentage (SR; %) strongly depends on the hydrophilic nature, microstructure, and chemical composition of the scaffold. Native CO shows hydrophilic properties with more amphiphilic properties than CGF **(Fig .38)**; the ability to uptake the porous scaffold structure seems to be the main explanation for the differences observed in the swelling ratio. The poor mechanical properties of native CO led to the collapse of the porous structure after it was removed from PBS solution[111, 112]. On the contrary, CGF possesses a higher elasticity that was helpful for the retention of the scaffold's original porous structure. Hence, the water uptake of the scaffolds increases with the increasing ratio of CGF in the composition of HBS **(Fig. 38).**

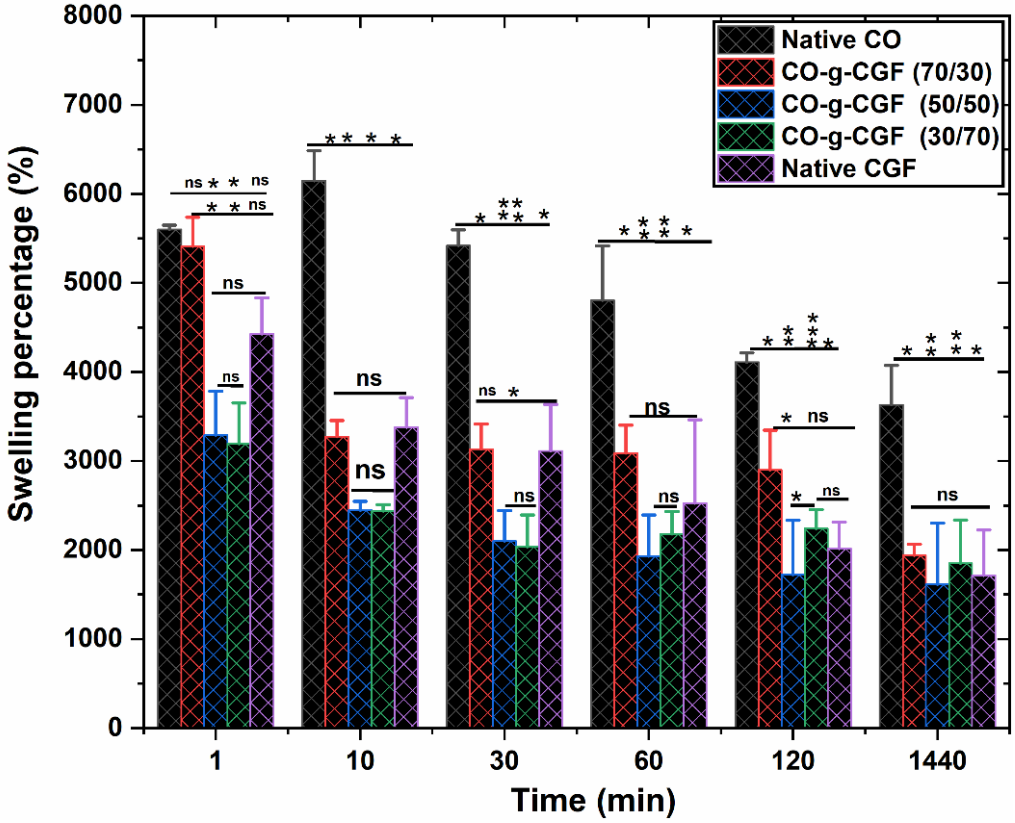

Fig. 38: Swelling percentage of native CO, CGF, and HBS scaffolds.

Notes: Data were represented as the mean ± SD, n=3; (*p<0.01, **p<0.0001, ***p<0.00001); ns: no significant differences. At 1 min: native CO>CO-g-CGF (50/50; 30/70); 10 min: native CO>CO-g-CGF (30/70, 50/50, 30/70, native CGF); 30 min CO>CO-g-CGF (30/70, 50/50, 30/70, native CGF); 120 min: CO>CO-g-CGF (30/70, 50/50, 30/70, native CGF); 1440 min: CO>CO-g-CGF (30/70, 50/50, 30/70, native CGF). After 1440 min, there were no significant differences between native CGF and all CO-g-CGF (70/30, 50/50, 30/70).

Fig. 38 shows the effect of the different ratios (70/30; 50/50, and 30/70) on the swelling percentage of HBS. The CO-g-CGF (100/0) scaffold exhibits a higher swelling ratio than CO-g-CGF (70:30) > (50/50)> (30/700)> (0/100). Within the first 20 minutes after absorption, the SR (%) was approximately the same in all native and hybrid scaffolds. An increased ratio of CGF decreases the uptake percentage of the scaffold (0, 30, 50, and 70 wt%). Due to the hydrophobic properties of CGF (chitin, chitosan, and glucan) and the strong chemical interaction between the functional groups of CO and CGF, it leads to decreased hydrophilicity of the CO matrix.

From the swelling values after one day of seeding the native and hybrid scaffold, the swelling percentage was significantly reduced after grafted collagen with complex fibers. Different ratios of complex fibers did not show a slight difference but were insignificant compared with the native chitosan-glucan complex scaffold. From swelling measurement, we have confirmed that the hydrophilic character left in the HBS plays a crucial role in the swelling /absorption ability.

3.3. Morphology and mechanical properties of native CO, CGF, and CO-g-CGF

Fig. 39 shows the surface morphology of native CO, CGF, and HBS with different grafting ratios of CGF. **Figs. 39 (ac) depict** micrographs of the 3D scaffold architecture and the pore size histogram of native CO. The CO scaffold shows a heterogeneous lamellar pore structure surrounded by flake-like collagen sheets with a mean pore size of 180 ± 109 µm (**Fig. 39c**). **Figure 39 (df)** shows the native CGF fibers scaffold with a very smooth and homogenous fiber surface and pore size was (57 ± 37 µm). The appearance of the collagen-grafted porous scaffold of chitosan-glucan fibers (CO-g-CGF) is shown in **Fig. 39 (g-o)**. SEM observation clearly showed the different pore structures of the grafted CO with different ratios of CGF (70/30; 50/50; 30;70) scaffolds synthesized in the presence of EDC/NHS. The porous CO-g-CGF (70/30) scaffold with spherical pores shape (134 ± 76 µm; **Fig. 39i**) was smaller than the native CO scaffold (**Fig. 39a-c**). The large spherical pores were evenly distributed throughout the volume and well stacked. The CGF adhered to the surface of the collagen matrix with physical/ chemical bonds as shown in **Fig. 39k** (blue rows) and kept an open pore with an interconnected network (**Fig. 39k**).

The pore size of the grafted scaffold (CO-g-CGF; 70/30; 50/50, 30/70) decreased significantly after the chemical modification of collagen (Fig.6B). The size of the pore of the grafted scaffold decreased with increasing complex fiber ratio but was not significant (Fig.6B). The fiber scaffold showed the smallest pore size compared to other scaffold groups **(Fig. 39B).** All scaffolds exhibit a highly porous structure with good adhering properties of CGF on the

surface of CO matrix. In addition, the interconnectivity of pores in the scaffold, as a significant structural property, affects the migration and proliferation of cells. HBS porosity of HBS was slightly decreased from 96.1± 0.10 (native CO) with an increase in the ratio of CGF from 30 to 70 % in the hybrid scaffold (96.1 ± 0.05, 95.4 ± 0.49, and 95.2 ± 0.12), respectively (**Fig. 40a**). There were no significant decreases in the porosity percentage from porosity measurements compared to all natives CO, CGF and grafted scaffolds with different ratios of complex fiber (70/30, 50/50, 30/70). Both the pore size and porosity of HBS decreased slightly compared with native CO due to the strong synergistic performance generating new bonds between CO and CGF that could weaken the interconnection network between CO fibrils and CGF[10, 111, 112].

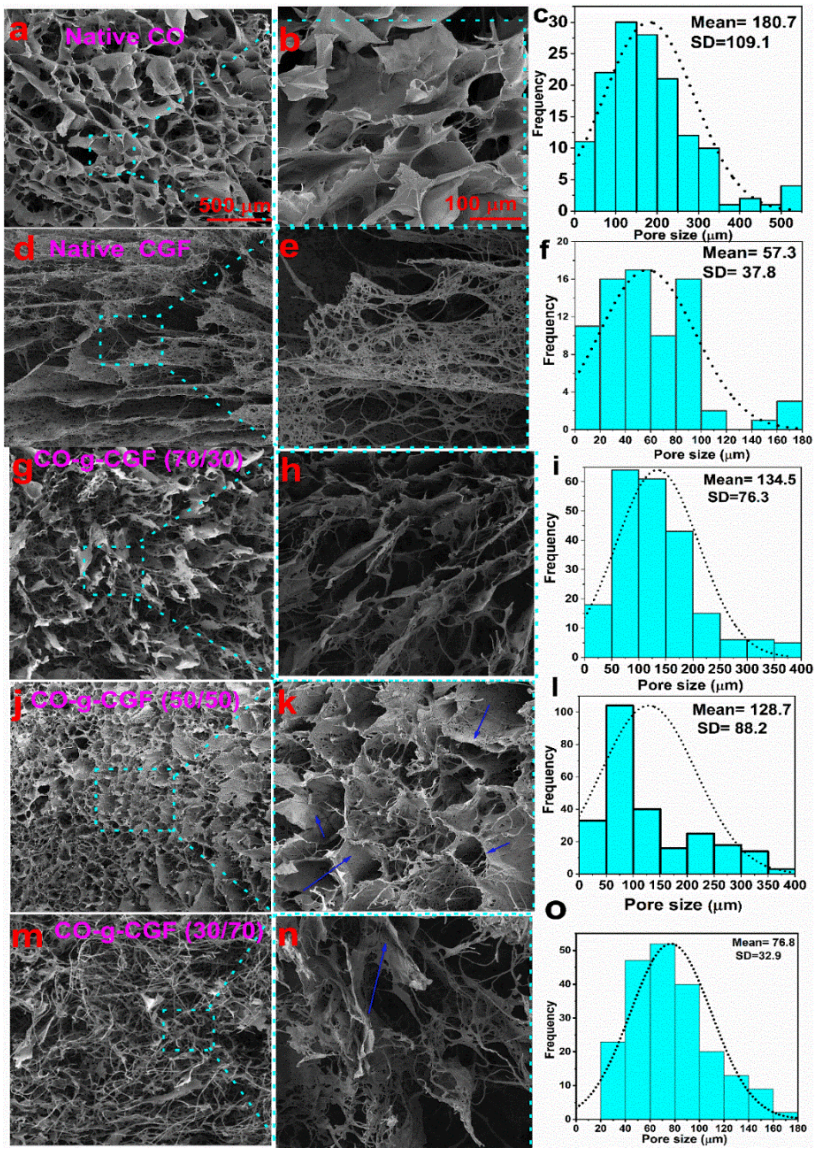

Fig. 39A. Surface morphology and pore size histograms of native CO, CGF and HBS scaffolds

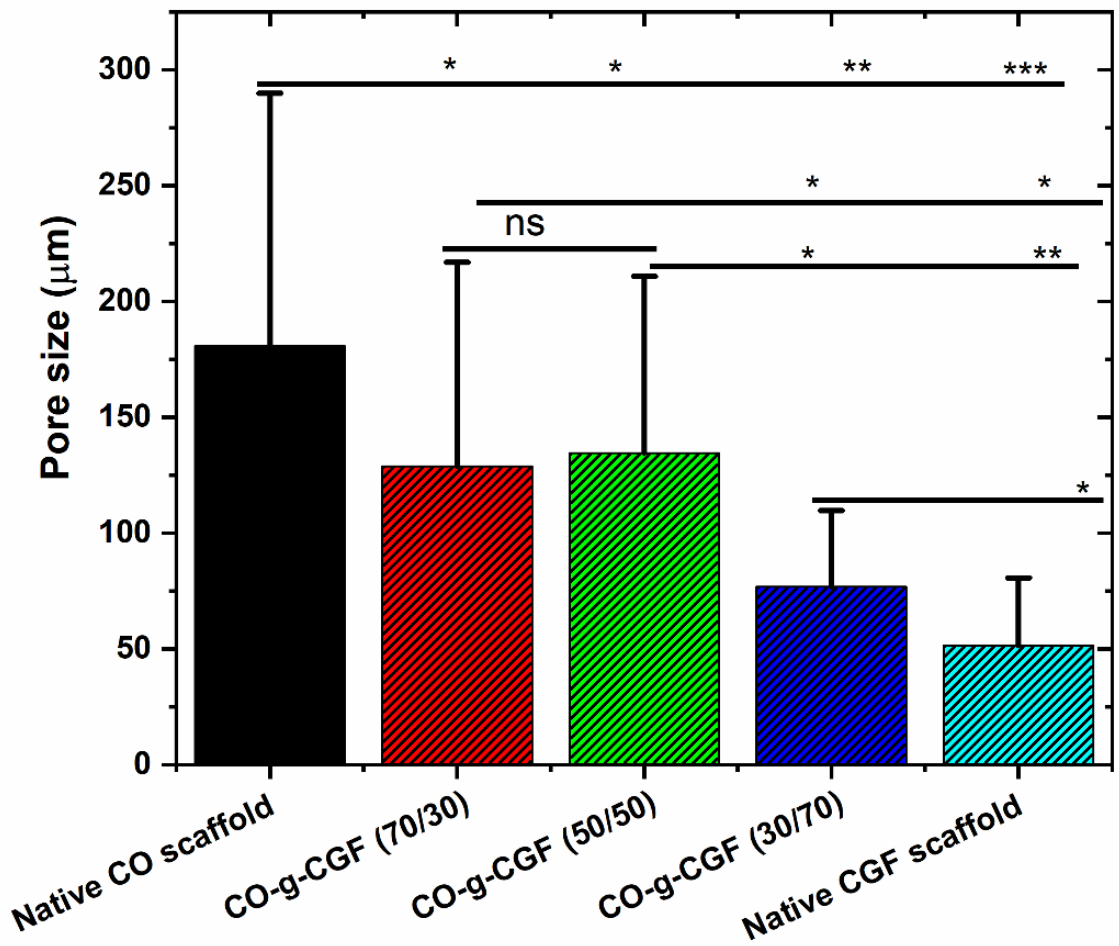

Fig. 39 B: Pore size of native CO, CGF, and HBS scaffolds.

Notes: Data were represented as the mean ± SD, n=3; (*p<0.01, **p<0.0001, ***p<0.00001) and ns: without significant differences. Native CO scaffold > CO-g-CGF (30/70,50/50, 70/30> native CGF scaffold). From porosity measurements, there were no significant changes between native CO, CGF, and grafted HBS.

The mechanical properties of HBS in different solution media were important for the hydrolytic stability of hybrid scaffolds for a long period of up to 60 days**.** Cylindrical 3D specimens were synthesized from CO-g-CGF-HBS (100/0;70/30; 50/50; 30/70; 0/100). Interestingly, there were strong synergistic effects between CGF concentrations and Young's modulus of HBS (**Fig. 40b)**.

The collagen scaffold shows a low young modulus of about 3.5 ± 1.2 KPa. Furthermore, after chemical modification with the chitosan-glucan complex fiber, the mechanical properties of the hybrid bioscaffold increase significantly with increased content of the complex fiber. Significant improvements of the module's values of the grafted scaffold were CO-g-CGF (30/70)> CO-g-CGF (50/50)> CO-g-CGF (70/30)> native CO scaffold. The improvement of the young modulus values of grafted scaffold was due to the strong physical and chemical

interactions in the presence of a cross-linked agent that could generate synergetic properties between both components. The native fiber scaffolds of the chitin-glucan complex showed the highest modulus value compared to the different grafting ratios of CO and the CGF and native collagen scaffold.

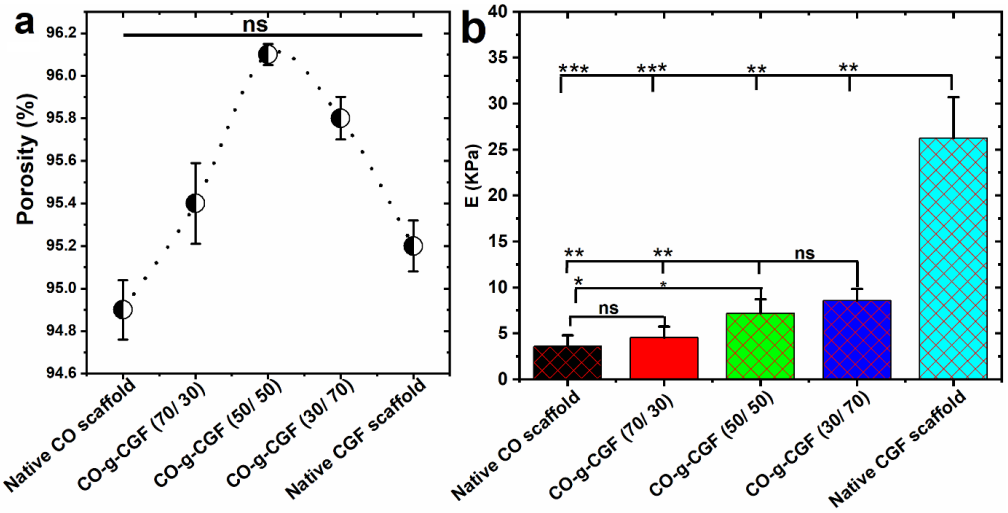

Fig. 40. Porosity (a) and mechanical properties of native CO, CGF, and HBS scaffolds (b). Notes: Data were represented as the mean ± SD, n=3; (*p<0.01, **p<0.0001, ***p<0.00001); ns: No significant differences. Native CGF scaffold > CO-g-CGF (30/70)> CO-g-CGF (50/50)> CO-g-CGF (70/30)> native CO scaffold). From porosity measurements, there were no significant changes between native CO, CGF, and grafted HBS.

3.4. *In vitro* measurements of native HBS and HBS scaffold

The native and hybrid biocomposite scaffolds (HBS) were seeded with mesenchymal stem cells (*MSCs)* and the cell adhesion as the surface area covered by the adhered cells and determined using fluorescence confocal microscopy images. *MSCs* were stained with DiOC6 and propidium iodide, and then visualized and measured using confocal microscopy before areas of the spread cell surface. As shown in **Fig. 41a,** the surface area of cells after CSGCF in comparison with native CSGCF. The highest cell adhesion was CO-g-CSGCF-HBS (70/30)> (50/50)> (300/70)> net CO> net CSGCF**.** Because of the higher interaction between the CO and CSGCF functional groups (covalent or noncovalent bonds), cell seeding of the scaffold was enhanced and promoted by increasing the ratio of the CSGCF components in the hybrid scaffold. From the adhesion evaluation, we can see that the CSGCF significantly enhanced the adhesion of *the MSC* anchored hybrid scaffold compared to the net CO scaffold.

The cell viability of the hybrid scaffold was determined by the *MTS* assay (**Fig. 41b**). *The MTS* assay revealed significantly higher metabolic activity of MSCc after 21 days of cultivation in CO-g-CSGCF (50/50) > native CO, CO-g-CSGCF (70/30; 50/50; 30/70) except plain CSGCF. Additionally, significantly higher cell metabolic activity was observed in CO-

g-CSGCF (50/50) on day 21 compared with the native CO scaffold. The increases in the number of cells, due to good proliferation, were estimated from DNA values measured using a Pico-Green (PG) assay test after 1,7,14 and 21 days with *MSC*. From cell viability measurements, all HBS has not any toxicity against *MSCs* for all time from 1 to 21 days without a problem with cell growth (**Fig. 41b**). The results of the Pico/Green assay on days 1, 7, 14, and 21 days indicated that substantial cell proliferation on the HBS, a significantly higher number of cells was observed on Days 7 and 14 on each HBS than on net CO and CSGCF, respectively.

To evaluate the viability of cells seeded in HBS, staining with propidium iodide and BCECF-AM staining. Maximum viability was noticed on the CO-g-CSGCF-HBS (50/50) after 21 days of cultivation and deteriorated with higher concentrations of CSGCF. For quantification and better comparison, the number of live/dead cells in each HBS was counted, and the viability was calculated as the percentage of live cells from the total number in a defined area. Lower cell viability was found with scaffolds containing pure CSGCF, CO-g-CSGCF (30/70), and native CO after 21 days of seeding. The viability of *MSCs* also increased with increasing amount of CSGCF. In particular, there was a progressive increase in MSC viability during cultivation in samples with a higher CSGCF fiber concentration. Due to the fibril structure of CSGCF with a short and very thin morphology, it could improve the movement/attachment of cells in the HBS and lead to enhancements in proliferation, adhesion, growth, and interaction between cells and HBS.

The viability and adherability of mesenchymal stem cells to the net and HBS were visualized using a fluorescent actin staining agent **(Fig. 41 (dh).** The viable cells were visualized to randomly grow in dispersed and continued ways along the rim of the pores in the HBS after incubation for 21 days. In **Fig. 41e** (70/30) the viability of cells was lower than the net CO scaffold. Interestingly, by increasing the concentration of CSGCF to 70 wt.%, the cell viability was increased compared to the CO scaffold. In net CSGCF, the number of live cells was decreased compared to the control CO scaffold. From a photograph of a confocal microscope, the number of live cells compared to dead cells in hybrid scaffold CO-g-CSGCF (30/70, **Fig. 41g**)>CO-g-CSGCF (50/50; **Fig. 41f**) > CO-g-CSGCF (30/70; **Fig. 41e**)>CO (**Fig. 41d**)>CSGCF (**Fig. 41h**). CO-g-CSGCF enhanced the exhibited good cell affinity compared with the CO, CSGCF and could effectively support the attachment and growth of *MSCs*. The synergetic characteristic of CSGCF improved the interaction between the matric and cells and significantly enhanced the cell viability compared to control, net CO and CSGCF alone (**Fig. 41**).

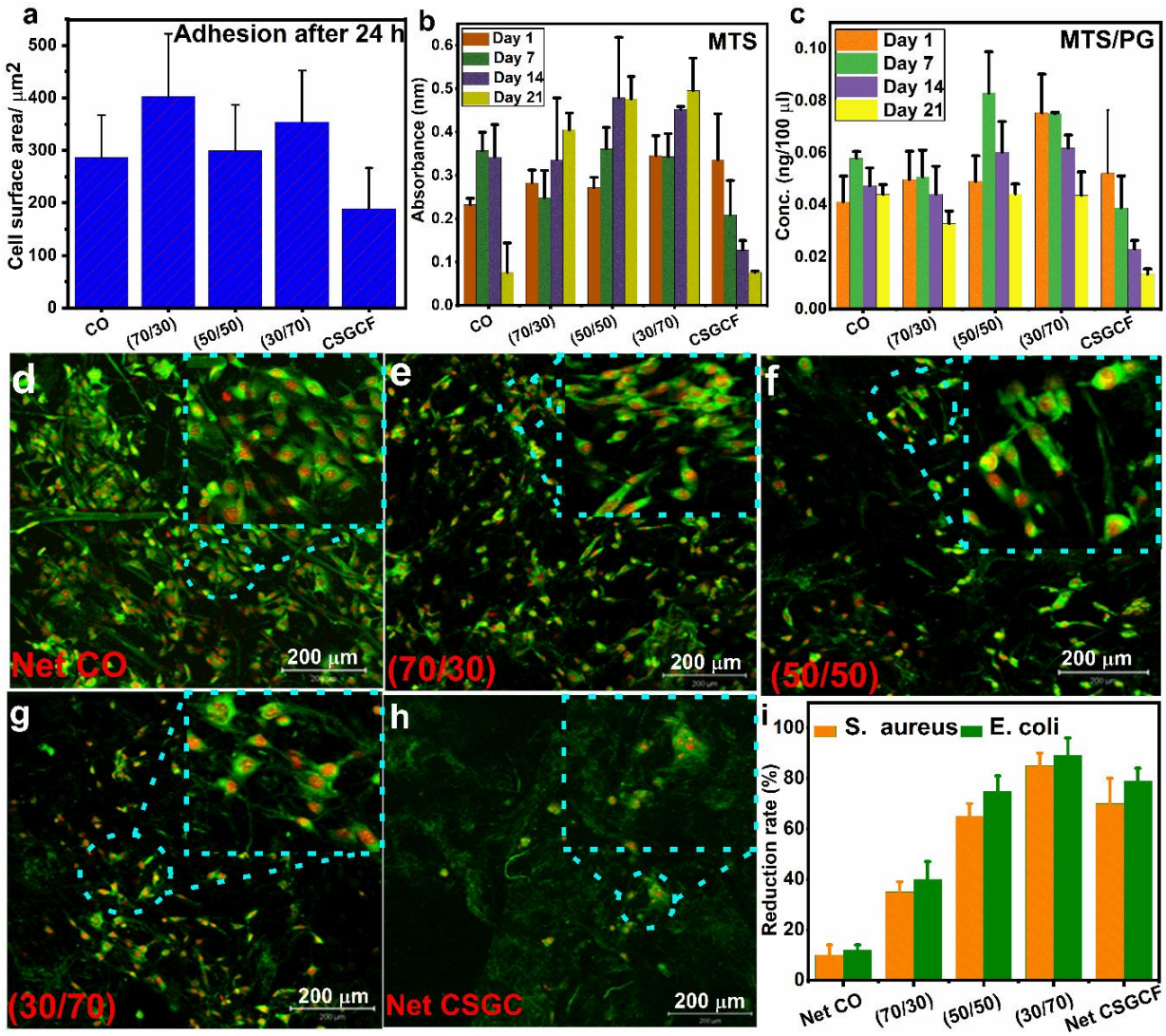

Fig. 41. Representative cell adhesion, proliferation, visualization, and antibacterial properties of native and HBS.

Notes:

(**a):** Adhesion of the MSC after seeding with the *MSCs* (24 h)**.** *The immobilized MSCs* within HBS were stained with a DiOC6 fluorescent dye to visualize living cells. The areas covered by adhered cells were measured using a confocal microscope and Ellipse software.

(b, c): Cell viability by the *MTS* test and cell viability calculated as a derivation of absorbance values from the *MTS* assay to cell count determined by the Pico-Green assay after 1,7,14, 21 days after MSC seeding. Values represent mean ± SD (n= 4). Differences are considered statistically significant as follows: $p < 0.05$ and $*p < 0.001$ (Student-Newman-Keuls method). **70/30**> CO>50/50>30/70>CSGCF; **50/50**>CO>CSGCF; **30/70**>CO>50/50>CSGCF. **Day 1 and 7**: No significant difference (ns). **Day 14**: CO>CSGCF; 50/50>CSGCF; 30/70>CSGCF. **Day 21**: CO>70/30>CSGCF; 50/50>30/70>CSGCF; 30/70>70/30>CSGCF.

(d-h): Fluorescence confocal microscopy of differentiated and adhesion MSC cells using DiOC6 staining (green cells-cytoplasm)/Propidium iodide (red cells-nuclei) after 21 days of seeded HBS scaffold. Visualized a net and HBS with different ratios grafted using a confocal microscope (Zeiss LSM 5 DUO), 10x. The scale bars were 200 μm**.**

Fig. 42 shows the antibacterial activity of native collagen, the chitosan-glucan complex, and the collagen grafted by the fiber of the chitosan-glucan complex with a different grafted ratio between CO and CGF. The collagen scaffold showed the lowest antibacterial properties against both types of bacteria (Fig. 8). The chitosan-glucan complex fiber scaffold showed high antibacterial activity against both types of bacteria (-/+ G) compared to that of the native collagen scaffold. The hybrid bioscaffold with different grafted ratios showed significantly enhanced antibacterial characteristics compared to the native collagen scaffold. The reduction rate (%) of both bacteria increased with an increase in the complex ratio in HBS (Fig. 42). One of the main components of the complex was chitosan (DDA= 72 %), which showed the cationic nature of the complex surface.

From the results obtained, there was a relationship between the amount of chitosan (part of the complex) and antibacterial activity against both negative / positive Grams (G- / +) of bacteria (Fig. 42). HBS antibacterial activity of the HBS mainly due to the presence of chitosan, which could bind with negatively charged bacterial cell wall causing dispersion of cells and disturbing the membrane permeability, followed by attaching to DNA, causing inhabitation of DNA replication and, subsequently, cell death[112, 219, 328, 330, 331]. The chitosan part in hybrid grafted bioscaffold could act as a chelating agent that selectively binds to trace metal elements, causing toxin production and inhibiting bacteria growth[5, 7, 71, 112, 220, 221, 328, 332]. HBS could also interact with the cell wall via electrostatic interaction with anionic components on the surface of the microorganism (like protein and liposaccharides) that could significantly reduce the bacteria's growth[219, 330, 333, 334]**.**

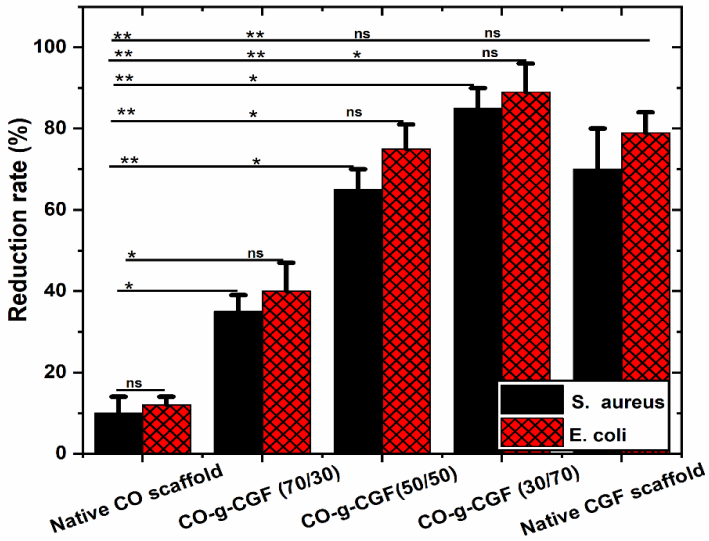

Fig. 42. Representative antibacterial properties of native CO, CGF, and HBS scaffolds.
Notes: Antibacterial activity of native CO, CGF and HBS with different ratios of CGF against (*G* +/-) bacteria. Data were represented as the mean ± SD, n=3; (*p<0.01, **p<0.0001); ns: no significant differences.

4. Conclusions

A new cell carrier for tissue engineering purposes was synthesized using the CO-g-chitosan-glucan complex fibers hybrid biocomposite scaffold (CO-g-CSGCF-HBS). Chemical interaction between CO and CSGCF was confirmed by ATR-FTIR, TGA, SEM, and X-ray diffraction. The obtained results, the formation of new ester bonds and improved crystallinity and thermal stability of HBS. The HBS exhibited significant hydrolytic stability and mechanical properties in comparison with net CO. From the SEM spectra, CSGCF adhered to the surface of the CO fibrils. CO-g-CSGCF-HBS exhibited a significant improvement in the adhesion, viability, and proliferation of *MSCs* compared to the control scaffolds, CO and CSGCF scaffolds. HBS exhibited excellent antibacterial activity against different types of bacteria (*G* -/+) compared with the control sample. The hybrid biocomposite scaffold showed a unique property, such as high swelling percentage, excellent antibacterial activity, no cytotoxicity, and high biocompatible properties with improving mechanical and hydrolytic stability. We believe that CO-g-CSGCF-HBS could be employed to control rug delivery purposes and as a new cell carrier for soft/hard tissue regeneration.

Supporting information

Characterization

Solid-state NMR spectroscopy*:* ^{13}C CP/MAS NMR spectra are recorded on a Bruker AVANCE III HD spectrometer (Larmor frequencies $\nu^{13}C$ = 125.783 MHz) using a 3.2 mm MAS probe. The spinning speed of the rotor sample is 20 kHz. The number of scans for the accumulation of ^{13}C CP/MAS NMR spectra is 2048, the repetition delay is 5 s, and spinlock of 1 ms. During detection, the high-power dipolar decoupling (SPINAL 64) is used to eliminate strong heteronuclear dipolar couplings. The isotropic chemical shift of the ^{13}C-NMR scale is calibrated with glycine as an external standard (176.03 ppm to carbonyl signal). In all cases, the dried samples are placed on the ZrO_2 rotors and all NMR experiments are performed at 303 K. Temperature calibration was performed on $Pb(NO_3)_2$. The molecular weight (mol) of chitin units was calculated according to the following equation. **1**.

$$mol\%(N-acetylglucosamine) = \frac{I_{C3}}{(I_{C1}+I_{C2}+I_{C3}+I_{C4}+I_{C5}+I_{C6})/6} \times 100 \qquad (\mathbf{1})$$

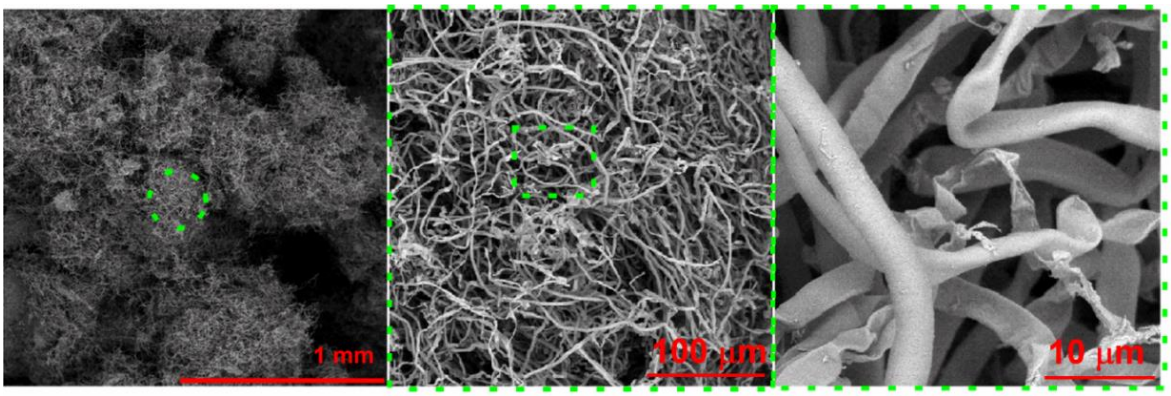

Fig.S1. SEM of native chitosan-glucan complex fiber (CGF) before the freeze-drying process.

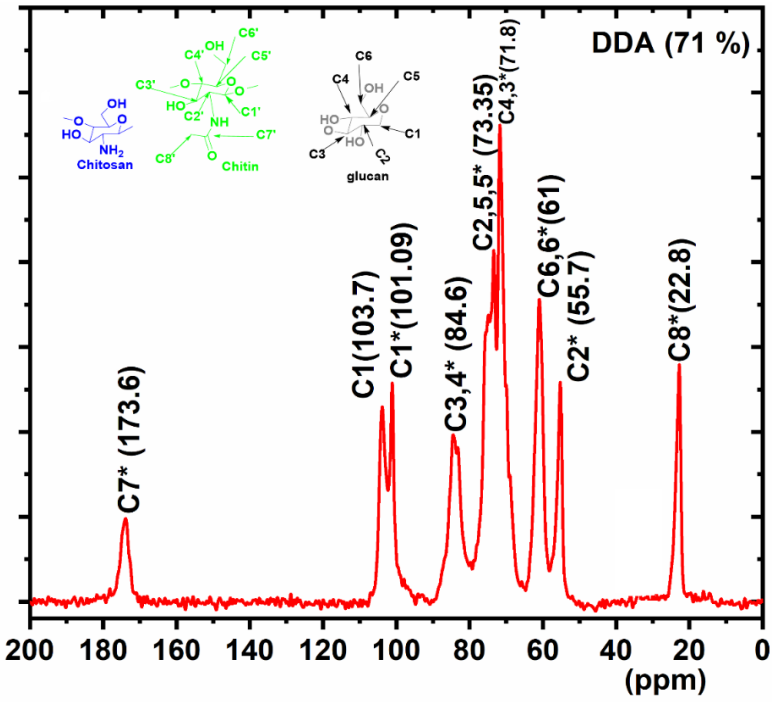

Fig. S2. Solid ^{13}C CP/MAS-NMR spectrum of CGF with a deacetylation degree (DDA) 71 %.

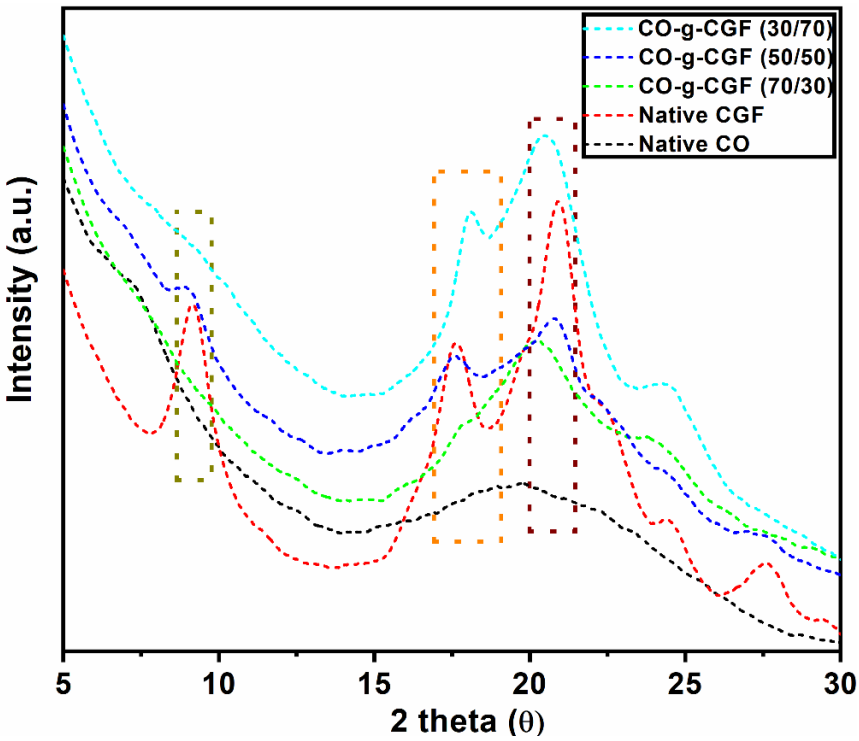

Fig. S3: X-ray diffraction patterns of native CO, CGF, and HBS scaffolds

References

References of thesis

[1] M. Rinaudo, Chitin and chitosan: Properties and applications, Progress in Polymer Science 31(7) (2006) 603-632.

[2] M.-K. Jang, B.-G. Kong, Y.-I. Jeong, C. Lee, J.-W. Nah, Physicochemical characterization of ?-chitin, ?-chitin, and ?-chitin separated from natural resources, Journal of Polymer Science Part A: Polymer Chemistry 42 (2004) 3423-3432.

[3] S. Caveney, J.W.S. Pringle, Cuticle reflectivity and optical activity in scarab beetles: the role of uric acid, Proceedings of the Royal Society of London. Series B. Biological Sciences 178(1051) (1971) 205-225.

[4] M.A. Elgadir, M.S. Uddin, S. Ferdosh, A. Adam, A.J.K. Chowdhury, M.Z.I. Sarker, Impact of chitosan composites and chitosan nanoparticle composites on various drug delivery systems: A review, Journal of Food and Drug Analysis 23(4) (2015) 619-629.

[5] A.S. Aly, A.M. Abdel-Mohsen, A. Hebeish, Innovative multifinishing using chitosan-O-PEG graft copolymer/citric acid aqueous system for preparation of medical textiles, The Journal of The Textile Institute 101(1) (2010) 76-90.

[6] R.M. Abdel-Rahman, V. Vishakha, I. Kelnar, J. Jancar, A.M. Abdel-Mohsen, Synergistic performance of collagen-g-chitosan-glucan fiber biohybrid scaffold with tunable properties, International Journal of Biological Macromolecules 202 (2022) 671-680.

[7] A.S. Aly, A.M. Abdel-Mohsen, R. Hrdina, A. Abou-Okeil, Preparation and Characterization of Polyethylene Glycol/Dimethyl Siloxane Adduct and Its Utilization as Finishing Agent for Cotton Fabric, Journal of Natural Fibers 8(3) (2011) 176-188.

[8] J.-B. Zeng, Y.-S. He, S.-L. Li, Y.-Z. Wang, Chitin Whiskers: An Overview, Biomacromolecules 13(1) (2012) 1-11.

[9] R.M. Abdelrahman, A.M. Abdel-Mohsen, M. Zboncak, J. Frankova, P. Lepcio, L. Kobera, M. Steinhart, D. Pavlinak, Z. Spotaz, R. Sklenářévá, J. Brus, J. Jancar, Hyaluronan biofilms reinforced with partially deacetylated chitin nanowhiskers: Extraction, fabrication, in-vitro and antibacterial properties of advanced nanocomposites, Carbohydrate Polymers 235 (2020) 115951.

[10] A.M. Abdel-Mohsen, J. Jancar, D. Massoud, Z. Fohlerova, H. Elhadidy, Z. Spotz, A. Hebeish, Novel chitin/chitosan-glucan wound dressing: Isolation, characterization, antibacterial activity and wound healing properties, International Journal of Pharmaceutics 510(1) (2016) 86-99.

[11] H. Sashiwa, S.-i. Aiba, Chemically modified chitin and chitosan as biomaterials, Progress in Polymer Science 29(9) (2004) 887-908.

[12] K. Kurita, Controlled functionalization of the polysaccharide chitin, Progress in Polymer Science 26(9) (2001) 1921-1971.

[13] F. Gaill, J. Persson, J. Sugiyama, R. Vuong, H. Chanzy, The chitin system in the tubes of deep sea hydrothermal vent worms, Journal of Structural Biology 109(2) (1992) 116-128.

[14] A.M. Abdel-Mohsen, A.S. Aly, R. Hrdina, A.S. Montaser, A. Hebeish, Biomedical Textiles Through Multifunctioalization of Cotton Fabrics Using Innovative Methoxypolyethylene Glycol-N-Chitosan Graft Copolymer, Journal of Polymers and the Environment 20(1) (2012) 104-116.

[15] J.D. Goodrich, W.T. Winter, α-Chitin Nanocrystals Prepared from Shrimp Shells and Their Specific Surface Area Measurement, Biomacromolecules 8(1) (2007) 252-257.

[16] R.M. Abdel-Rahman, A.M. Abdel-Mohsen, J. Frankova, F. Piana, L. Kalina, V. Gajdosova, L. Kapralkova, M.A. Thottappali, J. Jancar, Self-Assembled Hydrogel Membranes with Structurally Tunable Mechanical and Biological Properties, Biomacromolecules 25(6) (2024) 3449-3463.

[17] J. Li, J.-F. Revol, R.H. Marchessault, Effect of degree of deacetylation of chitin on the properties of chitin crystallites, Journal of Applied Polymer Science 65(2) (1997) 373-380.

[18] N. Yaghobi, F. Hormozi, Multistage deacetylation of chitin: Kinetics study, Carbohydrate Polymers 81(4) (2010) 892-896.
[19] M.N.V.R. Kumar, R.A.A. Muzzarelli, C. Muzzarelli, H. Sashiwa, A.J. Domb, Chitosan Chemistry and Pharmaceutical Perspectives, Chemical Reviews 104(12) (2004) 6017-6084.
[20] M. Larsson, W.-C. Huang, M.-H. Hsiao, Y.-J. Wang, M. Nydén, S.-H. Chiou, D.-M. Liu, Biomedical applications and colloidal properties of amphiphilically modified chitosan hybrids, Progress in Polymer Science 38(9) (2013) 1307-1328.
[21] Q. Song, Z. Wang, D. Xu, S. Liu, H. Liu, K. Zhang, Self-assembly of polysaccharide nanocrystals: from aggregation in suspensions to optical materials, Progress in Polymer Science 148 (2024) 101768.
[22] F.M. Kerton, Y. Liu, K.W. Omari, K. Hawboldt, Green chemistry and the ocean-based biorefinery, Green Chemistry 15(4) (2013) 860-871.
[23] B. Moussian, Chitin: Structure, Chemistry and Biology, Advances in experimental medicine and biology 1142 (2019) 5-18.
[24] N. Yan, X. Chen, Sustainability: Don't waste seafood waste, Nature 524(7564) (2015) 155-7.
[25] G.S. Watson, B.W. Cribb, J.A. Watson, How Micro/Nanoarchitecture Facilitates Anti-Wetting: An Elegant Hierarchical Design on the Termite Wing, ACS Nano 4(1) (2010) 129-136.
[26] R.H. Siddique, G. Gomard, H. Hölscher, The role of random nanostructures for the omnidirectional anti-reflection properties of the glasswing butterfly, Nature Communications 6(1) (2015) 6909.
[27] A. Miserez, T. Schneberk, C. Sun, F.W. Zok, J.H. Waite, The transition from stiff to compliant materials in squid beaks, Science (New York, N.Y.) 319(5871) (2008) 1816-9.
[28] H.N. Salvatierra, E.L. Regner, M.D. Baigorí, L.M. Pera, Orchestration an extracellular lipase production from Aspergillus niger MYA 135: biomass morphology and fungal physiology, AMB Express 11(1) (2021) 42.
[29] S.A. Lachke, S. Joly, K. Daniels, D.R. Soll, Phenotypic switching and filamentation in Candida glabrata, Microbiology (Reading, England) 148(Pt 9) (2002) 2661-2674.
[30] P. Orlean, Architecture and biosynthesis of the Saccharomyces cerevisiae cell wall, Genetics 192(3) (2012) 775-818.
[31] H. Merzendorfer, The cellular basis of chitin synthesis in fungi and insects: common principles and differences, European journal of cell biology 90(9) (2011) 759-69.
[32] F. Freitas, C. Roca, M. Reis, Fungi as Sources of Polysaccharides for Pharmaceutical and Biomedical Applications, 2015, pp. 61-103.
[33] T. Stalhberger, C. Simenel, C. Clavaud, V.G. Eijsink, R. Jourdain, M. Delepierre, J.P. Latgé, L. Breton, T. Fontaine, Chemical organization of the cell wall polysaccharide core of Malassezia restricta, The Journal of biological chemistry 289(18) (2014) 12647-56.
[34] D.F. Araújo, I. Ferreira, C. Torres, L. Neves, F. Freitas, Chitinous polymers: extraction from fungal sources, characterization and processing towards value-added applications, Journal of Chemical Technology & Biotechnology 95 (2020).
[35] C.E. Bracker, J. Ruiz-Herrera, S. Bartnicki-Garcia, Structure and transformation of chitin synthetase particles (chitosomes) during microfibril synthesis in vitro, Proceedings of the National Academy of Sciences of the United States of America 73(12) (1976) 4570-4.
[36] S. Bartnicki-Garcia, Chitosomes: Past, present and future, FEMS yeast research 6 (2006) 957-65.
[37] H. Merzendorfer, L. Zimoch, Chitin metabolism in insects: structure, function and regulation of chitin synthases and chitinases, The Journal of experimental biology 206(Pt 24) (2003) 4393-412.

[38] W.M.F.B.W. Nawawi, M. Jones, R.J. Murphy, K.-Y. Lee, E. Kontturi, A. Bismarck, Nanomaterials Derived from Fungal Sources—Is It the New Hype?, Biomacromolecules 21(1) (2020) 30-55.
[39] M. Jones, K. Weiland, M. Kujundzic, J. Theiner, H. Kählig, E. Kontturi, S. John, A. Bismarck, A. Mautner, Waste-Derived Low-Cost Mycelium Nanopapers with Tunable Mechanical and Surface Properties, Biomacromolecules 20(9) (2019) 3513-3523.
[40] P. Veronico, L.J. Gray, J.T. Jones, P. Bazzicalupo, S. Arbucci, M.R. Cortese, M. Di Vito, C. De Giorgi, Nematode chitin synthases: gene structure, expression and function in Caenorhabditis elegans and the plant parasitic nematode Meloidogyne artiellia, Molecular genetics and genomics : MGG 266(1) (2001) 28-34.
[41] S.E. Reynolds, The mechanical properties of the abdominal cuticle of Rhodnius larvae, The Journal of experimental biology 62(1) (1975) 69-80.
[42] C. Roncero, Y. Sánchez, Cell separation and the maintenance of cell integrity during cytokinesis in yeast: the assembly of a septum, Yeast (Chichester, England) 27(8) (2010) 521-30.
[43] A.M. Salaberria, J. Labidi, S.C.M. Fernandes, Chitin nanocrystals and nanofibers as nano-sized fillers into thermoplastic starch-based biocomposites processed by melt-mixing, Chemical Engineering Journal 256 (2014) 356-364.
[44] P. Ang-atikarnkul, A. Watthanaphanit, R. Rujiravanit, Fabrication of cellulose nanofiber/chitin whisker/silk sericin bionanocomposite sponges and characterizations of their physical and biological properties, Composites Science and Technology 96 (2014) 88-96.
[45] R.R. Mouriño-Pérez, M. Riquelme, Recent advances in septum biogenesis in Neurospora crassa, Advances in genetics 83 (2013) 99-134.
[46] H.-O. Fabritius, C. Sachs, P. Romano Triguero, D. Raabe, Influence of Structural Principles on the Mechanics of a Biological Fiber-Based Composite Material with Hierarchical Organization: The Exoskeleton of the Lobster Homarus americanus, Advanced Materials 21 (2009) 391-400.
[47] L.K. Grunenfelder, S. Herrera, D. Kisailus, Crustacean-derived biomimetic components and nanostructured composites, Small (Weinheim an der Bergstrasse, Germany) 10(16) (2014) 3207-32.
[48] S. Ling, D.L. Kaplan, M.J. Buehler, Nanofibrils in nature and materials engineering, Nature reviews. Materials 3(4) (2018).
[49] N. Suksangpanya, N.A. Yaraghi, D. Kisailus, P. Zavattieri, Twisting cracks in Bouligand structures, Journal of the mechanical behavior of biomedical materials 76 (2017) 38-57.
[50] J.C. Weaver, G.W. Milliron, A. Miserez, K. Evans-Lutterodt, S. Herrera, I. Gallana, W.J. Mershon, B. Swanson, P. Zavattieri, E. DiMasi, D. Kisailus, The stomatopod dactyl club: a formidable damage-tolerant biological hammer, Science (New York, N.Y.) 336(6086) (2012) 1275-80.
[51] F. Barthelat, Z. Yin, M.J. Buehler, Structure and mechanics of interfaces in biological materials, Nature Reviews Materials 1(4) (2016) 16007.
[52] S. Nikolov, M. Petrov, L. Lymperakis, M. Friák, C. Sachs, H.O. Fabritius, D. Raabe, J. Neugebauer, Revealing the design principles of high-performance biological composites using ab initio and multiscale simulations: the example of lobster cuticle, Advanced materials (Deerfield Beach, Fla.) 22(4) (2010) 519-26.
[53] J. Rivera, M.S. Hosseini, D. Restrepo, S. Murata, D. Vasile, D.Y. Parkinson, H.S. Barnard, A. Arakaki, P. Zavattieri, D. Kisailus, Toughening mechanisms of the elytra of the diabolical ironclad beetle, Nature 586(7830) (2020) 543-548.
[54] H. Merzendorfer, Insect chitin synthases: a review, Journal of comparative physiology. B, Biochemical, systemic, and environmental physiology 176(1) (2006) 1-15.

[55] L. Bai, L. Liu, M. Esquivel, B.L. Tardy, S. Huan, X. Niu, S. Liu, G. Yang, Y. Fan, O.J. Rojas, Nanochitin: Chemistry, Structure, Assembly, and Applications, Chem Rev 122(13) (2022) 11604-11674.
[56] Y. Ogawa, R. Hori, U.-J. Kim, M. Wada, Elastic modulus in the crystalline region and the thermal expansion coefficients of α-chitin determined using synchrotron radiated X-ray diffraction, Carbohydrate Polymers 83(3) (2011) 1213-1217.
[57] C. Valverde Serrano, H. Leemreize, B. Bar-On, F.G. Barth, P. Fratzl, E. Zolotoyabko, Y. Politi, Ordering of protein and water molecules at their interfaces with chitin nano-crystals, Journal of Structural Biology 193(2) (2016) 124-131.
[58] Y. Ogawa, S. Kimura, M. Wada, Electron diffraction and high-resolution imaging on highly-crystalline β-chitin microfibril, Journal of Structural Biology 176(1) (2011) 83-90.
[59] Y. Saito, J.L. Putaux, T. Okano, F. Gaill, H. Chanzy, Structural Aspects of the Swelling of β Chitin in HCl and its Conversion into α Chitin, Macromolecules 30(13) (1997) 3867-3873.
[60] Y. Noishiki, H. Takami, Y. Nishiyama, M. Wada, S. Okada, S. Kuga, Alkali-Induced Conversion of β-Chitin to α-Chitin, Biomacromolecules 4 (2003).
[61] G.L. Clark, A.F. Smith, X-ray Diffraction Studies of Chitin, Chitosan, and Derivatives, The Journal of Physical Chemistry 40(7) (1936) 863-879.
[62] K.M. Rudall, The Chitin/Protein Complexes of Insect Cuticles, Advances in Insect Physiology 1 (1963) 257-313.
[63] M. Kaya, M. Mujtaba, H. Ehrlich, A.M. Salaberria, T. Baran, C.T. Amemiya, R. Galli, L. Akyuz, I. Sargin, J. Labidi, On chemistry of γ-chitin, Carbohydr Polym 176 (2017) 177-186.
[64] C. Pillai, W. Paul, C.P. Sharma, Chitin and Chitosan Polymers: Chemistry, Solubility and Fiber Formation, Progress in Polymer Science (2009) 641-678.
[65] H. Yi, L.Q. Wu, W.E. Bentley, R. Ghodssi, G.W. Rubloff, J.N. Culver, G.F. Payne, Biofabrication with chitosan, Biomacromolecules 6(6) (2005) 2881-94.
[66] B. Chen, K. Sun, K. Zhang, Rheological properties of chitin/lithium chloride, N,N-dimethyl acetamide solutions, Carbohydrate Polymers 58 (2004) 65-69.
[67] J. Chang, K. Chang, M.-L. Tsai, Liquid-crystalline behavior of chitosan in malic acid, Journal of Applied Polymer Science - J APPL POLYM SCI 105 (2007) 2670-2675.
[68] M. Rinaudo, Chitin and Chitosan—General Properties and Applications, Progress in Polymer Science 38 (2007) 603-632.
[69] L. Bai, L. Liu, M. Esquivel, B.L. Tardy, S. Huan, X. Niu, S. Liu, G. Yang, Y. Fan, O.J. Rojas, Nanochitin: Chemistry, Structure, Assembly, and Applications, Chemical Reviews 122(13) (2022) 11604-11674.
[70] J.J. Thevarajah, M.P. Van Leeuwen, H. Cottet, P. Castignolles, M. Gaborieau, Determination of the distributions of degrees of acetylation of chitosan, Int J Biol Macromol 95 (2017) 40-48.
[71] R.M. Abdel-Rahman, R. Hrdina, A.M. Abdel-Mohsen, M.M.G. Fouda, A.Y. Soliman, F.K. Mohamed, K. Mohsin, T.D. Pinto, Chitin and chitosan from Brazilian Atlantic Coast: Isolation, characterization and antibacterial activity, International Journal of Biological Macromolecules 80 (2015) 107-120.
[72] S. Ifuku, H. Saimoto, Chitin nanofibers: preparations, modifications, and applications, Nanoscale 4(11) (2012) 3308-3318.
[73] L.C. Carvalho, F. Queda, C.V. Santos, M.M. Marques, Selective Modification of Chitin and Chitosan: En Route to Tailored Oligosaccharides, Chemistry, an Asian journal 11(24) (2016) 3468-3481.
[74] K. Gopalan Nair, A. Dufresne, Crab shell chitin whisker reinforced natural rubber nanocomposites. 1. Processing and swelling behavior, Biomacromolecules 4(3) (2003) 657-65.
[75] I. Anastopoulos, A. Bhatnagar, D.N. Bikiaris, G.Z. Kyzas, Chitin Adsorbents for Toxic Metals: A Review, International journal of molecular sciences 18(1) (2017).

[76] J. McKittrick, P.Y. Chen, Structural Biological Materials: Critical Mechanics-Materials Connections, Science (New York, N.Y.) 339 (2013) 773-9.
[77] I. Younes, M. Rinaudo, Chitin and chitosan preparation from marine sources. Structure, properties and applications, Marine drugs 13(3) (2015) 1133-74.
[78] H. El Knidri, R. Belaabed, A. Addaou, A. Laajeb, A. Lahsini, Extraction, chemical modification and characterization of chitin and chitosan, Int J Biol Macromol 120(Pt A) (2018) 1181-1189.
[79] K. Nyein Aye, W. Stevens, Improved chitin production by pretreatment of shrimp shells, Journal of Chemical Technology and Biotechnology 79 (2004) 421-425.
[80] X. Hu, Z. Tian, X. Li, S. Wang, H. Pei, H. Sun, Z. Zhang, Green, Simple, and Effective Process for the Comprehensive Utilization of Shrimp Shell Waste, ACS Omega 5(30) (2020) 19227-19235.
[81] D. Ramamoorthy, R. Dhamodharan, Pre-treatment in Hot Glycerol for Facile and Green Separation of Chitin from Prawn Shell Waste, ACS Sustainable Chemistry & Engineering 6 (2017).
[82] M. Borić, H. Puliyalil, U. Novak, B. Likozar, An intensified atmospheric plasma-based process for the isolation of the chitin biopolymer from waste crustacean biomass, Green Chemistry 20(6) (2018) 1199-1204.
[83] H. El Knidri, J. Dahmani, A. Addaou, A. Laajeb, A. Lahsini, Rapid and efficient extraction of chitin and chitosan for scale-up production: Effect of process parameters on deacetylation degree and molecular weight, Int J Biol Macromol 139 (2019) 1092-1102.
[84] M. Shams, S. Ifuku, M. Nogi, T. Oku, H. Yano, Fabrication of optically transparent chitin nanocomposites, Applied Physics A 102 (2011) 325-331.
[85] O.I. Bogdanova, A.P. Istomina, N.A. Glushkova, S.I. Belousov, N.M. Kuznetsov, D.K. Polyakov, S.N. Malakhov, S.V. Krasheninnikov, A.V. Bakirov, R.A. Kamyshinsky, A.L. Vasiliev, D.R. Streltsov, S.N. Chvalun, Effect of exfoliating agent on rheological behavior of β-chitin fibrils in aqueous suspensions and on mechanical properties of poly(acrylic acid)/β-chitin composites, Int J Biol Macromol 139 (2019) 161-169.
[86] Y. Lu, Q. Sun, X. She, Y. Xia, Y. Liu, J. Li, D. Yang, Fabrication and characterisation of α-chitin nanofibers and highly transparent chitin films by pulsed ultrasonication, Carbohydrate Polymers 98(2) (2013) 1497-1504.
[87] A. Isogai, Emerging Nanocellulose Technologies: Recent Developments, Advanced Materials 33(28) (2021) 2000630.
[88] K. Tanaka, K. Yamamoto, J. Kadokawa, Facile nanofibrillation of chitin derivatives by gas bubbling and ultrasonic treatments in water, Carbohydr Res 398 (2014) 25-30.
[89] Y. Fan, T. Saito, A. Isogai, Preparation of chitin nanofibers from squid pen beta-chitin by simple mechanical treatment under acid conditions, Biomacromolecules 9(7) (2008) 1919-23.
[90] S. Ifuku, R. Nomura, M. Morimoto, H. Saimoto, Preparation of Chitin Nanofibers from Mushrooms, Materials 4(8) (2011) 1417-1425.
[91] S. Ifuku, M. Nogi, K. Abe, M. Yoshioka, M. Morimoto, H. Saimoto, H. Yano, Preparation of Chitin Nanofibers with a Uniform Width as α-Chitin from Crab Shells, Biomacromolecules 10(6) (2009) 1584-1588.
[92] H.-P. Zhao, X.-Q. Feng, H. Gao, Ultrasonic technique for extracting nanofibers from nature materials, Applied Physics Letters 90(7) (2007).
[93] Q. Wu, E. Jungstedt, M. Šoltésová, N.E. Mushi, L.A. Berglund, High strength nanostructured films based on well-preserved β-chitin nanofibrils, Nanoscale 11(22) (2019) 11001-11011.
[94] N.E. Mushi, N. Butchosa, M. Salajkova, Q. Zhou, L.A. Berglund, Nanostructured membranes based on native chitin nanofibers prepared by mild process, Carbohydr Polym 112 (2014) 255-63.

[95] S. Ifuku, T. Urakami, H. Izawa, M. Morimoto, H. Saimoto, Preparation of a protein–chitin nanofiber complex from crab shells and its application as a reinforcement filler or substrate for biomineralization, RSC Advances 5(79) (2015) 64196-64201.
[96] A. Martinez Salaberria, S.C.M. Fernandes, R. Herrera Diaz, J. Labidi, Processing of α-chitin nanofibers by dynamic high pressure homogenization: Characterization and antifungal activity against A. niger, Carbohydrate Polymers 116 (2015) 286-291.
[97] Q. Wu, N.E. Mushi, L.A. Berglund, High-Strength Nanostructured Films Based on Well-Preserved α-Chitin Nanofibrils Disintegrated from Insect Cuticles, Biomacromolecules 21(2) (2020) 604-612.
[98] J. Wu, K. Zhang, N. Girouard, J.C. Meredith, Facile route to produce chitin nanofibers as precursors for flexible and transparent gas barrier materials, Biomacromolecules 15(12) (2014) 4614-20.
[99] Y. Habibi, L. Lucia, O. Rojas, Cellulose Nanocrystals: Chemistry, Self-Assembly, and Applications, Chemical reviews 110 (2010) 3479-500.
[100] J.B. Zeng, Y.S. He, S.L. Li, Y.Z. Wang, Chitin whiskers: an overview, Biomacromolecules 13(1) (2012) 1-11.
[101] N. Lin, J. Huang, A. Dufresne, Preparation, properties and applications of polysaccharide nanocrystals in advanced functional nanomaterials: a review, Nanoscale 4(11) (2012) 3274-3294.
[102] Y. Yuan, S. Hong, H. Lian, K. Zhang, H. Liimatainen, Comparison of acidic deep eutectic solvents in production of chitin nanocrystals, Carbohydrate Polymers 236 (2020) 116095.
[103] R.H. Marchessault, F.F. Morehead, N.M. Walter, Liquid Crystal Systems from Fibrillar Polysaccharides, Nature 184(4686) (1959) 632-633.
[104] A.A. Oun, J.W. Rhim, Effect of isolation methods of chitin nanocrystals on the properties of chitin-silver hybrid nanoparticles, Carbohydr Polym 197 (2018) 349-358.
[105] L. Liqin, F. Tunjung Seta, X. An, J. Yang, W. Zhang, H. Dai, H. Cao, Q. Xu, H. Liu, Facile isolation of colloidal stable chitin nano-crystals from Metapenaeus ensis shell via solid maleic acid hydrolysis and their application for synthesis of silver nanoparticles, Cellulose 27 (2020) 1-23.
[106] Y. Lu, L. Weng, L. Zhang, Morphology and properties of soy protein isolate thermoplastics reinforced with chitin whiskers, Biomacromolecules 5(3) (2004) 1046-51.
[107] S. Phongying, S.-i. Aiba, S. Chirachanchai, Direct chitosan nanoscaffold formation via chitin whiskers, Polymer 48(1) (2007) 393-400.
[108] A. Narkevicius, L.M. Steiner, R.M. Parker, Y. Ogawa, B. Frka-Petesic, S. Vignolini, Controlling the Self-Assembly Behavior of Aqueous Chitin Nanocrystal Suspensions, Biomacromolecules 20(7) (2019) 2830-2838.
[109] P.R. Chang, R. Jian, J. Yu, X. Ma, Starch-based composites reinforced with novel chitin nanoparticles, Carbohydrate Polymers 80(2) (2010) 420-425.
[110] G.A. Di Lullo, S.M. Sweeney, J. Korkko, L. Ala-Kokko, J.D. San Antonio, Mapping the ligand-binding sites and disease-associated mutations on the most abundant protein in the human, type I collagen, The Journal of biological chemistry 277(6) (2002) 4223-31.
[111] A.M. Abdel-Mohsen, R.M. Abdel-Rahman, I. Kubena, L. Kobera, Z. Spotz, M. Zboncak, R. Prikryl, J. Brus, J. Jancar, Chitosan-glucan complex hollow fibers reinforced collagen wound dressing embedded with aloe vera. Part I: Preparation and characterization, Carbohydrate Polymers 230 (2020) 115708.
[112] A.M. Abdel-Mohsen, J. Frankova, R.M. Abdel-Rahman, A.A. Salem, N.M. Sahffie, I. Kubena, J. Jancar, Chitosan-glucan complex hollow fibers reinforced collagen wound dressing embedded with aloe vera. II. Multifunctional properties to promote cutaneous wound healing, International Journal of Pharmaceutics 582 (2020) 119349.

[113] W. Friess, Collagen – biomaterial for drug delivery1Dedicated to Professor Dr. Eberhard Nürnberg, Friedrich-Alexander-Universität Erlangen-Nürnberg, on the occasion of his 70th birthday.1, European Journal of Pharmaceutics and Biopharmaceutics 45(2) (1998) 113-136.
[114] S. Chattopadhyay, R.T. Raines, Review collagen-based biomaterials for wound healing, Biopolymers 101(8) (2014) 821-33.
[115] V.R. Sherman, W. Yang, M.A. Meyers, The materials science of collagen, Journal of the mechanical behavior of biomedical materials 52 (2015) 22-50.
[116] K. Gelse, E. Pöschl, T. Aigner, Collagens—structure, function, and biosynthesis, Advanced Drug Delivery Reviews 55(12) (2003) 1531-1546.
[117] A. Pissarenko, M.A. Meyers, The materials science of skin: Analysis, characterization, and modeling, Progress in Materials Science 110 (2020) 100634.
[118] S. Ricard-Blum, The collagen family, Cold Spring Harbor perspectives in biology 3(1) (2011) a004978.
[119] L. Cen, W. Liu, L. Cui, W. Zhang, Y. Cao, Collagen Tissue Engineering: Development of Novel Biomaterials and Applications, Pediatric Research 63(5) (2008) 492-496.
[120] J.J. Wu, P.E. Woods, D.R. Eyre, Identification of cross-linking sites in bovine cartilage type IX collagen reveals an antiparallel type II-type IX molecular relationship and type IX to type IX bonding, The Journal of biological chemistry 267(32) (1992) 23007-14.
[121] H.P. Bächinger, K. Mizuno, J. Vranka, S. Boudko, Collagen Formation and Structure, 2010, pp. 469-530.
[122] M. van der Rest, R. Mayne, Type IX collagen proteoglycan from cartilage is covalently cross-linked to type II collagen, Journal of Biological Chemistry 263(4) (1988) 1615-1618.
[123] C.-W. Franzke, K. Tasanen, H. Schumann, L. Bruckner-Tuderman, Collagenous transmembrane proteins: collagen XVII as a prototype, Matrix biology : journal of the International Society for Matrix Biology 22 4 (2003) 299-309.
[124] K.E. Kadler, C. Baldock, J. Bella, R.P. Boot-Handford, Collagens at a glance, Journal of Cell Science 120(12) (2007) 1955-1958.
[125] E.J.W. Verwey, Theory of the Stability of Lyophobic Colloids, The Journal of Physical and Colloid Chemistry 51(3) (1947) 631-636.
[126] W. Yang, V. Sherman, B. Gludovatz, M. Mackey, E. Zimmermann, E. Chang, E. Schaible, Z. Qin, M. Buehler, R. Ritchie, Protective Role of Arapaima gigas Fish Scales: Structure and Mechanical Behavior, Acta Biomaterialia 10 (2014) 3599-3614.
[127] S. Kimura, Y. Takema, M. Kubota, Octopus skin collagen. Isolation and characterization of collagen comprising two distinct alpha chains, Journal of Biological Chemistry 256(24) (1981) 13230-13234.
[128] C. Dong, Y. Lv, Application of Collagen Scaffold in Tissue Engineering: Recent Advances and New Perspectives, Polymers 8(2) (2016).
[129] P.D. Toman, F. Pieper, N. Sakai, C. Karatzas, E. Platenburg, I. de Wit, C. Samuel, A. Dekker, G.A. Daniels, R.A. Berg, G.J. Platenburg, Production of recombinant human type I procollagen homotrimer in the mammary gland of transgenic mice, Transgenic research 8(6) (1999) 415-27.
[130] G. Chandrakasan, D.A. Torchia, K.A. Piez, Preparation of intact monomeric collagen from rat tail tendon and skin and the structure of the nonhelical ends in solution, Journal of Biological Chemistry 251(19) (1976) 6062-6067.
[131] J.H. Bowes, R.G. Elliott, J.A. Moss, The composition of collagen and acid-soluble collagen of bovine skin, The Biochemical journal 61(1) (1955) 143-50.
[132] J.W. Smith, Molecular Pattern in Native Collagen, Nature 219(5150) (1968) 157-158.
[133] A. Cooper, Thermodynamic studies of the assembly in vitro of native collagen fibrils, The Biochemical journal 118(3) (1970) 355-365.

[134] F.S. Steven, H.V. Thomas, Preparation of insoluble collagen from human cartilage (Short Communication), Biochemical Journal 135 (1973) 245-247.
[135] R. Sztrolovics, M. Van Der Rest, P.J. Roughley, Identification of type I collagen gene polymorphisms: Tolerance of sequence variation at an α2(I) Helix Y position, Matrix Biology 14(1) (1994) 9-19.
[136] C.H. Lee, A. Singla, Y. Lee, Biomedical applications of collagen, International Journal of Pharmaceutics 221(1) (2001) 1-22.
[137] C. Gao, E. Harvey, M. Chua, B. Chen, F. Jiang, Y. Liu, A. Li, H. Wang, J. Henderson, MSC-seeded dense collagen scaffolds with a bolus dose of VEGF promote healing of large bone defects, European cells & materials 26 (2013) 195-207.
[138] J. Glowacki, S. Mizuno, Collagen scaffolds for tissue engineering, Biopolymers 89(5) (2008) 338-344.
[139] K.M. Pawelec, A. Husmann, S.M. Best, R.E. Cameron, A design protocol for tailoring ice-templated scaffold structure, Journal of The Royal Society Interface 11(92) (2014) 20130958.
[140] J. Ashworth, M. Mehr, P. Buxton, S. Best, R. Cameron, Cell Invasion in Collagen Scaffold Architectures Characterized by Percolation Theory, Advanced healthcare materials 4 (2015).
[141] P. Divakar, K. Yin, U.G.K. Wegst, Anisotropic freeze-cast collagen scaffolds for tissue regeneration: How processing conditions affect structure and properties in the dry and fully hydrated states, Journal of the mechanical behavior of biomedical materials 90 (2019) 350-364.
[142] C.N. Grover, R.E. Cameron, S.M. Best, Investigating the morphological, mechanical and degradation properties of scaffolds comprising collagen, gelatin and elastin for use in soft tissue engineering, Journal of the mechanical behavior of biomedical materials 10 (2012) 62-74.
[143] C.N. Grover, J.H. Gwynne, N. Pugh, S. Hamaia, R.W. Farndale, S.M. Best, R.E. Cameron, Crosslinking and composition influence the surface properties, mechanical stiffness and cell reactivity of collagen-based films, Acta biomaterialia 8(8) (2012) 3080-3090.
[144] S. Macneil, Biomaterials for tissue engineering of skin, Materials Today 11 (2008).
[145] G. Monaco, R. Cholas, L. Salvatore, M. Madaghiele, A. Sannino, Sterilization of collagen scaffolds designed for peripheral nerve regeneration: Effect on microstructure, degradation and cellular colonization, Materials Science and Engineering: C 71 (2016).
[146] X. Duan, H. Sheardown, Dendrimer crosslinked collagen as a corneal tissue engineering scaffold: Mechanical properties and corneal epithelial cell interactions, Biomaterials 27(26) (2006) 4608-4617.
[147] L. Buttafoco, N.P. Boks, P. Engbers-Buijtenhuijs, D.W. Grijpma, A.A. Poot, P.J. Dijkstra, I. Vermes, J. Feijen, Porous hybrid structures based on P(DLLA-co-TMC) and collagen for tissue engineering of small-diameter blood vessels, Journal of Biomedical Materials Research Part B: Applied Biomaterials 79B(2) (2006) 425-434.
[148] J.M. McPherson, P.W. Ledger, S. Sawamura, A. Conti, S. Wade, H. Reihanian, D.G. Wallace, The preparation and physicochemical characterization of an injectable form of reconstituted, glutaraldehyde cross-linked, bovine corium collagen, Journal of Biomedical Materials Research 20(1) (1986) 79-92.
[149] D.G. Wallace, W. Rhee, H. Reihanian, G. Ksander, R. Lee, W.B. Braun, B.A. Weiss, B.B. Pharriss, Injectable cross-linked collagen with improved flow properties, Journal of Biomedical Materials Research 23(8) (1989) 931-945.
[150] S.L. Cusack, H.S. Minkowitz, M. Kuss, M. Jaros, L. Hemsen, A randomized, multicenter, pilot study comparing the efficacy and safety of a bupivacaine-collagen implant (XaraColl(®)) with the ON-Q PainBuster(®) Post-op Pain Relief System following open gynecological surgery, Journal of pain research 5 (2012) 453-61.

[151] G.J. Shaker, S. Ueda, J.A. LoCascio, J.V. Aquavella, Effect of a collagen shield on cat corneal epithelial wound healing, Investigative Ophthalmology & Visual Science 30(7) (1989) 1565-1568.
[152] S.J. Kew, J.H. Gwynne, D. Enea, R. Brookes, N. Rushton, S.M. Best, R.E. Cameron, Synthetic collagen fascicles for the regeneration of tendon tissue, Acta Biomaterialia 8(10) (2012) 3723-3731.
[153] S.J. Kew, J.H. Gwynne, D. Enea, M. Abu-Rub, A. Pandit, D. Zeugolis, R.A. Brooks, N. Rushton, S.M. Best, R.E. Cameron, Regeneration and repair of tendon and ligament tissue using collagen fibre biomaterials, Acta Biomater 7(9) (2011) 3237-47.
[154] C.N. McGhee, Pharmacokinetics of ophthalmic corticosteroids, The British journal of ophthalmology 76(11) (1992) 681-4.
[155] Z. Ruszczak, W. Friess, Collagen as a carrier for on-site delivery of antibacterial drugs, Advanced Drug Delivery Reviews 55(12) (2003) 1679-1698.
[156] A.M. Abdel-Mohsen, J. Jancar, R.M. Abdel-Rahman, L. Vojtek, P. Hyršl, M. Dušková, H. Nejezchlebová, A novel in situ silver/hyaluronan bio-nanocomposite fabrics for wound and chronic ulcer dressing: In vitro and in vivo evaluations, International Journal of Pharmaceutics 520(1) (2017) 241-253.
[157] R.M. Abdel-Rahman, A.M. Abdel-Mohsen, R. Hrdina, L. Burgert, Z. Fohlerova, D. Pavliňák, O.N. Sayed, J. Jancar, Wound dressing based on chitosan/hyaluronan/nonwoven fabrics: Preparation, characterization and medical applications, International Journal of Biological Macromolecules 89 (2016) 725-736.
[158] R.M. Abdel-Rahman, J. Frankova, R. Sklenarova, L. Kapralkova, I. Kelnar, A.M. Abdel-Mohsen, Hyaluronan/Zinc Oxide Nanocomposite-Based Membrane: Preparation, Characterization, and In Vitro and In Vivo Evaluation, ACS Applied Polymer Materials 4(10) (2022) 7723-7738.
[159] A.M. Abdel-Mohsen, D. Pavliňák, M. Čileková, P. Lepcio, R.M. Abdel-Rahman, J. Jančář, Electrospinning of hyaluronan/polyvinyl alcohol in presence of in-situ silver nanoparticles: Preparation and characterization, International Journal of Biological Macromolecules 139 (2019) 730-739.
[160] A.M. Abdel-Mohsen, R. Hrdina, L. Burgert, R.M. Abdel-Rahman, M. Hašová, D. Šmejkalová, M. Kolář, M. Pekar, A.S. Aly, Antibacterial activity and cell viability of hyaluronan fiber with silver nanoparticles, Carbohydrate Polymers 92(2) (2013) 1177-1187.
[161] A.M. Abdel-Mohsen, R. Hrdina, L. Burgert, G. Krylová, R.M. Abdel-Rahman, A. Krejčová, M. Steinhart, L. Beneš, Green synthesis of hyaluronan fibers with silver nanoparticles, Carbohydrate Polymers 89(2) (2012) 411-422.
[162] X. Zheng Shu, Y. Liu, F.S. Palumbo, Y. Luo, G.D. Prestwich, In situ crosslinkable hyaluronan hydrogels for tissue engineering, Biomaterials 25(7-8) (2004) 1339-48.
[163] T. Segura, B.C. Anderson, P.H. Chung, R.E. Webber, K.R. Shull, L.D. Shea, Crosslinked hyaluronic acid hydrogels: a strategy to functionalize and pattern, Biomaterials 26(4) (2005) 359-71.
[164] J. Kim, I.S. Kim, T.H. Cho, K.B. Lee, S.J. Hwang, G. Tae, I. Noh, S.H. Lee, Y. Park, K. Sun, Bone regeneration using hyaluronic acid-based hydrogel with bone morphogenic protein-2 and human mesenchymal stem cells, Biomaterials 28(10) (2007) 1830-7.
[165] K.Y. Lee, D.J. Mooney, Hydrogels for tissue engineering, Chem Rev 101(7) (2001) 1869-79.
[166] J.L. Drury, D.J. Mooney, Hydrogels for tissue engineering: scaffold design variables and applications, Biomaterials 24(24) (2003) 4337-51.
[167] J.A. Burdick, G.D. Prestwich, Hyaluronic acid hydrogels for biomedical applications, Advanced materials (Deerfield Beach, Fla.) 23(12) (2011) H41-56.
[168] A. Fakhari, C. Berkland, Applications and emerging trends of hyaluronic acid in tissue engineering, as a dermal filler and in osteoarthritis treatment, Acta Biomater 9(7) (2013) 7081-92.

[169] M.M.G. Fouda, A.M. Abdel-Mohsen, H. Ebaid, I. Hassan, J. Al-Tamimi, R.M. Abdel-Rahman, A. Metwalli, I. Alhazza, A. Rady, A. El-Faham, J. Jancar, Wound healing of different molecular weight of hyaluronan; in-vivo study, International Journal of Biological Macromolecules 89 (2016) 582-591.
[170] B.P. Toole, T.N. Wight, M.I. Tammi, Hyaluronan-cell interactions in cancer and vascular disease, The Journal of biological chemistry 277(7) (2002) 4593-6.
[171] P.W. Noble, Hyaluronan and its catabolic products in tissue injury and repair, Matrix Biol 21(1) (2002) 25-9.
[172] B.P. Toole, Hyaluronan in morphogenesis, Journal of internal medicine 242(1) (1997) 35-40.
[173] B. Oertli, X. Fan, R.P. Wüthrich, Characterization of CD44-mediated hyaluronan binding by renal tubular epithelial cells, Nephrology, dialysis, transplantation : official publication of the European Dialysis and Transplant Association - European Renal Association 13(2) (1998) 271-8.
[174] W.Y. Chen, G. Abatangelo, Functions of hyaluronan in wound repair, Wound repair and regeneration : official publication of the Wound Healing Society [and] the European Tissue Repair Society 7(2) (1999) 79-89.
[175] D.D. Allison, K.J. Grande-Allen, Review. Hyaluronan: a powerful tissue engineering tool, Tissue engineering 12(8) (2006) 2131-40.
[176] K.P. Vercruysse, D.M. Marecak, J.F. Marecek, G.D. Prestwich, Synthesis and in vitro degradation of new polyvalent hydrazide cross-linked hydrogels of hyaluronic acid, Bioconjugate chemistry 8(5) (1997) 686-94.
[177] Y. Luo, K.R. Kirker, G.D. Prestwich, Cross-linked hyaluronic acid hydrogel films: new biomaterials for drug delivery, Journal of controlled release : official journal of the Controlled Release Society 69(1) (2000) 169-84.
[178] Y. Liu, X. Zheng Shu, G.D. Prestwich, Biocompatibility and stability of disulfide-crosslinked hyaluronan films, Biomaterials 26(23) (2005) 4737-46.
[179] J. Baier Leach, K.A. Bivens, C.W. Patrick, Jr., C.E. Schmidt, Photocrosslinked hyaluronic acid hydrogels: natural, biodegradable tissue engineering scaffolds, Biotechnology and bioengineering 82(5) (2003) 578-89.
[180] J.A. Burdick, C. Chung, X. Jia, M.A. Randolph, R. Langer, Controlled degradation and mechanical behavior of photopolymerized hyaluronic acid networks, Biomacromolecules 6(1) (2005) 386-91.
[181] L. Cen, K.G. Neoh, Y. Li, E.T. Kang, Assessment of in vitro bioactivity of hyaluronic acid and sulfated hyaluronic acid functionalized electroactive polymer, Biomacromolecules 5(6) (2004) 2238-46.
[182] J.H. Collier, J.P. Camp, T.W. Hudson, C.E. Schmidt, Synthesis and characterization of polypyrrole-hyaluronic acid composite biomaterials for tissue engineering applications, J Biomed Mater Res 50(4) (2000) 574-84.
[183] J. Aigner, J. Tegeler, P. Hutzler, D. Campoccia, A. Pavesio, C. Hammer, E. Kastenbauer, A. Naumann, Cartilage tissue engineering with novel nonwoven structured biomaterial based on hyaluronic acid benzyl ester, J Biomed Mater Res 42(2) (1998) 172-81.
[184] A. Ramamurthi, I. Vesely, Evaluation of the matrix-synthesis potential of crosslinked hyaluronan gels for tissue engineering of aortic heart valves, Biomaterials 26(9) (2005) 999-1010.
[185] Y. Yeo, C.B. Highley, E. Bellas, T. Ito, R. Marini, R. Langer, D.S. Kohane, In situ cross-linkable hyaluronic acid hydrogels prevent post-operative abdominal adhesions in a rabbit model, Biomaterials 27(27) (2006) 4698-705.
[186] S.K. Kumar, B.C. Benicewicz, R.A. Vaia, K.I. Winey, 50th Anniversary Perspective: Are Polymer Nanocomposites Practical for Applications?, Macromolecules 50(3) (2017) 714-731.

[187] J. Jancar, J.F. Douglas, F.W. Starr, S.K. Kumar, P. Cassagnau, A.J. Lesser, S.S. Sternstein, M.J. Buehler, Current issues in research on structure–property relationships in polymer nanocomposites, Polymer 51(15) (2010) 3321-3343.
[188] L. David, V. Dulong, D. Le Cerf, L. Cazin, M. Lamacz, J.-P. Vannier, Hyaluronan hydrogel: An appropriate three-dimensional model for evaluation of anticancer drug sensitivity, Acta Biomaterialia 4(2) (2008) 256-263.
[189] H. Tan, J. Wu, L. Lao, C. Gao, Gelatin/chitosan/hyaluronan scaffold integrated with PLGA microspheres for cartilage tissue engineering, Acta Biomaterialia 5(1) (2009) 328-337.
[190] J. Lou, F. Liu, C.D. Lindsay, O. Chaudhuri, S.C. Heilshorn, Y. Xia, Dynamic Hyaluronan Hydrogels with Temporally Modulated High Injectability and Stability Using a Biocompatible Catalyst, Advanced Materials 30(22) (2018) 1705215.
[191] K. Zhu, H. Tu, P. Yang, C. Qiu, D. Zhang, A. Lu, L. Luo, F. Chen, X. Liu, L. Chen, Q. Fu, L. Zhang, Mechanically Strong Chitin Fibers with Nanofibril Structure, Biocompatibility, and Biodegradability, Chemistry of Materials 31(6) (2019) 2078-2087.
[192] M.-C. Li, Q. Wu, K. Song, H.N. Cheng, S. Suzuki, T. Lei, Chitin Nanofibers as Reinforcing and Antimicrobial Agents in Carboxymethyl Cellulose Films: Influence of Partial Deacetylation, ACS Sustainable Chemistry & Engineering 4(8) (2016) 4385-4395.
[193] P. Morganti, M. Palombo, G. Tishchenko, V.E. Yudin, F. Guarneri, M. Cardillo, P. Del Ciotto, F. Carezzi, G. Morganti, G. Fabrizi, Chitin-Hyaluronan Nanoparticles: A Multifunctional Carrier to Deliver Anti-Aging Active Ingredients through the Skin, Cosmetics 1(3) (2014) 140-158.
[194] M. Roman, W.T. Winter, Effect of Sulfate Groups from Sulfuric Acid Hydrolysis on the Thermal Degradation Behavior of Bacterial Cellulose, Biomacromolecules 5(5) (2004) 1671-1677.
[195] L. Suryanegara, H. Okumura, A.N. Nakagaito, H. Yano, The synergetic effect of phenylphosphonic acid zinc and microfibrillated cellulose on the injection molding cycle time of PLA composites, Cellulose 18(3) (2011) 689-698.
[196] J.H.H. Bongaerts, J.J. Cooper-White, J.R. Stokes, Low Biofouling Chitosan-Hyaluronic Acid Multilayers with Ultra-Low Friction Coefficients, Biomacromolecules 10(5) (2009) 1287-1294.
[197] S. Boddohi, N. Moore, P.A. Johnson, M.J. Kipper, Polysaccharide-Based Polyelectrolyte Complex Nanoparticles from Chitosan, Heparin, and Hyaluronan, Biomacromolecules 10(6) (2009) 1402-1409.
[198] P. Hariraksapitak, P. Supaphol, Preparation and properties of α-chitin-whisker-reinforced hyaluronan–gelatin nanocomposite scaffolds, Journal of Applied Polymer Science 117(6) (2010) 3406-3418.
[199] C. Peng, G. Chen, Preparation and Assessment of Heat-Treated α-Chitin Nanowhiskers Reinforced Poly(viny alcohol) Film for Packaging Application, Materials 11(10) (2018) 1883.
[200] J. Franková, V. Pivodová, H. Vágnerová, J. Juráňová, J. Ulrichová, Effects of Silver Nanoparticles on Primary Cell Cultures of Fibroblasts and Keratinocytes in a Wound-Healing Model, Journal of Applied Biomaterials & Functional Materials 14(2) (2016) 137-142.
[201] V. Tomšíčková, J. Frankova, P. Dolezel, J. Ulrichova, The Response of Osteoblast-Like SaOS-2 Cells to Modified Titanium Surfaces, 2013.
[202] G. Chaussard, A. Domard, New Aspects of the Extraction of Chitin from Squid Pens, Biomacromolecules 5(2) (2004) 559-564.
[203] M.H. Ottey, K.M. Vårum, O. Smidsrød, Compositional heterogeneity of heterogeneously deacetylated chitosans, Carbohydrate Polymers 29(1) (1996) 17-24.

[204] C. Roca, B. Chagas, I. Farinha, F. Freitas, L. Mafra, F. Aguiar, R. Oliveira, M.A.M. Reis, Production of yeast chitin–glucan complex from biodiesel industry byproduct, Process Biochemistry 47(11) (2012) 1670-1675.
[205] Y. Noishiki, H. Takami, Y. Nishiyama, M. Wada, S. Okada, S. Kuga, Alkali-Induced Conversion of β-Chitin to α-Chitin, Biomacromolecules 4(4) (2003) 896-899.
[206] P. Lepcio, F. Ondreas, K. Zarybnicka, M. Zboncak, O. Caha, J. Jancar, Bulk polymer nanocomposites with preparation protocol governed nanostructure: the origin and properties of aggregates and polymer bound clusters, Soft Matter 14(11) (2018) 2094-2103.
[207] P. Mahallati, M. Hassanabadi Hojjat, M. Wilhelm, D. Rodrigue, Rheological Characterization of Thermoplastic Elastomers (Tpe) Based on Pp and Recycled Epdm, Applied Rheology, 2016, p. 32.
[208] J. Jung, B.-K. Lee, S. Shin, Yield shear stress and disaggregating shear stress of human blood, Korea-Australia Rheology Journal 26(2) (2014) 191-198.
[209] P. Cassagnau, Melt rheology of organoclay and fumed silica nanocomposites, Polymer 49(9) (2008) 2183-2196.
[210] O. Akhlaghi, Y.Z. Menceloglu, O. Akbulut, Rheological behavior of poly(acrylonitrile) concentrated solutions: effect of Sb2O3 nanoparticles on shear and extensional flow, Colloid and Polymer Science 294(9) (2016) 1463-1473.
[211] G. Patras, G.G. Qiao, D.H. Solomon, Controlled Formation of Microheterogeneous Polymer Networks: Influence of Monomer Reactivity on Gel Structure, Macromolecules 34(18) (2001) 6396-6401.
[212] K. Gopalan Nair, A. Dufresne, Crab Shell Chitin Whisker Reinforced Natural Rubber Nanocomposites. 2. Mechanical Behavior, Biomacromolecules 4(3) (2003) 666-674.
[213] Y. Lu, L. Weng, L. Zhang, Morphology and Properties of Soy Protein Isolate Thermoplastics Reinforced with Chitin Whiskers, Biomacromolecules 5(3) (2004) 1046-1051.
[214] Y. Chen, C. Liu, P.R. Chang, X. Cao, D.P. Anderson, Bionanocomposites based on pea starch and cellulose nanowhiskers hydrolyzed from pea hull fibre: Effect of hydrolysis time, Carbohydrate Polymers 76(4) (2009) 607-615.
[215] J. Jancar, L. Recman, Particle size dependence of the elastic modulus of particulate filled PMMA near its T-g, Polymer 51(17) (2010) 3826-3828.
[216] J. Jancar, Review of the role of the interphase in the control of composite performance on micro- and nano-length scales, Journal of Materials Science 43(20) (2008) 6747-6757.
[217] R.M. Parker, B. Frka-Petesic, G. Guidetti, G. Kamita, G. Consani, C. Abell, S. Vignolini, Hierarchical Self-Assembly of Cellulose Nanocrystals in a Confined Geometry, ACS Nano 10(9) (2016) 8443-8449.
[218] B. Krajewska, P. Wydro, A. Jańczyk, Probing the Modes of Antibacterial Activity of Chitosan. Effects of pH and Molecular Weight on Chitosan Interactions with Membrane Lipids in Langmuir Films, Biomacromolecules 12(11) (2011) 4144-4152.
[219] P. Sahariah, B.E. Benediktssdóttir, M.Á. Hjálmarsdóttir, O.E. Sigurjonsson, K.K. Sørensen, M.B. Thygesen, K.J. Jensen, M. Másson, Impact of Chain Length on Antibacterial Activity and Hemocompatibility of Quaternary N-Alkyl and N,N-Dialkyl Chitosan Derivatives, Biomacromolecules 16(5) (2015) 1449-1460.
[220] H. Přichystalová, N. Almonasy, A.M. Abdel-Mohsen, R.M. Abdel-Rahman, M.M.G. Fouda, L. Vojtova, L. Kobera, Z. Spotz, L. Burgert, J. Jancar, Synthesis, characterization and antibacterial activity of new fluorescent chitosan derivatives, International Journal of Biological Macromolecules 65 (2014) 234-240.
[221] A.M. Abdel-Mohsen, A.S. Aly, R. Hrdina, A.T. El-Aref, A novel method for the preparation of silver/chitosan-O-methoxy polyethylene glycol core shell nanoparticles, Journal of Polymers and the Environment 20(2) (2012) 459-468.

[222] A. Zubareva, B. Shagdarova, V. Varlamov, E. Kashirina, E. Svirshchevskaya, Penetration and toxicity of chitosan and its derivatives, European Polymer Journal 93 (2017) 743-749.
[223] N. Haridas, M.J. Rosemary, Effect of steam sterilization and biocompatibility studies of hyaluronic acid hydrogel for viscosupplementation, Polymer Degradation and Stability 163 (2019) 220-227.
[224] Y. Fan, T. Saito, A. Isogai, Preparation of Chitin Nanofibers from Squid Pen β-Chitin by Simple Mechanical Treatment under Acid Conditions, Biomacromolecules 9(7) (2008) 1919-1923.
[225] L. Heux, J. Brugnerotto, J. Desbrières, M.F. Versali, M. Rinaudo, Solid State NMR for Determination of Degree of Acetylation of Chitin and Chitosan, Biomacromolecules 1(4) (2000) 746-751.
[226] J. Brus, Heating of samples induced by fast magic-angle spinning, Solid state nuclear magnetic resonance 16(3) (2000) 151-160.
[227] J. Spěváček, J. Brus, Solid-State NMR Studies of Polysaccharide Systems, Macromolecular Symposia 265(1) (2008) 69-76.
[228] S. Gong, W. Cui, Q. Zhang, A. Cao, L. Jiang, Q. Cheng, Integrated Ternary Bioinspired Nanocomposites via Synergistic Toughening of Reduced Graphene Oxide and Double-Walled Carbon Nanotubes, ACS Nano 9(12) (2015) 11568-11573.
[229] K.E. Prasad, B. Das, U. Maitra, U. Ramamurty, C.N.R. Rao, Extraordinary synergy in the mechanical properties of polymer matrix composites reinforced with 2 nanocarbons, Proceedings of the National Academy of Sciences 106(32) (2009) 13186-13189.
[230] H. Wang, R. Lu, J. Yan, J. Peng, A.P. Tomsia, R. Liang, G. Sun, M. Liu, L. Jiang, Q. Cheng, Tough and Conductive Nacre-inspired MXene/Epoxy Layered Bulk Nanocomposites, Angewandte Chemie International Edition 62(9) (2023) e202216874.
[231] J. Chang, M. Zhang, Q. Zhao, L. Qu, J. Yuan, Ultratough and ultrastrong graphene oxide hybrid films via a polycationitrile approach, Nanoscale Horizons 6(4) (2021) 341-347.
[232] C. Cheng, S. Li, A. Thomas, N.A. Kotov, R. Haag, Functional Graphene Nanomaterials Based Architectures: Biointeractions, Fabrications, and Emerging Biological Applications, Chemical Reviews 117(3) (2017) 1826-1914.
[233] D. Liu, X. Dong, B. Han, H. Huang, M. Qi, Cellulose nanocrystal/collagen hydrogels reinforced by anisotropic structure: Shear viscoelasticity and related strengthening mechanism, Composites Communications 21 (2020) 100374.
[234] S. Heinemann, C. Heinemann, M. Jäger, J. Neunzehn, H.P. Wiesmann, T. Hanke, Effect of Silica and Hydroxyapatite Mineralization on the Mechanical Properties and the Biocompatibility of Nanocomposite Collagen Scaffolds, ACS Applied Materials & Interfaces 3(11) (2011) 4323-4331.
[235] A. Orza, O. Soritau, L. Olenic, M. Diudea, A. Florea, D. Rus Ciuca, C. Mihu, D. Casciano, A.S. Biris, Electrically Conductive Gold-Coated Collagen Nanofibers for Placental-Derived Mesenchymal Stem Cells Enhanced Differentiation and Proliferation, ACS Nano 5(6) (2011) 4490-4503.
[236] L. Castaneda, J. Valle, N. Yang, S. Pluskat, K. Slowinska, Collagen Cross-Linking with Au Nanoparticles, Biomacromolecules 9(12) (2008) 3383-3388.
[237] J. Chen, Z. Ling, X. Wang, X. Ping, Y. Xie, H. Ma, J. Guo, Q. Yong, All bio-based chiral nematic cellulose nanocrystals films under supramolecular tuning by chitosan/deacetylated chitin nanofibers for reversible multi-response and sensor application, Chemical Engineering Journal 466 (2023) 143148.
[238] S. Zhang, D. Huang, H. Lin, Y. Xiao, X. Zhang, Cellulose Nanocrystal Reinforced Collagen-Based Nanocomposite Hydrogel with Self-Healing and Stress-Relaxation Properties for Cell Delivery, Biomacromolecules 21(6) (2020) 2400-2408.

[239] X. Wang, J. Peng, Y. Zhang, M. Li, E. Saiz, A.P. Tomsia, Q. Cheng, Ultratough Bioinspired Graphene Fiber via Sequential Toughening of Hydrogen and Ionic Bonding, ACS Nano 12(12) (2018) 12638-12645.
[240] Y. Yi, Y. Zhang, B. Mansel, Y.-n. Wang, S. Prabakar, B. Shi, Effect of Dialdehyde Carboxymethyl Cellulose Cross-Linking on the Porous Structure of the Collagen Matrix, Biomacromolecules 23(4) (2022) 1723-1732.
[241] W. Xia, X. Qin, Y. Zhang, R. Sinko, S. Keten, Achieving Enhanced Interfacial Adhesion and Dispersion in Cellulose Nanocomposites via Amorphous Interfaces, Macromolecules 51(24) (2018) 10304-10311.
[242] S. Muthuswamy, A. Viswanathan, R. Yegappan, V. Selvaprithiviraj, A.K. Vasudevan, R. Biswas, R. Jayakumar, Antistaphylococcal and Neutrophil Chemotactic Injectable κ-Carrageenan Hydrogel for Infectious Wound Healing, ACS Applied Bio Materials 2(1) (2019) 378-387.
[243] Y. Huang, M. Yao, X. Zheng, X. Liang, X. Su, Y. Zhang, A. Lu, L. Zhang, Effects of Chitin Whiskers on Physical Properties and Osteoblast Culture of Alginate Based Nanocomposite Hydrogels, Biomacromolecules 16(11) (2015) 3499-3507.
[244] M. Barbalinardo, M. Biagetti, F. Valle, M. Cavallini, G. Falini, D. Montroni, Green Biocompatible Method for the Synthesis of Collagen/Chitin Composites to Study Their Composition and Assembly Influence on Fibroblasts Growth, Biomacromolecules 22(8) (2021) 3357-3365.
[245] B. Zhang, M. Wang, H. Tian, H. Cai, S. Wu, S. Jiao, J. Zhao, Y. Li, H. Zhou, W. Guo, W. Qu, Functional hemostatic hydrogels: design based on procoagulant principles, Journal of Materials Chemistry B 12(7) (2024) 1706-1729.
[246] S. Olza, A.M. Salaberria, A. Alonso-Varona, A. Samanta, S.C.M. Fernandes, The role of nanochitin in biologically-active matrices for tissue engineering-where do we stand?, Journal of Materials Chemistry B 11(25) (2023) 5630-5649.
[247] F. Xing, Z. Chi, R. Yang, D. Xu, J. Cui, Y. Huang, C. Zhou, C. Liu, Chitin-hydroxyapatite-collagen composite scaffolds for bone regeneration, International Journal of Biological Macromolecules 184 (2021) 170-180.
[248] X. Li, Q. Feng, X. Liu, W. Dong, F. Cui, Collagen-based implants reinforced by chitin fibres in a goat shank bone defect model, Biomaterials 27(9) (2006) 1917-1923.
[249] J. Duan, S. Gong, Y. Gao, X. Xie, L. Jiang, Q. Cheng, Bioinspired Ternary Artificial Nacre Nanocomposites Based on Reduced Graphene Oxide and Nanofibrillar Cellulose, ACS Applied Materials & Interfaces 8(16) (2016) 10545-10550.
[250] S. Qiu, X. Ren, X. Zhou, T. Zhang, L. Song, Y. Hu, Nacre-Inspired Black Phosphorus/Nanofibrillar Cellulose Composite Film with Enhanced Mechanical Properties and Superior Fire Resistance, ACS Applied Materials & Interfaces 12(32) (2020) 36639-36651.
[251] P.L. Ritger, N.A. Peppas, A simple equation for description of solute release I. Fickian and non-fickian release from non-swellable devices in the form of slabs, spheres, cylinders or discs, Journal of Controlled Release 5(1) (1987) 23-36.
[252] V.O. Sousa Neto, C.C. Silva, A.F.L. Almeida, S.D. Figueiró, J.C. Góes, J.A.C. de Paiva, C.E.C. Magalhães, A.S.B. Sombra, Study of the electrical conductivity and piezoelectricity in iron doped collagen films, Solid State Sciences 4(1) (2002) 43-51.
[253] C.C. Silva, A.G. Pinheiro, S.D. Figueiró, J.C. Góes, J.M. Sasaki, M.A.R. Miranda, A.S.B. Sombra, Piezoelectric properties of collagen-nanocrystalline hydroxyapatite composites, Journal of Materials Science 37(10) (2002) 2061-2070.
[254] J. Juráňová, J. Aury-Landas, K. Boumediene, C. Baugé, D. Biedermann, J. Ulrichová, J. Franková, Modulation of Skin Inflammatory Response by Active Components of Silymarin, Molecules 24(1) (2019) 123.

[255] V. Pivodova, J. Frankova, P. Dolezel, J. Ulrichova, The response of osteoblast-like SaOS-2 cells to modified titanium surfaces, Int J Oral Maxillofac Implants 28(5) (2013) 1386-94.
[256] I. Rajzer, A. Kurowska, J. Frankova, R. Sklenářová, A. Nikodem, M. Dziadek, A. Jabłoński, J. Janusz, P. Szczygieł, M. Ziąbka, 3D-Printed Polycaprolactone Implants Modified with Bioglass and Zn-Doped Bioglass, Materials 16(3) (2023) 1061.
[257] M. Schu, E. Terriac, Scanning electron microscopy preparation of the cellular actin cortex: A quantitative comparison between critical point drying and hexamethyldisilazane drying, 16(7) (2021) e0254165.
[258] L. Vitagliano, G. Némethy, A. Zagari, H.A. Scheraga, Stabilization of the triple-helical structure of natural collagen by side-chain interactions, Biochemistry 32(29) (1993) 7354-9.
[259] A. Bhattacharjee, M. Bansal, Collagen structure: the Madras triple helix and the current scenario, IUBMB Life 57(3) (2005) 161-72.
[260] J.M. Anaya Mancipe, M. Lopes Dias, R.M.D.S. Moreira Thiré, Type I collagen – poly(vinyl alcohol) electrospun nanofibers: FTIR study of the collagen helical structure preservation, Polymer-Plastics Technology and Materials 61(8) (2022) 846-860.
[261] K.J. Payne, A. Veis, Fourier transform ir spectroscopy of collagen and gelatin solutions: Deconvolution of the amide I band for conformational studies, Biopolymers 27(11) (1988) 1749-1760.
[262] M.C. Chang, J. Tanaka, XPS study for the microstructure development of hydroxyapatite–collagen nanocomposites cross-linked using glutaraldehyde, Biomaterials 23(18) (2002) 3879-3885.
[263] M.R. Karim, M. Harun-Ur-Rashid, A.B. Imran, Effect of sizes of vinyl modified narrow-dispersed silica cross-linker on the mechanical properties of acrylamide based hydrogel, Scientific Reports 13(1) (2023) 5089.
[264] P. Das, V.C. Mai, H. Duan, Flexible Bioinspired Ternary Nanocomposites Based on Carboxymethyl Cellulose/Nanoclay/Graphene Oxide, ACS Applied Polymer Materials 1(6) (2019) 1505-1513.
[265] J. Wang, Q. Cheng, L. Lin, L. Jiang, Synergistic Toughening of Bioinspired Poly(vinyl alcohol)–Clay–Nanofibrillar Cellulose Artificial Nacre, ACS Nano 8(3) (2014) 2739-2745.
[266] T. Li, S. He, A. Stein, L.F. Francis, F.S. Bates, Synergistic Toughening of Epoxy Modified by Graphene and Block Copolymer Micelles, Macromolecules 49(24) (2016) 9507-9520.
[267] S. Wan, J. Peng, Y. Li, H. Hu, L. Jiang, Q. Cheng, Use of Synergistic Interactions to Fabricate Strong, Tough, and Conductive Artificial Nacre Based on Graphene Oxide and Chitosan, ACS Nano 9(10) (2015) 9830-9836.
[268] W.-T. Cao, F.-F. Chen, Y.-J. Zhu, Y.-G. Zhang, Y.-Y. Jiang, M.-G. Ma, F. Chen, Binary Strengthening and Toughening of MXene/Cellulose Nanofiber Composite Paper with Nacre-Inspired Structure and Superior Electromagnetic Interference Shielding Properties, ACS Nano 12(5) (2018) 4583-4593.
[269] J. Xu, L. Liu, J. Yu, Y. Zou, W. Pei, L. Zhang, W. Ye, L. Bai, Z. Wang, Y. Fan, Q. Yong, O.J. Rojas, Simple synthesis of self-assembled nacre-like materials with 3D periodic layers from nanochitin via hydrogelation and mineralization, Green Chemistry 24(3) (2022) 1308-1317.
[270] A.G.B. da Cruz, J.C. Góes, S.D. Figueiró, J.P.A. Feitosa, N.M.P.S. Ricardo, A.S.B. Sombra, On the piezoelectricity of collagen/natural rubber blend films, European Polymer Journal 39(6) (2003) 1267-1272.
[271] Z. Ma, S. Kang, J. Ma, L. Shao, Y. Zhang, C. Liu, A. Wei, X. Xiang, L. Wei, J. Gu, Ultraflexible and Mechanically Strong Double-Layered Aramid Nanofiber–Ti3C2Tx MXene/Silver Nanowire Nanocomposite Papers for High-Performance Electromagnetic Interference Shielding, ACS Nano 14(7) (2020) 8368-8382.

[272] A. Fakhry, G.B. Schneider, R. Zaharias, S. Şenel, Chitosan supports the initial attachment and spreading of osteoblasts preferentially over fibroblasts, Biomaterials 25(11) (2004) 2075-2079.
[273] X. Li, J. Xie, X. Yuan, Y. Xia, Coating Electrospun Poly(ε-caprolactone) Fibers with Gelatin and Calcium Phosphate and Their Use as Biomimetic Scaffolds for Bone Tissue Engineering, Langmuir 24(24) (2008) 14145-14150.
[274] X. Li, J. Xie, J. Lipner, X. Yuan, S. Thomopoulos, Y. Xia, Nanofiber Scaffolds with Gradations in Mineral Content for Mimicking the Tendon-to-Bone Insertion Site, Nano Letters 9(7) (2009) 2763-2768.
[275] J.F. Mano, G.A. Silva, H.S. Azevedo, P.B. Malafaya, R.A. Sousa, S.S. Silva, L.F. Boesel, J.M. Oliveira, T.C. Santos, A.P. Marques, N.M. Neves, R.L. Reis, Natural origin biodegradable systems in tissue engineering and regenerative medicine: present status and some moving trends, 2007.
[276] S.V. Madihally, H.W.T. Matthew, Porous chitosan scaffolds for tissue engineering, Biomaterials 20(12) (1999) 1133-1142.
[277] Z.-M. Huang, Y.Z. Zhang, M. Kotaki, S. Ramakrishna, A review on polymer nanofibers by electrospinning and their applications in nanocomposites, Composites Science and Technology 63(15) (2003) 2223-2253.
[278] I.K. Kwon, T. Matsuda, Co-Electrospun Nanofiber Fabrics of Poly(l-lactide-co-ε-caprolactone) with Type I Collagen or Heparin, Biomacromolecules 6(4) (2005) 2096-2105.
[279] L. Marinucci, C. Lilli, M. Guerra, S. Belcastro, E. Becchetti, G. Stabellini, E.M. Calvi, P. Locci, Biocompatibility of collagen membranes crosslinked with glutaraldehyde or diphenylphosphoryl azide: An in vitro study, Journal of Biomedical Materials Research Part A 67A(2) (2003) 504-509.
[280] A. Ibara, H. Miyaji, B. Fugetsu, E. Nishida, H. Takita, S. Tanaka, T. Sugaya, M. Kawanami, Osteoconductivity and Biodegradability of Collagen Scaffold Coated with Nano-β-TCP and Fibroblast Growth Factor 2, Journal of Nanomaterials 2013 (2013) 11.
[281] P.A. Marone, F.C. Lau, R.C. Gupta, M. Bagchi, D. Bagchi, Safety and toxicological evaluation of undenatured type II collagen, Toxicology Mechanisms and Methods 20(4) (2010) 175-189.
[282] B. Marelli, D. Le Nihouannen, S.A. Hacking, S. Tran, J. Li, M. Murshed, C.J. Doillon, C.E. Ghezzi, Y.L. Zhang, S.N. Nazhat, J.E. Barralet, Newly identified interfibrillar collagen crosslinking suppresses cell proliferation and remodelling, Biomaterials 54(0) (2015) 126-135.
[283] K. Merrett, W. Liu, D. Mitra, K.D. Camm, C.R. McLaughlin, Y. Liu, M.A. Watsky, F. Li, M. Griffith, D.E. Fogg, Synthetic neoglycopolymer-recombinant human collagen hybrids as biomimetic crosslinking agents in corneal tissue engineering, Biomaterials 30(29) (2009) 5403-5408.
[284] C. Yao, M. Markowicz, N. Pallua, E. Magnus Noah, G. Steffens, The effect of cross-linking of collagen matrices on their angiogenic capability, Biomaterials 29(1) (2008) 66-74.
[285] E. Jorge-Herrero, P. Fernández, J. Turnay, N. Olmo, P. Calero, R. García, I. Freile, J.L. Castillo-Olivares, Influence of different chemical cross-linking treatments on the properties of bovine pericardium and collagen, Biomaterials 20(6) (1999) 539-545.
[286] K.S. Weadock, E.J. Miller, L.D. Bellincampi, J.P. Zawadsky, M.G. Dunn, Physical crosslinking of collagen fibers: Comparison of ultraviolet irradiation and dehydrothermal treatment, Journal of Biomedical Materials Research 29(11) (1995) 1373-1379.
[287] S. Dhawan, A.K. Singla, V.R. Sinha, Evaluation of mucoadhesive properties of chitosan microspheres prepared by different methods, AAPS PharmSciTech 5(4) (2004) 122-128.

[288] J. Yang, F. Tian, Z. Wang, Q. Wang, Y.-J. Zeng, S.-Q. Chen, Effect of chitosan molecular weight and deacetylation degree on hemostasis, Journal of Biomedical Materials Research Part B: Applied Biomaterials 84B(1) (2008) 131-137.
[289] P. Pochanavanich, W. Suntornsuk, Fungal chitosan production and its characterization, Letters in Applied Microbiology 35(1) (2002) 17-21.
[290] F. Streit, F. Koch, M.C.M. Laranjeira, J.L. Ninow, Production of fungal chitosan in liquid cultivation using apple pomace as substrate, Brazilian Journal of Microbiology 40(1) (2009) 20-25.
[291] A. Chen, F. Pan, T. Zhang, C. Yu, Y. Xiao, S. Li, H. Xu, X. Xu, M. Han, Z. Xu, Characterization of chitin-glucan complex from Tremella fuciformis fermentation residue and evaluation of its antibacterial performance, International Journal of Biological Macromolecules 186 (2021) 649-655.
[292] H. Kim, S. Kang, K. Li, D. Jung, K. Park, J. Lee, Preparation and characterization of various chitin-glucan complexes derived from white button mushroom using a deep eutectic solvent-based ecofriendly method, International Journal of Biological Macromolecules 169 (2021) 122-129.
[293] Y. Liu, Q. Wu, X. Wu, S.A. Algharib, F. Gong, J. Hu, W. Luo, M. Zhou, Y. Pan, Y. Yan, Y. Wang, Structure, preparation, modification, and bioactivities of β-glucan and mannan from yeast cell wall: A review, International Journal of Biological Macromolecules 173 (2021) 445-456.
[294] R. Kollár, B.B. Reinhold, E. Petráková, H.J.C. Yeh, G. Ashwell, J. Drgonová, J.C. Kapteyn, F.M. Klis, E. Cabib, Architecture of the Yeast Cell Wall: β(1→6)-GLUCAN INTERCONNECTS MANNOPROTEIN, β(1→3)-GLUCAN, AND CHITIN*, Journal of Biological Chemistry 272(28) (1997) 17762-17775.
[295] E. Machová, K. Kvapilová, G. Kogan, J. Šandula, Effect of ultrasonic treatment on the molecular weight of carboxymethylated chitin–glucan complex from Aspergillus niger, Ultrasonics Sonochemistry 5(4) (1999) 169-172.
[296] Y.A. Skorik, A.V. Pestov, Y.G. Yatluk, Evaluation of various chitin-glucan derivatives from Aspergillus niger as transition metal adsorbents, Bioresource Technology 101(6) (2010) 1769-1775.
[297] N.E. Mushi, A review on native well-preserved chitin nanofibrils for materials of high mechanical performance, International Journal of Biological Macromolecules 178 (2021) 591-606.
[298] A. Hassainia, H. Satha, S. Boufi, Chitin from Agaricus bisporus: Extraction and characterization, International Journal of Biological Macromolecules 117 (2018) 1334-1342.
[299] M. Blumfield, K. Abbott, E. Duve, T. Cassettari, S. Marshall, F. Fayet-Moore, Examining the health effects and bioactive components in Agaricus bisporus mushrooms: a scoping review, The Journal of Nutritional Biochemistry 84 (2020) 108453.
[300] W.M.F.W. Nawawi, K.-Y. Lee, E. Kontturi, A. Bismarck, A. Mautner, Surface properties of chitin-glucan nanopapers from Agaricus bisporus, International Journal of Biological Macromolecules 148 (2020) 677-687.
[301] D. Araújo, V.D. Alves, S.A.C. Lima, S. Reis, F. Freitas, M.A.M. Reis, Novel hydrogels based on yeast chitin-glucan complex: Characterization and safety assessment, International Journal of Biological Macromolecules 156 (2020) 1104-1111.
[302] I.C. Ferreira, D. Araújo, P. Voisin, V.D. Alves, A.A. Rosatella, C.A.M. Afonso, F. Freitas, L.A. Neves, Chitin-glucan complex – Based biopolymeric structures using biocompatible ionic liquids, Carbohydrate Polymers 247 (2020) 116679.
[303] J. Liao, H. Huang, Magnetic chitin hydrogels prepared from Hericium erinaceus residues with tunable characteristics: A novel biosorbent for Cu2+ removal, Carbohydrate Polymers 220 (2019) 191-201.

[304] M.H. Mohammed, P.A. Williams, O. Tverezovskaya, Extraction of chitin from prawn shells and conversion to low molecular mass chitosan, Food Hydrocolloids 31(2) (2013) 166-171.
[305] N. Nwe, T. Furuike, H. Tamura, Chapter One - Isolation and Characterization of Chitin and Chitosan from Marine Origin, in: K. Se-Kwon (Ed.), Advances in Food and Nutrition Research, Academic Press2014, pp. 1-15.
[306] S. Bartnicki-Garcia, Cell Wall Chemistry, Morphogenesis, and Taxonomy of Fungi, Annual Review of Microbiology 22(1) (1968) 87-108.
[307] R.A.A. Muzzarelli, F. Tanfani, G. Scarpini, Chelating, film-forming, and coagulating ability of the chitosan–glucan complex from Aspergillus niger industrial wastes, Biotechnology and Bioengineering 22(4) (1980) 885-896.
[308] L. Burgert, R. Hrdina, V. Velebny, A.M. Abdel-Lattif, R. Sulakova, L. Sobotka, J. Betak, D. Smirnou, Method of Preparation of Polysaccharide Fibres, Wound Covers that Contain Them, Method of Manufacturing of Wound Covers, and Apparatus for Preparation of Polysaccharide Fibres, Google Patents, 2015.
[309] B. Chagas, I. Farinha, C.F. Galinha, F. Freitas, M.A.M. Reis, Chitin–glucan complex production by Komagataella (Pichia) pastoris: impact of cultivation pH and temperature on polymer content and composition, New Biotechnology 31(5) (2014) 468-474.
[310] R. Kale, A. Bajaj, Ultraviolet spectrophotometric method for determination of gelatin crosslinking in the presence of amino groups, J Young Pharm 2(1) (2010) 90-94.
[311] D.V. Bax, N. Davidenko, S.W. Hamaia, R.W. Farndale, S.M. Best, R.E. Cameron, Impact of UV- and carbodiimide-based crosslinking on the integrin-binding properties of collagen-based materials, Acta Biomaterialia 100 (2019) 280-291.
[312] M. Nair, S.M. Best, R.E. Cameron, Crosslinking Collagen Constructs: Achieving Cellular Selectivity Through Modifications of Physical and Chemical Properties, Applied Sciences 10(19) (2020) 6911.
[313] L. Mohee, G.S. Offeddu, A. Husmann, M.L. Oyen, R.E. Cameron, Investigation of the intrinsic permeability of ice-templated collagen scaffolds as a function of their structural and mechanical properties, Acta Biomaterialia 83 (2019) 189-198.
[314] A. Daskalova, C.S.R. Nathala, I. Bliznakova, E. Stoyanova, A. Zhelyazkova, T. Ganz, S. Lueftenegger, W. Husinsky, Controlling the porosity of collagen, gelatin and elastin biomaterials by ultrashort laser pulses, Applied Surface Science 292(0) (2014) 367-377.
[315] M. Miron-Mendoza, J. Seemann, F. Grinnell, The differential regulation of cell motile activity through matrix stiffness and porosity in three dimensional collagen matrices, Biomaterials 31(25) (2010) 6425-6435.
[316] A. Nagaraja, Y.M. Puttaiahgowda, A. Kulal, A.M. Parambil, T. Varadavenkatesan, Synthesis, Characterization, and Fabrication of Hydrophilic Antimicrobial Polymer Thin Film Coatings, Macromolecular Research 27(3) (2019) 301-309.
[317] M. He, H. Xiao, Y. Zhou, P. Lu, Synthesis, characterization and antimicrobial activities of water-soluble amphiphilic copolymers containing ciprofloxacin and quaternary ammonium salts, Journal of Materials Chemistry B 3(18) (2015) 3704-3713.
[318] T. Ristic, L. Zemljič, M. Novak Babič, M. Kralj Kuncic, S. Sonjak, N. Gunde-cimerman, S. Strnad, Antimicrobial efficiency of functionalized cellulose fibres as potential medical textiles, 2011, pp. 37-51.
[319] L. Su, Y. Yu, Y. Zhao, F. Liang, X. Zhang, Strong Antibacterial Polydopamine Coatings Prepared by a Shaking-assisted Method, Scientific reports 6 (2016) 24420-24420.
[320] S. Li, T. Zhu, J. Huang, Q. Guo, G. Chen, Y. Lai, Durable antibacterial and UV-protective Ag/TiO(2)@ fabrics for sustainable biomedical application, International journal of nanomedicine 12 (2017) 2593-2606.

[321] J.S. Pieper, T. Hafmans, J.H. Veerkamp, T.H. van Kuppevelt, Development of tailor-made collagen–glycosaminoglycan matrices: EDC/NHS crosslinking, and ultrastructural aspects, Biomaterials 21(6) (2000) 581-593.
[322] L.-P. Yan, Y.-J. Wang, L. Ren, G. Wu, S.G. Caridade, J.-B. Fan, L.-Y. Wang, P.-H. Ji, J.M. Oliveira, J.T. Oliveira, J.F. Mano, R.L. Reis, Genipin-cross-linked collagen/chitosan biomimetic scaffolds for articular cartilage tissue engineering applications, Journal of Biomedical Materials Research Part A 95A(2) (2010) 465-475.
[323] N. Davidenko, J.J. Campbell, E.S. Thian, C.J. Watson, R.E. Cameron, Collagen–hyaluronic acid scaffolds for adipose tissue engineering, Acta Biomaterialia 6(10) (2010) 3957-3968.
[324] A.J. van der Slot-Verhoeven, E.A. van Dura, J. Attema, B. Blauw, J. DeGroot, T.W.J. Huizinga, A.-M. Zuurmond, R.A. Bank, The type of collagen cross-link determines the reversibility of experimental skin fibrosis, Biochimica et Biophysica Acta (BBA) - Molecular Basis of Disease 1740(1) (2005) 60-67.
[325] L.H.H. Olde Damink, P.J. Dijkstra, M.J.A. van Luyn, P.B. van Wachem, P. Nieuwenhuis, J. Feijen, Cross-linking of dermal sheep collagen using a water-soluble carbodiimide, Biomaterials 17(8) (1996) 765-773.
[326] Z. Xia, X. Yu, X. Jiang, H.D. Brody, D.W. Rowe, M. Wei, Fabrication and characterization of biomimetic collagen-apatite scaffolds with tunable structures for bone tissue engineering, Acta biomaterialia 9(7) (2013) 7308-7319.
[327] G.L. Clark, A.F. Smith, X-ray Diffraction Studies of Chitin, Chitosan, and Derivatives, The Journal of Physical Chemistry 40(7) (1935) 863-879.
[328] A.M. Abdel-Mohsen, A.S. Aly, R. Hrdina, A. El-Aref, A novel method for the preparation of silver/chitosan-O-methoxy polyethylene glycol core shell nanoparticles, Journal of Polymers and the Environment 20(2) (2012) 459-468.
[329] R.H. Marchessault, Y. Deslandes, K. Ogawa, P.R. Sundararajan, X-Ray diffraction data for β-(1 → 3)-D-glucan, Canadian Journal of Chemistry 55(2) (1977) 300-303.
[330] J. Li, S. Zhuang, Antibacterial activity of chitosan and its derivatives and their interaction mechanism with bacteria: Current state and perspectives, European Polymer Journal 138 (2020) 109984.
[331] J. Li, X. Tian, T. Hua, J. Fu, M. Koo, W. Chan, T. Poon, Chitosan Natural Polymer Material for Improving Antibacterial Properties of Textiles, ACS Applied Bio Materials 4(5) (2021) 4014-4038.
[332] A.M. Abdel-Mohsen, R.M. Abdel-Rahman, R. Hrdina, A. Imramovský, L. Burgert, A.S. Aly, Antibacterial cotton fabrics treated with core–shell nanoparticles, International Journal of Biological Macromolecules 50(5) (2012) 1245-1253.
[333] S.J. Jeon, M. Oh, W.-S. Yeo, K.N. Galvão, K.C. Jeong, Underlying Mechanism of Antimicrobial Activity of Chitosan Microparticles and Implications for the Treatment of Infectious Diseases, PLOS ONE 9(3) (2014) e92723.
[334] S. Karunakaran, S. Pandit, B. Basu, M. De, Simultaneous Exfoliation and Functionalization of 2H-MoS2 by Thiolated Surfactants: Applications in Enhanced Antibacterial Activity, Journal of the American Chemical Society 140(39) (2018) 12634-12644.

Chapter 5

Summary, Conclusions and Future Work

The chapter's thesis summarizes the research work and findings of the dissertation. The conclusions are discussed here followed by a description of future research work.

1. Summary

These dissertations focused on the preparation of chitin nanocrystals, partially deacetylated chitin nanocrystals, chitosan-glucan fibrils complex, and preparation of nanocomposite materials (films, hydrogel membrane, and 3D scaffold). Chitin nanocrystals and their derivates were used as filler material to enhance the prepared matrix performance.

The **first part** of this dissertation presents some background on chitin/chitosan, sources, preparation of chitin nanocrystals, collagen, uses in medical purposes, hyaluronan derivatives, sources, and applications. In the **second part**, we prepared chitin nanocrystals (ChNCs) via a chemical process from an animal source (shrimp shell). The effects of time, temperature, and acid concentration on the morphology (width, length) were investigated and optimized. The NCs obtained after acid treatment were investigated and characterized by XRD, SEM, TEM, and ^{13}C-ssNMR. The results showed that there were no significant effects of acid treatment on the DDA of the NCs, but there were significant changes in the dimensions of the NCs. The width and length of the NCs decreased from 36 and 1265 nm to 20 and 420 nm, with an increase in the treatment time from 1 to 6 h with 3M HCl, respectively.

Hyaluronan nanocomposite films were prepared via an evaporation-induced self-assembly method using ChNCs as a nanofiller polymer (HA-ChNCs) and showed enhanced mechanical properties compared to those of HA films with a high-volume fraction of the NCs. The mechanical and fracture morphology results visualized using SEM showed enhanced interfacial bonding via the formation of stronger electrostatic and chemical attractions at the ChNWs-HA interface. Hyaluronan/ chitin nanocrystal composite films exhibited good antibacterial properties against different types of bacteria (-/+ G) which was improved with the increasing volume fraction of the NCs loaded into the HA matrix.

The novel films significantly enhanced cell viability (NHDF, Saos-2) without any toxicity. It was expected that the present work would not only enrich the high value of seafood wastes utilized but also provide an alternative way to prepare edible, sustainable, environmentally friendly, mechanical enhancement, and antibacterial films for active food packaging application, drug-carrier application as well as for tissue regeneration purposes.

A novel method for creating a layered nacre-like material has been introduced, using triple-helical tropocollagen (CO) and partially deacetylated chitin nanocrystals (ChNCs), along with Octenidine dihydrochloride nanosphere particles (OCT). ChNCs play a crucial role in enhancing the stability of the triple-helical structure of tropocollagen and promoting fibrillar arrangement through hydrogen bonding and other weaker electrostatic interactions.

This hierarchical microstructure formation resulted in the development of a layer material, referred to as LHM. The LHM exhibited remarkable improvements in mechanical properties, including increased modulus, strength, and toughness, compared to the LHM prepared without ChNCs. These enhancements were attributed to the incorporation of ChNCs and OCT, a drug model. The synergy between ChNCs and OCT further contributed to the enhanced mechanical performance of the material, surpassing that of natural nacre and other synthetic layered composite materials. A notable aspect of the synthesized nacre-like material was its excellent biocompatibility, demonstrated by its ability to support the adhesion, spread, and proliferation of *NHDF* and *Saos-2* cells. By varying the ratios of ChNCs, the material properties may be tailored to meet specific requirements.

A new cell carrier for tissue engineering purposes was synthesized using the CO-g-CSGCF-HBS hybrid biocomposite scaffold of the collagen-chitosan-glucan complex fibrils. The chemical interaction between CO and CSGCF was confirmed by ATR-FTIR, TGA, SEM, and XRD. The obtained results, the formation of new ester bonds improved the crystallinity and thermal stability of HBS. The HBS exhibited significant hydrolytic stability and mechanical properties in comparison with net CO. From the SEM spectra, CSGCF adhered to the surface of the CO fibrils. CO-g-CSGCF-HBS exhibited a significant improvement in the adhesion, viability, and proliferation of *MSCs* compared to the control, CO, and CSGCF scaffolds. HBS exhibited excellent antibacterial activity against different types of bacteria (*G* -/+) compared to the control sample. The hybrid biocomposite scaffold showed a unique property, such as high swelling percentage, excellent antibacterial activity, noncytotoxicity, and high biocompatible properties with improving mechanical and hydrolytic stability.

2. Conclusions

This dissertation represented new nanocomposite materials based on chitin nanocrystals and their derivatives, and the preparation of film, hydrogel membrane, and 3D scaffold. From the data obtained, chitin nanocrystals are considered promising nanofiller organic polymers in nanocomposite applications. From the biological activity and the results of the cytotoxicity, we can conclude that all prepared chitin nanocrystals-based nanocomposites can be used and applied for medical purposes, especially in implantable purposes, such as wound dressing/bone and healthcare and hygiene applications and control drug delivery applications.

3. Future work

Based on the findings of this dissertation, the following future studies are recommended:

- Preparation of hydrophilic and hydrophobic chitin nanocrystals via chemical modification of the ChNCs with hydrophilic/hydrophobic polymers.
- Chemical modification of ChNCs with acrylate end groups and use as filler polymer for 3D printing materials.
- More biological measurements such as in vitro and in vivo tests to prove the concept that chitin nanocrystal composite-based materials are safe for many medical applications

Author publications and other output

1. Publications

1.1. First author papers used in thesis

1. **Rasha M. Abdel-Rahman**, A. M. Abdel-Mohsen, M. Zboncak, J. Frankova, P. Lepcio, L. Kobera, M. Steinhart, D. Pavlinak, Z. Spotz, R. Sklenářévá, J. Brus, J. Jancar. Hyaluronan Films Reinforced with Partially Deacetylated Chitin Nanowhiskers: Extraction, Fabrication, *In-vitro* and Antibacterial Properties of Advanced Nanocomposites. Carbohydrate Polymers**,** 2020, 235,115951.
2. **Rasha M. Abdel-Rahman**, A. M. Abdel-Mohsen, Jana Frankova, Francesco Piana, Lukas Kalina, Veronika Gajdosova, Ludmila Kapralkova, Muhammed Arshad Thottappali, Josef Jancar. Self-assembled hydrogel membranes with structurally tunable mechanical and biological properties. ACS Biomacromolecues, 2024, 25, 6, 3449–3463.
3. **Rasha M. Abdel-Rahman**, V. Vishakha, I. Kelnar, J. Jancar, A. M. Abdel-Mohsen. Synergistic Performance of Collagen-g-Chitosan-Glucan Fiber Biohybrid Scaffold with Tunable Properties. International journal of biological macromolecules **2022,** 202, 671-680.

1.2. Other first and Co-author papers

1. **Rasha M. Abdel-Rahman**, AM Abdel-Mohsen. Marine Biomaterials: Hyaluronan. Marine Drugs. **2023**, 21 (8), 426
2. A. M. Abdel-Mohsen, **Rasha M. Abdel-Rahman**, L. Kalina, V. Vishakha, L. Kaprelkova, P. Nemecek, J. Jancar. Effect of Chitin Nanocrystal Deacetylation on a Nature-Mimicking Interface in Carbon Fiber Composites. Journal of Composites Science.**2024**, 8 (5), 163.
3. Ivan Kelnar, Ludmila Kaprálková, Pavel Němeček, Jiří Dybal, **Rasha M Abdel-Rahman**, Michaela Vyroubalová, Martina Nevoralová, A.M. Abdel-Mohsen. The Effects of the Deacetylation of Chitin Nanowhiskers on the Performance of PCL/PLA Bio-Nanocomposites. Polymers **2023,** 15(14), 3071.
4. Ehsan Naderi Kalali, A. M. Abdel-Mohsen, O Pop-Georgievski, **Rasha M Abdel-Rahman**, Chengshou Zhao, Xin Wang, Nima Esmaeili, Josef Petrus. An eco-friendly, highly efficient, and transparent coating derived from guar gum and citric acid for flame retardant treatment of cotton fabrics. International Journal of Biological Macromolecules **2023**,253, 127506.
5. **Rasha M. Abdel-Rahman**, J. Frankova, R. Sklenářévá, L. Kapralkova, I. Kelnar, A. M. Abdel-Mohsen. Hyaluronan/zinc oxide nanocomposite-based Membrane: Preparation, Characterization, In vitro and In vivo Evaluation. ACS Applied Polymer Materials. ACS Appl. Polym. Mater. **2022**, 4, 7723−7738.
6. A.M. Abdel-Mohsen, **Rasha M. Abdelrahman**, J. Frankova, M. Steinhart, D, J. Jancar. Chitosan-glucan Complex Hollow Fibers Reinforced Collagen Wound Dressing Embedded with Aloe vera. Part II: multifunctional properties to promote wound healing. International Journal of Pharmaceutics,582, **2020**, 119349.
7. AM Abdel-Mohsen, **Rasha M. Abdel-Rahman**, I Kubena, L Kobera, Z Spotez, M Zboncak, R Prikryl, J Brus, J Jancar. Chitosan-glucan Complex Hollow Fibers Reinforced Collagen Wound Dressing Embedded with Aloe vera. Part I: Preparation and Characterization. Carbohydrate Polymers, **2020,** 115708,
8. AM Abdel-Mohsen, D Pavliňák, M Čileková, P Lepcio, **Rasha M. Abdel-Rahman**, J Jančář. Electrospinning of hyaluronan/polyvinyl alcohol in presence of in-situ silver nanoparticles: Preparation and characterization. International journal of biological macromolecules, **2019,** 139, 730-739.
9. A.M. Abdel-Mohsen, J. Jancar, **Rasha M. Abdel-Rahman**, L. Vojtek, P. Hyršl, M. Dušková, H. Nejezchlebová. A novel in situ silver/hyaluronan bio-nanocomposite fabrics for wound and chronic ulcer dressing: In vitro and in vivo evaluations. International Journal of Pharmaceutics, 520, 1–2, **2017,** 241-253.
10. **Rasha M. Abdel-Rahman**, A.M. Abdel-Mohsen, R. Hrdina, L. Burgert, Z. Fohlerova, D. Pavlinak. Sayed, J. Jancar. Wound dressing based on chitosan/hyaluronan/nonwoven fabrics: Preparation, characterization, and medical applications. International Journal of Biological Macromolecules 89, **2016,** 725–736.

1.3. National and international conferences

- ✓ **Rasha M. Abdel-Rahman,** M. Abdel-Mohsen, Josef. Jančář. In situ silver/Hyaluronan Bio-nanocomposite Fabrics for Wound and Chronic Ulcer Dressing: In Vitro and In Vivo Evaluations. 29th Annual Congress of the European Society for Biomaterials. 9–13 September 2018, Maastricht, Netherlands.
- ✓ **Rasha M. Abdel-Rahman,** A.M. Abdel-Mohsen, Radim Hrdina, Josef Jančář. 3D scaffold based on chitosan-glucan hollow fiber/ collagen for tissue engineering applications. 50th National Coloristic Conference, TEXCHEM, Pardubice, Czech Republic. 08-09.11.2018.
- ✓ J. Frankova, **Rasha M. Abdel-Rahman**, A. M. Abdel-Mohsen, J. Jančář, J. ULRICHOVÁ. Biocompatibility and toxicity of selected biomaterials. 70th Chemical Congress on behalf of the Czech Chemical Society, 9-12-9 2018, Zelin City, Czech Republic.
- ✓ **Rasha M. Abdel-Rahman** J. Jancar, A. M. Abdel-Mohsen, I. Kelnar. Hyaluronan films reinforced with deacetylated chitin nanocrystal 7th International Conference of polysaccharide, 10-15 October 2021, Nantes, France
- ✓ **Rasha M. Abdel-Rahman**, A. M. Abdel-Mohsen, J. Jancar, I. Kelnar. Chitosan-glucan complex reinforced collagen wound dressing with multi-functional properties for cutaneous wound healing. 7th International Conference of polysaccharide, 10-15 October 2021, Nantes, France
- ✓ A. M. Abdel-Mohsen, **Rasha M. Abdel-Rahman**, J. Jancar, I. Kelnar. Chitosan-glucan/collagen hybrid scaffold: preparation and characterization. Book of Abstracts. Graz: Graz University of Technology, 2023, s. 90.8th EPNOE International Polysaccharide Conference. Graz, Austria, 17.-22.9.2023.
- ✓ **Rasha M. Abdel-Rahman**, A. M. Abdel-Mohsen, J. Jancar. Preparation, and characterization of hyaluronan/zinc oxide nanocomposite-based membrane. Book of Abstracts. Graz: Graz University of Technology, 2023, s. 247. 8th EPNOE International Polysaccharide Conference Graz, Austria, 17.-22.9.2023.

Projects (PI, team member)

- ✓ Bridge Fund Project, Czech Science Foundation (2018-2019)
- ✓ Nanotechnologies and Novel Materials I (2017- 2019)

Scholarships

- ✓ Educational Award: Full Scholarship from Czech Republic, Central European Institute of Technology, Brno University of Technology, Brno, Czech Republic
- ✓ Martina Roeselová Memorial Fellowship (2020-2021)